NIST Special Publication 1000-5

June 2004
Progress Report on the Federal Building and Fire Safety Investigation of the World Trade Center Disaster

Volume 5
Contains Appendices J, K, L, and M

NIST National Institute of Standards and Technology • Technology Administration • U.S. Department of Commerce

NIST Special Publication 1000-5

June 2004
Progress Report on the Federal Building and Fire Safety Investigation of the World Trade Center Disaster

Volume 5
Contains Appendices J, K, L, and M

June 2004

U.S. Department of Commerce
Donald L. Evans, Secretary

Technology Administration
Phillip J. Bond, Under Secretary for Technology

National Institute of Standards and Technology
Arden L. Bement, Jr., Director

Disclaimer

Certain commercial entities, equipment, products, or materials are identified in this document in order to describe a procedure or concept adequately or to trace the history of the procedures and practices used. Such identification is not intended to imply recommendation, endorsement, or implication that the entities, products, materials, or equipment are necessarily the best available for the purpose. Nor does such identification imply a finding of fault or negligence by the National Institute of Standards and Technology.

Disclaimer

The policy of NIST is to use the International System of Units (metric units) in all publications. In this document, however, units are presented in metric units or the inch-pound system, whichever is prevalent in the discipline.

Use in Legal Proceedings

No part of any report resulting from a NIST investigation into a structural failure or from an investigation under the National Construction Safety Team Act may be used in any suit or action for damages arising out of any matter mentioned in such report (15 USC 281a; as amended by P.L. 107-231).

National Institute of Standards and Technology Special Publication 1000-5
Natl. Inst. Stand. Technol. Spec. Publ. 1000-5, 1,054 pages (June 2004)
CODEN: NSPUE2

U.S. GOVERNMENT PRINTING OFFICE
WASHINGTON: 2004

For sale by the Superintendent of Documents, U.S. Government Printing Office
Internet: bookstore.gpo.gov — Phone: (202) 512-1800 — Fax: (202) 512-2250
Mail: Stop SSOP, Washington, DC 20402-0001

Master Table of Contents

Volume 3

Volume 4

Volume 5

Volume 6

This page intentionally left blank.

List of Acronyms and Abbreviations

AAPOR	American Association of Public Opinion Research
ABC	American Broadcasting Company
ACI	American Concrete Institute
AISC	American Institute of Steel Construction
AISI	American Iron and Steel Institute
ALE	Arbitrary-Lagrangian-Evlerian
AMCBO	Association of Major City/County Building Officials
ANSI	American National Standards Institute
ANSYS	finite element model
ARA	Applied Research Associates, Inc.
ASCE	American Society of Civil Engineers
ASHRAE	American Society of Heating, Refrigerating and Air-Conditioning Engineers, Inc.
ASME	American Society of Mechanical Engineers
ASTM	ASTM International
AWS	American Welding Society
BOCA	Building Officials and Code Administrators
BOCA/BBC	BOCA Basic Building Code
BPAT	Building Performance Assessment Team
BPS	Building Performance Study
BSI	British Standards Institution
C/F	cancer free
CATI	computer-assisted telephone interviews
CBR	chemical, biological, and radiological
CBS	Columbia Broadcasting System
CERF	Civil Engineering Research Foundation
CFD	computational fluid dynamics
CIB	International Council for Research and Innovation in Building and Construction
CII	Construction Industry Institute
CNN	Cable News Network

CPP	Cermak Peterka Peterson, Inc.
CPU	central processing unit
CRT	cathode-ray tube
CTB&UH	Council on Tall Buildings and Urban Habitat
CTE	coefficients of thermal expansion
DC/F	BlazeShield DC/F fire protective insulation
DL	dead load
DTAP	dissemination and technical assistance program
EMS	Emergency Medical Service
EMT	Emergency Medical Team
ER&S	Emory Roth & Sons
FBI	Federal Bureau of Investigation
FCA	Flux cored arc
FDNY	New York City Fire Department
FDS	Fire Dynamics Simulator
FE	finite element
FEA	finite element analysis
FEM	finite element model
FEMA	Federal Emergency Management Agency
FMRC	Factory Mutual Research Corp.
FSI	Fire-Structure Interface
FVM	Finite Volume Method
GFI	Government Furnished Information
GG	glass over glass
GHz	gigahertz
GMS, LLP	Gilsanz Murray Steficek, LLP
HAZ	heat affected zone
HNSE	Hugo Nue Schnutzer East
HRR	heat release rate
HVAC	heating, ventilating, and air conditioning
IAQ	indoor air quality
IBC	International Building Code

ICBO	International Conference of Building Officials
ICC	International Code Council
IMTI	Integrated Manufacturing Technology
JFK	John F. Kennedy International Airport
JIS	Japan Industrial Standard
LERA	Leslie E. Robertson Associates
LES	Large Eddy Simulation
LL	live load
LSTC	Livermore Software Technology Corporation
MBC	BOCA National Building Code
MCC	Municipal Code of Chicago
MPI	Message Passing Interface
NBC	National Broadcasting Company
NBFU	National Board of Fire Underwriters
NCSBCS	National Conference of States on Building Codes & Standards, Inc.
NCST	National Construction Safety Team
NEMA	National Electrical Manufacturers Association
NFPA	National Fire Protection Association
NIBS	National Institute of Building Sciences
NIST	National Institute of Standards and Technology
NYC	New York City
NYCBC	New York City Building Code
NYCDOB	New York City Department of Buildings
NYPD	New York City Police Department
NYSBC	New York State Building Construction Code
P.L.	Public Law
PANYNJ	Port Authority of New York and New Jersey
PAPD	Port Authority Police Department
PC&F	Pacific Car and Foundry
PDM	Pittsburg-Des Moines
PONYA	Port of New York Authority
R&D	research and development

RWDI	Rowan Williams Davis and Irwin, Inc.
SBCCI	Southern Standard Building Code
SDL	superimposed dead load
SDO	standards development organization
SEAoNY	Structural Engineers Association of New York
SFPE	Society of Fire Protection Engineering
SFRM	spray-on fire resistant material or sprayed fire resistive materials
SHCR	Skilling, Helle, Christiansen, & Robertson
SI	metric
SLB	short legs back-to-back
SMA	Shielded Metal Arc
SOD	Special Operations Division
SOM	Skidmore, Ownings & Merrill
SPH	Smoothed Particle Hydrodynamics
SQL	Structured Query Language
SWMB	Skilling, Ward, Magnussen, and Barkshire
TL	Truss Lower Chord
TM	Truss Middle Chord
TU	Truss Upper Chord
UBC	Uniform Building Code
UL	Underwriters' Laboratories, Inc.
USC	United States Code
USM	United States Mineral Products Co.
VCBT	Virtual Cybernetic Building Testbed
WABC	WABC-TV New York
WCBS	WCBS-TV New York
WF	wide flange (a type of structural steel shape now usually called a W-shape). ASTM A 6 defines them as "doubly-symmetric, wide-flange shapes with inside flange surfaces that are substantially parallel."
WNBC	NBC4 New York
WNYW	FOX5 New York
WPIX	WPIX-TV New York
WTC	World Trade Center

WTC 1	World Trade Center Tower 1
WTC 2	World Trade Center Tower 2
WTC 7	World Trade Center Building 7

Abbreviations

×	by
±	plus or minus
°C	degrees Celsius
°F	degrees Fahrenheit
μm	micrometer
2D	two dimensional
3D	three dimensional
cm	centimeter
ft	foot
ft^2	square foot
F_y	yield strength (AISC usage)
g	acceleration (gravity)
g	gram
gal	gallon
h	hour
in.	inch
kg	kilogram
kip	a stress unit equal to 1,000 pounds
kJ	kilojoule
kN	kilonewton
kPa	kilopascal
klb	1,000 pounds
ksi	1,000 pounds per square inch
kW	kilowatt
kW/m^2	kilowatts per square meter
L	liter
lb	pound
m	meter
m^2	square meter
mm	millimeter
m/s	meters per second

min	minute
MJ	megajoule
MPa	megapascal
mph	miles per hour
ms	microsecond
Msi	millions pounds per square inch
MW	megawatt
N	newton
Pa	pascal
pcf	pounds per cubic foot
plf	pounds per linear foot
psf	pounds per square foot
psi	pounds per square inch
s	second

This page intentionally left blank.

METRIC CONVERSION TABLE

To convert from	to	Multiply by
AREA AND SECOND MOMENT OF AREA		
square foot (ft^2)	square meter (m^2)	9.290 304 E-02
square inch (in^2)	square meter (m^2)	6.4516 E-04
square inch (in^2)	square centimeter (cm^2)	6.4516 E+00
square yard (yd^2)	square meter (m^2)	8.361 274 E-01
ENERGY (includes WORK)		
kilowatt hour (kW * h)	joule (J)	3.6 E+06
quad (1015 BtuIT)	joule (J)	1.055 056 E+18
therm (U.S.)	joule (J)	1.054 804 E+08
ton of TNT (energy equivalent)	joule (J)	4.184 E+09
watt hour (W * h)	joule (J)	3.6 E+03
watt second (W * s)	joule (J)	1.0 E+00
FORCE		
dyne (dyn)	newton (N)	1.0 E-05
kilogram-force (kgf)	newton (N)	9.806 65 E+00
kilopond (kilogram-force) (kp)	newton (N)	9.806 65 E+00
kip (1 kip=1000 lbf)	newton (N)	4.448 222 E+03
kip (1 kip=1000 lbf)	kilonewton (kN)	4.448 222 E+00
pound-force (lbf)	newton (N)	4.448 222 E+00
FORCE DIVIDED BY LENGTH		
pound-force per foot (lbf/ft)	newton per meter (N/m)	1.459 390 E+01
pound-force per inch (lbf/in)	newton per meter (N/m)	1.751 268 E+02
HEAT FLOW RATE		
calorieth per minute (calth/min)	watt (W)	6.973 333 E-02
calorieth per second (calth/s)	watt (W)	4.184 E+00
kilocalorieth per minute (kcalth/min)	watt (W)	6.973 333 E+01
kilocalorieth per second (kcalth/s)	watt (W)	4.184 E+03

To convert from	to	Multiply by
LENGTH		
foot (ft)	meter (m)	3.048 E-01
inch (in)	meter (m)	2.54 E-02
inch (in)	centimeter (cm)	2.54 E+00
micron (m)	meter (m)	1.0 E-06
yard (yd)	meter (m)	9.144 E-01
MASS and MOMENT OF INERTIA		
kilogram-force second squared per meter (kgf * s^2/m)	kilogram (kg)	9.806 65 E+00
pound foot squared (lb * ft^2)	kilogram meter squared (kg * m^2)	4.214 011 E-02
pound inch squared (lb * in^2)	kilogram meter squared (kg * m^2)	2.926 397 E-04
ton, metric (t)	kilogram (kg)	1.0 E+03
ton, short (2000 lb)	kilogram (kg)	9.071 847 E+02
MASS DIVIDED BY AREA		
pound per square foot (lb/ft^2)	kilogram per square meter (kg/m^2)	4.882 428 E+00
pound per square inch (*not* pound force) (lb/in^2)	kilogram per square meter (kg/m^2)	7.030 696 E+02
MASS DIVIDED BY LENGTH		
pound per foot (lb/ft)	kilogram per meter (kg/m)	1.488 164 E+00
pound per inch (lb/in)	kilogram per meter (kg/m)	1.785 797 E+01
pound per yard (lb/yd)	kilogram per meter (kg/m)	4.960 546 E-01
PRESSURE or STRESS (FORCE DIVIDED BY AREA)		
kilogram-force per square centimeter (kgf/cm^2)	pascal (Pa)	9.806 65 E+04
kilogram-force per square meter (kgf/m^2)	pascal (Pa)	9.806 65 E+00
kilogram-force per square millimeter (kgf/mm^2)	pascal (Pa)	9.806 65 E+06
kip per square inch (ksi) (kip/in^2)	pascal (Pa)	6.894 757 E+06
kip per square inch (ksi) (kip/in^2)	kilopascal (kPa)	6.894 757 E+03
pound-force per square foot (lbf/ft^2)	pascal (Pa)	4.788 026 E+01
pound-force per square inch (psi) (lbf/in^2)	pascal (Pa)	6.894 757 E+03
pound-force per square inch (psi) (lbf/in^2)	kilopascal (kPa)	6.894 757 E+00
psi (pound-force per square inch) (lbf/in^2)	pascal (Pa)	6.894 757 E+03
psi (pound-force per square inch) (lbf/in^2)	kilopascal (kPa)	6.894 757 E+00

To convert from	to	Multiply by
TEMPERATURE		
degree Celsius (°C)	kelvin (K)	T/K = t/ °C + 273.15
degree centigrade	degree Celsius (°C)	t/ °C ≈ t /deg. cent.
degree Fahrenheit (°F)	degree Celsius (°C)	t/ °C = (t/ °F 2 32)/1.8
degree Fahrenheit (°F)	kelvin (K)	T/K = (t/ °F + 459.67)/1.8
kelvin (K)	degree Celsius (°C)	t /°C = T/ K 2 273.15
TEMPERATURE INTERVAL		
degree Celsius (°C)	kelvin (K)	1.0 E+00
degree centigrade	degree Celsius (°C)	1.0 E+00
degree Fahrenheit (°F)	degree Celsius (°C)	5.555 556 E-01
degree Fahrenheit (°F)	kelvin (K)	5.555 556 E-01
degree Rankine (°R)	kelvin (K)	5.555 556 E-01
VELOCITY (includes SPEED)		
foot per second (ft/s)	meter per second (m/s)	3.048 E-01
inch per second (in/s)	meter per second (m/s)	2.54 E-02
kilometer per hour (km/h)	meter per second (m/s)	2.777 778 E-01
mile per hour (mi/h)	kilometer per hour (km/h)	1.609 344 E+00
mile per minute (mi/min)	meter per second (m/s)	2.682 24 E+01
VOLUME (includes CAPACITY)		
cubic foot (ft^3)	cubic meter (m^3)	2.831 685 E-02
cubic inch (in^3)	cubic meter (m^3)	1.638 706 E-05
cubic yard (yd^3)	cubic meter (m^3)	7.645 549 E-01
gallon (U.S.) (gal)	cubic meter (m^3)	3.785 412 E-03
gallon (U.S.) (gal)	liter (L)	3.785 412 E+00
liter (L)	cubic meter (m^3)	1.0 E-03
ounce (U.S. fluid) (fl oz)	cubic meter (m^3)	2.957 353 E-05
ounce (U.S. fluid) (fl oz)	milliliter (mL)	2.957 353 E+01

This page intentionally left blank.

TABLE OF CONTENTS

List of Figures

List of Tables

This page intentionally left blank.

Appendix J
INTERIM REPORT ON EXPERIMENTS TO SUPPORT FIRE DYNAMICS AND THERMAL RESPONSE MODELING

J.1 INTRODUCTION

The reconstruction of the World Trade Center (WTC) fires involves two computation models:

- Fire Dynamics Simulator (FDS): This is the first large-domain CFD fire model that predicts and visualizes the spread, growth and suppression of a fire based on the underlying scientific principles governing fluid motion. The model numerically solves the conservation equations of mass, momentum and energy that govern low-speed, thermally driven flows with an emphasis on smoke and heat transport from fires. The companion software package, called Smokeview, graphically presents the results of the FDS three-dimensional (3D) time-dependent simulation. Smokeview animates in three dimensions the smoke particulates, heat fluxes, temperatures and fluid velocities within a building. Users of the package can view the enclosure from any angle and from inside or outside.

- Fire-Structure Interface (FSI): This code effects the transfer of radiant and convective heat from a CFD fire model, such as FDS, to a coupled, transient, three-dimensional finite element model for the thermal response of structural members, such as ANSYS. The members may be simple (e.g., bare steel) or complex (e.g., insulation-coated steel).

For application to the Investigation, each of these needs experimental data (a) to guide adaptation/development of the models for this specific purpose and (b) with which to ascertain the accuracy of the model predictions. Ideally the uncertainty in the agreement with experiments will be much smaller than the effect of varying the unknowns in the actual conditions on September 11, 2001.

The following text describes three sets of experiments designed to accomplish this. All three sets have been completed, and the analysis of the data is under way. Full reports are in preparation and will be completed in summer 2004. Attachment 1 is a short paper on the modeling and experiments that will be presented at Interflam in July 2004.

J.2 EXPERIMENTS FOR ACCURACY ASSESSMENT OF THERMAL ENVIRONMENT MODELING

The purposes of these experiments, conducted in the National Institute of Standards and Technology (NIST) Large-scale Fire Laboratory from March 10 through 26, 2003, were to:

- Assess the accuracy with which FDS predicts the thermal environment in a burning compartment and;

- Establish a data set to validate the prediction of the temperature rise of structural steel elements using FSI.

Within a large test compartment, assorted steel members were exposed to controlled fires of varying heat release rate (HRR) and radiative intensity. The steel members were bare or coated with spray-applied fireproofing of two thicknesses. The thermal profile of the fire was measured at multiple locations within the compartment. Temperatures were also recorded at multiple locations on the surfaces of the steel, the insulation, and the compartment. Prior to each test, a prediction of the thermal environment in the compartment was determined using FDS. Following the tests, the prediction and experimental results were compared.

J.2.1 Description of Experiments

The test compartment consisted of a steel stud frame lined with calcium silicate board. The internal dimensions of the compartment were 3 m high, 7 m deep, and 4 m wide. There were four openings in the west wall through which air entered the room; they totaled 1.75 m^2 (10.8 ft^2) in area and were located 1 m (3.3 ft) above the floor. There were four openings in the east wall through which heat and combustion products were emitted; they also totaled 1.75 m^2 (10.8 ft^2) in area and were located 2 m above the floor. A photograph is shown in Fig. J–1 and a schematic in Fig. J–2.

In each of the six tests, the four test subjects were a bar, two trusses, and a thin-walled tubular column. These are depicted in Figs. J–3 through J–5. Depending on the test, these specimens were either left unprotected or were coated with spray-applied fire protective insulation material, BlazeShield DC/F. The fibrous insulation was applied by an experienced applicator who took considerable care to apply an even coating of the specified thickness. As such, the insulated test subjects represent a best case in terms of thickness and uniformity.

The fires consisted of liquid hydrocarbon fuels sprayed by a two-nozzle spray burner onto a 1 m × 2 m (3.3 ft × 6.6 ft) pan. The fuels were (a) heptanes and (b) a mixture of nominally 60 percent (by mass) heptanes with 40 percent toluene. The latter fuel produced a significantly sootier flame.

The instrumentation for the tests comprised up to 352 channels of data.

- The combustion products were collected in a 6 m × 6 m (21.5 ft × 21.5 ft) hood. Instrumentation in the exhaust duct enabled calculation of the rate of heat release throughout a test.

- Fourteen heat flux gauges were placed strategically around the compartment to measure the transport of radiant energy; in addition, there were four slug calorimeters measuring the total heat flux parallel to the trusses.

Most of the channels were for thermocouples that measured the temperatures on the surface of the walls and ceiling, within the walls, on the surface of the steel components, and at the surface of the spray-applied insulation. With the large number of measurements, it was possible to go beyond the traditional point-by-point comparison and discover why the model either under- or overpredicted a given measurement. A description of the test series appears in Table J–1. Table J–2 shows the dimensions and variability of the spray-applied insulation. The measurements were taken at numerous locations along the perimeter and length of each specimen using a pin-thickness gauge specifically designed for this type of insulation.

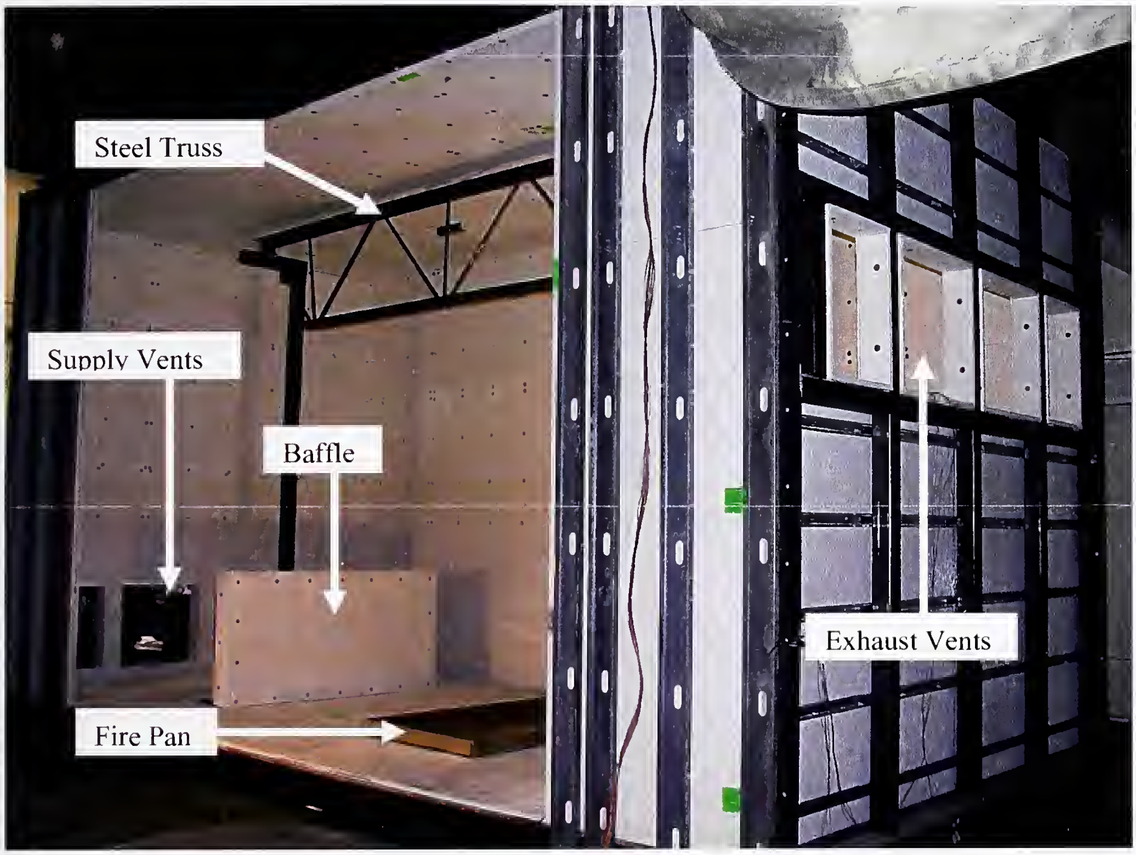

Figure J–1. Experimental enclosure during construction, viewed with access panels removed.

PLAN VIEW

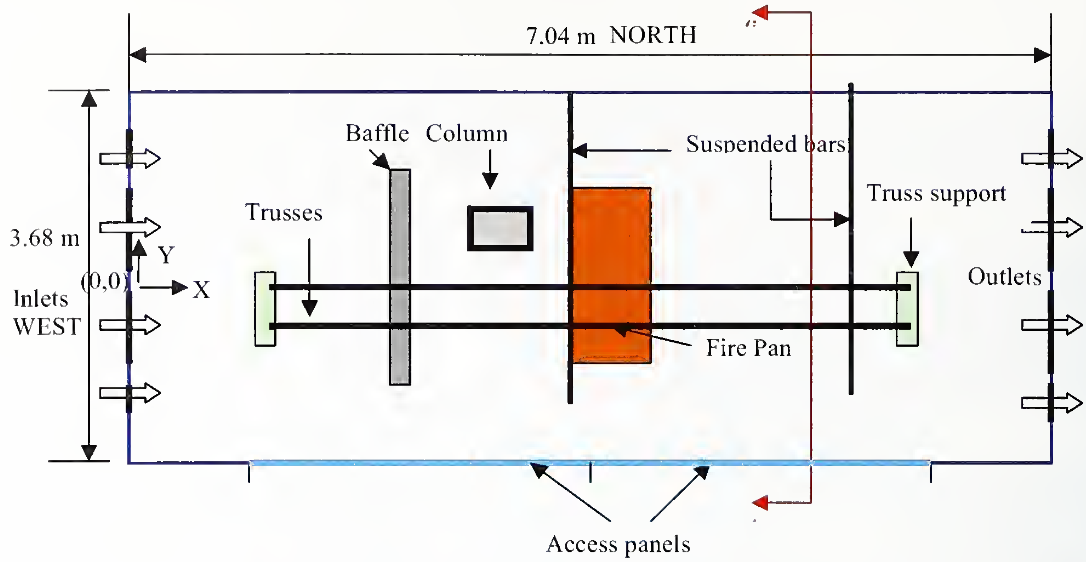

1.2 SECTION A-A

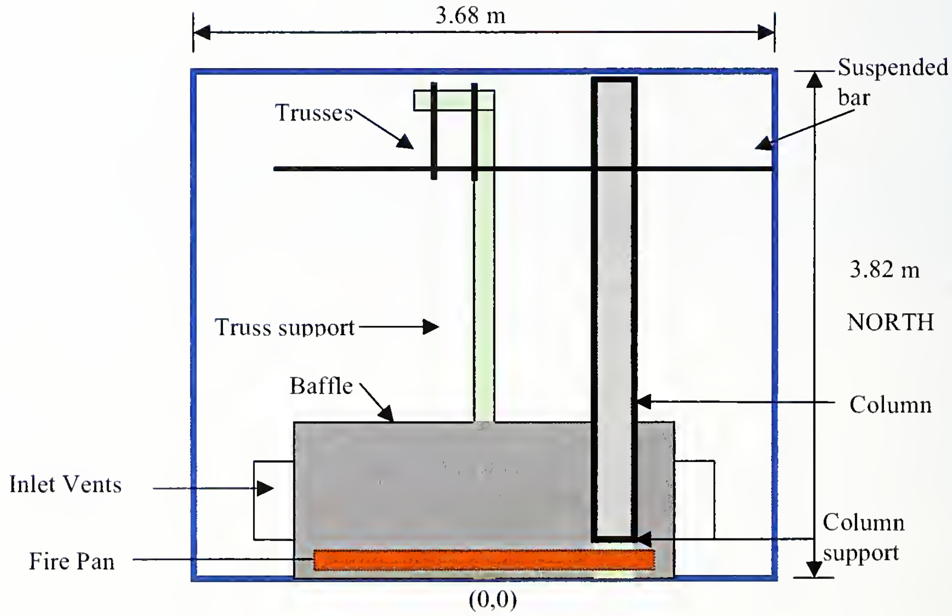

Figure J–2. Compartment content layout (not to scale).

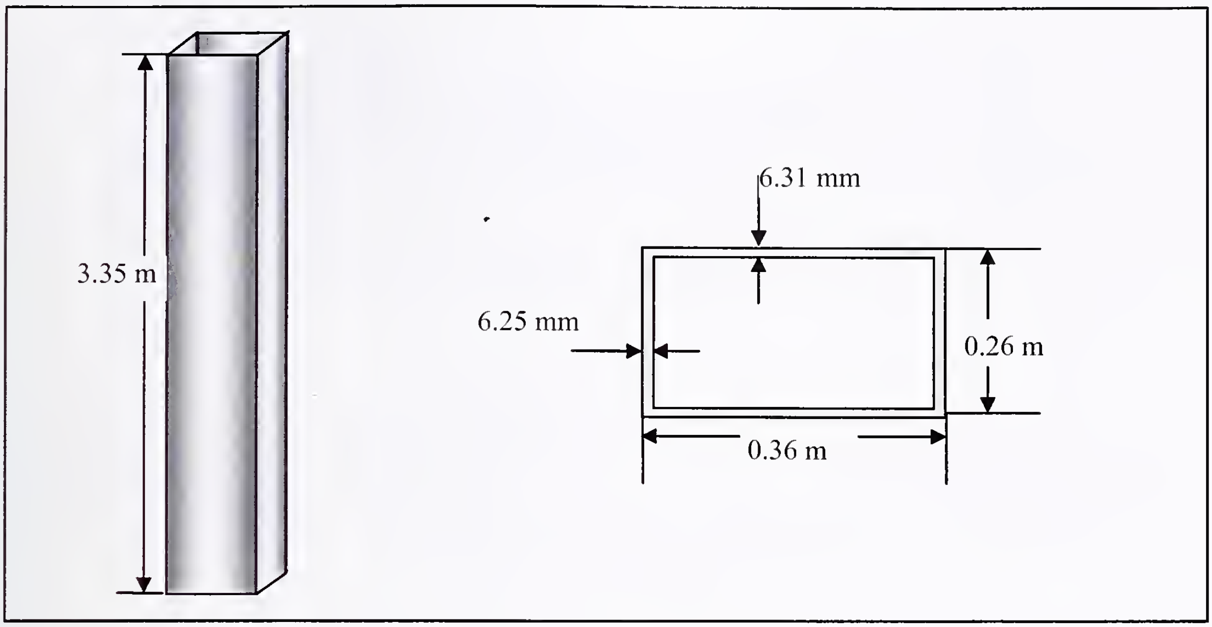

Figure J–3. Tubular column.

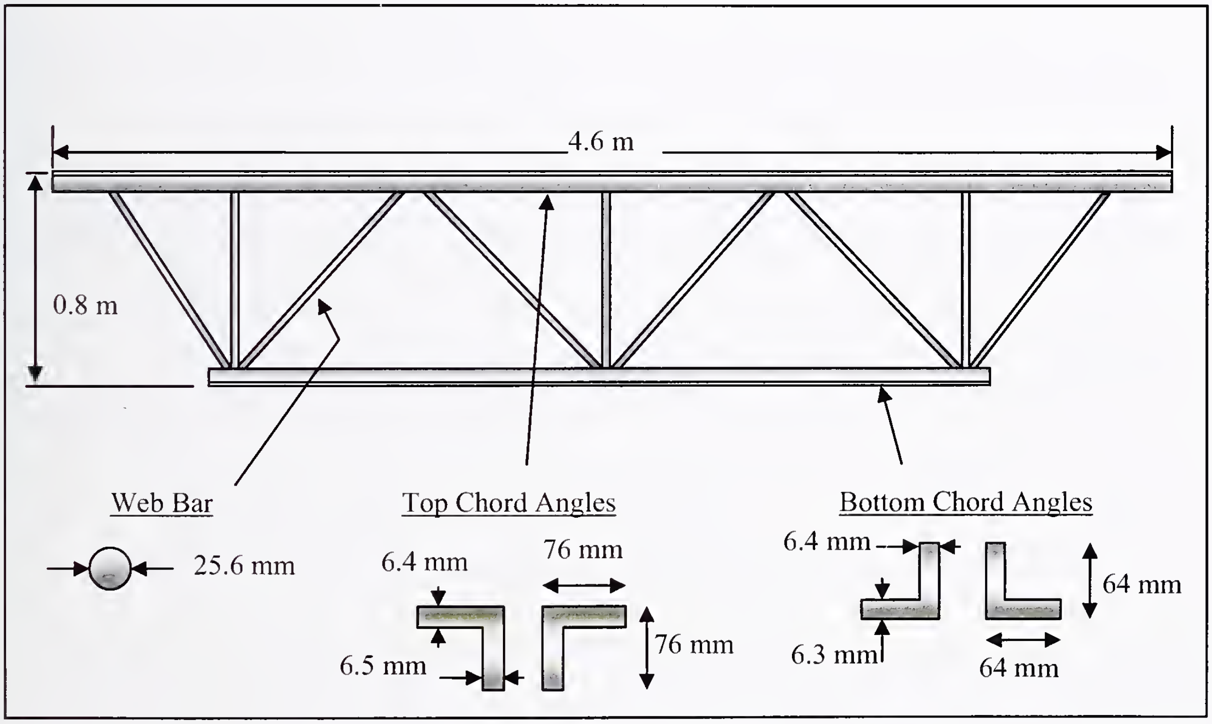

Figure J–4. Bar joist.

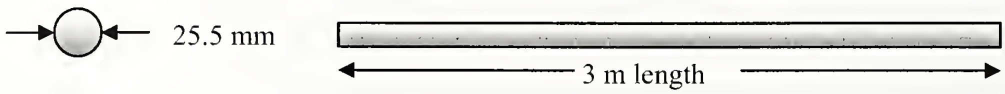

Figure J–5. Simple bar.

Table J–1. Test matrix.

Test	Measured Heat Release Rate (MW)	Fuel	Planned Insulation Thickness (mm)	Planned Test Duration (min)
1	2.0	Heptanes	None	15
2	2.4	Heptanes/toluene	None	15
3	2.0	Heptanes/toluene	None	15
4	3.2	Heptanes	Same as test 5	15
5	3.0	Heptanes	See Table J–2	50
6	3.0	Heptanes	See Table J–2	50

Table J–2. Summary of insulation on steel components.

Test	Item	Specified Thickness (mm)	Applied Thickness (mm)	
			Mean	Std. Deviation
5	Bar	19.1	23.0	5.5
	Column	38.1	41.0	3.0
	Truss A	19.1	26.9	7.3
	Truss B	38.1	40.5	8.2
6	Bar	19.1	25.3	4.6
	Column	19.1	21.4	3.5
	Truss A	19.1	26.0	6.9
	Truss B	19.1	25.6	6.9

The HRR are shown in Fig. J–6. The important features of the HRR curves are:

- The expected (from the calorific value of the fuels) and measured heat release rates agreed within the relative expanded experimental uncertainty of ±11%.
- The heat release rates are steady over the time interval in which the burner was turned on.

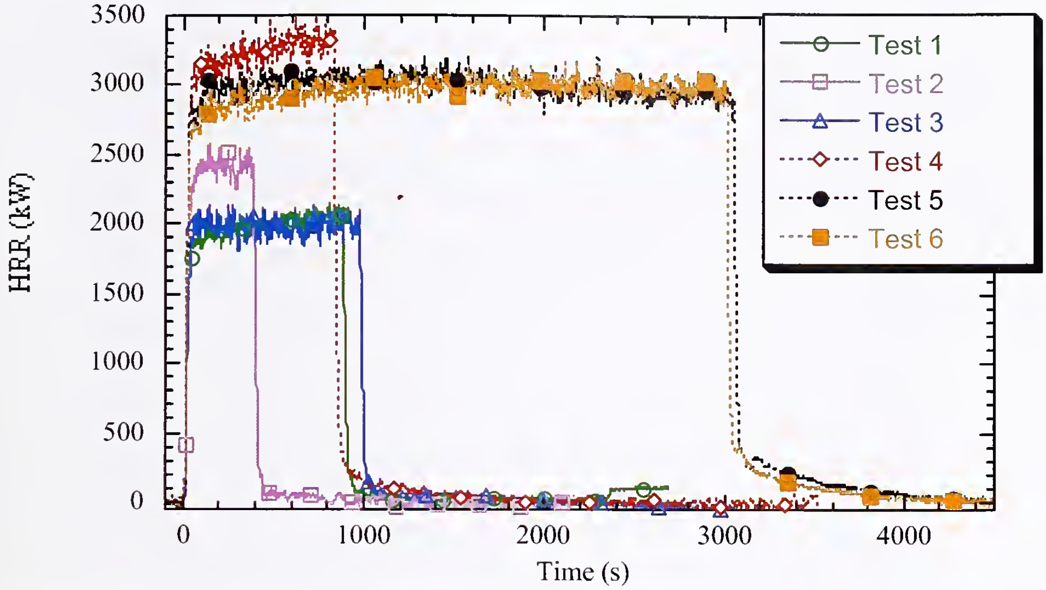

Figure J–6. Measured heat release rate as a function of time during tests 1–6.

In each test, the baseline signals from all the measurement devices were established; then the burner was ignited and continued burning at a steady rate until the temperature at any steel surface approached approximately 600 °C. (Above this temperature, there was concern that loss of strength might lead to collapse and accordant damage to the test facility.) At that point, the burner was turned off. In test 2, the steel reached the target temperature at about 6 min and was terminated at that time. During test 4, the Omega GG glass braid wire thermocouple extension cables failed leading to erroneous thermocouple readings. This was likely due to the opening-up of the Kaowool thermal insulation protective blanket around the thermocouple wires and subsequent shorting. Thus the test was terminated early, and the data have not been processed. To prevent reoccurrence of this problem during tests 5 and 6, the extensions were water cooled and double wrapped with Kaowool insulation. Each layer of Kaowool insulation was secured to the thermocouples using steel wire. Additionally, the thermocouple extensions were rerouted through the cooler west side of the compartment. After tests 5 and 6, the thermocouple extensions were visually inspected and were found to be undamaged.

J.2.2 Preliminary Results

Figure J–7 shows typical temperature data obtained in the tests. These data are for truss A in test 5. The thermocouple location notation is as follows: TU: Truss Upper Chord, TM: Truss Middle (Web), TL: Truss Lower Chord; 1 to 4: locations across the length of the test specimen; S: on the steel surface, I: on the outer surface of the insulation; A: truss A. For the informative nature of this progress report, it is only important to note the following:

- The curves that rise sharply from the beginning of the test are those for temperatures on the outside of the insulation.
- The curves that rise more gently are those for temperatures at the interface between the steel and the insulation.

From the figure, one can see that:

- The 19.1 mm (0.75 in.) insulation delays the rise to a peak steel temperature by almost an hour at all locations.
- The highest temperature reached at the steel surface is approximately 300 °C lower than the temperature at the outside face of the insulation material.

The curve patterns for the other steel specimens in the tests with insulated steel are similar in shape.

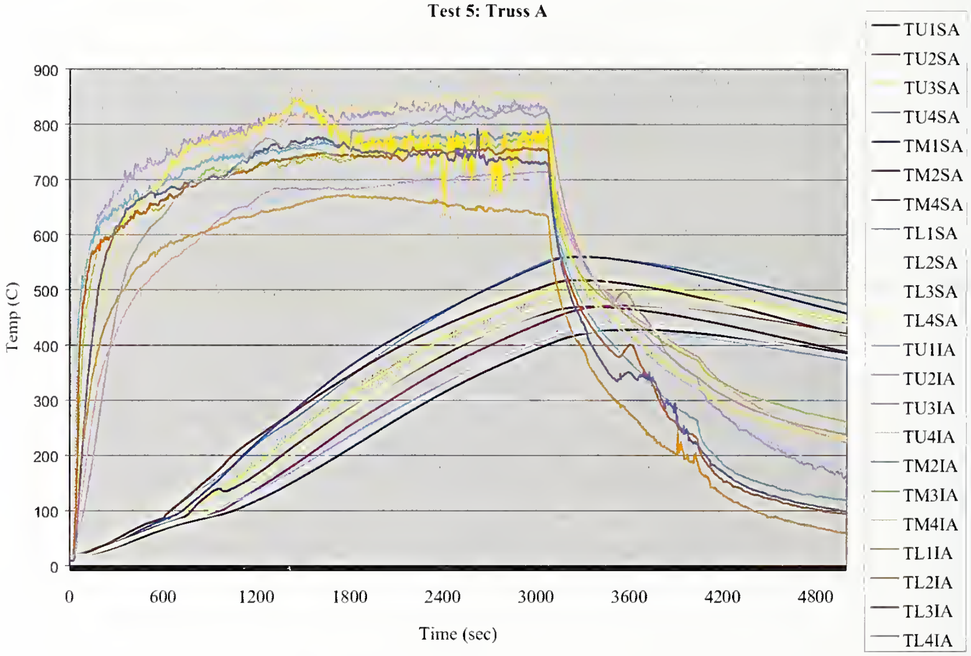

Figure J–7. Temperature-time history for truss A in test 5.

By contrast, Fig. J–8 shows the same plot for truss A from test 3, in which the truss was not insulated and the fire was of shorter duration and lower intensity. Nonetheless, the outer surface of the steel reached the targeted maximum temperature (just short of 600 °C) in about one-third the time. As expected, this result is typical of the fire response of the uninsulated steel specimens in tests 1 through 3.

Figures J–9 through J–12 show comparisons of the modeled and measured temperatures and heat fluxes for tests 3 (2.0 MW heptanes/toluene fire) and test 5 (3.0 MW heptanes fire). The agreement for the highest temperatures is excellent. Analysis of both the model and the thermocouple measurements is under way to determine the source of their differences at the lower temperatures, especially in test 5. The spikes in the heat flux plots are artifacts—the result of the periodic nitrogen blasts to reduce soot accumulation on the gage surface.

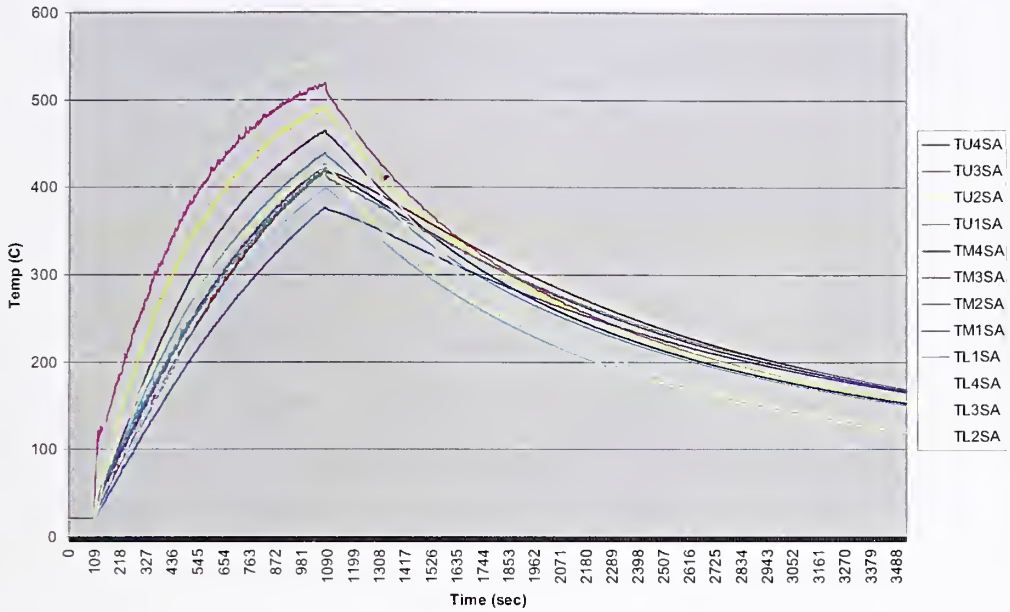

Figure J–8. Temperature-time history for truss A in test 3.

While the data analysis is not yet complete, the following are valuable preliminary observations:

- The prediction of the upper layer temperatures was within experimental uncertainty. Since the heat flux to the walls and objects within the upper layer is highly dependent on the upper layer temperature, these predictions were also accurate.The prediction of the time for the steel surfaces to reach 600 °C was accurate.

- The sootier burning fuel led to similar temperature rise in the ceiling and the steel above the fire plume.

- The model predicted the asymmetric shape of the fire plume, caused by obstructions to uniform flow through the compartment.

Further analysis will use Smokeview for visual comparison of the test results and the model predictions. This will determine how well FDS captures both the fire phenomena and the thermal patterns in the compartment. Quantitative analysis of the data will then determine the numerical accuracy of the predictions. Similar analysis will be performed to determine the accuracy of the finite element modeling of the thermal patterns within the bare and insulated steel components.

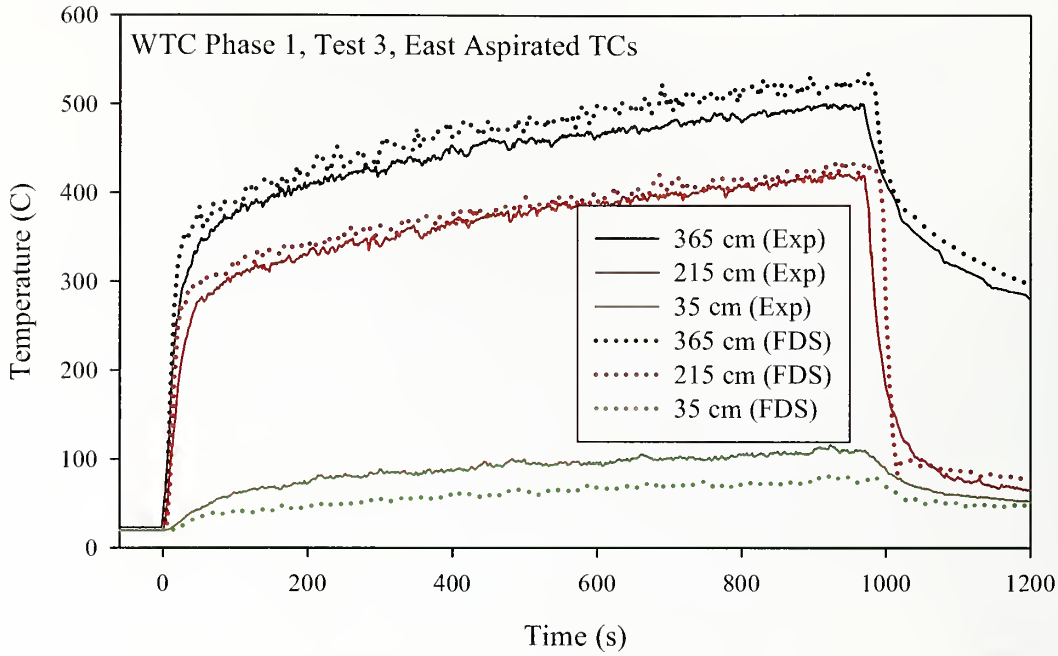

Figure J–9. Comparison of gas temperatures, test 3, exhaust side of compartment.

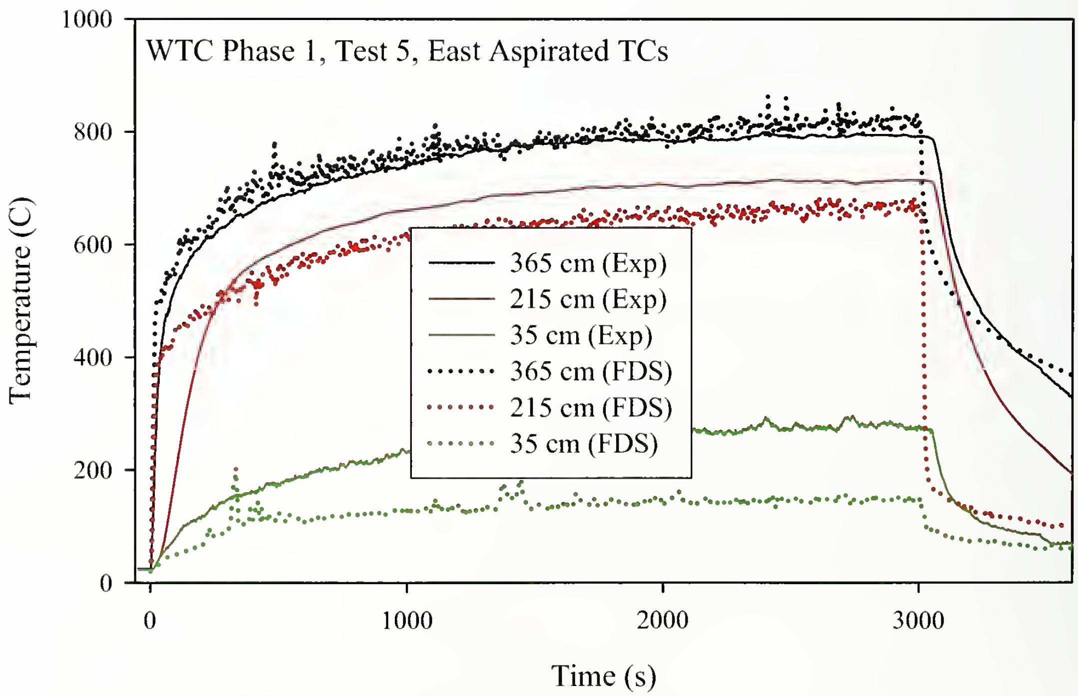

Figure J–10. Comparison of gas temperatures, test 5, exhaust side of compartment.

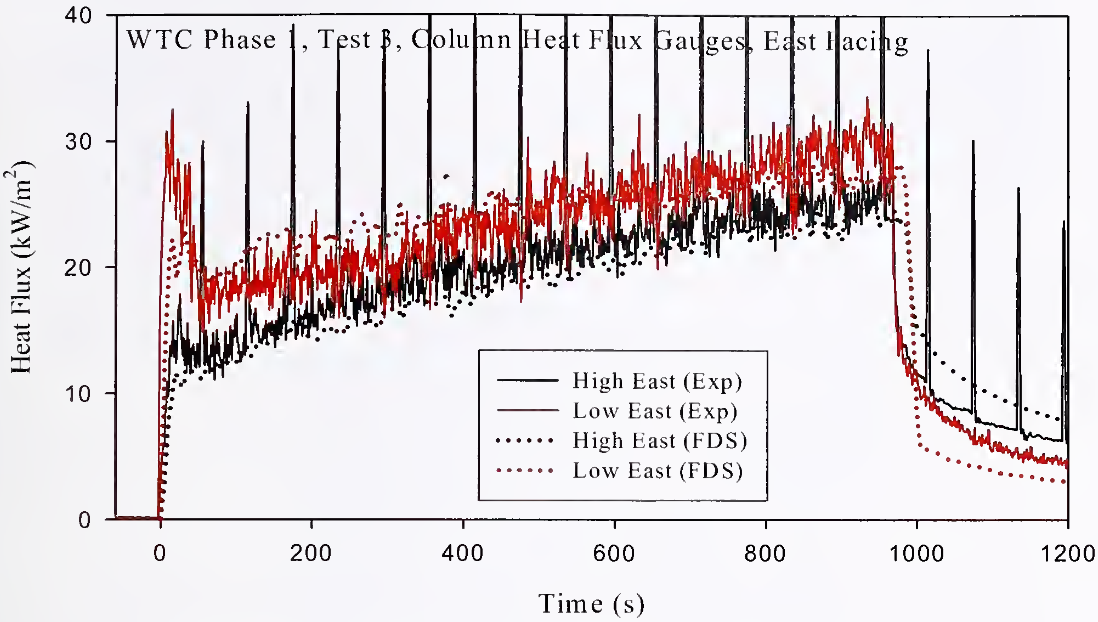

Figure J–11. Comparison of heat fluxes to column, test 3.

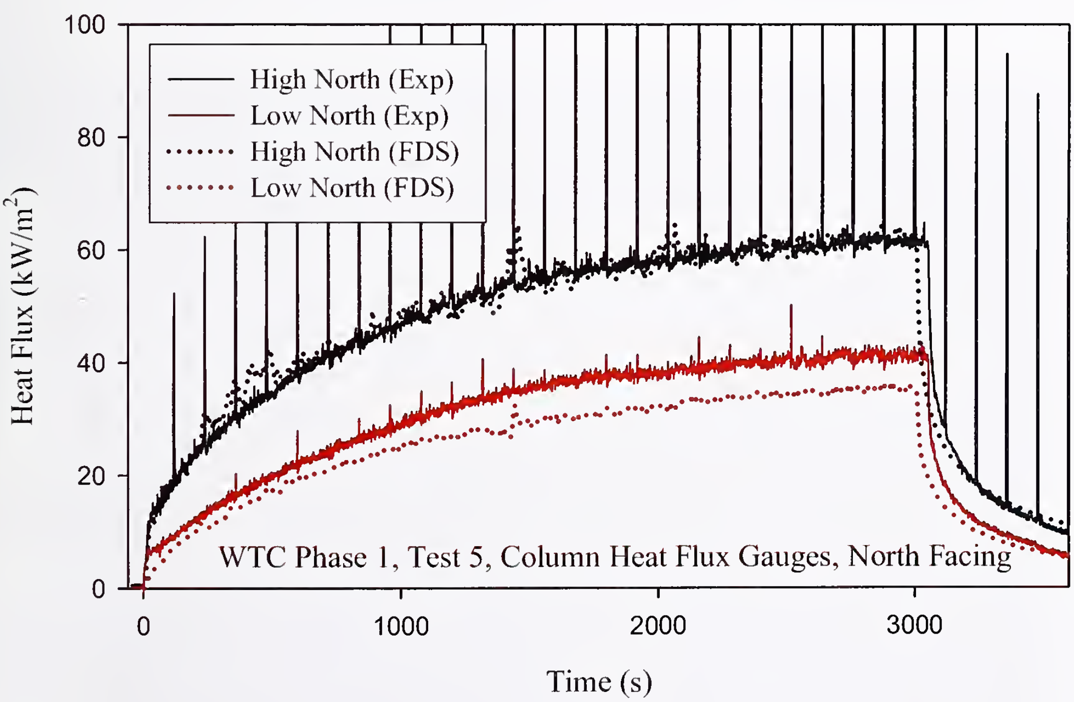

Figure J–12. Comparison of heat fluxes to column, test 5.

J.3 EXPERIMENTS FOR GUIDING THE FDS FIRE GROWTH PREDICTIONS

In the early stages of this Investigation, the FDS combustion module was enhanced to enable the inclusion of charring materials, such as those that comprise much of the office furniture. Thermophysical property data from the combustion of small (100 mm × 100 mm) samples of the furnishings were obtained using the Cone Calorimeter. These data became input to the fire simulation. A set of real-scale experiments was then designed and performed (July and August 2003) to identify any need for further enhancements to the fire model. In each of these experiments, a single workstation (i.e., an office cubical or module), similar to those in the WTC offices, was burned under a hood. A soffitted ceiling allowed for the collection of hot fire effluent and the accordant thermal radiation to the test specimen. Some of the tests examined the effects on the burning rate of jet fuel and/or noncombustible material occluding a fraction of the workstation surfaces.

J.3.1 Description of the Experiments

Materials

Workstations come in a variety of styles and finishes. However, they tend toward similar size and mass. They are also fabricated of materials with similar burning behavior, e.g., the work surfaces are generally laminated particleboard or wood. Most of the workstations burned here were of a single generic type. For comparison, one high-end unit (identical to those in the aircraft impact floors in WTC 1) was also burned in a manner identical to one of the tests of the generic units.

The generic workstation examined is shown photographically in Figs. J–13 and J–14. The layout, including the placement of the various nonstationary items, was suggested by personnel from a company that supplied office furnishings to the occupants of WTC 1. Information on the distribution of papers and other office items was provided by a frequent visitor to these offices. The workstation covered a footprint nominally 2.44 m × 2.44 m (8 ft × 8 ft) and was surrounded by privacy panels.

- The panels were 1.22 m (4 ft) high, except that on one side the panel was 1.52 m (5 ft) tall and supported a bookcase. On the side opposite the bookcase, there was a 1.22 m (4 ft) wide open entrance opening. The panels were made of a steel and softwood frame, covered on both sides with layers of fiberglass padding and perforated steel and a thermoplastic cover fabric. A few sheets of copier paper were tacked to the cubicle walls on three sides.

- The work surfaces were formed from four sections of laminated medium density fiberboard supported by steel brackets from the wall panels. Four document boxes contained a total of four reams of copier paper. Additional paper was stacked horizontally on the desk surface.

- The seat and back of the office chair were a nonthermoplastic fabric over polyurethane foam supported by a one-piece thermoplastic shell; its five-legged base was thermoplastic with steel framing and support elements.

Figure J–13. Photograph of right side of generic workstation.

Figure J–14. Photograph of left side of generic workstation.

- The three file cabinets (0.91 m wide, 0.51 m deep, 0.68 m high [36 in. × 20 in. × 27 in.], with two horizontal drawers) were painted steel; they rested directly on the carpet. Two of the cabinets contained two reams each of copier paper as a rough means of assessing the extent to which paper in file drawers might contribute to a fire.

- The bookcase (1.22 m [48 in.] long) had a steel shelf and top but these were supported only on their ends by combustible end panels; the steel front closure panel was fabric-covered steel and it was open (on top of the bookcase). Ten document boxes held about 13 reams of copier paper.

- The carpet tiles were nylon fiber-faced over a dense foam rubber backing. A square area 2.74 m × 2.74 m (9 ft × 9 ft) was covered with 36 carpet tiles.

- The computer monitor was a nominally 17 in. CRT-based unit. Its front face was taped with fiberglass tape and it was pointed toward the wall panel opposite the cubicle opening for safety in the event of an implosion. The keyboard was placed in its normal location, parallel to the sloped segment of the work surface. The computer processor (tower-type container with plastic only on the front face of the container) was placed on the floor next to a waste paper basket (both on the side opposite the cubicle opening).

- The wastebasket was thermoplastic and contained one ream of copier paper atop five balled-up paper ream wrappers.

Thermophysical characterizations of six of the generic workstation materials (carpet, panels, work surface, chair seat, paper stack, and computer monitor shell) were obtained using the Cone Calorimeter. These data were to serve as input to FDS. Since the physical behavior of at least some of the work station materials (and the objects from which they were taken) was expected to be more complex than was revealed in the Cone tests, it was anticipated that these full-scale tests would provide clues as to necessary empirical adjustments in the FDS predictions.

The high-end unit was similar to the generic workstation, with the principal differences being:

- The wall panel construction was somewhat different having a 3 mm (0.125 in) layer of flame-retarded polyester fiber beneath the outer fabric, a more open steel panel beneath this, a central fiberboard layer (3 mm thick) and an all steel peripheral frame (no wood). The fiberboard roughly doubled the amount of woody fuel within the wall panels of the enclosure and put it into a much higher surface area form in which it could be expected to burn appreciably faster. It should be noted, however, that this increase in woody fuel was only about 10 percent to 15 percent of the total available in the desk surfaces. Also, its enclosure deep within the wall panels delays its burning.

- The file cabinets (four, with a total face length of 2.67 m rather than three with a total face length of 2.44 m) had a flammable, charring plastic surface on the drawer fronts that added 15 percent to 20 percent of flammable area.

The chair was constructed somewhat differently (seat and back as separate pieces) and behaved as if its upholstered surfaces were flame-retarded. The high-end workstation is shown in Fig. J–15.

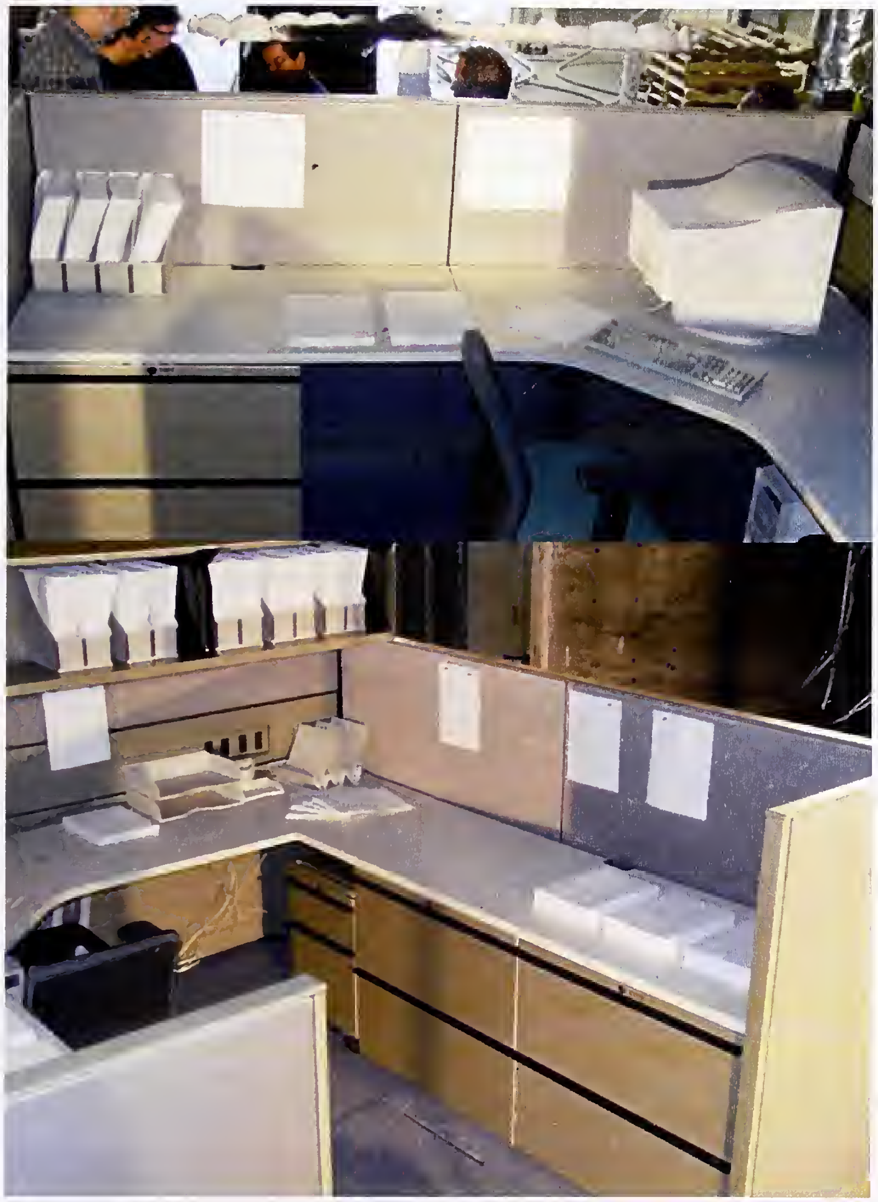

Figure J–15. Photographs of high-end workstation.

Test Configuration and Instrumentation

The workstation to be tested was placed on top of a double layer of 13 mm (1/2 in) thick calcium silicate sheets. These in turn rested on a set of four weighing cells, one at each corner. Each workstation (including furnishings) weighed approximately 730 kg (1,600 lb) and contained approximately 300 kg (660 lb) of combustible material. The weighing cells are accurate to ±0.1 kg (0.2 lb). The entire assembly was placed beneath the hood of the NIST 10 MW calorimeter hood to allow continuous heat release rate measurement.

A fire typically forms a layer of hot, smoky combustion products near the ceiling of a room. Thermal radiation from this layer plays a significant role in fire spread. Thus the test fixture included partitions to hold the combustion products from these test fires. The ceiling was a 3.66 m × 3.66 m (12 ft × 12 ft) section of 13 mm thick calcium silicate board. It was supported on a water-cooled steel frame 2.74 m (9 ft) above the floor of the workstation. To keep the gases from flowing quickly across the ceiling and thus not forming an appropriate layer, the ceiling was surrounded on all four sides by a steel skirt that draped down 0.61 m (2 ft) from the ceiling.

The test instrumentation included:

- Instrumentation in the hood exhaust duct for measurement of rate of heat release.
- Four video cameras placed to record the progression of flame spread over the objects in the cubicle. Their view of the combustibles became observed by the wall panels and the flames themselves as the fire grew in intensity. An observer narrated the fire growth to supplement what the cameras recorded directly.
- In two tests, an upward-facing, water-cooled Schmidt-Boelter total heat flux gage 127 mm (5 in) above the cubicle floor, near the cubicle center.
- An external total heat flux gage mounted so as to view the entire fire from one side. This provided a signal that was proportional to the instantaneous HRR of the fire and was useful for certain timing issues.
- In two tests, six 24-gage chromel/alumel thermocouples to follow the progress of the fire on the underside of the desk surfaces.

Ignition Scenario

The initiation of the tests was in keeping with the workstation being one of a large array on a given floor of a large office space and a fire propagating through the array. Thus a large ignition source (a 2 MW, four-nozzle spray burner over a 2 m × 1 m pan) was placed immediately adjacent to the exterior of one wall panel of the test station, simulating the burning of the adjacent workstation. The size and placement (pan bottom 0.81 m above the floor) of this ignition source were guided by preliminary FDS predictions.

The igniter fire was supported by a flow of commercial-grade liquid heptanes (mixed isomers) sprayed at a nominally steady rate from the four nozzles pointing downward toward the pan. The heptane mix was supplied from a reservoir by a variable-speed pump. The desired fuel flow was preset before the test and measured in triplicate by catching the flow from each nozzle in a volumetric cylinder for a typical period of 20 s. The nominally 2 MW fire supported by the heptane flow typically impinged almost continually on the ceiling above the igniter. There was thus an essentially continuous wall of flames radiating toward the workstation along the central three-fourths of the length of one panel. In addition, the workstation was subject to radiation from the hot ceiling and the hot smoke captured below the ceiling.

Test Variables

There are numerous variables that might influence the burning of a workstation such as that examined here, starting with the nature of the materials and their spatial arrangement, the ignition conditions, etc. There are also variables unique to the WTC fires: the amount of paper-based clutter in a workstation, the possible presence of jet fuel (and its amount), the possible presence and amount of inert rubble generated by the airplane impact (fallen ceiling tiles, inert dust from pulverized concrete and/or wallboard), varying degrees of impact-induced break-up and compaction of the work station itself, and presence of combustible solids from the airplane.

The tests were designed keeping the purposes in mind: (a) identify the current capability of FDS to predict complex burning behavior using combustion data from small-scale specimens and (b) obtain clues to improving the combustion algorithm should the predictions be of insufficient accuracy. Thus the two selected variables were those that could affect the workstation fires in manners that test FDS and are important in the WTC context: the presence or absence of both jet fuel and of inert rubble. The inert rubble was taken to be representative of fallen ceiling tiles.

The primary test set thus focused on two levels of two variables examined in a full factorial design. This calls for four tests: (1) no inert rubble and no jet fuel, (2) rubble but no jet fuel, (3) jet fuel but no rubble and (4) rubble and jet fuel. The levels of the two variables were estimated to produce differences in burning behavior that would be clearly observable. Thus the inert rubble was chosen to cover approximately 30 percent of the horizontal surfaces facing the hot ceiling. As performed, 24 of the 40 ceiling tiles were on the horizontal desk surfaces; 14 were on the central, open floor area; and 2 were on the chair seat. The fraction of the plan view horizontal area covered by these tiles was approximately 31 percent. A total of 4 L (approximately 1 gal) of Jet A was spread over these same horizontal surfaces.[1]

Two additional tests were conducted. The first test (in the entire series) utilized what was nominally one-half of a generic workstation, though it included both a full chair and full computer. This was done to gage the burning behavior of what was an entirely unknown system. The fourth test was of the high-end workstation. Both of these were conducted with no jet fuel and no inert rubble present.

Test Procedure

The workstation was assembled a few hours before a test. Since the ambient humidity was high (approximately 70 percent) for most of the tests, the paper was covered with plastic sheeting if it was to be exposed for more than 2 hours, although this probably did not preclude significant moisture pick-up in the outer portions of the paper piles. That moisture would be expected to somewhat slow the ignition process relative to a more normal humidity of 50 percent.

At the beginning of each test, all instruments were calibrated. [The heat release rate was also measured for a few minutes after the test ended in order to verify the calorimeter baseline.] The heptanes flow was measured in triplicate. The test was initiated by starting the heptanes flow and immediately igniting it with a torch. This defined time zero. The heptanes flow was left on until late in the test unless there was

---

[1] Areas close to the impact could have been drenched with higher quantities. The workstations would also have had to be extensively fragmented, which is not a situation being examined here. Another pragmatic factor that kept the jet fuel loading down was the probability that higher levels would have pushed the calorimeter beyond its maximum allowable capacity.

an indication that the fire was going to significantly exceed the 10 MW calorimeter capacity; this happened only once (test 5). The full test was video taped by all four cameras and a narration was fed to one camera, describing the sequence of ignition events that spread the fire over the accessible flammable surfaces. In two cases (tests 3 and 4) the residual weight of the paper piles in the two file drawers was obtained as a measure of the participation of this paper in the overall fire.

In the two tests in which jet fuel was placed on the horizontal surfaces prior to the start of a test, this was done just before ignition of the 2 MW spray burner. A sprinkling can was used in two separate operations, each involving 2 L of the liquid fuel. First, the liquid was sprinkled on the horizontal desk surfaces and the objects on them (i.e., the various paper stacks or document boxes, the computer monitor and the keyboard) using a timed movement that attempted to allot an equal amount of liquid to each one-third section of the total work surface. The desk surface had been leveled after installation so that the liquid would not run preferentially in one direction. Next, an equal amount of the liquid was sprinkled in a similarly timed manner on the central open section of the carpet (not under the desk surfaces). Since the chair occupied a portion of this space, the allotment for that portion went onto the chair seat and back surfaces. For the objects on or in contact with the desk surface, there was some tendency for the jet fuel to wick into them if they were porous. This was true of the paper, the inert tiles and the wall panel fabric just above the desk surface.

J.3.2 Preliminary Results

Figures J–16 and J–17 show the workstation early in a test and at a time just before the peak heat release was reached. Figures J–18 through J–23 show the heat release rate curves from the six fire tests.

Figure J–16. Photograph of workstation soon after ignition in test 2.

Figure J–17. Photograph of workstation near the peak heat release rate in test 2.

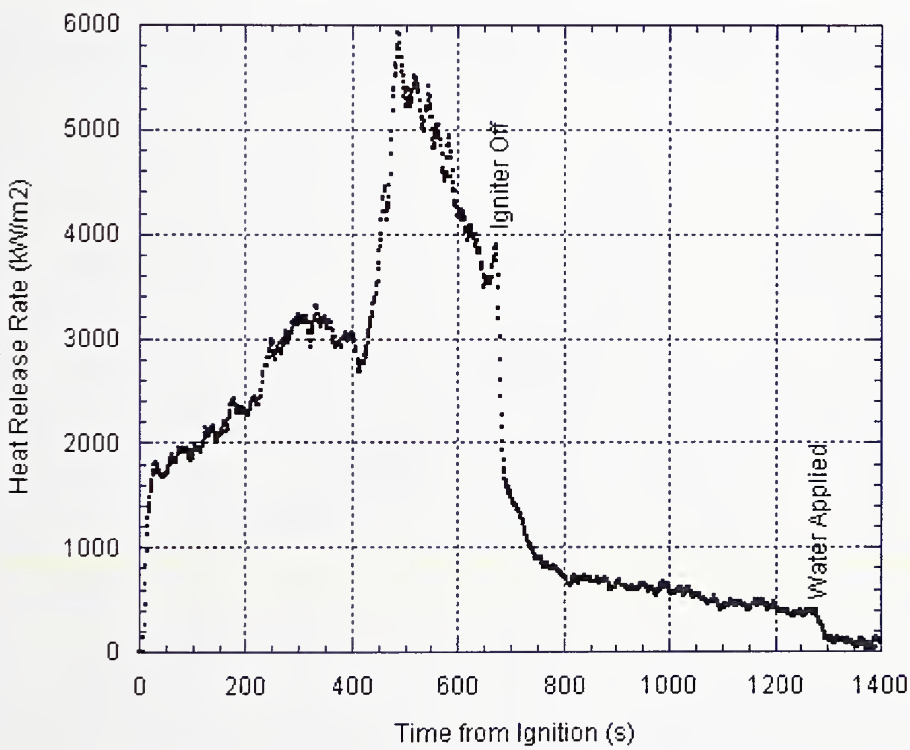

Figure J–18. Heat release rate versus time for single workstation test 1.

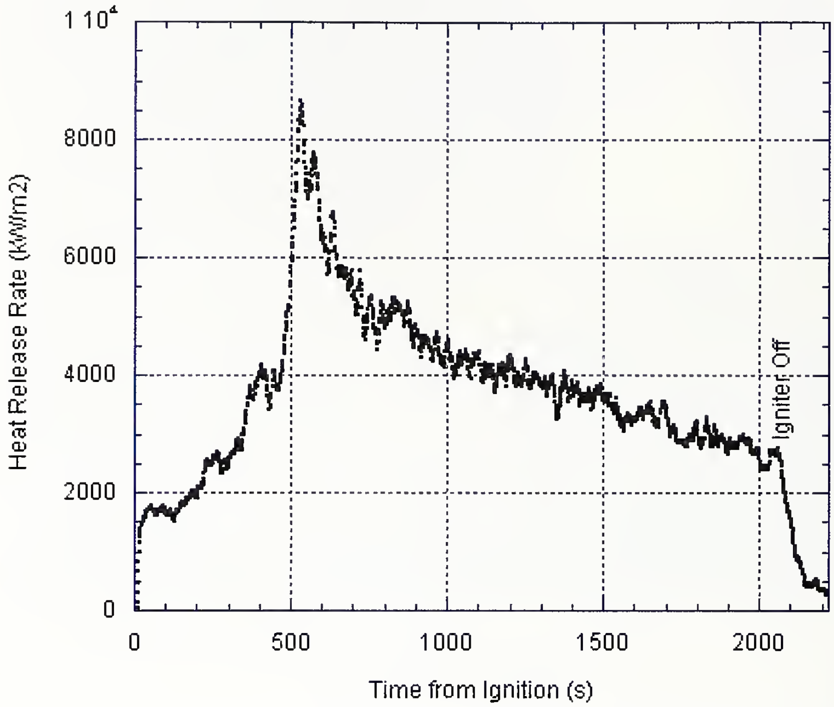

Figure J–19. Heat release rate versus time for single workstation test 2.

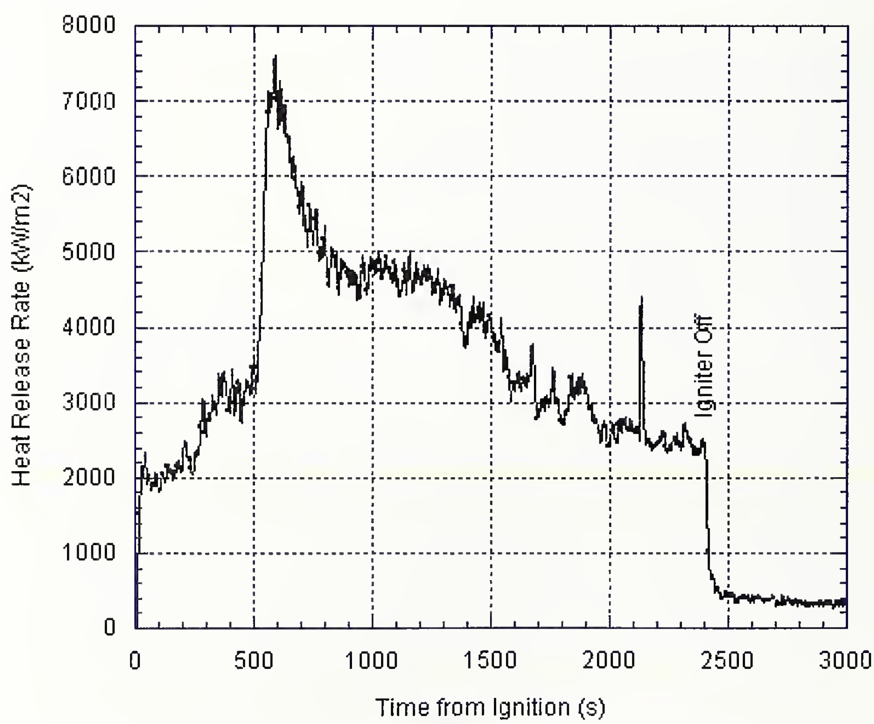

Figure J–20. Heat release rate versus time for single workstation test 3.

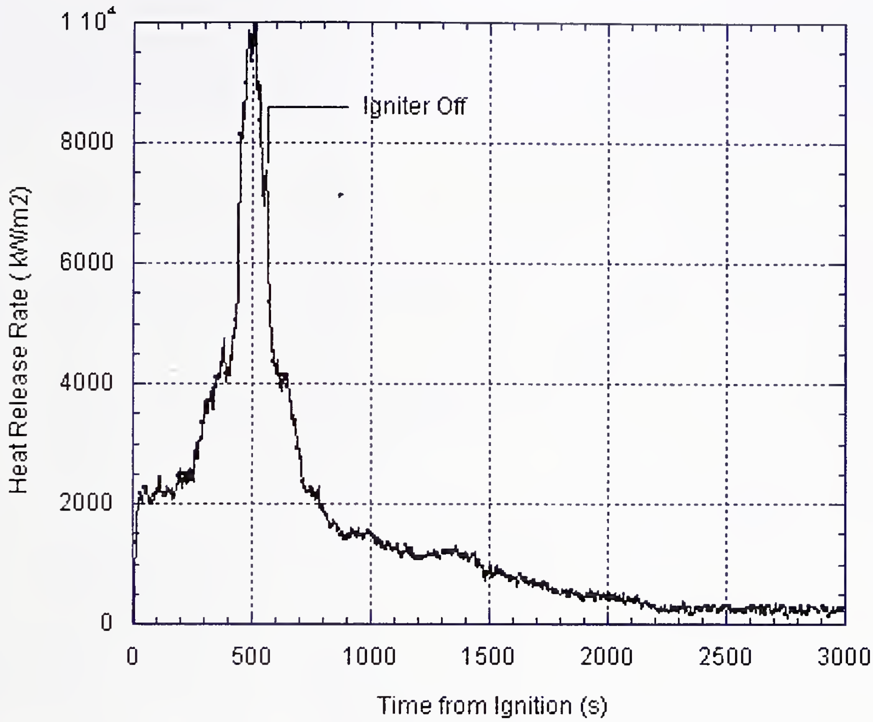

Figure J–21. Heat release rate versus time for single workstation test 4.

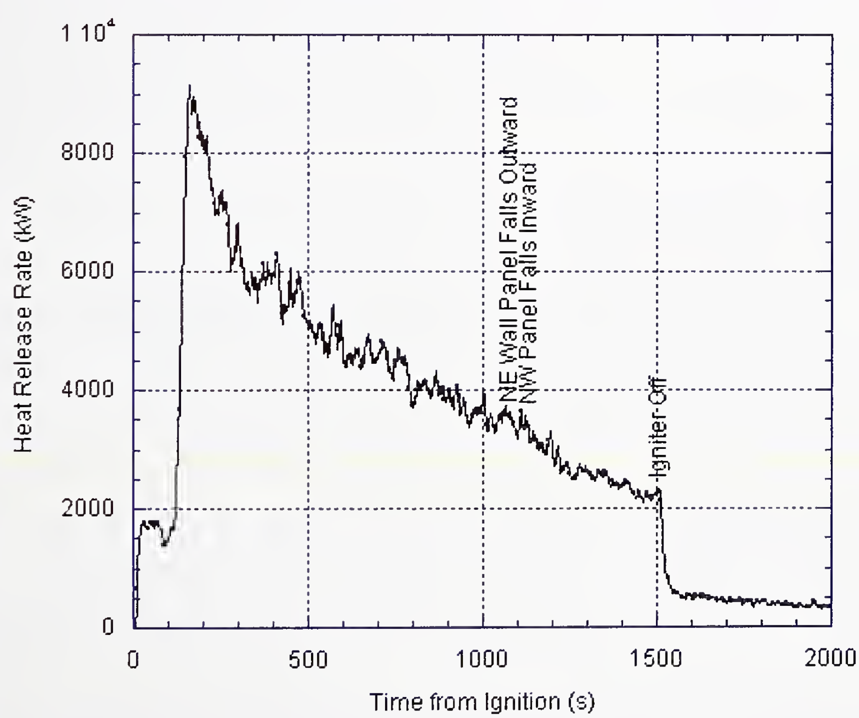

Figure J–22. Heat release rate versus time for single workstation test 5.

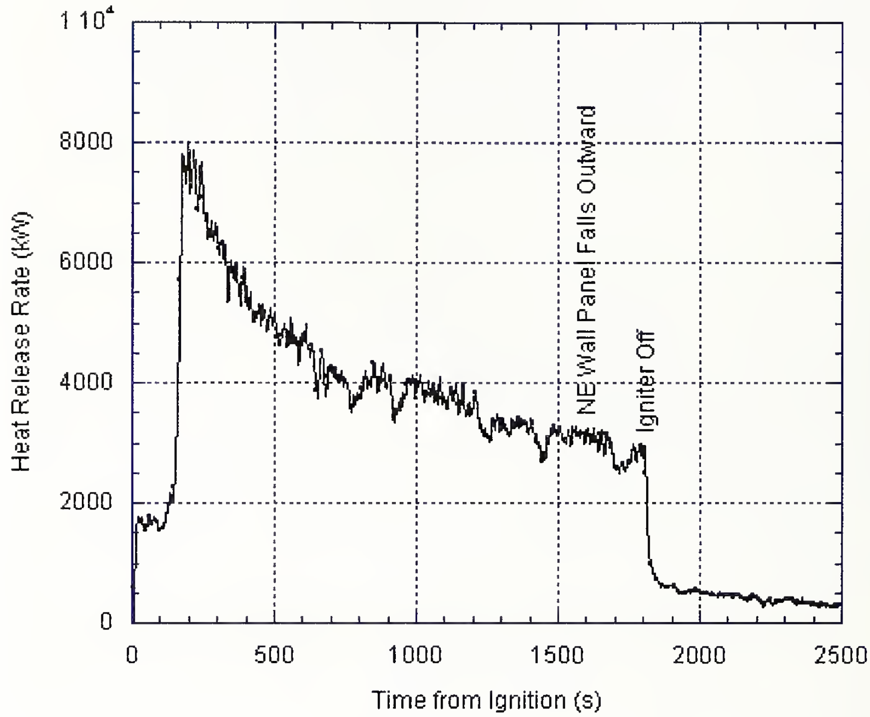

Figure J–23. Heat release rate versus time for single workstation test 6.

Table J–3 lists the peak HRR values from each test plus the time to that peak, rounded to the nearest 10 s. The HRR peak is given in two ways: first, as the absolute highest single reading recorded (for a 1 s interval) and second, as the average of the value at this peak plus values up to 5 s to either side of this peak. The latter compensates for both noise in the calorimeter system and in the fire itself; it is doubtful that objects in a real room can respond in any meaningful way to small HRR fluctuations in a fire that is under 10 s in duration. The averaged values are about 3 percent lower than the absolute peak values, a result of the sharpness of the peaks in every case.

Table J–3. Peak heat release rates and times to peak.

Test	Test Specimen	Jet Fuel (Yes/No)	Inert Tiles (Yes/No)	Peak HRR (kW)	Time to Peak HRR (s)
1	Half of generic workstation	N	N	5920/5770	490
2	Generic work station	N	N	8700/8480	530
3	Generic work station	N	Y	7560/7300	590
5	Generic work station	Y	N	9120/8910	160
4	High-end work station	N	N	9890/9660	510
6	Generic work station	Y	Y	7960/7690	200

The videotapes of the fires show that the peak HRR corresponds closely to simultaneous burning of all the “accessible” combustible surfaces in the workstation interior. This included the top of the desk surface, the objects on it, the exposed area of the materials in the bookcase, the full chair area (but see below), the exposed area of the carpet (i.e., not that under the three steel file cabinets), objects on the carpet (computer processor case and wastebasket) and the underside of the desk, except above the steel file cabinets where the air access was limited. The interior surfaces of the wall panels contributed negligibly because the thermoplastic fabric melted and rolled downward into a mass having much less surface area than the original fabric prior to igniting. This type of behavior is not captured in Cone Calorimeter tests.

The following observations emerge from comparison of the results in Table J–3:

- The peak fire intensity from the half workstation is about two-thirds that of the full workstation. This is probably primarily the result of two factors:

  - The same chair was present in both cases; this chair has an estimated HRR peak in the neighborhood of 1/2 MW by itself.

  - The inert steel file cabinets cover twice as much of the carpet in the second half of the workstation, precluding its participation in the HRR peak; this lowers the HRR contribution from the second half of the workstation.

- The computer was also totally combusted within the first half of the experiments, though this was a substantially lesser heat source than was the chair.

- The ceiling tiles reduced the peak HRR in proportion to their coverage of the burning surfaces; both just under 15 percent. While there was 30 percent coverage of the upward facing horizontal surfaces, there was no coverage of the underside of the desk, the carpeting below the desk or the underside and back of the chair. As noted above, all of these were burning at the peak. (The reduction might become more than linear if nearly all of the upward facing horizontal surfaces were covered since this could preclude the progressive flame spread that gets all accessible surfaces involved)

- The principal effect of the presence of 4 L of Jet A on the horizontal surfaces was in shortening the time to involvement of all accessible combustible surfaces, and thus the time to the peak HRR. The peak itself was boosted upward only about 5 percent, presumably because the Jet A helped boost the overall fuel gasification rate somewhat while adding its high heat of combustion. When the inert tiles were also present, the Jet A was poured across their top surfaces temporarily rendering these surfaces flammable. Since the tiles were porous, the Jet A burning rate on them was reduced, however, and the tiles still managed to produce a 13 percent to 14 percent reduction in the peak HRR relative to the case with Jet A and no tiles.

From examination of the videotapes and the commentary, NIST determined that, when there was no Jet A present, there was a fairly reproducible progression of ignition events leading up to the HRR peak:

- The onset of the igniter fire bathed the entire workstation in radiant heat.

- The igniter fire was not the pilot flame that ignited other objects, although FDS simulations suggest that the peak fluxes on surfaces facing the igniter were of the order of 30 kW/m^2 or more, well above the minimum flux for piloted ignition of the various exposed surfaces. Even the top of the computer monitor shell, which gasified extensively only 20 cm from the spray burner flames, did not appear to ever have directly been ignited by those flames. Instead the progression of flaming was initiated by the top sheets on the paper stacks. Its presence in many places made it highly instrumental in spreading the flames to the computer monitor shell, the desktop and the top of the chair back. Flaming material from the chair fell onto the carpet, igniting it. Subsequent spread on the carpet was delayed, however, until the chair was fully involved, along with the remainder of the upward-facing surfaces of the desktop. Later, paper ignition brought flames to the two other sides of the desk area in the workstation.

- Once the entire area at and above the top of the desk surface was burning, the "compartment" under the desk flashed over from the radiant heat from the upper compartment and especially the heat from the burning chair. With all flammable surfaces ignited, the HRR quickly peaked. The specific construction of the chair and its location were critical to this fire growth process:

  - One corner of the seat was deliberately placed to extend approximately 15 cm under the desk surface on which the computer keyboard rested. This assured that some heat would reach this space early on, even though the chair flames would contact the relatively ignition resistant underside of the desk.

  - When only the upholstered surfaces of its seat and back were burning, the chair retained its original shape, and little of its heat reached the lower compartment area.

  - When the thermoplastic support shell of the chair began to melt and flow to the floor, extensive heat flowed directly into the "compartment" under the desk.

  - The partial steel skeleton kept the chair from collapsing and maintained burning from desk level to floor level. The flame radiation to the cavity under the desk quickly ignited the materials located there, while the upper part of the chair flames played on the desk, assisting ignition of its underside.

Since chairs of different designs (and thus different burning behavior) could be fabricated from the same materials, the detailed fire behavior of the chair cannot be inferred simply from the Cone Calorimeter data for the component materials. Thus, empirical treatment of its HRR process is necessary.

As expected, the progression of ignition events in the presence of Jet A was different. Ignition of the materials in the cubicle occurred more quickly. However, the manner of the acceleration was not what might have been expected.

- Since the flash point of Jet A is at least 46 °C (approximately 20 °C above the ambient temperature), initially there would be no flammable mixture of vapors above the liquid fuel surface. As the strong radiant flux from the spray burner bathes the workstation, the videos show an increasingly dense aerosol rising from the various wetted surfaces near the spray burner. These did not ignite, as evidently turbulent mixing of the vapor plume above the surfaces quickly diluted the fuel vapor below the lean flammable limit. Instead, in the first Jet A test, a random piece of flaming material rose from the burner area and drifted down on top of the desk, immediately igniting the Jet A. In the second test, a flaming piece of debris from the burner landed on top of the bookcase where there was no jet fuel and it had no effect. The paper stacks on the work surface next to the spray burner finally dried out, began to char, and then transitioned into flaming, igniting the jet fuel.

- The Jet A flames then spread rapidly, but did not sweep continuously around the desktop. Presumably the initial evaporation period left some dry spots that stopped the spread.

- The carpet was ignited by flaming matter dropping from the chair. Apparently the turbulent vapor plume dilution process mentioned above prevented the flames from jumping downward to the carpet from the flaming desk surface, even though the carpet was emitting an aerosol. At any rate, the subsequent flame spread on the carpet was rapid.

- None of these steps is resolved in the HRR curves of Figs. J–21 and J–22 due to the rapidity with which the curves jumped rapidly to their peak values soon after the Jet A ignited. As in the "dry" tests, the peak corresponds to all accessible combustible surfaces burning simultaneously.

The rapid decay in HRR after the peaks in all tests presumably reflects several factors that should be captured in the combustion algorithm in FDS:

- The various paper piles developed a thick ash layer that would drive down their burning rate.

- Char formation on the desk surfaces drove down its burning rate.

- The carpet began to burn out.

However, a number of geometric changes occurred that are beyond the capability of FDS to reproduce:

- The chair fire rapidly collapsed to a pool fire on the floor whose reduced burning area meant a reduced HRR.

- The front of the bookcase, resting on top of that unit, typically fell, changing the location of its 13 reams of paper.

- The desk surface bowed progressively as it charred through, and then it collapsed, with separate sections doing so at differing times. The initial desk collapse probably did not greatly affect its burning rate, but ultimately what was left was a complex rubble pile whose burning would not be predictable from any knowledge of the original configuration coupled with Cone Calorimeter data.

- The wall panels collapsed at random times, both inward and outward, typically rather late in the fire.

Thus, the further one goes out on the HRR curve, past the peak, the less it is predictable by an FDS calculation that retains the original geometry. Fortunately, the major effects appear to occur well after the desk surfaces collapse and the time when contiguous workstations would become ignited and dominate the heat release.

Numerical grids of 10, 20, and 40 cm were used to model the fires and ensure that the model was not sensitive to grid cell size. Figure J–24 shows a preliminary comparison of the FDS HRR prediction with the measured values for test 2 (no jet fuel, no inert tiles). The quality of fit is typical of the test series.

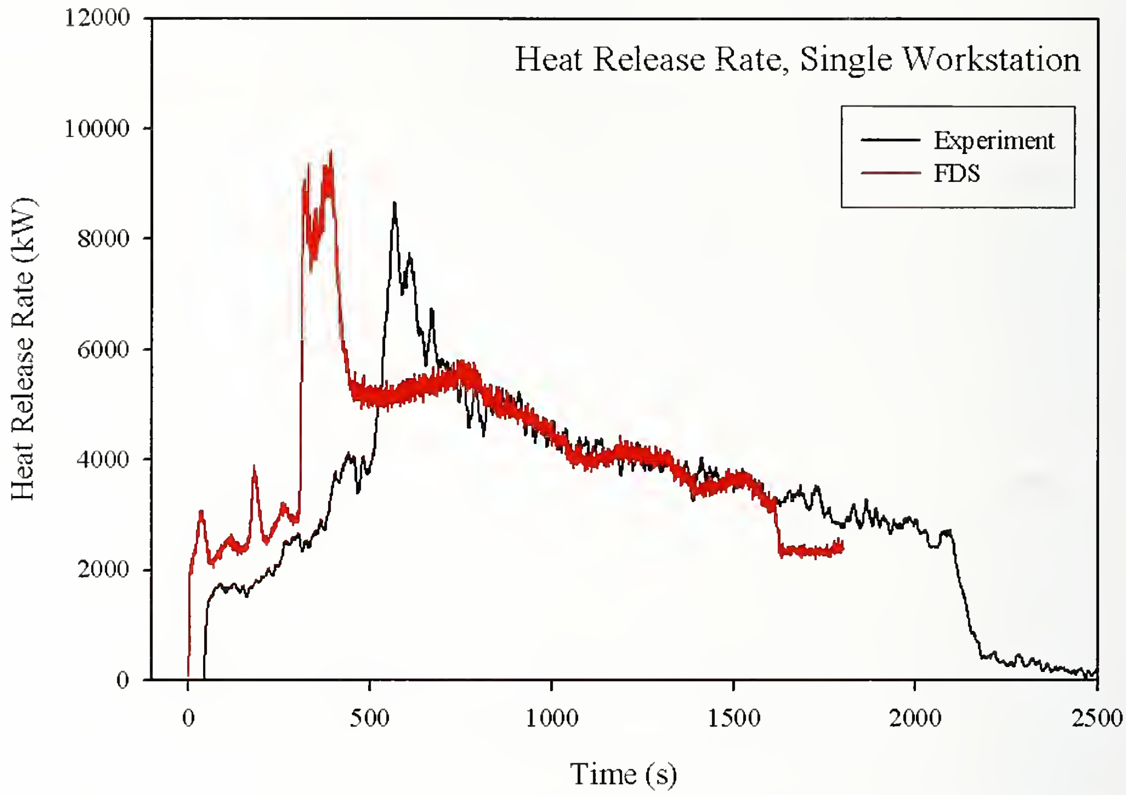

Figure J–24. Preliminary comparison of predicted and measured HRR values.

For these simulations, the thermal properties of the major materials making up the workstations were derived from Cone Calorimeter experiments. The carpet and privacy panel were modeled as thermoplastics, that is, the burning rate was assumed to be proportional to the heat flux from the surrounding gases. The desk was modeled as a charring solid, in which a pyrolysis front propagates through the material leaving a layer of char behind that insulates the material and reduces the burning rate. Details of the pyrolysis models can be found in the *FDS Technical Reference Guide* (McGrattan et al. 2002). Each feature of the experimental curve was related (using annotations made during the tests and from the video tapes) to specific aspects of the workstation combustion.

There are similarities and discrepancies between the experimental data and this prediction.

- The shape and magnitude of the two curves is encouragingly similar, as is the total heat release (area under the curves).
- The peak HRR occurred sooner in the simulation. In the experiment, the time to peak HRR was strongly influenced by the melting of the chair plastic onto the carpet. As noted above, this level of detail is not captured in the numerical model.

- At long times, the simulation drops to the residual HRR of the 2 MW burner somewhat more abruptly than does the experimental curve, indicating that it has run out of combustible mass sooner. The importance of this effect is modest, given the geometric changes during the test (listed above) and the similarity of the total heat released.

A more complete analysis will be detailed in the forthcoming documentation report.

J.4 EXPERIMENTS FOR FIRE MODEL VALIDATION

Following the experiments described above and the accordant improvements in FDS, a series of large-scale experiments was conducted in the NIST Large Fire Laboratory between November 4 and December 10, 2003. The six experiments were designed to assess the accuracy with which FDS predicts the fire spread, heat release rate, and thermal environment in a compartment burning multiple workstations in a configuration characteristic of that found in the WTC buildings. In each of these experiments, sets of three workstations, identical to the generic ones tested in Section J.3, were burned in a large compartment (see Fig. J–25). The challenges to the model included varying the location of the ignition burner (and thus the fire ventilation), adding jet fuel and/or noncombustible material occluding a fraction of the workstations' surfaces, and "rubblizing" the workstations. FDS simulation of each test was carried out before the test was conducted.

The steel-frame experimental enclosure was 10.8 m long × 7.0 m wide × 3.4 m tall (35.5 ft × 23 ft × 11 ft) and was lined with three layers of 13 mm (0.5 in) calcium silicate board (see Fig. J–26). There was a subfloor (not included in the above dimensions) to house instrumentation. The enclosure had openings on the front mimicking window openings through which fresh air entered and heat and combustion products were emitted. The narrowed openings limited the amount of fresh air that entered the burning enclosure.

Each of three workstations was placed on an isolated platform made of calcium silicate board. The top surface of each platform was flush with the floor of the compartment. Each platform was supported on water-cooled load cells, located in the subfloor, to monitor the mass of the workstation throughout the test. The load cells were the same as those described in Section J.3.

Two of the workstations were contiguous, exemplifying a part of the type of cluster that exists in many large office spaces. The third workstation was separated from the other two by an aisle, representing a part of a second cluster. This array was to enable assessment of FDS's ability to replicate two different modes of cubicle-to-cubicle fire spread: direct flame impingement and radiative ignition from the hot ceiling layer.

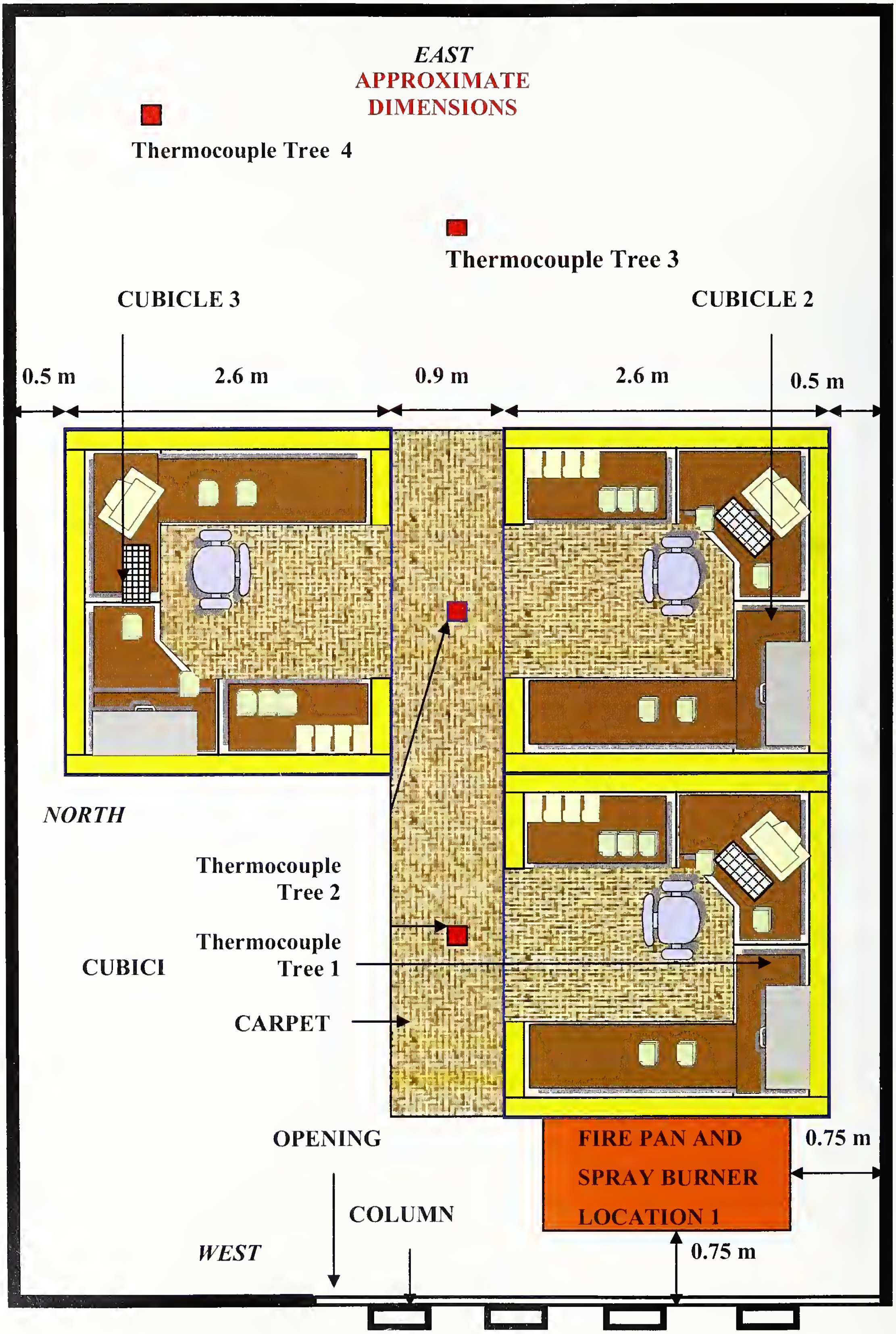

Figure J–25. Plan view of test configuration.

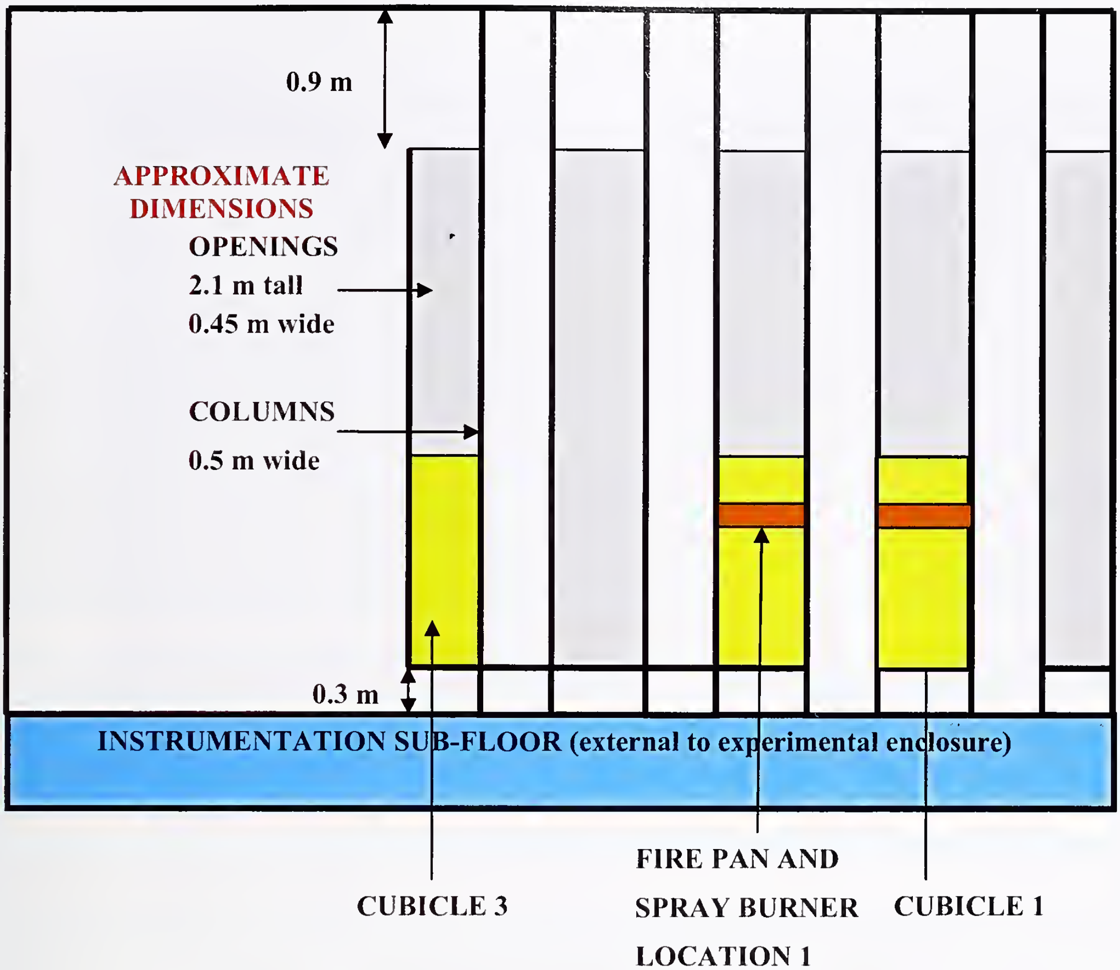

Figure J–26. Elevation view of test configuration.

The west end of the enclosure was located under a 10 m × 12 m hood for collection of the effluent and measurement of the heat release rate.

Other instrumentation included:

- Four floor-to-ceiling trees of thermocouples to measure vertical profiles of temperature(see Fig. J–27);
- Thermocouples on the desk surfaces to track flame spread;
- Two downward-facing, water-cooled Schmidt-Boelter total heat flux gages in the ceiling to measure radiative heat flux;
- Two water-cooled Schmidt-Boelter total heat flux gages mounted on the west wall; and
- Four video cameras placed to record the progression of flame spread over the objects in the cubicle.

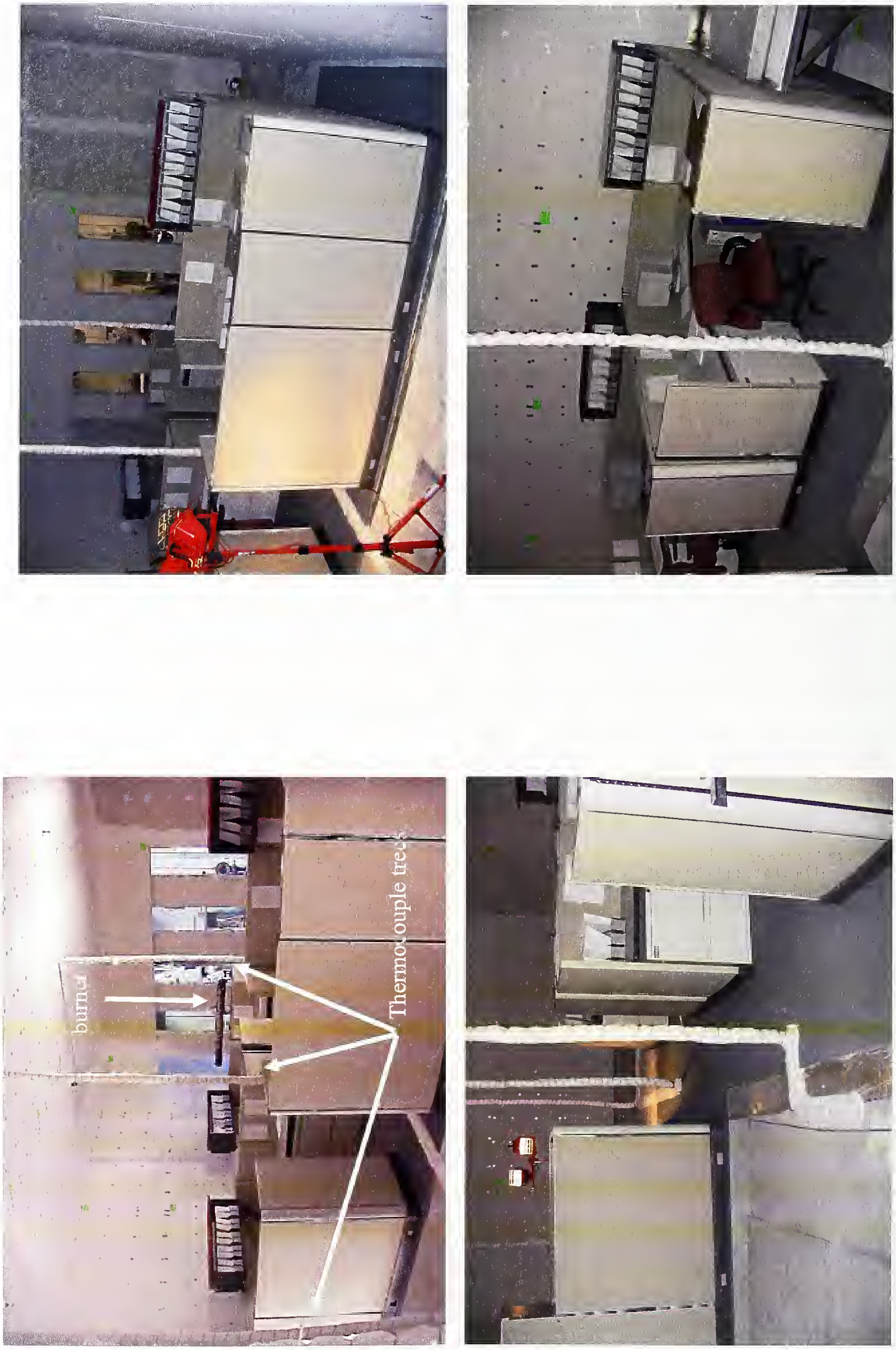

Figure J–27. Views of interior of test fixture.

The liquid spray burner, pan, and fuel (mixture of heptanes) were the same as used in the Section J.3 experiments. Depending on the test, the burner was located abutting the top of a workstation partition at the east end of cubicle 1 or the west end of cubicle 2. The ignition fire intensity was a nominal 2 MW fire. The spray burner was operated for the first few minutes of the tests, for either 2 min or 10 min depending on the test scenario.

Materials

The workstations were of the same type as the generic units used in the experiments reported in Section J.3. The carpet tiles, which covered the floor of the cubicles and the aisle, were also the same type used in experiments reported in Section J.3.

Test Variables

The experimental matrix is shown in Table J–4. The experiments investigated the impact of several parameters on the fire behavior:

Table J–4. Test matrix.

Test	Ceiling Tiles	Jet Fuel	Burner Location	Workstations	Windows
1	None	None	Front	Intact	No
2	None	None	Front	Intact	No
3	Present	Present	Front	Intact	No
4	Present	None	Rear	Intact	No
5	Present	Present	Rear	"Rubble"	No
6	None	Present	Rear	Intact	Yes

- Location of the burner. This was placed either abutting the west end of cubicle 1 or abutting the east end of cubicle 2. These two sites resulted in significantly different access to the air needed for combustion. In the former ("front") location, much of the oxygen in the air initially entering the enclosure was consumed by the burner and the burning cubicle 1, with the result that limited oxygen was available for combustion in the middle and rear of the compartment. With the burner in the latter ("rear") location, the fresh air passed directly to the rear of the compartment.

- The application of 12 L of jet fuel evenly distributed about each workstation. The procedure was the same as used in the experiments reported in Section J.3.The presence of fallen ceiling tiles. Having seen the effect of coverage of 30 percent of the top surfaces in the previous test series, NIST covered approximately 70 percent of the top surfaces here.

- Fractured furniture. In one experiment (test 5), NIST investigated the effect of different degrees of "rubblizing" the furniture.

  – In cubicle 1, the workstation pieces were placed unassembled on top of each other, occupying the same footprint as the assembled workstation. The same mass of combustibles was present as in the fully assembled cubicle tests. No steel filling cabinets were used. Ceiling tiles and broken up drywall were intermixed with the rubble.

- Cubicle 2 was the same as cubicle 1, except without the drywall.
- For cubicle 3, the workstation was partially assembled. The same mass of ceiling tile and drywall as in cubicle 1 were intermixed with the cubicle components.
- Window breakage. Test 6 had four glass windows mounted on the north end of the west wall. During the course of the fires in the WTC towers, a number of windows were broken, presumably by the heat from the fires. These result in a change in both the degree and pattern of ventilation.

Test Procedure

This was similar to that followed in the experiments reported in Section J.3, except that the ignition burner was turned off after approximately 2 min for tests 3, 5, and 6 (when jet fuel was present) and for 10 min for Tests 1, 2, and 4. The tests continued until the HRR fell below 0.5 MW, which was typically 60 min after ignition.

J.4.1 Preliminary Results

Figures J–28 and J–29 show the east view of the compartment before and during a test, respectively. A few observations about the tests were:

- The peak HRR was approximately 11 MW for four of the tests. In test 5, the peak value was only approximately 6 MW. In test 6, the peak HRR reached almost 16 MW.
- As in the single workstation tests, the peak value was reached earlier when jet fuel was present.

Figure J–30 shows how the enclosure was represented in FDS. The computational grid size was 0.4 m (1.3 ft) on a side. Note that the chair, computer monitor, and paper have been collected together into "boxes" with comparable mass to the various items that were spread throughout the workstations. To the right are five windows that are similar in size to those of WTC 1 and WTC 2.

The preliminary plot in Fig. J–31 depicts the degree to which the heat release rate measurements agreed with those predicted by FDS.

The overall degree of agreement between the model and the experimental data is quite good, despite some modest local differences. In the analysis leading to candidate improvements in the modeling, it is important to maintain perspective of the effect of these differences on the accuracy needed in reconstructing the actual WTC fires. For fires that are sufficiently severe that they threaten the structural integrity of the building, many such workstations will be burning concurrently. These workstations will be at various stages of their combustion. Thus, for example, features occurring at long times in Fig. J–31 may not merit closer replication, while those features occurring at short times (and thus have a bearing on the ease of fire spread among workstations) may merit attention.

Figure J–28. View of fire compartment before the start of test 6.

Figure J–29. View of fire compartment 2 minutes after the start of test 6.

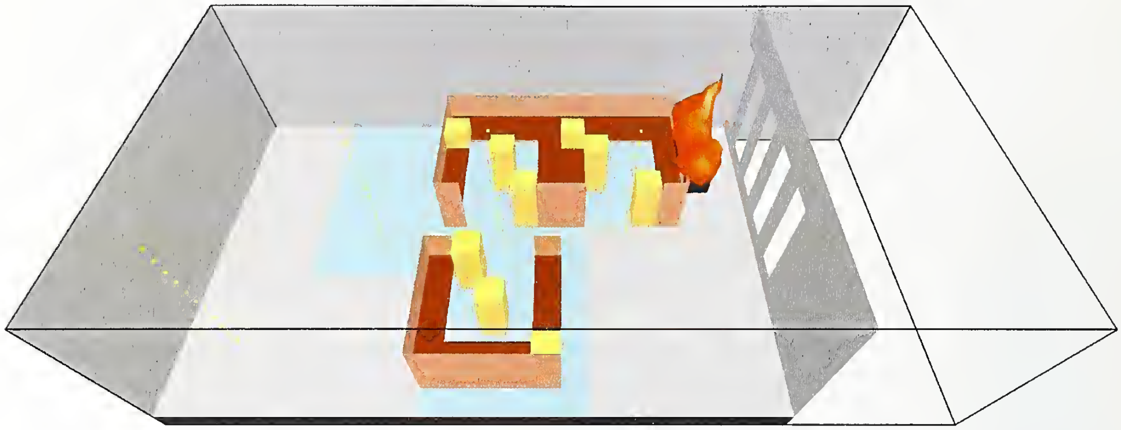

Figure J–30. Fire Dynamics Simulator 3D rendition of experimental enclosure.

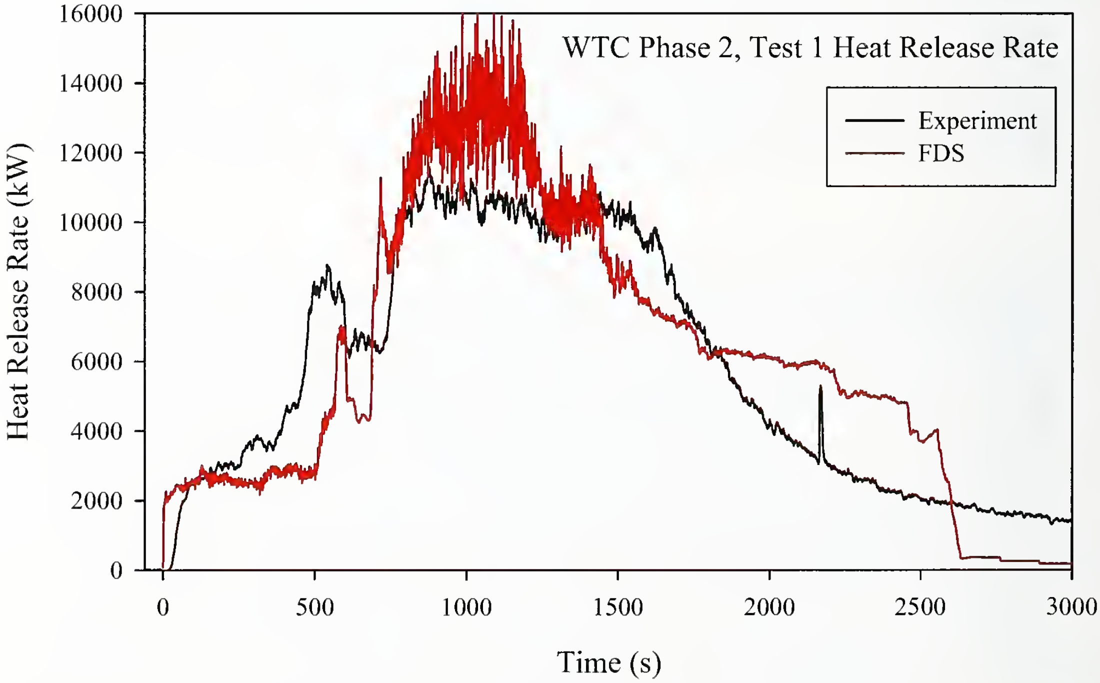

Figure J–31. Comparison of measured and predicted heat release rate for test 1.

J.5 REFERENCES

McGrattan, K.B., H.R. Baum, R.G. Rehm, G.P. Forney, J.E. Floyd, K. Prasad and S. Hostikka. 2002. Fire Dynamics Simulator (Version 3), Technical Reference Guide. NISTIR 6783. National Institute of Standards and Technology, Gaithersburg, MD.

Attachment 1
Simulating the Fires in the World Trade Center

1.1 INTRODUCTION

In the months following the attacks on the World Trade Center (WTC) and the Pentagon, there was an active debate in the fire protection engineering community about the fires that erupted following the impact of the aircraft on the buildings. Because fires of this magnitude in these types of buildings are rare, there is a wide spectrum of opinion about the fire temperatures and their effect on the structural steel. Much of the fire literature consists of empirical correlations derived from experiments ranging from bench scale to room scale. Extrapolating these well-known correlations to the WTC requires a reexamination of the underlying assumptions. Many of these correlations are appropriate for a narrow range of fire sizes and building geometries, and cannot be directly applied to the WTC fire scenarios. As a result, computer fire models that have been developed over the past decade are being applied to the analysis.

As part of the investigation, the National Institute of Standards and Technology (NIST) has conducted simulations of the fires in each building using a computational fluid dynamics (CFD) model known as the Fire Dynamics Simulator (FDS). This attachment will describe the experiments conducted at NIST to calibrate and validate the FDS model for use in the WTC project, and it will describe the techniques developed to simulate the very extensive fires that spread over 6 to 12 floors in the different buildings.

1.1.1 Experimental Program

Two large-scale test series were conducted to provide validation for the FDS, plus various small-scale experiments were conducted to provide the model with input data for different materials. The large-scale test programs are referred to as Phase 1 and Phase 2. Both test series involved fires in compartments with the same ceiling height as a floor in WTC 1 or WTC 2. Phase 1 was a series of fire tests with a liquid fuel spray burner generating a fixed amount of energy in a compartment with various targets and obstructions, like columns, trusses and other steel objects. These tests were designed to test the accuracy of the model, and its sensitivity to changes in various input parameters. Phase 2 was a series of fire tests in which office workstations similar to those used in WTC 1, WTC 2, and WTC 7 were burned in a compartment with limited openings to simulate the under-ventilated conditions of the WTC fires. These tests were designed to test the model's ability to characterize the burning behavior of real furnishings under conditions typical of the WTC fires. Only the Phase 2 work will be discussed in this attachment.

1.1.2 NIST Fire Dynamics Simulator

FDS is a CFD model of fire-driven fluid flow. It solves numerically a form of the Navier-Stokes equations appropriate for low-speed, thermally-driven flow with an emphasis on smoke and heat transport from fires (McGrattan et al. 2002). Version 1 was publicly released in February 2000. The core algorithm is an explicit predictor-corrector scheme, second order accurate in space and time. Turbulence is treated by means of the Smagorinsky form of Large Eddy Simulation (LES). For most applications, FDS uses a mixture fraction combustion model. The mixture fraction is a conserved scalar quantity that is defined as the fraction of gas at a given point in the flow field that originated as fuel. The model assumes that combustion is mixing-controlled, and that the reaction of fuel and oxygen is infinitely fast. The mass fractions of all of the major reactants and products can be derived from the mixture fraction by means of "state relations," empirical expressions arrived at by a combination of simplified analysis and measurement.

Radiative heat transfer is included in the model via the solution of the radiation transport equation for a non-scattering gray gas, and in some limited cases using a wide band model. The equation is solved using a technique similar to finite volume methods for convective transport; thus the name given to it is the Finite Volume Method (FVM). Using approximately 100 discrete angles, the finite volume solver requires about 15 percent of the total CPU time of a calculation, a modest cost given the complexity of radiation heat transfer. FDS approximates the governing equations on a rectilinear grid. The user prescribes rectangular obstructions that are forced to conform with the underlying grid.

All solid surfaces are assigned thermal boundary conditions, plus information about the burning behavior of the material. Usually, material properties are stored in a database and invoked by name by the user. An extensive effort was undertaken to characterize the thermal properties of common items found in an office setting, like privacy panels, stacks of paper, computer monitors, office chairs, pressboard tables, desks, and carpeting. These materials will be described next.

1.2 CALIBRATION AND VALIDATION EXPERIMENTS

The experimental program concentrated on the thermal properties of the office furnishings that constituted the bulk of the combustible fuel within the WTC buildings under study. Several types of office workstations typical of those used in WTC 1 and WTC 2 were purchased at area office supply stores. The thermal properties of the major materials making up the workstations were derived from cone calorimeter experiments. These properties were input into FDS, which was used to simulate the burning behavior of a single workstation burning under a 2.5 m ceiling with baffles to contain a hot layer of smoke above the burning workstation. Other than the baffled ceiling, no walls surrounded the workstation other than its own privacy panels. The thermal properties of the workstation components were adjusted slightly so that the FDS prediction of the heat release rate would match the experiment. Then the model was used to predict the heat release rate of 3 workstations burning within a large enclosure. The purpose of this exercise was to determine if FDS could simulate the dynamics of a fire in a setting similar to WTC 1, WTC 2, and WTC 7.

1.2.1 Description of the Workstation Components

Cone calorimeter experiments at three different heat fluxes were performed for the carpet, desk (wood), computer monitor, chair, privacy panel, and stacked paper. For the simulations of the WTC fires, only the carpet, desk and privacy panel data were used directly. The carpet and privacy panel were modeled as thermoplastics, that is, the burning rate is assumed to be proportional to the heat flux from the surrounding gases. The desk was modeled as a charring solid, in which a pyrolysis front propagates through the material leaving a layer of char behind that insulates the material and reduces the burning rate. Details of the pyrolysis models can be found in the FDS Technical Reference Guide (McGrattan et al. 2002).

The desk was modeled as a charring solid. The thermal properties of the wood and its char were taken from both the calorimeter experiments and the work of Ritchie et al. (1997). It is 2.8 cm thick with density 450 kg/m^3, specific heat 1.2 kJ/kg/K at 20 °C and 1.6 kJ/kg/K at 900 °C, conductivity 0.13 W/m/K at 20 °C and 0.16 W/m/K at 900 °C. The ignition temperature is 360 °C and the heat of combustion is 14,000 kJ/kg ± 800 kJ/kg. Its total available energy content is 210 MJ/m^2 ± 50 MJ/m^2.

The carpet was modeled as a thermoplastic with density 750 kg/m^3, specific heat 4.5 kJ/kg/K, conductivity 0.16 W/m/K, ignition temperature 290 °C, thickness 6 mm, heat of vaporization 2,000 kJ/kg, heat of combustion 22,300 kJ/kg ± 600 kJ/kg, and total available energy content 61 MJ/m^2 ± 2 MJ/m^2.

The privacy panel was modeled as a thermally-thin thermoplastic. The product of specific heat, thickness and density is 0.73 kJ/m^2/K. Its surface density is 0.25 kg/m^2, ignition temperature 380 °C, heat of vaporization 6,000 kJ/kg, heat of combustion 30,000 kJ/kg ± 500 kJ/kg. Its total available energy content is 6.0 MJ/m^2 ± 1.3 MJ/ m^2.

The test compartment walls and ceiling were made of three layers of 1.27 cm (0.5 in) thick Marinite I, a product of BNZ Materials, Inc. (http://www.bnzmaterials.com).[2] The manufacturer provided the thermal properties of the material used in the calculation. The density is 737 kg/m^3, conductivity 0.12 W/m/K. The specific heat ranged from 1.2 kJ/kg/K at 93 °C to 1.4 kJ/kg/K at 425 °C.

In the simulations of the fires within the WTC, the chair, computer, paper, and other miscellaneous items within the workstation were modeled as a single item by lumping the mass together into large "boxes" and distributing them throughout the workstation. It is common practice in fire protection engineering to use surrogate materials for fire experiments, and this practice has been extended to numerical modeling. Over the years, various items have been developed that are representative of various types of commodities. For example, wood cribs are often used to represent ordinary combustibles found in residential or light industrial settings. Paper cartons with various amounts of plastic within are also used as surrogates for a wide range of retail commodities. One in particular is called the FMRC (Factory Mutual Research Corp.) Standard Plastic Commodity, or more commonly, Group A Plastic. This test fuel is often used in sprinkler approval testing at Factory Mutual and Underwriters Laboratories in the US, and similar test fuels have been developed in Europe. In the late 1990s, FDS was used to simulate large scale rack storage fires to determine the effectiveness of the combined use of sprinklers, roof vents and draft curtains (curtain boards). As part of this effort, a considerable amount of work was done to characterize the thermal properties of Group A Plastic (Hamins and McGrattan 2003). Because Group A Plastic has been shown to be fairly representative of fires fueled by a mixture of paper (cellulosic materials) and plastic, and because it has been used in numerous FDS simulations, it was decided to model the contents of the office workstations with a fuel similar to Group A Plastic. Blind predictions of the single open workstation burns were made using the material properties obtained during the sprinkler/roof vent study, and then these properties were adjusted to match the results of the experiments. Thus, the single workstation burns served to calibrate the model. They were not intended to be validation experiments. The validation experiments consisted of burning 3 workstations at a time in an under-ventilated compartment.

[2] Certain commercial equipment, instruments, or materials are identified in this document. Such identification does not imply recommendation or endorsement by the National Institute of Standards and Technology, nor does it imply that the products identified are necessarily the best available for the purpose.

The surrogate fuel is modeled as a homogenous solid whose density is 172 kg/m^3. The paper carton is treated as a thermally-thin material whose density × specific heat × thickness is 1.0 $kJ/m^2/K$. Its ignition temperature is 370 °C and the heat of combustion is 30,000 kJ/kg. The heat release rate of the boxes ramps up to 450 kW/m^2 in about 1 min. Note that this fuel package is similar, but not the same, as Group A Plastic. The density has been increased to account for all the miscellaneous items within the workstation. Also note that unlike the desk, partition and carpet, the boxes are simply given a burning rate rather than a heat of vaporization, meaning that the boxes will burn at the given rate regardless of the heat flux upon them as long as the surface temperature remains above its ignition temperature. The reason for this is that it is not possible to predict the burning rate using the heat feedback approach because the geometry of the scattered fuel is too complex to directly predict the response of the material to the thermal insult. By collecting all the scattered items into boxes, the geometry of the combustibles is greatly simplified, and as a result the burning behavior must be simplified as well.

1.2.2 Description of the Simulations

The geometry of the compartment is relatively simple. The overall enclosure is rectangular, as are the vents and most of the obstructions. Numerical grids of 20 and 40 cm were used to model the fires. The purpose of the grid variation was to ensure that the model was not sensitive to the change in grid cell size. Typically, enclosures of this size are modeled using 10 cm grid cells. However, for the simulations of WTC 1, WTC 2, and WTC 7, a 40 cm grid was used. By simulating the experiments at 20 cm and 40 cm, NIST can test if the model produces significantly different results with grid cells of different sizes. Figure 1–1 is a snapshot of a simulation showing the fire and the major geometric features of the compartment for the simulations. Note that the surrogate fuel packages are placed roughly where the computer monitor, chair and paper were located. Six tests were performed, with various ignitor locations and fuel arrangements. A 2 MW burner was pl aced either near the windows of the compartment overlooking the workstation nearest the openings in Tests 1, 2, and 3. The burner was placed towards the rear of the compartment overlooking the workstation in the rear of the compartment in Tests 4, 5, and 6. In Tests 3, 5, and 6 Jet A fuel was poured over the workstations and surrounding carpet. To simulate this in the model, spray nozzles were positioned over the center of each workstation, 2 m above the floor. These nozzles are normally used to simulate water sprinklers, but in this case, the water was replaced by a liquid having similar properties to Jet A. The nozzles were activated for 2 s, in which time the equivalent amount of liquid as in the tests was ejected and spread over the furnishings.

In Test 5, Workstations 1 and 2 were disassembled prior to the burn and the contents were piled on top of the respective load cells. To model this scenario, the burning rate of the collective fuel packages was reduced by one half to account for the decrease in burning area of the fuel pile. The choice of one half was somewhat ad hoc. No free burns of workstation parts had been performed. This was the only test in which the simulated fuel packages had to be modified from their free-burn values. In this regard, Test 5 was used to calibrate, not validate, the model.

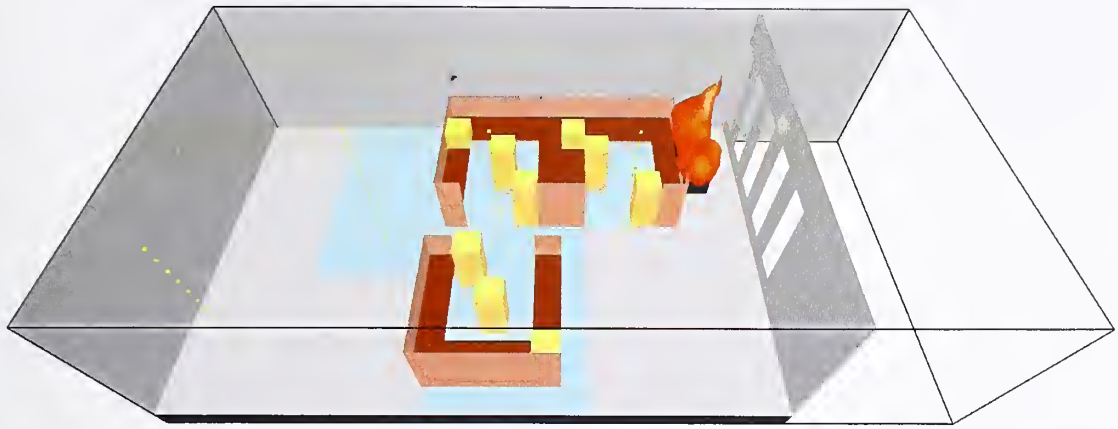

Figure 1–1. Geometry of the Phase 2 simulations.

From a modeling perspective, the objective of the simulations of the Phase 2 experiments was to demonstrate that a simplified model of an office workstation can be used to predict the burning behavior of a group of workstations in an enclosure with features similar to WTC 1, WTC 2, and WTC 7. Because of the magnitude of the simulations of the building fires, the model of the workstation had to be fairly crude. However, because of the many uncertainties in the initial conditions of the fire simulations, the lack of detail in the model is not considered to be a problem. The model fires had similar growth patterns, peak heat release rates, decay patterns, and compartment temperatures.

The model also captured the major features of the individual tests. For example, Tests 1 and 4 were similar in design except for the burner location. In Test 1 the burner was near the windows; in Test 4 it was near the rear of the compartment. The peak heat release rate was reached in about 15 min in Test 1, whereas it was reached in about 10 min in Test 4. The model shows a similar trend. The faster growth of Test 4 is probably due to the fact that the compartment heated up more quickly with the fire deep inside rather than near the windows, leading to more rapid spread of the fire across the pre-heated furnishings. Even though ceiling tiles were distributed over the desk and carpet in Test 4, this did not seem to have a noticeable effect on the growth, or at the very least the burner position seemed to have a far greater role in explaining the difference between Tests 1 and 4. The comparison of HRR between model and experiment is shown for Test 1 in Figs. 1–2. The upper layer temperature in the rear of the compartment for this same test is shown in Figs.1–3. The results for the other tests are comparable. The peak HRR and temperature are predicted well, as well as the duration of the fires. Both the peak values and the duration of the burning are important for the WTC simulations because it is not only important to predict the temperatures that the structural steel was exposed to, but also the duration of the exposure.

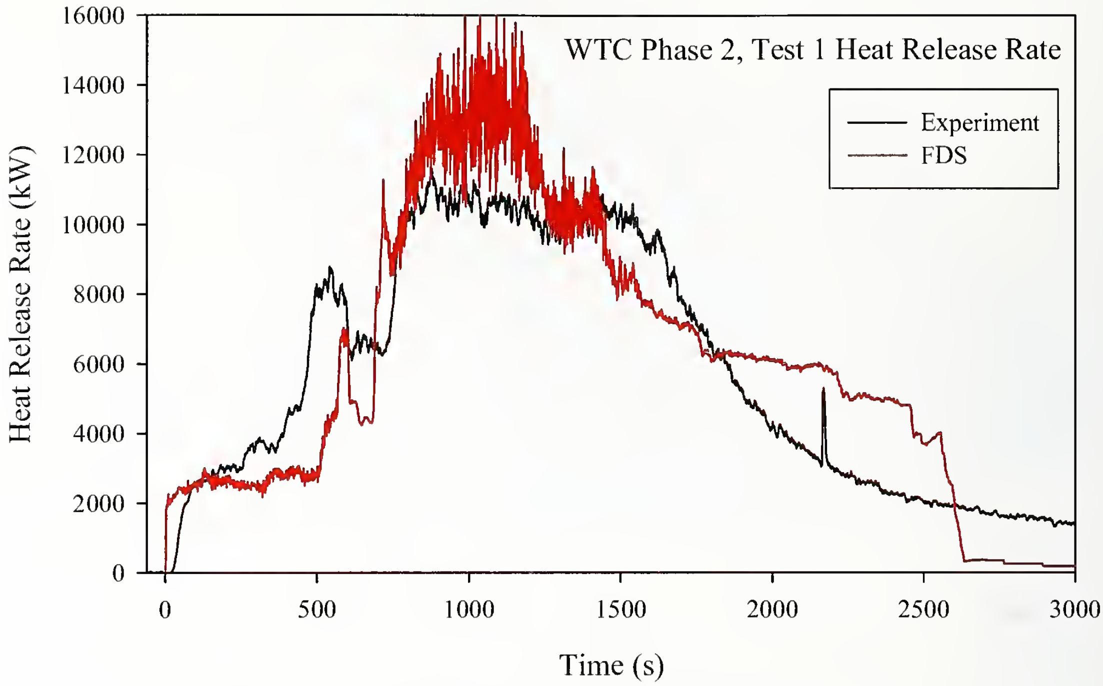

Figure 1–2. Comparison of HRR for Phase 2, Test 1.

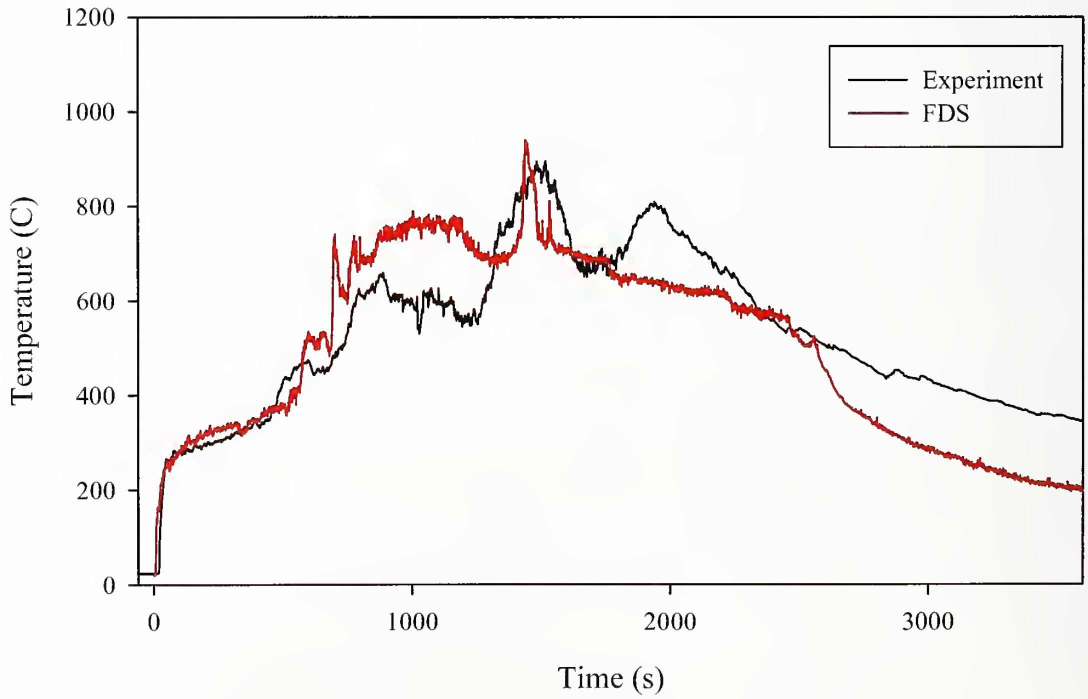

Figure 1–3. Upper layer gas temperature in the rear of the compartment, Phase 2, Test 1.

1.3 SIMULATIONS OF THE FIRES IN WTC 1 AND WTC 2

This section describes how the physical geometry of the buildings was described in the numerical model. Information about the layout of the relevant floors was obtained from architectural drawings provided by the occupants. For floors where information was not available, the geometry of a nearby floor or a floor of similar use was substituted. Information about exterior damage and window breakage was obtained by studying thousands of photographs and videos. There was no attempt made to predict the window breakage in the simulations. This information was provided as a boundary condition.

1.3.1 Numerical Grid

The windows in WTC 1 and WTC 2 were nominally spaced 1 m apart. In addition, the external columns plus their aluminum cladding were assumed to be 0.5 m wide. The slab-to-slab floor spacing was assumed to be 3.6 m. Because of these approximations, a uniform numerical mesh consisting of cells whose dimensions were 0.5 m × 0.5 m × 0.4 m was used. In the model, each tower face consisted of 58 windows, 61 columns, and two 0.5 m spacers next to each corner column. In the real tower geometry, these spacers formed the bevel. Figure 1–4 shows a single floor of the WTC 1 as it is approximated by the numerical model.

The numerical grid for each floor of WTC 1 and WTC 2 was of dimension 128 × 128 × 9 cells. The 128 cells in the horizontal directions allow for several meters of simulation outside of the external walls. The calculations were run in parallel, thus each floor was assigned to a different processor. The floor slabs, core walls, and workstations were approximated as thin obstructions. As described in the previous section, the contents of each workstation were collected into boxes and distributed throughout.

Penetrations in the floor slabs representing elevator shafts and HVAC ducts were created in the model by defining rectangular plates on top of the floor slab that were removed at the start of the calculation. This served to carve out holes in the floor. Window breakage was modeled by removing thin obstructions serving as windows at times obtained from the analysis of photographs and videos. Broken external columns were removed the same way.

1.3.2 Parallel Processing

Modeling the fires on multiple floors of WTC 1 and WTC 2 is computationally intensive, both in terms of CPU time and memory. Up to this point in its development, FDS has been limited to calculations small enough to run on a single CPU and fit into the memory of a desktop personal computer. The WTC study is an example of a large-scale fire modeling problem that is impossible to analyze without the use of parallel processing. In terms of parallelization, the exact details of FDS are not important. The approach taken to run the code on a cluster of machines can be applied to virtually any CFD code, in particular those that involve three spatial dimensions and time. In such cases, the computational demand is fairly well represented by the product of the number of computational grid cells and the number of time steps taken to advance the solution of the governing equations in time. For example, if the computational grid consists of 1 million cells and the simulation requires ten thousand time steps, the demand is 10^{10} cell-cycles. The overall demand can be broken down into memory requirement and CPU time. The memory requirement is a function of the number of grid cells; the CPU time is a function of the number of time steps.

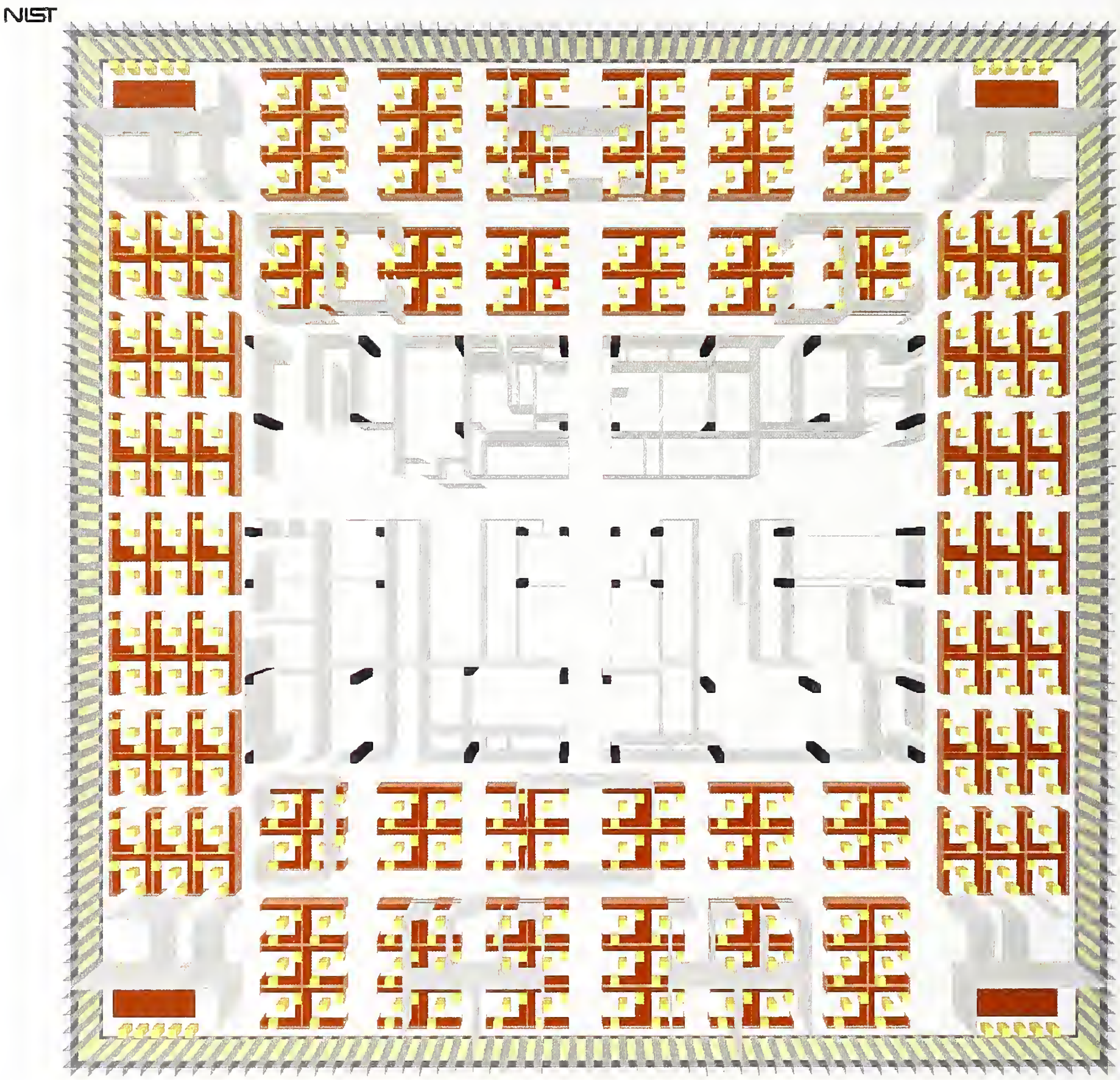

Figure 1–4. Plan view of a typical floor in WTC 1.

Roughly speaking, state of the art 32 bit processors can complete roughly 100,000 FDS cell-cycles per second. Realistic simulations of fires such as those in the WTC require on the order of 500,000,000,000 cell-cycles, or about two months of calculation on a single 2 GHz processor. Plus, the calculation would require 6 to 12 gigabytes of memory (RAM), well over the 4 gigabyte address space of 32 bit processors. Because of this, the WTC calculations are not only impractical on single processor systems, they are impossible on any 32 bit processor. A 64 bit processor system may theoretically handle the static memory requirements of a large simulation time, but the run times for large calculations remain prohibitive.

Because of the computational and memory issues of large fire simulations, a parallel version of the fire model must meet the two fundamental requirements discussed above, as well as satisfy a number of practical implementation concerns. Both the computational and the memory requirements must be distributed across multiple processors. The simulation must be done so that each processor uses less than

4 gigabytes of memory, while enough processors must be used to reduce the simulation to a practical length of time, of the order of one week.

Because the computational load is distributed throughout much of the source code, NIST has chosen to break up the calculation into multiple spatial blocks, with each block essentially doing the same type of calculation. A feature common to most CFD codes is multi-block or multi-mesh structure in which more than one structured grid is used in the calculation. This feature is exploited by simply putting the data and computation for each block on a different processor. This has advantages and some limitations. The advantages are (1) a natural and scalable extension of the existing code, (2) the amount of data communication will be kept to a minimum, since only overlap information needs to be communicated, rather than the data for full blocks, (3) source code changes are localized in small communication routines, (4) development is fairly fast. The disadvantages to the multi-block approach are (1) equal distribution of work across processors (load balancing) depends on spatial symmetry in the simulation, such as the translationally symmetric geometry of the WTC floors, (2) the level of parallelism and the speed up of the calculation is limited to the number of spatial blocks that can be used in the calculation. These limitations are not severe in many cases, including the WTC.

Because NIST is interested in a scalable, portable code, Message Passing Interface (MPI) is used. This is a standard, well-documented system of implementing parallel processing, that can work with shared memory, distributed memory, or combinations of those architectures (Gropp, 1999). Our goal in using MPI was to produce a code that, except for the requirement of the MPI library, would be as portable and standardized as the sequential version. The parallel code runs on most computer platforms, including networked Windows-based PCs. NIST opted for a cluster of commodity personal computers running Linux, connected by a gigabit ethernet network. The individual processors are in the range of 2.0 to 2.8 GHz, and dual processor machines were chosen to save space and to allow the addition of OpenMP code as a future extension to the MPI-based code. For production work in the NIST laboratory, two clusters are used: a smaller, development cluster to develop and debug the code, and a larger cluster with 128 processors. Using both clusters provides the capability to run six to eight large parallel processing jobs simultaneously.

1.3.3 Sample Simulation

Shown in Fig. 1–5 is a sequence of snapshots showing the predicted upper layer temperatures on a floor of WTC 1 at time increments of 15 min. The first image is a cut-away showing the damage to the north face of the tower and the layout of the walls and furnishings. The subsequent images are color coded by temperature, with the red (or dark) patches representing temperatures in the vicinity of 1,000 °C. Initially, these hot areas of active burning are near the impact zone at the north end (foreground of picture), but migrate towards the south as the combustible furnishings are exhausted. Driving the progress of the fires is the breaking of windows that provide air to the oxygen starved fire. The window breakage is not predicted by the model; it is an imposed boundary condition resulting from the analysis of thousands of photographs and videos recorded that day by eye witnesses. The uncertainty in the window break times is on the order of 5 min in areas not obscured by smoke.

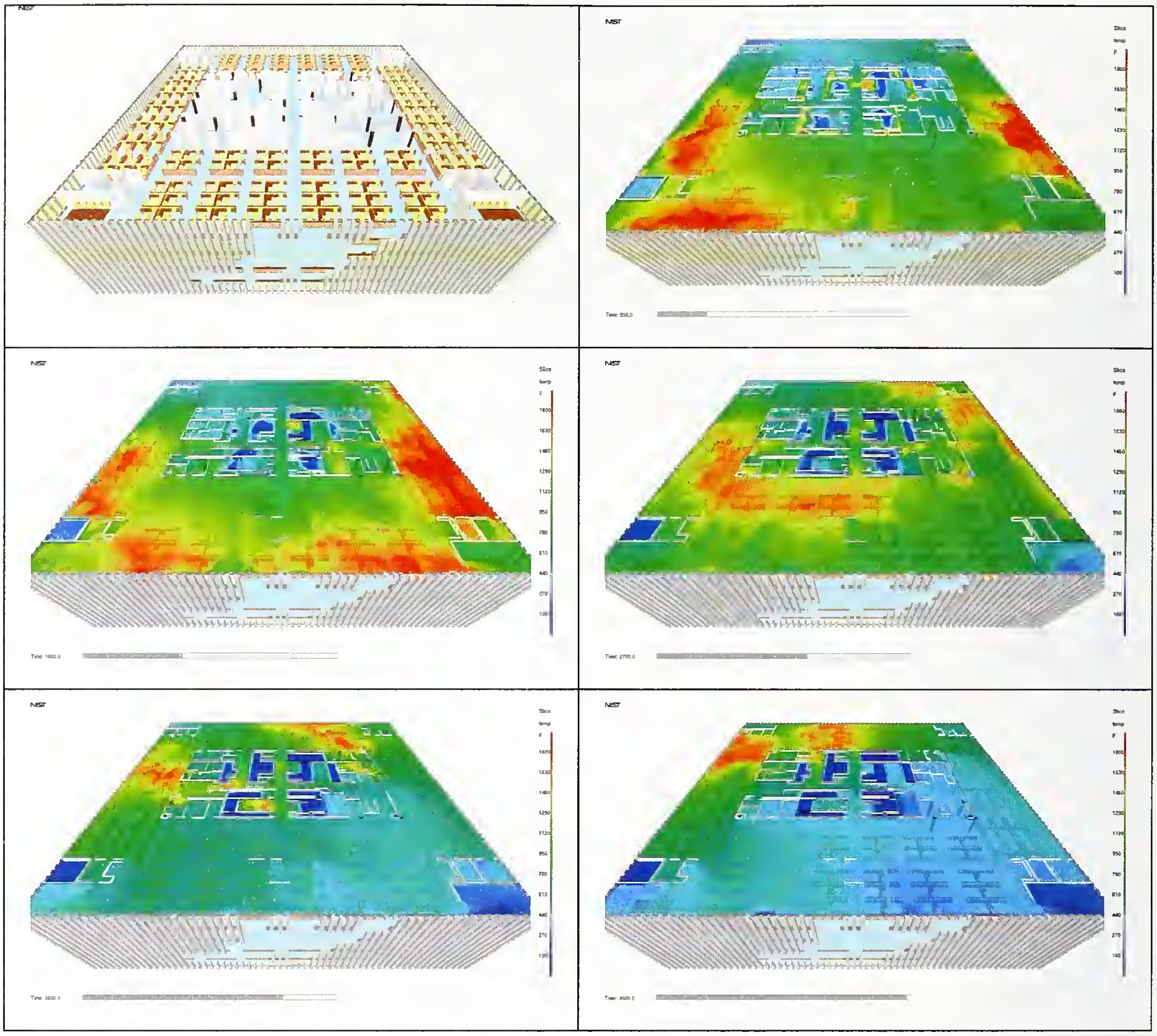

Figure 1–5. Predicted upper layer temperatures of a floor of WTC 1.

The burning behavior shown by the simulation is similar to that of the fires in experiments conducted by Ian Thomas and Ian Bennetts (1999). They looked at fire spread in long and wide enclosures with a single ventilation opening, where the fires were ignited at various points deep within the bench-scale compartments used. The fires would rapidly spread across the liquid or solid fuels covering the floor without consuming much of the fuel. The fires would then surround the compartment opening and burn back into the compartment as the fuel near the opening was exhausted. In the WTC simulations, fires are ignited over a wide area by simulated spray nozzles ejecting a liquid with properties of aircraft fuel. Much of the available oxygen is consumed rapidly, driving the fires to the openings created by the aircraft. The fires move away from the initial impact area as the nearby furnishings are exhausted, and as windows are broken out away in other parts of the building.

1.4 SUMMARY

The investigation into the cause of the collapse of WTC 1, WTC 2, and WTC 7 by NIST will not be completed until the fall of 2004. Work is on-going to simulate the weakening of the structural steel due to the aircraft impacts and the fires. Nevertheless, the fire experiments and simulations performed to date have improved our ability to analyze the response of any large building or structure to fire. In the years ahead, these techniques will become increasingly widespread due to faster computers and the ability to harness an entire set of off-the-shelf personal computers to perform very large calculations. Effective modeling is a combination of fast computers, efficient algorithms, and well-planned small and large scale experiments to provide both input to the model and a validation of results. Projects as complicated as the WTC study are rarely conducted using modeling alone. There is and will always be a need to coordinate computation and experiment to reconstruct the dynamics of large fires.

1.5 REFERENCES

Gropp, W., E. Lusk, and A. Skjellum. 1999. *Using MPI*, MIT Press, Cambridge, Massachusetts, USA.

Hamins, A., and K.B. McGrattan. 2003. Reduced-Scale Experiments on the Water Suppression of a Rack-Storage Commodity Fire for Calibration of a CFD Fire Model. Fire Safety Science: Proceedings of the Seventh International Symposium. International Association for Fire Safety Science.

McGrattan, K.B., H.R. Baum, R.G. Rehm, G.P. Forney, J.E. Floyd, K. Prasad and S. Hostikka. 2002. Fire Dynamics Simulator (Version 3), Technical Reference Guide. NISTIR 6783. National Institute of Standards and Technology, Gaithersburg, MD.

Ritchie, S.J., K.D. Steckler, A. Hamins, T.G. Cleary, J.C. Yang, and T. Kashiwagi. 1997. The Effect of Sample Size on the Heat Release Rate of Charring Materials. Fire Safety Science: Proceedings of the Fifth International Symposium. International Association for Fire Safety Science.

Thomas, I.R. and I.D. Bennetts. 1999. Fires in Enclosures with Single Ventilation Openings–Comparison of Long and Wide Enclosures. Fire Safety Science: Proceedings of the Sixth International Symposium. International Association for Fire Safety Science.

This page intentionally left blank.

Table of Contents

List of Figures

LIST OF TABLES

Appendix K
INTERIM REPORT ON SUBSYSTEM STRUCTURAL ANALYSIS OF THE WTC TOWERS

K.1 PURPOSE

Project 6 addresses the first primary objective of the technical investigation led by the National Institute of Standards and Technology (NIST) of the World Trade Center (WTC) disaster: to determine why and how the WTC towers (WTC 1 and WTC 2) collapsed following the initial impacts of the aircraft. Specifically, the objectives of this project are to determine the response of the structural components and systems to the fire environment in WTC 1 and WTC 2 and to identify probable structural collapse mechanisms. This appendix documents the progress achieved to date on Project 6 in thermal/structural modeling of WTC 1 and WTC 2.

Project 6 seeks to determine the response of structural components and systems to the fire environment in the WTC 1 and WTC 2 and to identify probable structural collapse mechanisms by (1) evaluating the response of floor and column systems under fire conditions, (2) evaluating the response of the WTC towers without and with aircraft impact damage under fire conditions, (3) conducting tests of structural components and systems under fire conditions, and (4) evaluating competing failure hypotheses for the WTC towers.

K.2 SCOPE OF WORK

The scope of the work consists of the following three tasks:

- **Task 1, Subsystem Structural Analysis.** The objective of Task 1 includes structural analysis of components and two subsystems, a full-floor subsystem, and an exterior wall subsystem. Task 1 is intended to provide guidance for the development of the global finite element models (FEMs) with respect to element types and sizes, appropriate constitutive models, and failure criteria for any given structural component. The subsystem analyses also will help to validate the accuracy of the global analyses, and correlate the results of the fine mesh component analyses with the coarser mesh global analyses of Task 2 and Task 3.

- **Task 2, Global Analysis of the WTC Towers' Response to Fire without Impact Damage.** The objectives of this task are to determine the general vulnerability of the towers to fire-initiated collapse and the role of fire in the towers with respect to structural stability, sequential failures of components and subsystems, and collapse initiation for the towers without impact damage.

- **Task 3, Global Analysis of the WTC Towers' Response to Fire with Impact Damage.** The objectives of this Task are to determine the relative roles of the impact damage and fires in the towers with respect to structural stability and sequential failures of the components and subsystems and to determine probable structural collapse initiation sequences.

Work under Task 1 includes the following:

- Develop and validate ANSYS models of the full floor and exterior wall subsystems.
- Evaluate structural responses for the following loading conditions.
  - Service loads due to gravity (dead and live loads).
  - Elevated structural temperatures.
- Identify the possible, likely and most likely failure modes and failure sequences, and the associated temperatures at failure and times-to-failure.
- Identify the changes in mechanical properties or geometry at initiation of component and subsystems collapse.
- Identify simplifications for the global structural models and/or analyses of subsystem models to use in Task 2 and Task 3.

The scope of this report is to present the progress made in Task 1 work.

K.3 DESCRIPTION OF SUBSYSTEM STRUCTURES

The full floor subsystem modeled is floor 96 of WTC 1. The model is believed to be typical in the upper floors of both towers. The exterior wall subsystem is a nine-column (three-panel) wide by nine-story (three-panel) high section of the WTC 1 between floor 91 and floor 100 and column 150 and column 158. This area is typical of the exterior walls of the towers and connects to a part of the floor system near the corner with different types of trusses.

K.3.1 Full Floor Subsystem Description

Floor 96 of WTC 1 was identified as an office floor with typical floor construction and loading and, therefore, was selected as the basis for this model. Components of the floor subsystem are examined for performance under loads and elevated temperatures in different possible failure modes. Understanding of these component behaviors is used to define the floor models for global analyses of WTC 1 and WTC 2.

The full floor subsystem of floor 96 of WTC 1 includes both office area and core area horizontal framing, as well as columns immediately above and below this floor.

The floor support in the office area consisted of pairs of steel floor trusses (nominally 60 ft in north-south and 36 ft in east-west directions) that span between exterior walls and the central core at 6 ft 8 in. on center. Each of these primary trusses consisted of top and bottom chords fabricated from steel angles and diagonals fabricated from round bars that extended 3 in. above the top chord at the panel points into the concrete slab in the form of a knuckle. The top chords of the primary trusses were supported at the central core by truss seats connected to a steel channel that ran continuously between the core columns. Each pair of trusses was connected to this channel with a seat that included two 1 3/4 in. long slotted holes and two 5/8 in. bolts (one bolt in each truss) as shown in Fig. K–25. Note that the floor truss was not welded to the seat support.

At the exterior wall, the truss pair was supported by a seat angle and fastened with two 5/8 in. diameter bolts in 2 in. long slotted holes. In addition, a gusset plate welded to the spandrel and to the truss top chord tied the supporting column to the truss, and a pair of straps welded to the top chord and to adjacent columns tied those columns into the primary trusses. Primary trusses were interconnected by a transverse bridging system consisting of bridging trusses and bridging angles. These bridging trusses were of similar construction to the primary trusses, although the knuckles for the diagonals did not project above the top chords. The top chord of the bridging trusses sat 1 1/2 in. below the top chord of the primary trusses and provided support for the 1 1/2 in., 22 gauge steel deck and the 4 in. thick lightweight concrete slab. At each corner of the building core, a 36 ft long transfer truss extended out from the corner core column to the exterior wall and supported the 60 ft long primary trusses. The core area floor consisted of a 5 in. thick normal-weight concrete slab on 1 1/2 in., 22 gauge steel deck, supported by wide flange girders and beams connected to the core columns.

Task 1 analyses use the nominal dimensions and design details shown on the drawings, without modifications resulting from any construction deviations or tenant modifications. Those modifications are considered in subsequent Task 3 analyses, which are based on the reference model developed by Leslie E. Robertson Associates (LERA) under a contract for Project 2. Material properties are based on information provided by Project 3.

K.3.2 Exterior Wall Subsystem Description

Each side of the towers' exterior wall consisted of fifty-nine 14 in. square box columns spaced at 3 ft 4 in. on center, with 52 in. deep spandrel plates at each floor level. The exterior wall was constructed from shop-welded prefabricated panels, each consisting, in general, of three columns and three spandrel beams, 13 ft 4 in. wide by 36 ft high. Except at mechanical floors, the base and top of the structure, vertical splices in prefabricated panels were staggered such that within any story, every third prefabricated panel had a vertical splice. Exterior column splices at the upper stories typically consisted of four 7/8 in. diameter ASTM A325 bolts fastened through the welded butt plates at the tops and bottoms of adjoining columns. Special prefabricated panels existed for the mechanical floors where no stagger existed at floors 7, 41, 75, and 108. At these mechanical floors, the column splice detail included supplemental field welding in addition to the bolted connection. Horizontal (spandrel-to-spandrel) connections between prefabricated panels were all field-bolted using splice plates. Corner panels that connected the orthogonal walls at corners were two-stories tall (24 ft) and consisted of two columns, two spandrel plates, and a third column midway between the two columns on alternate floors.

Various grades of steel, having yield strengths ranging between 42 ksi and 100 ksi, were specified to fabricate the perimeter column and spandrel plates. However, fewer grades were actually used with somewhat coarser gradation in yield strength than specified. Plate thicknesses also varied, both vertically and around the building perimeter. Plate thicknesses in the exterior wall were as thin as 1/4 in. at the upper stories, and increased toward the base of the building. The specified plate thicknesses and material yield strengths differed between the two towers, among NS and EW directions and through the height of the tower.

An exterior wall subsystem model, nine columns wide and nine floors high, was selected to study the structural behavior and failure modes of the exterior wall system. This subsystem model represents the exterior wall of WTC 1 between floors 91 and 100 and includes column lines 150 through 158. This area is located near the corner of the tower (column 159 is at the corner of the north face of WTC 1. See Fig. K–27.) The wall subsystem allows evaluations of the interaction of the wall subsystem with thermal expansion of the floor near the corners. It also connects to various types of trusses with different behaviors.

K.4 LOADS

The subsystems and components are analyzed for Dead (D), Live (L), and thermal (T_a) loads. The dead load consists of structural weights and superimposed dead loads. The superimposed dead loads for floors outside the core consist of the weights of ceiling, mechanical and electrical, fireproofing, and floor finish, estimated at 8 psf. The superimposed dead load and design live load are defined in the World Trade Center Design Criteria (LERA 2001). Twenty five (25) percent of the design live load is selected as a reasonable approximation of the load that likely existed at the time of the collapse. (For example, 25 percent of the design live load results in a load of 13.75 psf for the long-span trusses in the two way zone of floor 96 with 55 psf design live load.) The service dead and live loads are applied first, followed by the thermal loads.

The dead and live loads are defined as weights, so that during the collapse process, the gravity loads remain acting on the structure. The weight of debris from the plane will be considered where provided by Project 2.

The thermal loads, T_a, are temperature time histories for all structural members provided by Project 5 for the standard test fire ASTM E119 and between three and five representative building fire scenarios of different intensities and three fire protection conditions.

For analysis of some of the components, discrete values of temperature or temperature distributions in the form of a ramp from 0 °C to 700 °C (or to a temperature below 700 °C that results in the failure of the component) over 0.5 h followed by a constant temperature of 700 °C for another 0.5 h are used. Failure modes of the components are evaluated at room temperature and at different elevated temperatures, as failure modes and failure loads may change with increasing temperature.

Although wind may have had a minor role in the collapse of the towers, Task 1 analyses do not include wind load effects.

K.5 MATERIALS

The mechanical properties of both steel and concrete are affected significantly by temperature. In the following sections, the material properties used in this project are specified as a function of temperature. A material properties catalog is prepared and made accessible to all analysis models. For use in ANSYS, each material is identified with a number; steels are Material ID 1 through Material ID 29, and concretes are Material ID 51 through Material ID 83.

K.5.1 Concrete

Aggregate Types

Two types of concrete were generally used for the flooring inside the towers; lightweight concrete was used in the office areas, and normal-weight concrete in the core area. Thermal properties of normal-weight concrete depend on the type of aggregate. Petrographic inspection by SGH of several samples of lightweight concrete taken from the debris at NIST showed siliceous sand in the lightweight concrete. Because source of coarse and fine aggregates is usually the same, the available data for normal-weight concrete with siliceous aggregates are used.

Actual Compressive Strength

Specified concrete strength for lightweight concrete is 3,000 psi and for normal-weight concrete either 3,000 psi or 4,000 psi, as shown on Drawing Book 8, Sheet AB1–2.1 (SHCR 1973). The actual strength, f_a, of in-place concrete at room temperature is calculated from the specified strength, f'_c, as follows:

$$f_a = f'_c \cdot F_1 \cdot F_2 \cdot F_3 \qquad (1)$$

where the factor F_1 is the ratio of the average strength of cylinders to specified strength, F_2 is the ratio of in-situ 28-day strength to 28-day cylinder strength, and F_3 accounts for the change in concrete strength with age.

By using $F_1 = 1.25$ and $F_2 = 0.95$ (Bartlett and MacGregor 1996) and $F_3 = 1.16$ based on the formula specified in Section 2.2.1 of American Concrete Institute (ACI) 209 for change of concrete strength with age of concrete, the mean of the ratio of actual strength of in-place concrete to the specified concrete strength $f_a / f'_c = 1.38$. Based on this mean value, the actual strength of in-place concretes are $f_a = 5{,}500$ psi for the specified 4,000 psi normal-weight concrete, 4,100 psi for the specified 3,000 psi normal-weight concrete, and 4,100 psi for the specified 3,000 psi lightweight concrete.

Concrete Properties

The unit weight of the lightweight concrete is 100 pcf according to the WTC Design Criteria (LERA 2003): however, 110 pcf is used based on the two concrete samples described above. The unit weight of the normal-weight concrete is 150 pcf, according to LERA.

Poisson's ratio, ν_c, of 0.17 is used for both normal-weight and lightweight concrete at all temperatures.

Temperature dependent properties of concrete are modulus of elasticity, instantaneous coefficient of thermal expansion, compressive strength, and tensile strength:

Modulus of elasticity at room temperature is evaluated by the following formula:

$$E_c(RT) = 33\gamma_c^{\,1.5}\sqrt{f_a} \qquad (2)$$

The actual strength, f_a, is used as room temperature compressive strength, and $5\sqrt{f_a}$ is used as room temperature tensile strength. Effects of elevated temperature on the listed properties are based on NIST research (Phan 1996, 2003), and plotted in Fig. K–1.

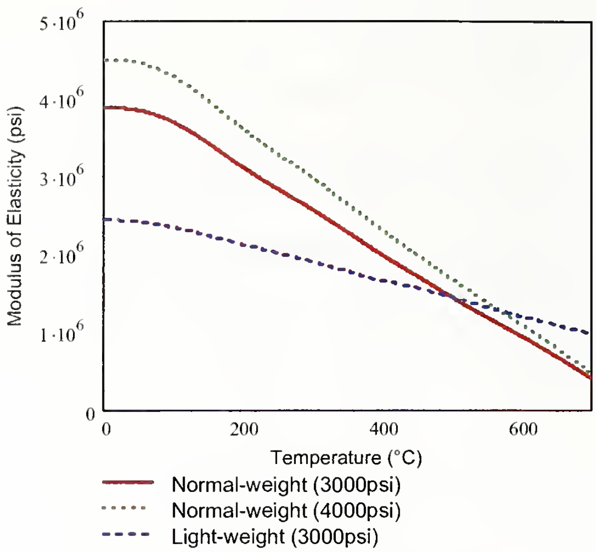

(a) Modulus of elasticity

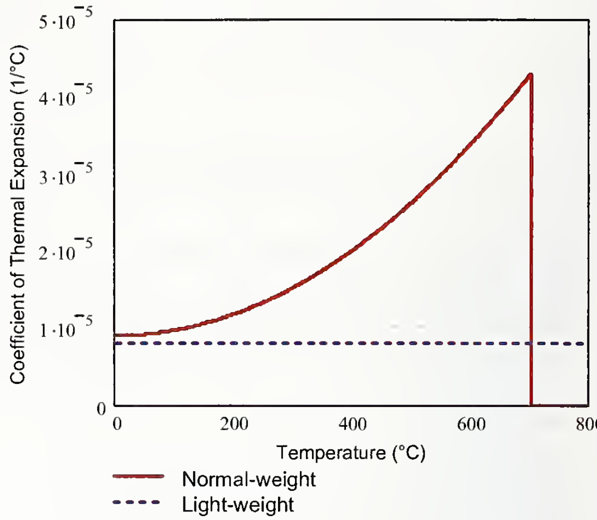

(b) Instantaneous coefficient of thermal expansion

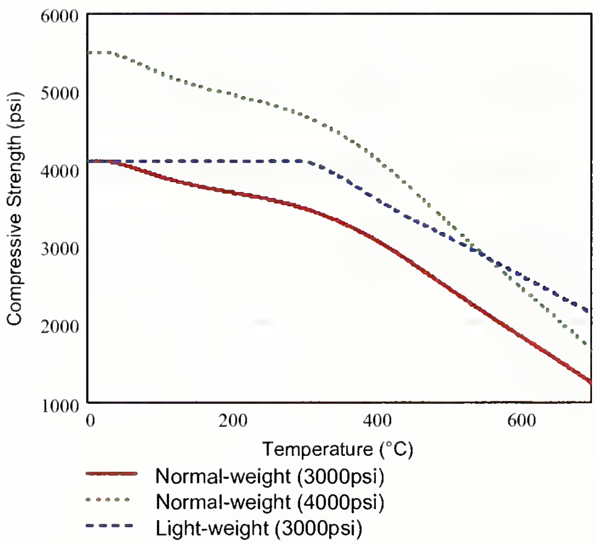

(c) Compressive strength

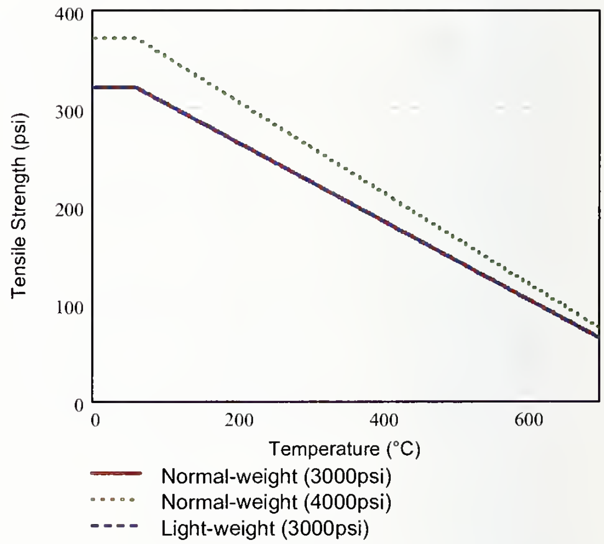

(d) Tensile strength

Figure K–1. Temperature–dependent concrete properties.

Concrete Stress-Strain Relationships

The compressive stress-strain curve, based on the formula by Seanz (1964), is given by:

$$\sigma = \frac{K_c f_c \left(\frac{\varepsilon}{\varepsilon_{c1}}\right)}{1 + a\left(\frac{\varepsilon}{\varepsilon_{c1}}\right) + b\left(\frac{\varepsilon}{\varepsilon_{c1}}\right)^2 + c\left(\frac{\varepsilon}{\varepsilon_{c1}}\right)^3} \tag{3}$$

where:

$$c = \frac{K_s - 1}{(K_e - 1)^2} K_c - \frac{1}{K_e}, \quad b = 1 - 2c, \quad a = c + K_c - 2,$$

$$K_c = 2, \quad K_s = \frac{1}{0.85}, \quad K_e \doteq 1.41, \quad \varepsilon_{c1} = K_c \frac{f_c}{E_c}$$

In tension, stress increases linearly up to the tensile strength. When strained in tension beyond its strength will soften and the stress will drop. However, the descending branch of stress-strain relationship causes significant numerical instability problems which can be avoided by assuming that concrete becomes plastic in tension. Figure K–2 shows a few examples of concrete stress-strain curves at room and elevated temperatures.

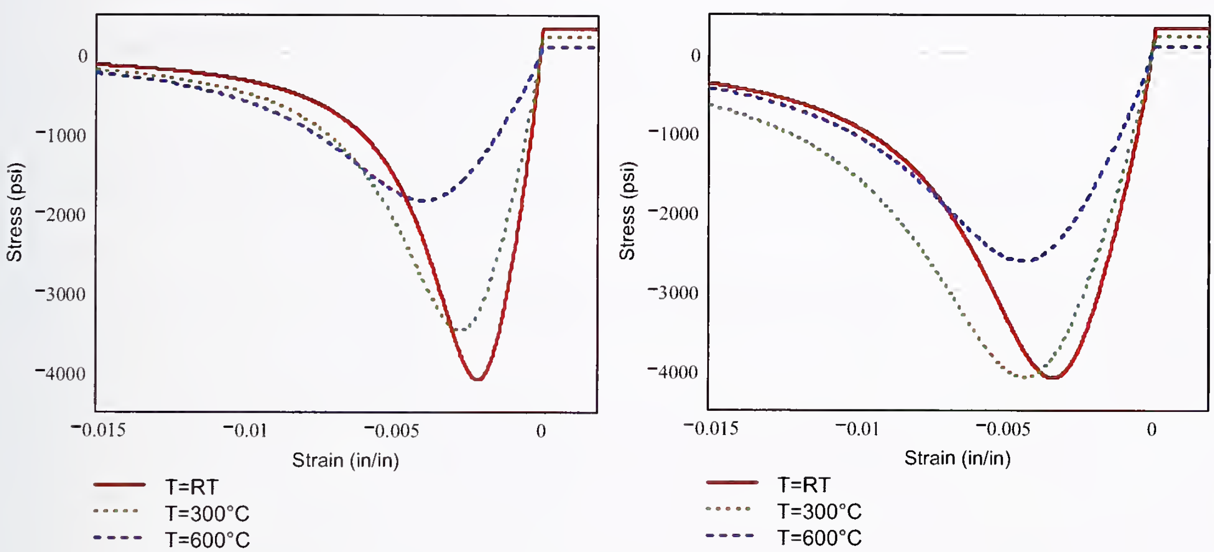

(a) Normal-weight concrete (3000psi)

(b) Light-weight concrete

Figure K–2. Concrete stress-strain curves.

For the knuckle model in LS-DYNA, solid concrete elements are modeled with Pseudo Tensor material model, where the cap model is used. Since this material model is not temperature dependent, different material types are specified for the lightweight concrete at RT, 150 °C, 300 °C, 450 °C, 600 °C, and 750 °C (Material IDs 51 through 56) with their different stress-strain relationships.

The concrete slab in the truss is modeled with SHELL181 elements with a concrete material model that accounts for different behaviors in tension and compression. One such material model in ANSYS is the cast iron plasticity model which uses the Rankine maximum stress criterion in tension, and the expression for von Mises yield criterion in compression (ANSYS, Inc. 2004). Cast iron plasticity material models for specified 3,000 psi normal-weight concrete, specified 4,000 psi normal-weight concrete, and specified 3,000 psi lightweight concrete are assigned to Material ID 81, 82, and 83, respectively.

K.5.2 Steel

Steels used in WTC 1 and WTC 2 are listed in Table K–1 along with the yield and tensile strengths used in our analysis.

Steel Properties

Figure K–3 shows mechanical properties of steel at high temperatures: (a) modulus of elasticity; (b) Poisson's ratio; (c) yield strength reduction factor; (d) tensile strength reduction factor; and (e) instantaneous coefficient of thermal expansion. All properties, except yield and tensile strength reduction factors for bolt steels, are the same for all steels shown in Table K–1.

Stress–Strain Relationship

Plasticity: Stress-strain relationships at room temperature were provided by Project 3. They were constructed from mill report data, actual test data, and literature information using the Voce hardening law.

Stress–strain relationships at elevated temperatures, without consideration of creep, are obtained by the power law:

$$\sigma = R_{TS} R_C K(T) \varepsilon_{ep}^{n(T)} \tag{4}$$

where:

$$K(T) = (k4 - k0)\exp\left\{-0.5\left[\left(\frac{T}{tk1}\right)^{k1} + \left(\frac{T}{tk2}\right)^{k2}\right]\right\} + k0 \tag{5}$$

$$n(T) = (n4 - n0)\exp\left\{-0.5\left[\left(\frac{T}{tn1}\right)^{n1} + \left(\frac{T}{tn2}\right)^{n2}\right]\right\} + n0 \tag{6}$$

The steel stress-strain relationships at different temperatures vary depending on the type of steel used in the construction of the towers. Values for R_{TS}, R_C, given in Table K–1, and parameters of $K(T)$ and n(T) given in Table K–2, were provided by Project 3. The stress-strain curve is linear with Young's modulus up to the "linearity limit": At the linearity limit, the linear stress-strain curve intersects the power law stress strain curve. (Stress at the linearity limit is not necessarily equal to the yield stress. The linearity limit is required for ANSYS input.)

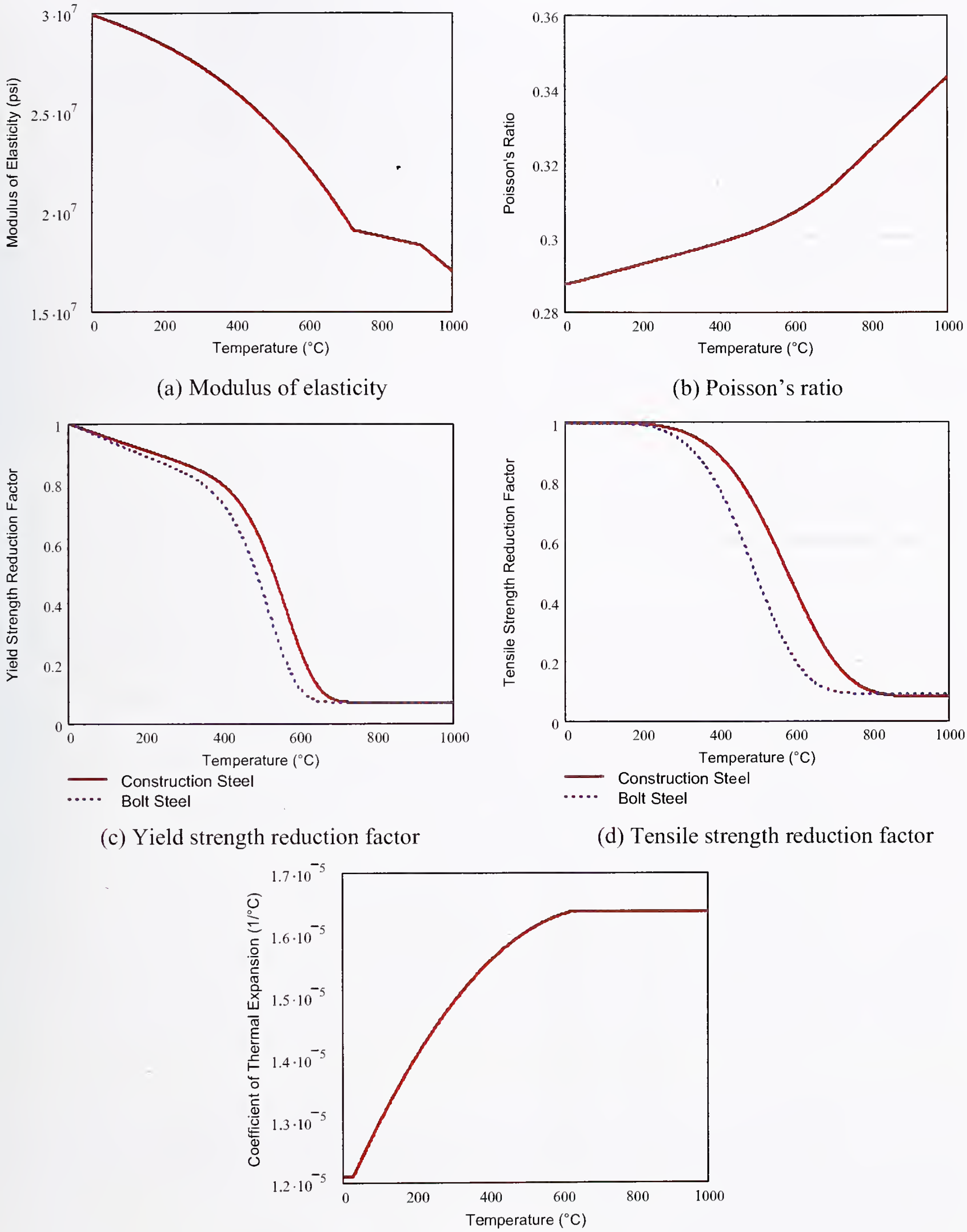

(a) Modulus of elasticity

(b) Poisson's ratio

(c) Yield strength reduction factor

(d) Tensile strength reduction factor

(e) Instantaneous coefficient of thermal expansion

Figure K–3. Temperature-dependent properties for all steels.

Table K–1. Steel types used in WTC 1 and WTC 2.

Material ID	Description	σ_{yRT} (psi)	σ_{uRT} (psi)	RTS	RC
1	All 36 ksi core box columns, plates, straps[a]	36,720	64,470	1.086	0.857
2	All 36 ksi core WF, channels, and tubes 36 ksi large area and large inertia "rigid" beams in SAP2000 model[a]	37,000	63,450	1.069	0.954
3	All 42 ksi box columns (1<=0.75 in.)	51,400	79,200	1.070	0.884
4	All 42 ksi box columns (0.75 in. < t <= 1.5 in.)	47,000	74,800	1.010	0.884
5	All 42 ksi box columns (t > 1.5 in.)	42,600	70,400	0.951	0.880
6	42 ksi or 45 ksi Group 3 WF core columns	53,800	74,400	1.005	0.977
7	42 ksi or 45 ksi Group 3 WF core columns	49,000	71,040	0.960	0.954
8	42 ksi Group 4&5 WF core columns	44,200	66,640	0.900	0.948
9	45 ksi Group 4&5 WF core columns	47,800	71,074	0.960	0.939
10	All 36 ksi Plates 1, 2, and 4 in perimeter columns	35,630	61,170	1.031	0.875
11	All (42, 45, or 46) ksi Plates 1, 2, and 4 in. perimeter columns	53,051	74,864	1.011	0.948
12	All 50 ksi Plates 1, 2, and 4 in. perimeter columns. All 50 ksi channels and plates[a]	53,991	75,618	1.021	0.978
13	All 55 ksi Plates 1, 2, and 4 with t<=1.5 in. in perimeter columns	60,817	82,558	1.115	0.903
14	All 60 ksi Plates 1, 2, and 4 with t<=1.25 in. in perimeter columns	62,027	87,250	1.178	0.894
15	All 65 ksi Plates 1, 2, and 4 with t<=0.5 in. in perimeter columns[b]	69,642	90,442	1.221	0.979
16	All 70 ksi Plates 1, 2, and 4 in. perimeter columns	76,735	91,951	1.242	0.955
17	All 75 ksi Plates 1, 2, and 4 in perimeter columns	82,469	96,821	1.308	0.936
18	All 80 ksi perimeter columns steels, regardless of plate	91,517	99,442	1.343	0.987
19	All (85, 90, 100) ksi perimeter column steels, regardless of plate	104,783	115,983	1.566	0.976
20	Laclede truss web bar rounds specified as A36	38,067	59,567	1.004	0.935
21	Laclede truss chord angels (regardless of ASTM Spec) and all rounds specified as A242	55,332	74,050	1.000	0.959
22	A325 bolts[c]	104,783	115,983	1.566	0.976
23	All 42 ksi Plate 3 in perimeter columns	42,600	67,216	0.900	0.912
24	All 45 ksi Plate 3 in perimeter columns	45,900	69,831	0.940	0.921
25	All 50 ksi Plate 3 in perimeter columns	51,400	74,188	1.000	0.935
26	All 55 ksi Plate 3 in perimeter columns	56,900	78,546	1.070	0.906
27	All 60 ksi Plate 3 in perimeter columns	62,400	83,903	1.130	0.949
28	All 65 ksi Plate 3 in perimeter columns	67,900	87,261	1.190	0.975
29	All 70 ksi and 75 ksi Plate 3 in perimeter columns	78,900	95,976	1.310	0.997

a. Steels in the following members are assumed to have the properties shown in the table:
36 ksi plates and straps (Material 1).
36 ksi channels, tubes, and "rigid" beams (Material 2).
50 ksi channels and plates (Material 12).
b. 65 ksi steels in perimeter columns with t>0.5 in. are assumed to have the same properties as those in Material 15.
c. In the column model, stress-strain relationships of bolts are used.
Note: Bolt properties are assumed to be the same as those in Material 19.

Table K–2. Parameters for *k(T) and n(T)*.

	σ_{yRT} = 36,000 psi	σ_{yRT} > 36,000 psi
tk1, °C	524.1812	511.8266
tk2, °C	523.6799	511.8938
k0, psi	29049.2	26472.1
k1	9.4346	6.5764
k2	9.3532	6.5971
k4, psi	121605.6	122516.7
tn1, °C	524.4304	519.634
tn2, °C	521.241	499.6031
n0, psi	0.1235	0.0342
n1	19.0000	10.0000
n2	19.0000	10.0000
n4, psi	0.2168	0.1511

Figure K–4 shows stress-strain curves of Material ID 1 (see Table K–1 for the material description) at room and elevated temperatures. Figure K–4 (a) is a close-up view of a low strain range, while Fig. K–4 (b) shows strain levels up to 0.3.

The elastic-plastic behavior of steels is modeled with ANSYS material model "Multi–linear isotropic hardening von Mises plasticity."

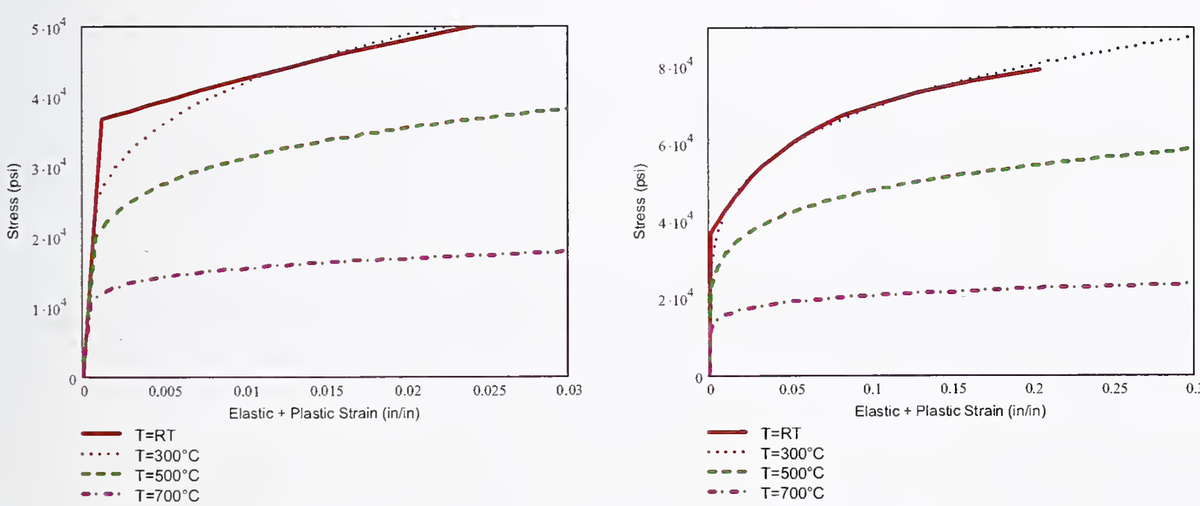

(a) Strain < 0.03 (b) Strain < 0.30

Figure K–4. Stress-strain relationships for Material ID 1 steel.

Creep: Steel creeps at elevated temperatures ($T \geq 350°C$), and the creep behavior for steels is based on the creep model by Fields and Fields (1991), expressed as:

$$\varepsilon_{cr}(t,T,\sigma) = \frac{1}{100} a(T) \left(\frac{t}{60} \right)^{b(T)} \left(35.5 \frac{\sigma}{\sigma_{yRT}} \right)^{c(T)} \tag{7}$$

where:

$$a(T) = \begin{cases} 0 & \text{for} \quad T < 350°C \\ 10^{-(6.1+0.00573T)} & \text{for} \quad 350°C \leq T < 500°C \\ 10^{-(13.25-0.00851T)} & \text{for} \quad 500°C \leq T < 725°C \end{cases}$$

$$b(T) = -1.1 + 0.0035T \quad \text{for} \quad T < 725°C$$

$$c(T) = 2.1 + 0.0064T \quad \text{for} \quad T < 725°C$$

This model is valid for the temperature range of $350°C \leq T \leq 725°C$. ANSYS uses the "time hardening creep" model, where creep strain rate is given by:

$$\frac{d\varepsilon_{cr}}{dt} = C_1(T)\sigma^{C_2(T)} t^{C_3(T)} \tag{8}$$

and $C_1(T)$, $C_2(T)$, and $C_3(T)$ are temperature-dependent parameters determined by Fields' (1991) creep model given as:

$$C_1(T) = \frac{1}{100} a(T) b(T) \left(\frac{1}{60} \right)^{b(T)} \left(\frac{35.5}{\sigma_{yRT}} \right)^{c(T)}$$

$$C_2(T) = c(T)$$

$$C_3(T) = b(T) - 1$$

Figure K–5 illustrates creep behavior of steel at elevated temperatures for Material ID 1. Figure K–5 (a) shows creep strain rate at different stress levels and different temperatures, and Fig. K–5 (b) compares elastic, plastic, creep, elastic plus plastic, and total strains at $T = 400°C$ and after constant loading for 1,800 s.

Failure Criteria

The failure criteria for steel are defined in terms of plastic strains. The multiaxial fracture strain criterion for different steels and temperatures (Fields 2004) is as follows:

$$\bar{\varepsilon}_f = \alpha(T) \exp\left[-\frac{3}{2} \frac{\sigma_m}{\bar{\sigma}} \right] \tag{9}$$

where stress and strain are true stress and true strain.

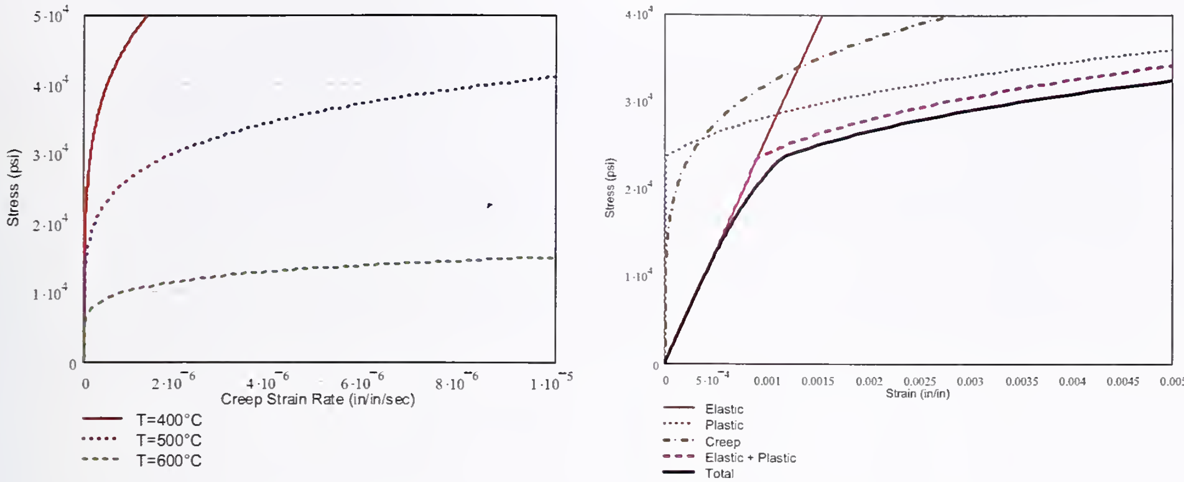

(a) Creep strain rate

(b) Comparison of different strains at T=400 °C and t=1,800 s

Figure K–5. Creep behavior at elevated temperatures for Material ID 1 steel.

For the uniaxial stress condition, the plastic strain at fracture reduces to:

$$\bar{\varepsilon}_{f\_uni} = \exp(-0.5)\alpha(T) \tag{10}$$

Table K–3 shows the uniaxial plastic strain at fracture, $\bar{\varepsilon}_{f\_uni}$, at different temperatures calculated by the equation above. This criterion is valid for the finite element analysis (FEA) with very fine mesh. For coarse mesh, the equivalent steel fracture criterion was determined numerically as follows. A standard tension test specimen was modeled in ANSYS. The gauge length, width, and thickness of the specimen were 8 in, 1.5 in, and 1 in., respectively, and Material ID 1 steel properties were used. Six different models (Model 0 to 5) were created, each having a different mesh size. Element sizes of Models 0 to 5 were 0.025 in., 0.050 in., 0.0125 in., 0.250 in., 0.375 in., and 0.75 in. It was assumed that Model 0 was able to capture tensile fracture in a uniaxial tension.

Model 0 was subjected to tension until the maximum plastic strain in the direction of applied displacement reached the uniaxial fracture strain determined by Eq. (10) for uniaxial stress condition, and the corresponding elongation of the specimen, Δ_0, was obtained. Models 1 to 5 were then subjected to the same elongation, Δ_0, and the maximum plastic strain in the direction of applied displacement was measured for each model. The maximum plastic strain due to the elongation of Δ_0 is defined as the limiting plastic strain (equivalent fracture plastic strain) for the corresponding element size.

From these six cases, a relationship between element size and equivalent uniaxial fracture plastic strain was established. This process was repeated for temperatures 20 °C, 100 °C, 300 °C, 500 °C, and 700 °C. Figure K–6 (a) shows the ratio of the maximum plastic strain in the direction of applied displacement due to displacement Δ_0 to uniaxial plastic strain by Eq. (10) vs. element size at different temperatures. The FEA results were extrapolated up to the element size of 50 in. Plastic strain shown in Fig. K–6 (b) is used as fracture criterion for the corresponding element size in the FEA.

Table K–3. Uniaxial plastic strain at fracture by Eq. (10).

Material ID	Plastic Strain at Fracture in the Uniaxial Test					
	20	100	300	500	700	1000
1	0.8411	0.6989	0.6610	1.0446	1.8100	3.5862
2	0.8411	0.6989	0.6610	1.0446	1.8100	3.5862
3	0.4908	0.4078	0.3857	0.6095	1.0561	2.0924
4	0.4908	0.4078	0.3857	0.6095	1.0561	2.0924
5	0.4908	0.4078	0.3857	0.6095	1.0561	2.0924
6	0.4908	0.4078	0.3857	0.6095	1.0561	2.0924
7	0.4908	0.4078	0.3857	0.6095	1.0561	2.0924
8	0.4908	0.4078	0.3857	0.6095	1.0561	2.0924
9	0.4908	0.4078	0.3857	0.6095	1.0561	2.0924
10	0.8891	0.7388	0.6987	1.1042	1.9142	3.7907
11	0.4908	0.4078	0.3857	0.6095	1.0561	2.0924
12	0.4908	0.4078	0.3857	0.6095	1.0561	2.0924
13	0.2846	0.2364	0.2236	0.3534	0.6123	1.2132
14	0.3774	0.3136	0.2965	0.4686	0.8120	1.6088
15	0.5338	0.4436	0.4195	0.6629	1.1486	2.2758
16	0.5623	0.4672	0.4418	0.6983	1.2099	2.3972
17	0.7752	0.6442	0.6092	0.9628	1.6681	3.3051
18	0.6545	0.5439	0.5143	0.8129	1.4084	2.7906
19	0.4254	0.3535	0.3343	0.5283	0.9154	1.8137
20	0.8411	0.6989	0.6610	1.0446	1.8100	3.5862
21	0.4908	0.4078	0.3857	0.6095	1.0561	2.0924

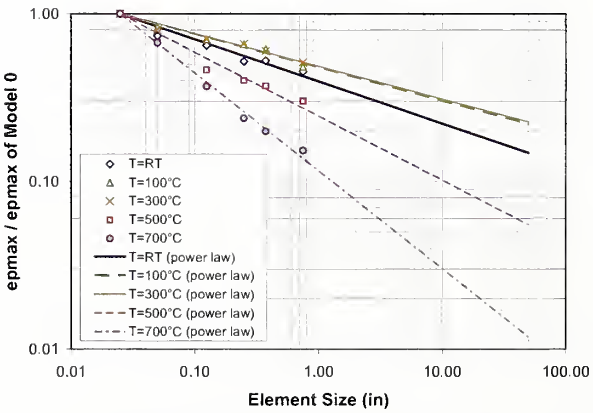

(a) FEA Results and Extrapolation

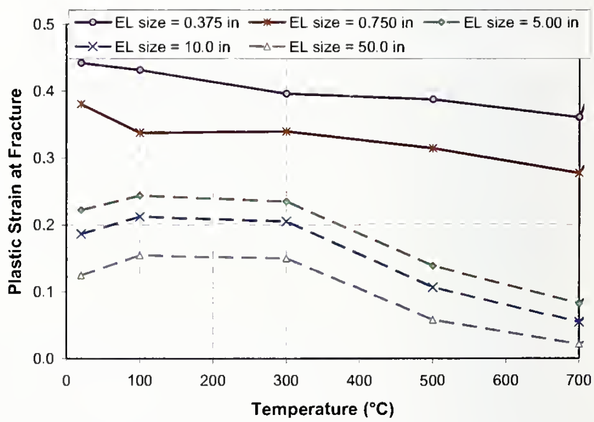

(b) Recommended Limiting Plastic Strain

Figure K–6. Maximum plastic strain from the finite element analysis and limiting plastic strain.

K.5.3 Welds

The weld properties at all temperatures are assumed to be the same as those of the base metal of the same ultimate tensile strength. This assumption is validated by the following observations: the exterior column welds are strong enough to fail the base metal; the observed fractures in the exterior columns are mostly through the base metal; and the welds in trusses are resistance welds with no filler added. For the core columns, the area of the welds is significantly less than that of the base metal, and several fractures through the welds have been observed. Fractures in the truss seats and truss connections have also been observed. High temperature properties of the welding metals have not been found in the literature. Susceptibility of existing cracks in the welds to growth (fracture toughness) does not increase with temperature (Stevick 1994).

K.5.4 Bolts

A load-elongation relationship for 7/8 in. A325 bolt with 4 in. length at room temperature was provided by Project 3. Load-elongation relationships at elevated temperatures are constructed by scaling the loads by the yield and ultimate tensile strength reduction factors for bolt steels shown in Fig. K–3 (c) and (d). Figure K–7 shows the load-elongation relationships of a 7/8 in. bolt at different temperatures. Load-elongation relationships of A325 bolts of different size are scaled by proportioning the load by the ratio of the bolt thread area to the bolt body area for a 7/8 in. bolt.

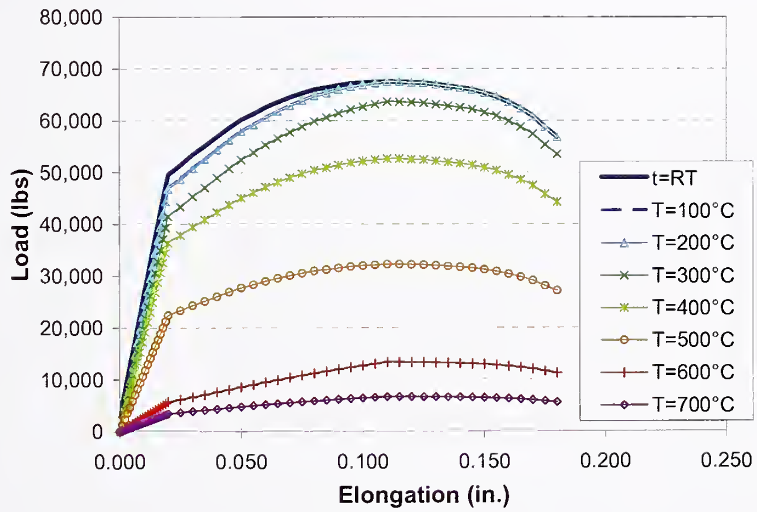

Figure K–7. 7/8 in. A325 bolt load-elongation curves at elevated temperatures.

The load-elongation relationship for bolts with a different length than 4.0 in. is expected to be very similar to the load-elongation relationship of 4.0 in. length as deformations are localized.

Based on the AISC formulas, C-J3–2 to C-J3–4, (AISC 2003), the shear strength for a single shear plane is calculated as 0.67 of the tensile strength given in Fig. K–7 when threads are excluded from the shear plane. When threads are not excluded from the shear plane, the nominal shear strength for a single shear plane is 0.53 of the tensile strength given in Fig. K–7. No shear ductility is assumed at failure.

K.5.5 Coefficient of Friction

The coefficient of friction of 0.33 for calculation of shear in friction-type connections is the AISC LRFD (2003) friction coefficient for uncoated clean mill scale steel surfaces, or surfaces with Class A coatings on blast-cleaned steel surfaces.

K.5.6 Symbols

$\alpha(T)$ = temperature-dependent material property that defines fracture criterion

$\alpha_c(T)$ = instantaneous coefficient of thermal expansion of concrete

$\alpha_s(T)$ = instantaneous coefficient of thermal expansion of steel

$\beta_y(T)$ = steel yield strength reduction factor due to elevated temperature

$\beta_u(T)$ = steel ultimate strength reduction factor due to elevated temperature

γ_c = unit weight of concrete (110 pcf and 150 pcf for lightweight and normal-weight concrete, respectively)

γ_s = Unit weight (490 pcf = 0.284 pci for all steel types at any temperature)

ε_{c1} = concrete strain at maximum compressive stress

ε_{cr} = creep strain of steel

ε_e = elastic strain

ε_{ep} = elastic plus plastic strain

$\bar{\varepsilon}_f$ = effective plastic strain at fracture

$\bar{\varepsilon}_{f\_uni}$ = uniaxial plastic strain at fracture

ε_p = plastic strain

ε_{t1} = concrete strain at maximum tensile strength

ε_{tu} = concrete strain at full crack formation (separation) in tension

ν_c = Poisson's ratio of concrete

ν_s = Poisson's ratio of steel

$\bar{\sigma}$ = effective stress

σ_m = mean stress

σ_{yRT} = room temperature yield strength of steel

σ_{uRT} = room temperature tensile strength of steel

$E_s(T)$ = modulus of elasticity of steel

$E_c(T)$ = modulus of elasticity of concrete

F_1 = mix design factor = ratio of the actual 28 day cylinder strength to f_c'

F_2 = in-situ factor = ratio of in-situ 28 day strength to the 28 day cylinder strength

F_3 = aging factor = ratio of mature concrete strength to 28 day concrete strength

f_a = actual strength of in-place concrete

f_c' = specified 28 day strength

$f_c(T)$ = compressive strength of concrete

$f_t(T)$ = tensile strength of concrete

$K(T)$ = sigmoidal function of temperature with six parameters

$n(T)$ = sigmoidal function of temperature with six parameters

R_C = correction factor that has the following two functions: (1) to correct the strain rate effect introduced in the material testing and create the stress-strain curve for zero strain rate, and (2) to match the room temperature stress-strain curve at strain of 0.05

R_{TS} = ratio of the room temperature tensile strength of the steel of interest to the room temperature tensile strength of the steel used to develop the power law model

K.6 MODEL CONVERSION FROM SAP TO ANSYS

The SAP2000 (SAP) floor 96 Model of WTC 1 and the SAP Global Model of WTC 1 are converted into ANSYS. The goal of the conversion is to develop ANSYS models that match the SAP baseline models developed by Project 2 and can be used as a basis of the detailed thermal-structural evaluation. The converted ANSYS models will be modified to incorporate the nonlinear behaviors of the components and simplified for the thermal/structural evaluation of collapse initiation study.

K.6.1 Translation Procedure

Automatic translation software was developed to partially convert the floor model and global model from SAP2000 to ANSYS 8.0:

- The Joints, Frames, and Shells in the SAP model were translated into ANSYS Keypoints, Lines, and Areas. Using geometry definition instead of nodes and elements directly allows for ease in local mesh refinement.

- Lines were meshed with both section and real constants so that a translation between BEAM44 and BEAM188 elements can be achieved by simply changing element types. Areas were meshed with SHELL63 elements in ANSYS to match the Shell elements in SAP. Eventually, Lines and Areas will be changed to nonlinear BEAM188 and SHELL181 elements with a type change.

- Material properties were assigned according to the Criteria Document based on the material definitions and Frame section properties in SAP.

- Frame section properties in SAP were converted into Real Constants for BEAM 44 in ANSYS. Cross section properties in SAP were retained for future conversion into cross section data for BEAM188 elements. Shell thicknesses in SAP were converted into Real Constants for SHELL63 in ANSYS.

- Joint restraints in SAP were translated into DOF constraints in ANSYS.

- Frame distributed loads and area uniform loads were translated into surface loads on Lines and Areas in ANSYS.

- The ANSYS BEAM44 elements support element moment releases, but the ANSYS nonlinear BEAM188 elements do not. Therefore, Frame releases in SAP were modeled by coincident nodes with coupled (CP) degrees of freedom in ANSYS.

- The ANSYS BEAM44 elements allow beam end offsets in three directions, but the ANSYS nonlinear BEAM188 elements only allow beam end offsets perpendicular to the element axis through section offset (SECOFFSET) command. Frame insertion points in SAP were converted in two ways. For offsets along the element axis, additional nodes and rigid MPC184 elements with the proper lengths were used in ANSYS. For offsets perpendicular to the element axis, beam end offsets were defined using Real Constants for BEAM 44, and eventually will be defined using SECOFFSET command for nonlinear BEAM 188.

- Frame offsets and rigid panel factor in SAP were modeled by adding additional nodes and rigid MPC184 elements with the proper lengths in ANSYS.

Those parts of the model that were not converted by the translation software were converted manually.

K.6.2 Challenges

During the conversion of the SAP Floor Model, the following conditions were encountered and were resolved:

- The SAP Floor Model allows automatic division of the frames at joints. This causes problems in the translation software because the frame connectivities in the Graphical User Interface do not show the actual internal element connectivities used in the SAP analysis engine. In order to resolve this problem, the translation software was modified to use the internal element connectivities. The table of internal connectivities was exported from the SAP model after the execution of the analysis.

- Automatic offsets in the SAP model are not available in the ASCII SAP input file prior to the execution of the analysis. The table of element offsets was exported after the execution of the analysis.

- There are both intentional and unintentional duplicate elements in the SAP Floor Model. Each leads to problems in the translator since ANSYS cannot have duplicate lines sharing the same key points. Some duplicate elements are used to model additional steel plates at the ends of the trusses. The duplicate elements were manually deleted and the section properties of the remaining elements were modified to account for the additional steel. Some duplicate elements are from frame elements which have different lengths and are overlapping each other. These were manually corrected.

K.6.3 Status

The automatic translation software developed to convert models from SAP2000 to ANSYS was applied to the floor model and will be applied to the global model shortly. Figures K–8 through K–11 show the converted floor model.

The following analyses were performed to validate the converted ANSYS floor model against the original SAP model.

- One static analysis with gravity loads as defined in SAP as Load Case "DEAD" which include self-weight plus 3.5 psf uniform load in the office area.
- One modal analysis, using structural mass only.

Table K–4 summarizes the comparison of the SAP and ANSYS results for the gravity load case. The total reactions for the SAP and ANSYS models are within 0.1 percent of each other. The maximum slab displacement predicted by the ANSYS model is 3.2 percent smaller than that obtained from the SAP model. This discrepancy is currently under study and is being resolved. The deformed shapes of the gravity load case for the SAP and ANSYS models are shown in Figs. K–12 and K–13.

Table K–4. Comparison of SAP and ANSYS results for gravity load case.

	SAP	ANSYS (BEAM 188)
Total reaction, kip	2,212.81	2,210.85 (-0.09 %)
Maximum slab displacement, in.	0.718	0.695 (-3.2 %)

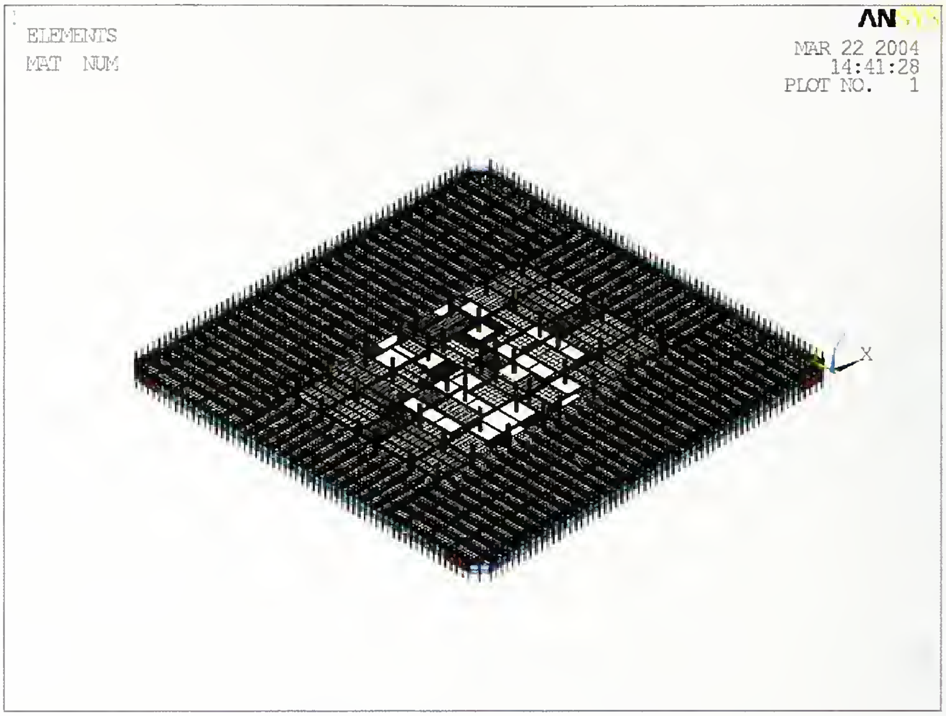

Figure K–8. Converted ANSYS model for floor 96 of WTC 1: overall view.

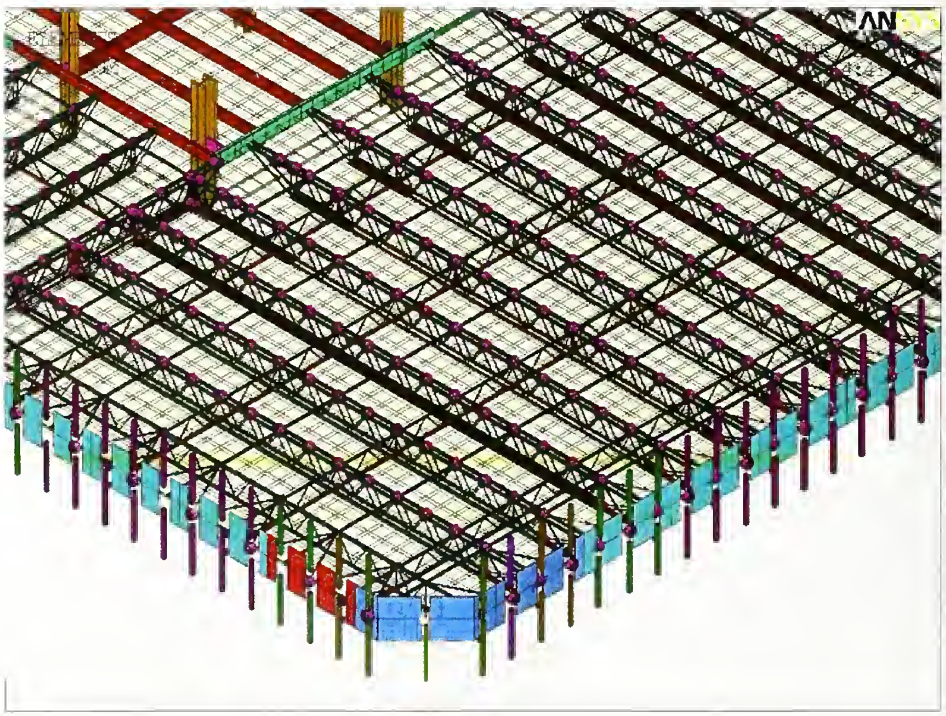

Figure K–9. Converted ANSYS model for floor 96 of WTC 1: partial view near corner of building.

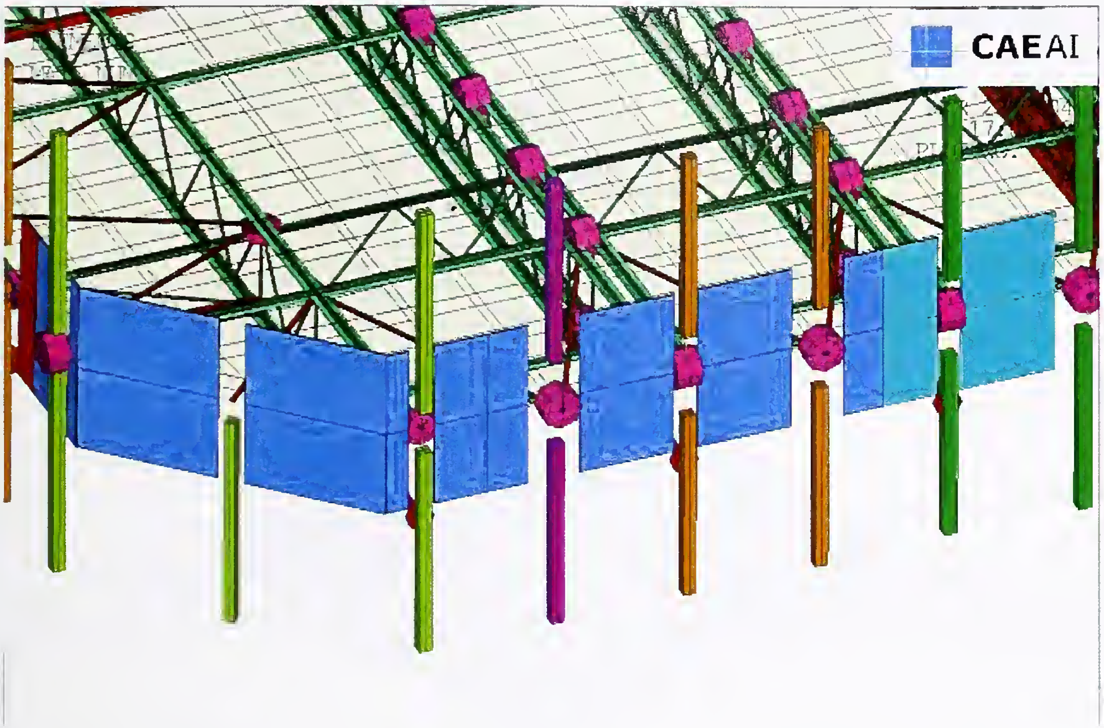

Figure K–10. Converted ANSYS model for floor 96 of WTC 1: close-up view at corner of building.

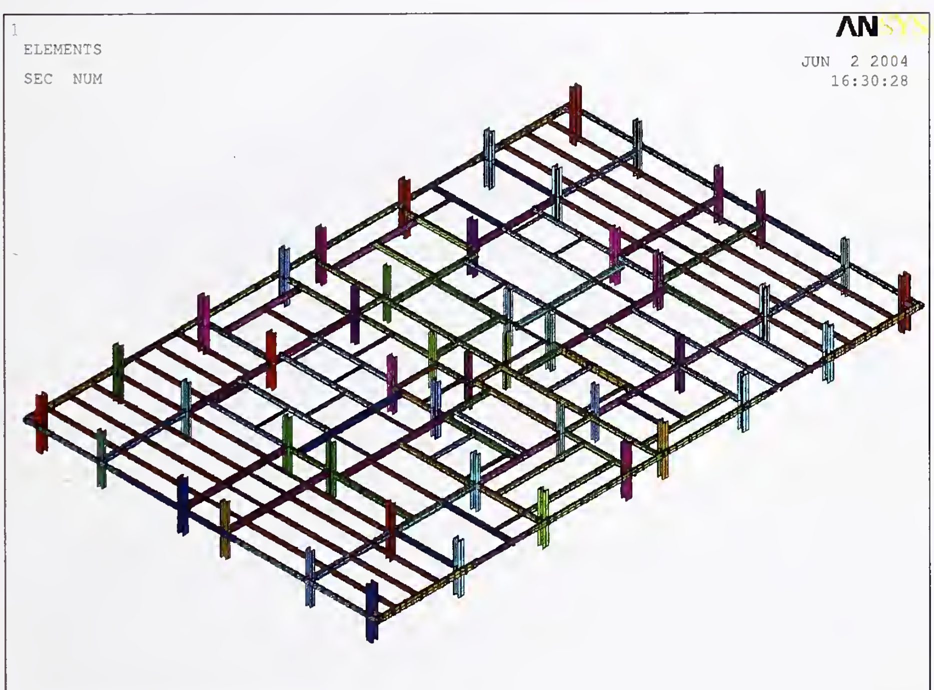

Figure K–11. Converted ANSYS model for floor 96 of WTC 1: view of floor beams and columns.

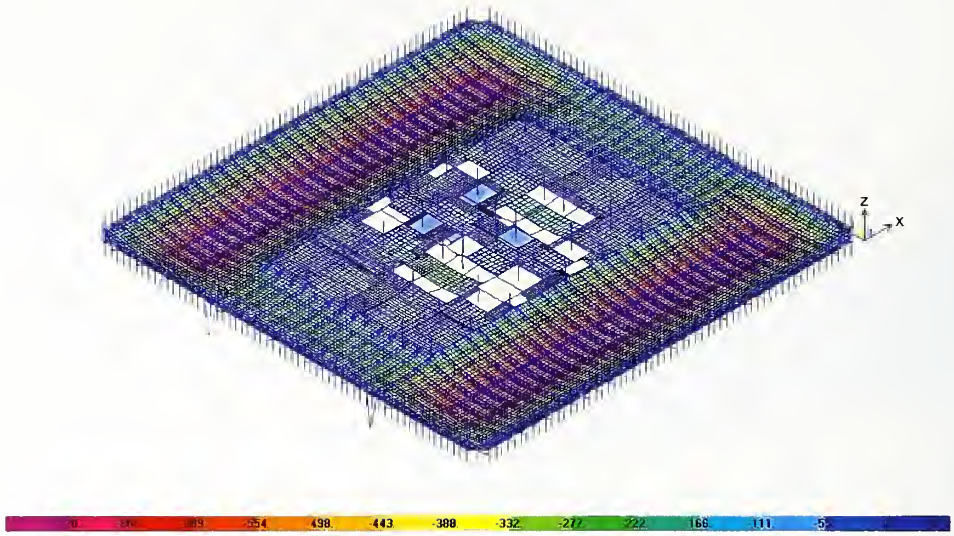

Figure K–12. Deformed shape (x100) of gravity load case for SAP floor model.

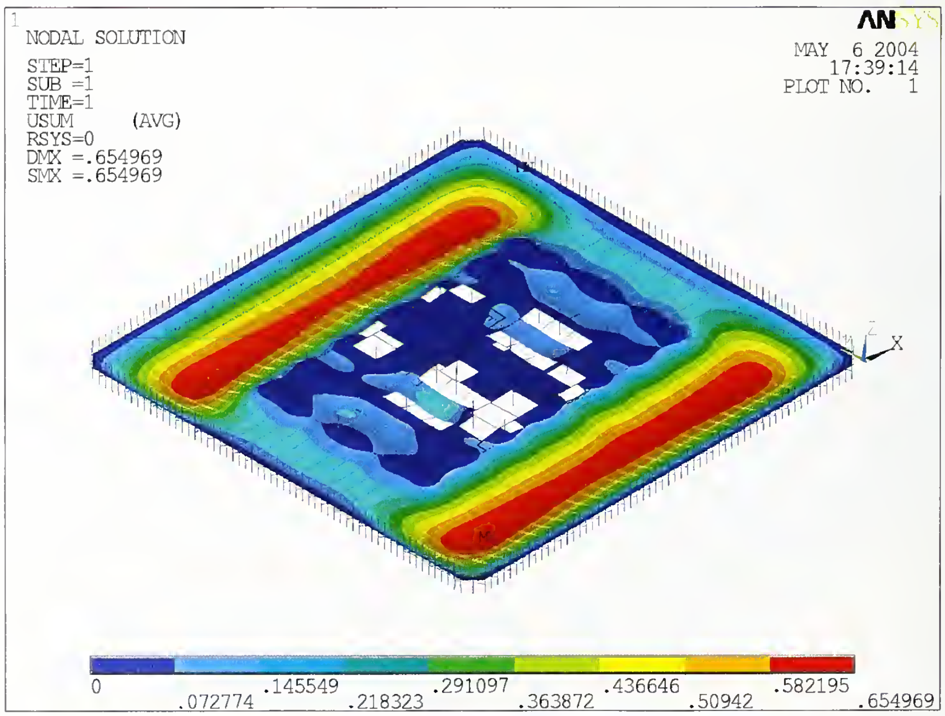

Figure K–13. Deformed shape (x100) of gravity load case for ANSYS floor model with BEAM44 (Euler beam) elements.

Table K–5 summarizes the comparison of the SAP and ANSYS results for the modal analysis. The total masses of the SAP and ANSYS models are within 0.02 percent of each other. The dominant natural frequency of the floor predicted by the ANSYS model is 2.5 percent higher than that obtained from the

SAP model. This discrepancy is consistent with the discrepancy observed for gravity displacement, and is currently under study and is being resolved. The dominant mode shapes of the floor for SAP and ANSYS models are shown in Figs. K–14 and K–15.

Table K–5. Comparison of SAP and ANSYS Modal Analysis Results.

	SAP	ANSYS (BEAM 188)
Total mass, lb·sec^2/in.	5448.7	5447.7 (-0.018 %)
Dominant natural frequency of floor, Hz	4.32	4.43 (+2.5 %)

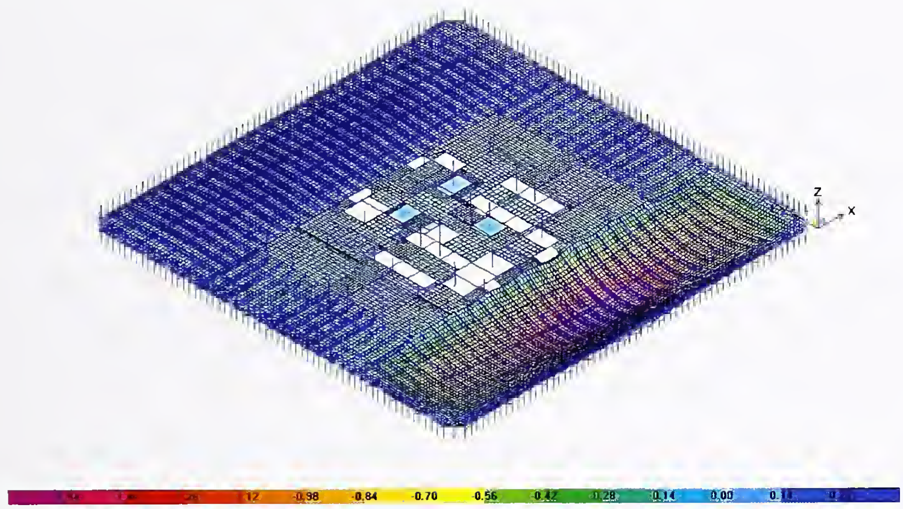

Figure K–14. Dominant mode shape (frequency = 4.32 Hz) of floor structure for SAP floor model.

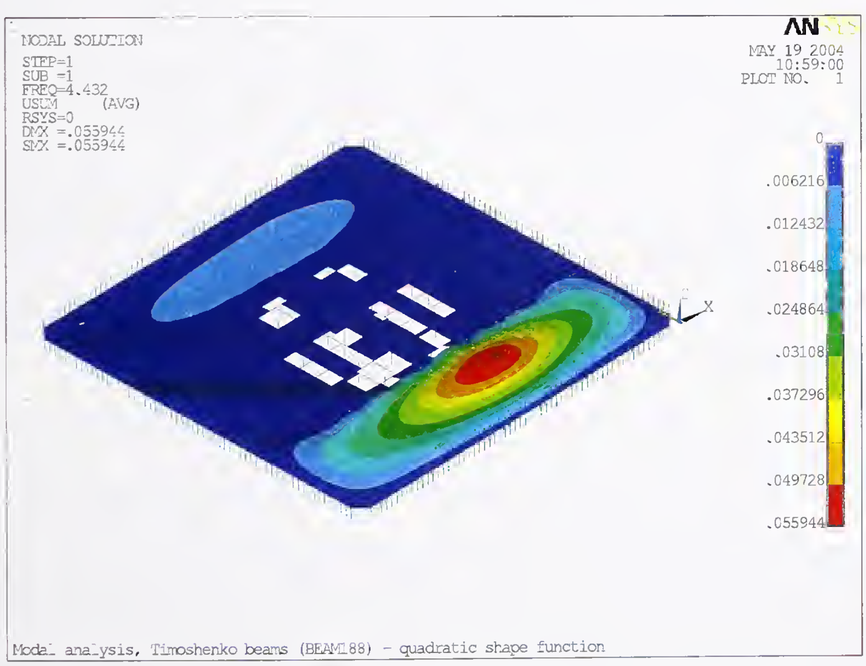

Figure K–15. Dominant mode shape (frequency = 4.43 Hz) of floor structure for ANSYS floor model.

K.7 FULL FLOOR SUBSYSTEMS

The full floor model is analyzed using the ANSYS general purpose finite element program Version 8.0. The objectives of the analysis are:

- To identify the most likely failure modes,
- To evaluate
  - Failure loads,
  - Temperatures at failure,
  - Time-to-failure, and
  - Changes in mechanical properties and geometry at failure.
- To simplify the model and to reduce the computational efforts for incorporation into the global model.

The failure modes and the failure loads of different components of the full floor subsystem are evaluated through analysis of detailed models of those components, using either hand calculations or FEAs. Simplified models that capture the failure loads and failure modes are then developed for each component. These simplified models of components are incorporated in the full floor subsystem model.

In this chapter, after a general description of the full floor model, the analyses of important components are presented and discussed.

K.7.1 Full Floor Model

Model Description

The floor model is developed using the converted SAP2000 model for floor 96, with the following modifications:

1. Combine two adjacent trusses into a single truss. The elements in the truss model have double the areas of elements in each real truss.

2. Change rigid beams at knuckle locations to user-defined elements with the properties of the knuckle determined by the component knuckle model.

3. For compression diagonals, add user-defined elements to account for buckling of diagonals.

4. For truss ends and connections, add user-defined elements to account for truss seat failure.

5. Pin concrete slab for out-of-plane rotation at both its interior and exterior edges.

6. Use user-defined elements along the edge nodes of the concrete slab to model the tensile strength of the concrete slab and the in-plane shear capacity at the connection to the spandrel plate.

7. Remove the spandrels defined as beam sections in SAP2000 model and replace them with SHELL181 elements in ANSYS. (This modification eliminates the need for defining panel zone stiffness.) The new spandrels will wrap continuously around the floor. Each spandrel plate between columns will be represented by 16 elements, 4 in. height and 4 in. width. Material and geometry assignments are carried through to ANSYS.

8. Change the elastic column elements as translated into ANSYS to user-defined sections with BEAM189 elements with plasticity and creep.

9. Make new column sections within the limits of the spandrels with reduced Plate 3 thickness, say 0.005 in. in thickness, to insure correct modeling of torsional stiffness. Spandrel thicknesses should be reduced within the limits of the column by the same thickness. Connect the centerline of column to spandrel with rigid elements.

Material Properties

ANSYS's multilinear isotropic hardening von Mises plasticity with time hardening for temperatures below 350 °C is used for the beam elements representing the truss system, girders, beams, and columns in areas where plasticity is either anticipated or expected to occur by analysis. This material model with creep is used for temperatures above 350 °C. This material model is used for shell elements representing the spandrel plates, when appropriate.

Loading

The full floor model is analyzed for dead and live loads first, and then thermal loads are applied to model the path dependent nonlinear response. The thermal loads are provided by Project 5 and include temperatures and temperature gradient time-histories for all structural members in the full floor model for (1) standard fire, (2) representative building fire scenarios, and (3) different fire protection scenarios.

Boundary Conditions

The beam elements representing the columns are restrained vertically at floor 95. The outward and tangential displacements and all rotations of the column ends at floors 95 and 97 are fixed to restrain thermal expansion. Mass elements defined by the tributary dead and live loads are added to the top of the columns and at connections to floor 96.

Failure Modes

The possible failure modes of the floor subsystem are as follows:

1. Sagging: Floor sagging along the axis of the main trusses may be caused by (1) loss of stiffness and softening of truss at high temperature, (2) catenary action of the truss due to plastic bending or buckling of critical members required for truss action, or (3) loss of composite action of floor-to-knuckle failure. These are discussed in some detail under truss failure modes. Floor sagging may result in component failure due to tension in the truss seats, tension in the floor subsystem, tension on the connections to the exterior walls, lateral

loads on columns, and increased demand on other components of the floor subsystem, for example, bridging trusses and transfer trusses and their connections.

2. Edge Sagging: Edge sagging results from failure of truss seat connections at either the interior or exterior supports and is evidenced in videos. Edge sagging, similar to sagging, increases demand on other components of the floor subsystem, reduces buckling strength of columns, and can lead to failure of a floor.

3. Loss of Support: Abrupt failure of the floor subsystem can result from loss of truss support for a large number of adjacent parallel trusses. Loss of a truss support can occur due to (1) vertical shear load due to debris and/or impact load of the dropping floor above, (2) vertical and horizontal shear loads resulting from slab expansion acting on column truss seats (3) tension acting on column truss seats, and (4) cooling of a truss shortened by plastic deformation and loss of composite action. Failure of truss support will increase the demand on the adjacent trusses and can result in sequence of truss seat failure, edge sagging, and ultimately failure of the floor subsystem.

4. Expansion of Floor System: Expansion of floor results in deformation of columns and forces at corners of the exterior wall subsystem. Such corner forces can initiate a failure sequence of columns near the corners. Such a failure includes development of horizontal shear in the gusset plates and the exterior column truss seats, large forces in the straps, and large lateral x and y forces in columns, especially near the corners.

K.7.2 Knuckle Analysis

The "knuckle" is formed by the extension of the truss diagonals into the concrete slab and provides for composite action of the steel truss and concrete slab. The composite action is due to the shear transfer between the knuckle and the concrete slab both in the truss transverse and longitudinal directions.

The objective of this analysis is to predict the knuckle capacity when the truss and concrete deck act as a composite member and to develop a simplified model of the knuckle behavior to be included in the full floor subsystem model.

Knuckle Shear Tests

Two sets of experiments were performed in 1967 at Laclede Steel Company in Saint Louis, Missouri, to determine the transverse and longitudinal shear capacities of the knuckle.

The transverse shear test consists of double knuckles placed into two reinforced concrete blocks that were confined on the corners by angles as shown in Fig. K–16. The concrete density of 110 pcf corresponds to the lightweight concrete in the office areas. The concrete compressive strengths reported for 7 day and 27 day cylinder tests were 1,330 psi, and 2,600 psi, respectively. The inner ends of the two knuckles were connected through channels to a #11 rebar and the rebar was loaded until the concrete failed. The tests were conducted at concrete age of 6 and 27 days. The primary failure mode observed was concrete shear failure. The pictures from the tests show formation of the shear crack in one of the concrete blocks and edging of the channel into the concrete. The transverse shear capacity of the knuckle as the average of the

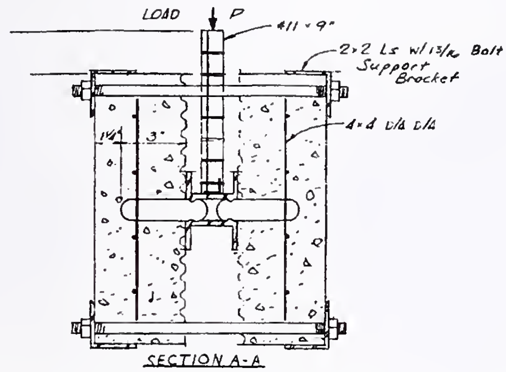

Drawing provided by Laclede Steel.

Figure K–16. Transverse shear test of a knuckle.

two reported tests is 16.9 kip per knuckle. After adjusting it for the strength of in-place, mature, lightweight concrete in the slab of 4,100 psi relative to the average strength of the lightweight concrete used in the test of 1,965 psi, by multiplying by the ratio of 4,100 to 1,965 psi, the transverse shear capacity of the knuckle is approximately 35 kip per knuckle.

The longitudinal shear test consists of double knuckles placed into two concrete blocks as shown in Fig. K–17. The test specification shows corner angles confining concrete blocks and no reinforcement for the concrete. However, the test pictures show reinforcement in both directions for each concrete block, with the corner angles dismantled. The test specification calls for concrete density of 152 pcf, which corresponds to a normal-weight concrete. The slab in office areas is of lightweight concrete. The average strength of two 28 day cylinders tested is 4,290 psi. A third sample, tested after 96 days, showed a strength of 2,850 psi. The test specification does not identify the weld size connecting the inner ends of the two knuckles to two channels. However, the primary failure mode observed for three tests is weld failure. Weld failure is not identified as the failure mode of the knuckle for the other two tests. The results of the shear tests of the knuckle in the longitudinal direction based only on these two tests are approximately 28.3 kip per knuckle. After adjusting for the strength of in-place, mature, lightweight concrete in the slab of 4,100 psi relative to the 28 day corrected average strength of the normal-weight concrete used in the test of 3,707 psi, by multiplying by the ratio of 4,100 psi to 3,707 psi, the longitudinal shear capacity of the knuckle is approximately 31 kip per knuckle.

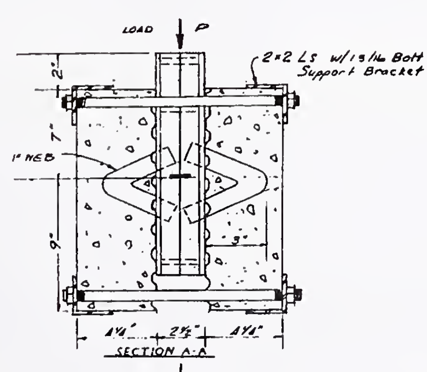

Drawing provided by Laclede Steel.

Figure K–17. Longitudinal shear test of a knuckle.

The effect of temperature on the knuckle is as follows:

- The steel knuckle conducts the temperature of the diagonal without much loss into the cool concrete. Concrete has a low coefficient of conductivity and does not respond rapidly to the rise of temperature.

- Concrete in the intermediate proximity of the metal knuckle will heat to a temperature close to that of the steel.

- Shear failure of the knuckle is initiated by the failure of concrete in close proximity to the knuckle. Final failure will engage not only the hot concrete in close proximity of knuckle, but the cooler concrete farther away.

- It is reasonable to assume that for gas temperatures in the range of RT to 450 °C, 650 °C, 850 °C, and 1050 °C , the knuckle metal temperature is below 375 °C, 550 °C, 725 °C, and 900 °C, and the average concrete temperature is below 300 °C, 450 °C, 600 °C, and 750 °C, respectively.

Neglecting the difference in thermal expansion of concrete and steel, for gas temperatures of RT, 450 °C, 650 °C, 850 °C , and 1050 °C, the expected concrete strength is in the range of 4,100 psi, 3,300 psi, 2,600 psi, and 2,000 psi, and the knuckle capacity in either direction is 30 kip, 24 kip, 19 kip, and 15 kip, respectively.

Knuckle Test Finite Element Model

Finite element models, shown in Fig. K–18, represent one quarter of the knuckle test specimens. The knuckle and channel members in the test set up are modeled by solid steel elements. Concrete Pseudo Tensor model and the LS-DYNA computer program were used for the analysis. An imposed ramped displacement was applied to the angle member.

The concrete strength used in the finite element model for the longitudinal shear of the knuckle was 4,100 psi and for the transverse shear of the knuckle was 2,500 psi. In addition 0.47 percent steel reinforcement representing welded wire fabric reinforcement of the slab was added in a distributed way to the concrete. Also, two different assumptions were made about the interface condition between the concrete and the steel: fully bonded and frictionless.

The results of the analysis are shown in Figs. K–19 through K–22. They show significant dependence on the characteristic of the interface between the steel and concrete. The longitudinal shear test FEA results, shown in Fig. K–21, show that each knuckle has strength in the range of 15 kip to 35 kip, depending on interface. The test results show that the interface is closer to fully bonded case. For the transverse shear, the FEM results, Fig. K–22, show that transverse knuckle strength is about 24 kip for 2,500 psi concrete, corresponding to 39 kip for 4,100 psi concrete. Figure K–20 shows that for transverse shear concrete crushes in a small region next to the knuckle and extending in front of the shear load. Figure K–20 also shows large regions of crushing at the lower boundary of the model. These regions are the result of imposing the boundary condition UY=0. This boundary condition, and the crushing at the boundary, although realistic for the test, would not obtain in a pair of transversely loaded knuckles of the double

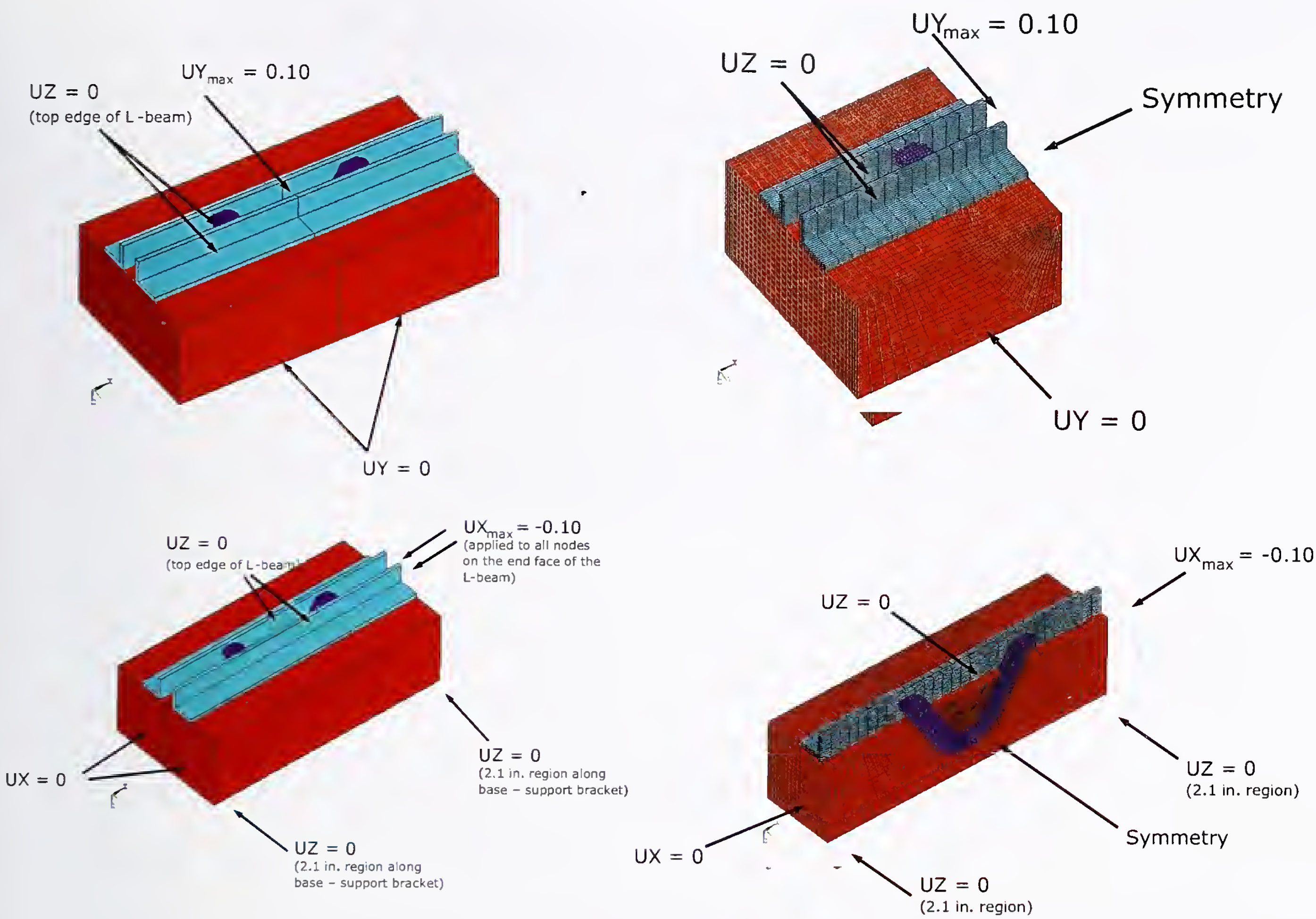

Figure K–18. Finite element models of knuckle shear tests.

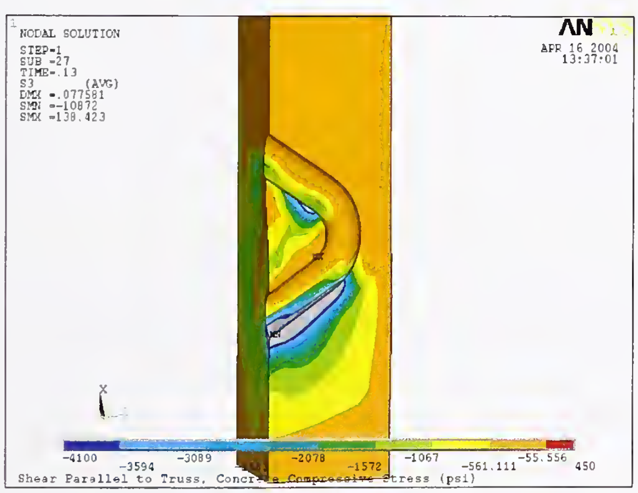

Figure K–19. Compressive stresses in longitudinal shear finite element model.

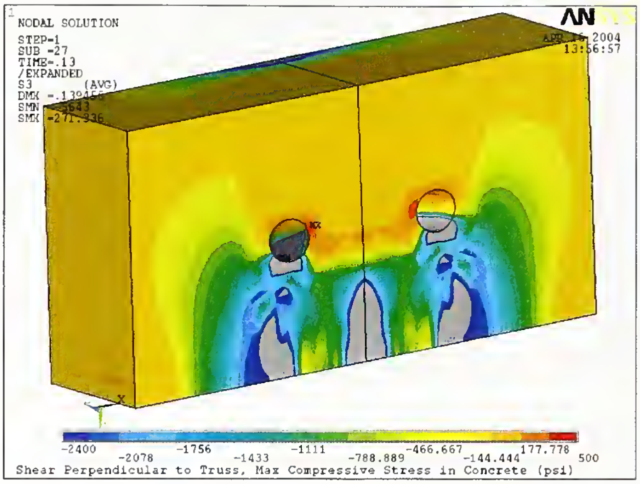

Figure K–20. Compressive stresses in transverse shear finite element model.

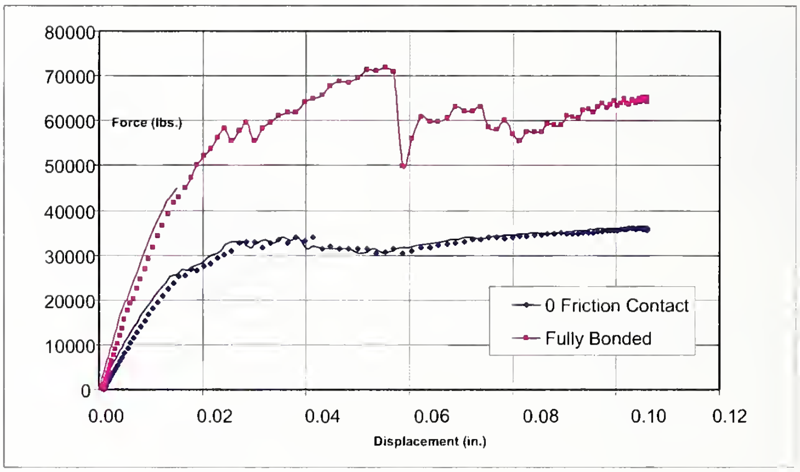

Figure K–21. Shear force versus displacement from finite element model for longitudinal shear of two knuckles.

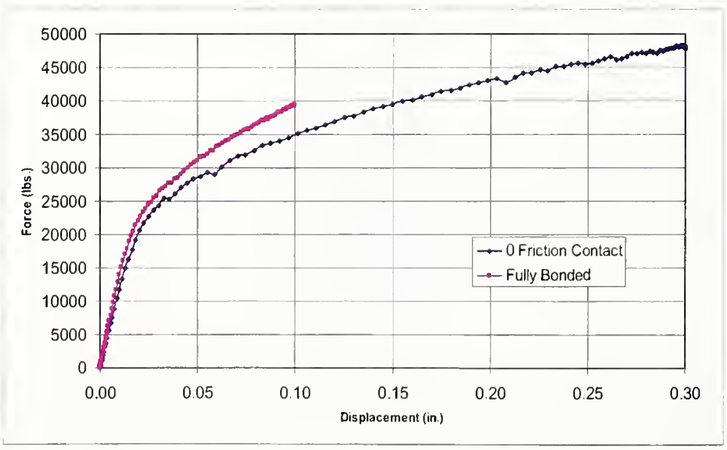

Figure K–22. Shear force versus displacement from finite element model for transverse shear of two knuckles.

truss. The small crushing regions at the knuckle indicate that a pair of knuckles in a double truss can be expected to behave nearly independently of each other, and, therefore, have nearly double the capacity of a single knuckle. Unfortunately, test results are not available that would confirm this conclusion.

Although the analysis shows the sensitivity of the results to the interface assumptions, it justifies the shear capacities computed from the test results.

Knuckle Model

The purpose of the detailed finite element analysis of the knuckle is to provide a basis for deriving a simple model for use in analyses of the full floor. The knuckle model includes segments of concrete floor and truss diagonal that protrudes into the 4 in. thick concrete. The dimensions of the concrete included in the model are one half of the double truss spacing of 40 in. The diameter of the truss diagonal included in the model is 1.09 in., and the center line of the knuckle is 3 9/16 in. from the center line of the double truss. The concrete slab wire mesh reinforcement is modeled by distributed reinforcement properties.

The model is bounded by four planes. Two of these planes are parallel to the chord of the truss, and the other two planes are perpendicular to the chord. Symmetry conditions are applied to these planes consistent with the loads. For the tension loading, in addition to the symmetry conditions, the model is supported vertically at both symmetry planes that are perpendicular to the truss chord. For the shear load parallel to the chord, the model is supported ahead of the shear load in the direction parallel to the chord.

The knuckle has the properties of ASTM A36 (Material ID 20) round bar steels and the concrete has lightweight concrete properties specified for LS-DYNA with concrete-cap model.

K.7.3 Column Truss Seats

In this section, likely failure modes of truss seats are identified, and the corresponding failure loads are determined. The following loading conditions were considered: vertical force, horizontal tensile force, horizontal compressive force, and combined vertical and horizontal force.

Description of Column Truss Seats

The floor truss is supported at the exterior wall and at the core by seats. The truss seat at the exterior wall and at the core will be referred to as *exterior seat* and *interior seat*, respectively.

The interior seat consists of a horizontal plate with two vertical plate stiffeners as shown in Fig. K–23. These plates are fillet welded together and fillet welded to the core channel beam. Two 5/8 A325 bolts (one bolt in each truss) connect the truss to the seat. The bolt connection is a friction type connection with 1 3/4 in. long slotted holes in the seat and 7/8 in. oversize holes in the bearing angles.

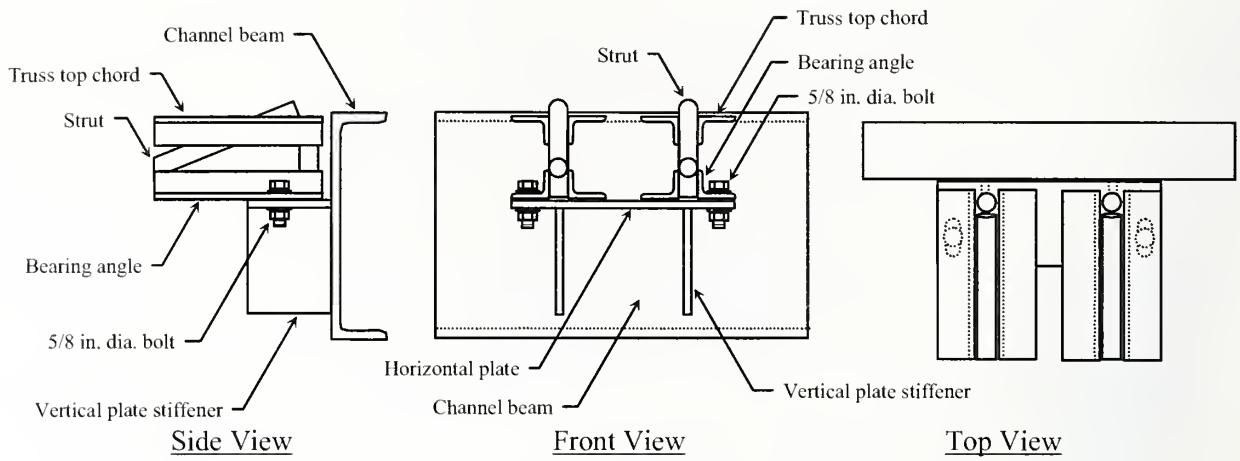

Figure K–23. Interior seat.

The exterior seat consists of a seat angle attached to the spandrel with two vertical plates (stand-off plates), and a gusset plate as shown in Fig. K–24. Fillet welds connect the seat angle to the stand-off, the stand-off to the column/spandrel, and the gusset plate to truss top chord. A complete-joint-penetration groove weld connects the gusset plate to the column/spandrel. Similar to the interior seat, each pair of trusses is attached to the exterior seat by two 5/8 in. A325 bolts. The bolt connection is a friction type connection with 2 in. long slotted holes in the seat angle and 7/8 in. oversize holes in the truss-bearing angle.

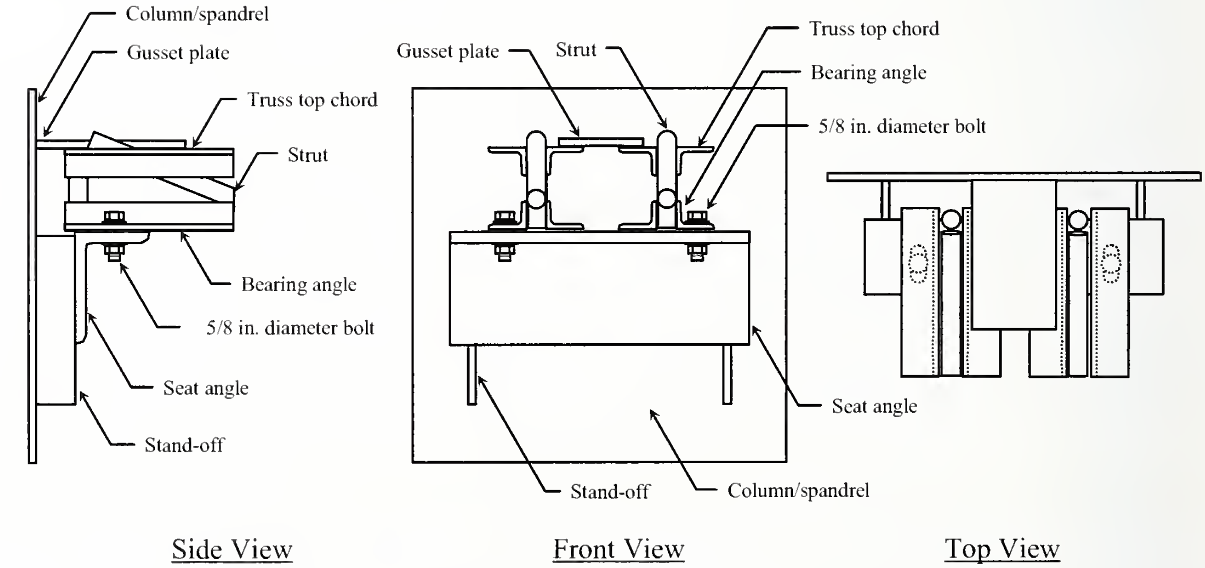

Figure K–24. Exterior seat.

In floor 96 of WTC 1, there are seven types of interior seats and eight types of exterior seats. The different types of interior seats are identified with Detail Numbers 15, 17, 20, 21, 22, 23, and 226A; and the exterior seats with Detail Numbers 1013, 1111, 1212, 1311, 1313, 1411, 1511, and 1611, as shown in Fig. K–25.

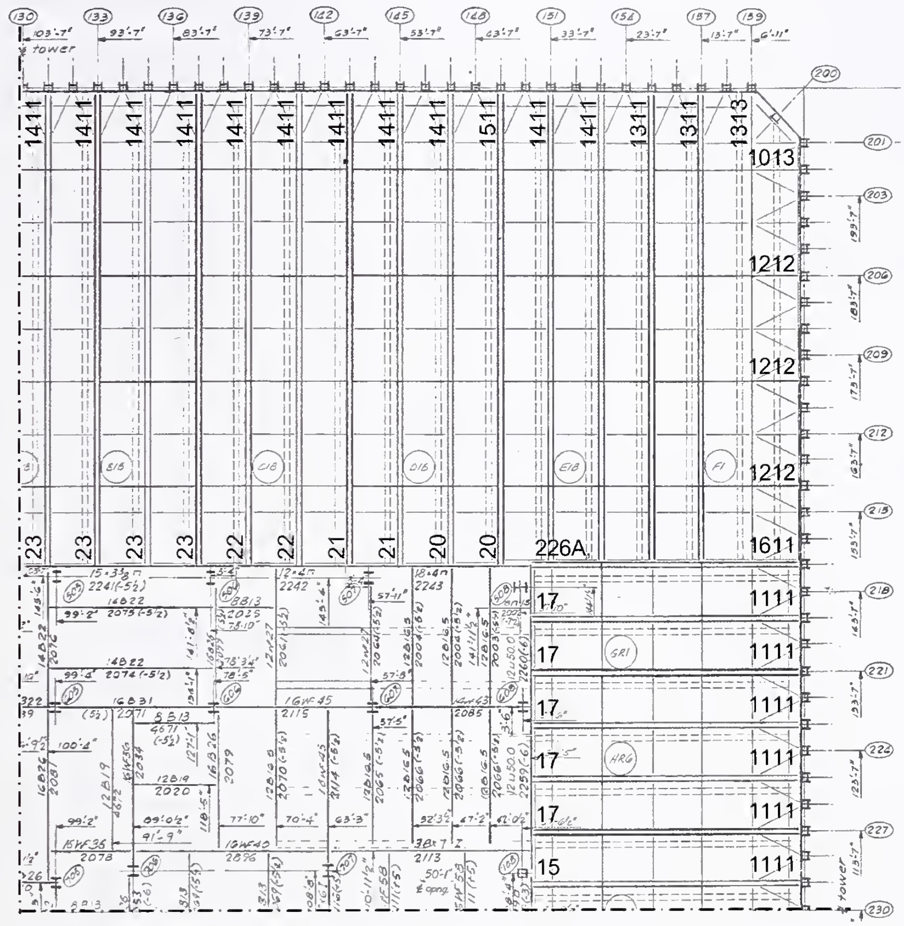

Original drawing provided with permission from PANYNJ.

Figure K–25. Truss seat detail location on northeast quadrant of floor 96 of WTC 1.

All types of interior seats are similar in their design, but are all unique because of the variation in the size of the vertical and horizontal plates, the location of the bolt holes, and the size of the fillet welds. The thickness of the plates ranges from 0.375 in. to 0.75 in.; the distance between bolt holes ranges from 8.5 in. to 10.5 in.; and the size of the fillet welds ranges from 0.25 in. to 0.375 in. All types of exterior seats are also similar in their design, but are all unique because of the variation in the size of the stand-off, and size of the seat angle, the size and shape of the gusset plate, the location of the bolt holes, and the size of fillet welds. The vertical height of the stand-off ranges from 8 in. to 11 in. The smallest seat angle size is L4 × 4 × 1/2, and the largest is L6 × 4 × 3/4. The shapes of the gusset plate are rectangular and trapezoid, and the plate ranges in width from 4.5 in. to 6 in. The distance between bolt holes ranges from 3.25 in. to 10.5 in., where it is 3.25 in. when the seat is supporting a single truss. The size of the fillet welds ranges from 0.2125 in. to 0.375 in.

Truss Seat Material Properties

The material properties used in the calculations were selected from Table K–1 to best match the material properties indicated in the design drawings. Figure K–3 was used to determine the material mechanical properties at high temperature. The material properties used for truss seat calculations are summarized in Table K– 6.

Table K–6. Material properties used for truss seat calculations.

Description		Selected Material ID
Exterior and interior seat	A325 bolts	Material 22
	Fillet welds	Material 7
	Truss bearing angles	Material 21
Exterior seat	Seat angle	Material 1
	Gusset plate	Material 12
	Stand-off	Material 23
	Truss top chord angles	Material 21
	Cover plate for bridging truss top chord	Material 1
Interior seat	Vertical plate stiffener	Material 12
	Horizontal plate	Material 12

Truss Seat Failure Modes and Sequence

The failure modes of different truss seats are identified for vertical force, horizontal tensile force, horizontal compressive force, and combined vertical and horizontal force.

Failure Modes of Interior Seat against Vertical Force: The location of the vertical load on the truss seat is eccentric to the plane of fillet weld connection between the truss seat and the channel beam. Hand calculations have shown that the fillet welds at this connection, which must resist shear and bending, control the truss seat capacity. The failure mode is fracture of the fillet welds at this connection, which results in loss of the truss vertical support.

Failure Modes of Interior Seat against Horizontal Tensile Force: The failure modes considered are (1) bolt shearing, (2) bolt bearing, (3) bolt tear-out, and (4) block shear failure. Hand calculations have shown that the bolt shear strength controls the truss seat capacity. Bolt shear by itself, however, does not cause the truss to lose its vertical support, but it is the prerequisite to the truss walking off the seat. The travel distance required for the truss to walk off of the seat is 4 in.

Failure Modes of Interior Seat against Horizontal Compressive Force: The concrete slab above the truss seat connection provides the compressive force resistance. If the concrete slab fails, the truss seat has resistance against compressive force from bolt friction and surface friction between the seat and bearing angles. Additional resistance is developed when the truss comes into contact with the channel beam. Travel distance for the truss to come into contact with the channel beam is 1/2 in. Under compressive force, the truss will not lose its vertical support.

Failure Modes of Interior Seat against Combined Vertical and Horizontal Forces: Under combined vertical and horizontal forces, the failure modes are a combination of the individual failure modes for vertical and horizontal forces.

Failure Modes of Exterior Seat against Vertical Force: The location of the vertical load on the seat is eccentric to the plane of connection between the seat and the spandrel. Because of this eccentricity, the truss seat must resist both shear and bending. Finite element analysis of the truss seat was used to determine load paths and evaluate the behavior of the seat connection.

Figure K–26 shows the finite element model of the seat connection, where half of the seat was modeled and symmetry boundary conditions were applied. The results of the finite element analysis show that shear force is carried primarily by the stand-off plates shown in Fig. K–24, while the bending moment is resisted by tensile force in the gusset plate and compressive force in the stand-off plate. The seat restrains the moment until horizontal force in the connection causes slippage between the seat angle and bearing angle. Fillet welds at the stand-off to spandrel connection, which must resist shear, bending, and compression, control the seat capacity. The failure mode is fracture of the fillet welds as this connection, which results in loss of truss vertical support.

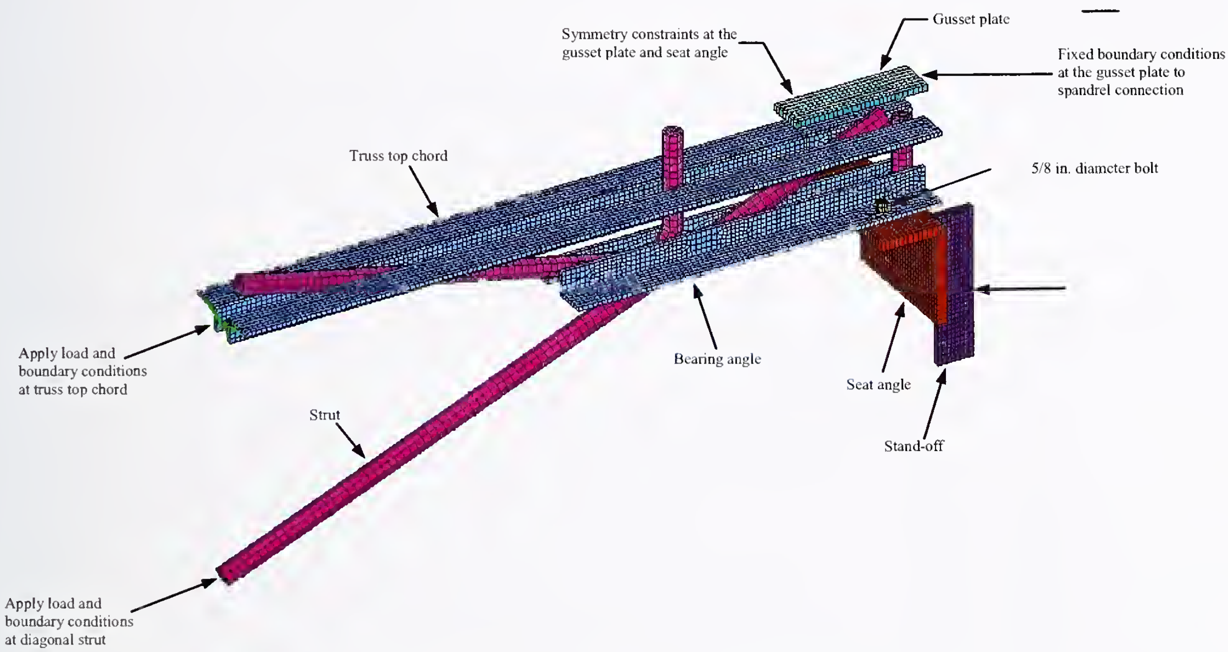

Figure K–26. Finite element model of exterior seat.

Failure Modes of Exterior Seat against Horizontal Tensile Force: The failure modes considered are: (1) failure of the groove weld between gusset plate and spandrel, (2) failure of the fillet weld between the gusset plate and the truss top chord, (3) tensile failure of the gusset plate, (4) bolt shearing off, (5) bolt bearing, (6) bolt tear-out, and (7) block shear failure. For calculation purposes, the bolts are assumed to be centered in the slotted holes. The typical failure sequence of the truss seat is as follows: first the gusset plate yields, then it fractures, followed by truss deformation and bolt bearing against the slotted hole, the bolt shears off, and then finally the truss walks off the seat. The travel distance for the truss to walk off of the seat is 4 5/8 in. This failure sequence is illustrated in Fig. K–27 as path (A) and shown in Fig. K–28, where the relationship between the tensile force resistance from the seat connection and the truss travel distance is plotted. In this plot, frictional resistance between the seat angle and bearing angle was not included.

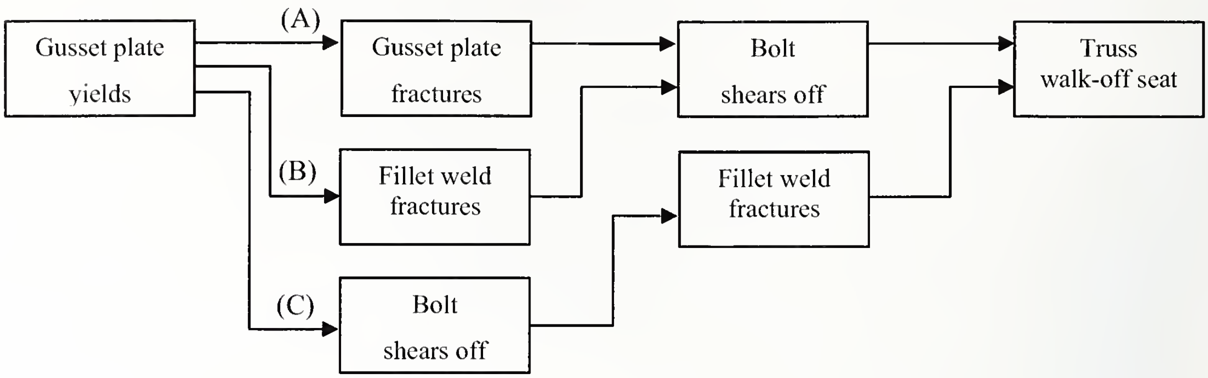

(A) Seat details 1111, 1311, 1411, 1511, and 1611 at all temperatures.
(B) Seat detail 1013 at temperatures below 100 °C.
(C) Seat details 1212 and 1313 at all temperatures, and detail 1013 at temperatures more than or equal to 100 °C.

Figure K–27. Failure sequence of the exterior seats against tensile force.

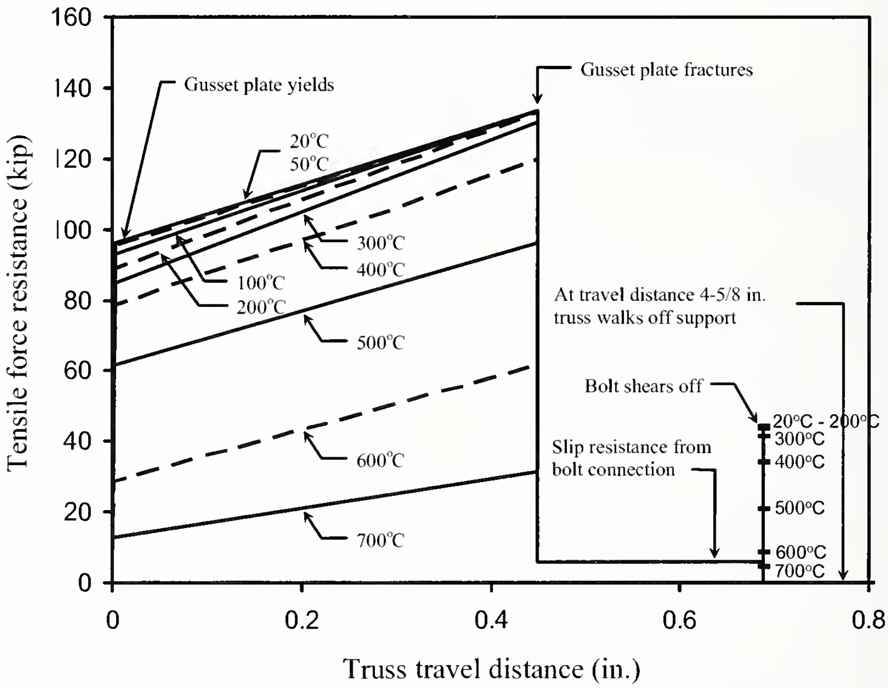

Figure K–28. Typical tensile force resistance from exterior seat (Detail 1411).

Seat details 1212 and 1313 have a wider gusset plate and follow path (C) which differs from the typical sequence where the bolts will bear against the slotted hole then shear off before the gusset plate connection fails. The failure sequence of seat detail 1013 is temperature-dependent. At temperatures below 100 °C, the fillet weld connection between the gusset plate and the truss top chord fractures before bolts shear off. At temperatures greater than or equal to 100 °C the failure sequence is the same as for Details 1212 and 1313.

Failure Modes of Exterior Seat against Horizontal Compressive Force: The concrete slab above the truss seat connection provides the compressive force resistance. If the concrete slab fails, the truss seat has resistance against compressive force provided by the gusset plate until it buckles, and from bolt friction and bolt shear until the bolt bears against the slotted hole and then shears off. Surface friction between the seat angle and bearing angles will also provide some resistance. Additional resistance is developed when the truss comes into contact with the spandrel. Travel distance for the truss to come into contact with the column spandrel is 1 1/2 in. Under compressive force, the truss will not lose its vertical support.

Failure Modes of Exterior Seat against Combined Vertical and Horizontal Force: Under combined vertical and horizontal forces, the failure modes are a combination of the individual failure modes for vertical and horizontal forces.

Truss Seat Capacity Calculations

In this section, truss seat capacities corresponding to the failure modes described in the previous section are given. The capacity is computed for the different types of the truss seat at different temperatures. Calculation of the connection capacity was performed using the methods in the *Manual of Steel Construction: Load and Resistance Factor Design* (AISC 2001) with the resistance factor, ϕ, assumed to be equal to one.

Capacity of Interior Seat against Vertical Force: Failure mode of the truss seat against vertical force is fracture of the fillet welds at the seat-to-channel beam connection. Strengths of the fillet welds at this connection are summarized in Table K–7. The symbol # in this table refers to seat detail number.

Table K–7. Interior seat capacity against vertical force.

Temp. (°C)	Connection Capacity Against Vertical Force (kip)						
	#15	#17	#20	#21	#22	#23	#226A
20	226	226	265	221	187	187	385
50	226	226	265	221	187	187	385
100	226	226	265	221	187	187	384
200	225	225	264	220	187	187	383
300	220	220	258	215	182	182	374
400	201	201	236	197	167	167	343
500	160	160	188	156	132	132	272
600	98	98	116	96	82	82	167
700	45	45	53	44	37	37	76

Capacity of Interior Seat against Horizontal Tensile Force: Failure loads were computed for the failure modes described above. Table K–8 summarizes the results for Seat Detail 22. This table shows that the shear strength of the two bolts controls the horizontal tensile strength of the truss seat connection. As can be seen from this table at temperature 500 °C, bolt shear capacity is reduced by half, and at 600 °C it is reduced to less than a quarter of the original capacity at room temperature. Other seat details also have the same failure mode, and, therefore, the same failure load.

Table K–8. Interior seat capacity against tensile force.

Temp. (°C)	Resistance against Tensile Force (kip)							
	Bolt Slip Critical	Bolt Shearing Off	Bolt Bearing		Bolt Tear-out		Block Shear	
			On Seat	On Truss	From Seat	From Truss	Of Seat	Of Truss
20	6	44	124	69	87	101	60	59
50	6	44	124	69	87	101	60	59
100	6	44	124	69	87	101	60	59
200	6	44	124	69	87	100	59	59
300	6	42	121	68	85	98	58	57
400	6	34	111	62	77	90	53	52
500	6	21	88	49	61	71	42	42
600	6	9	54	30	38	44	24	24
700	6	4	25	14	17	20	10	10

Capacity of Interior Seat against Horizontal Compressive Force: Under compressive force, the truss will come into contact with the channel beam before the bolt bears against the slotted hole. The truss seat connection does not fail under compressive force.

Capacity of Interior Seat against Combined Vertical and Horizontal Force: A typical interaction relationship for combined vertical and horizontal tensile force is shown in Fig. K–29. As can be seen from this figure, the vertical shear strength of the seat reduces because of the additional horizontal tensile force that the fillet weld connection between the truss seat and the channel beam must resist.

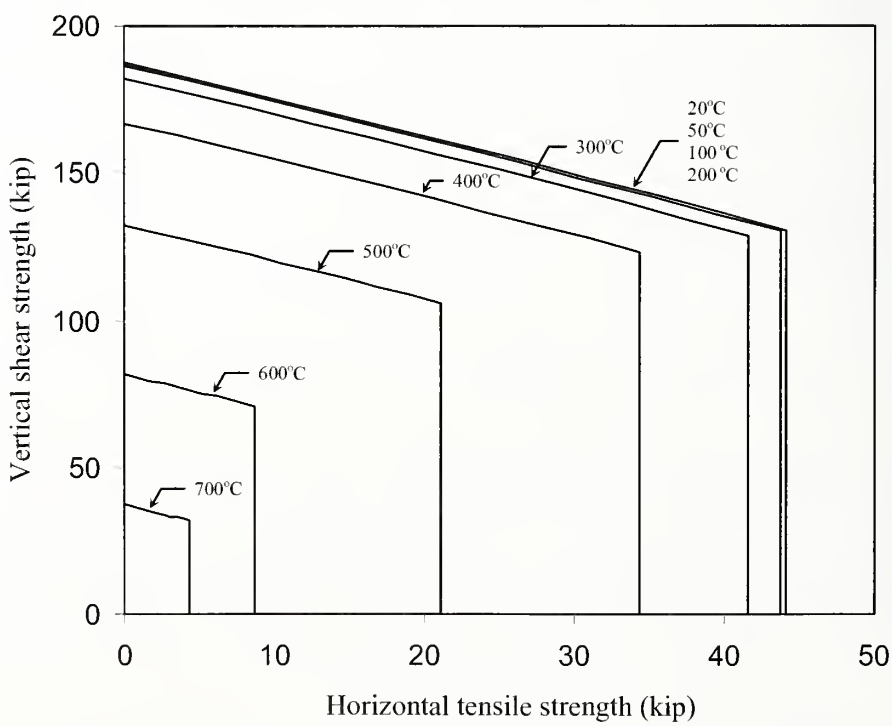

Figure K–29. Strength of combined vertical and horizontal force (Detail 22).

Capacity of Exterior Seat against Vertical Force: The failure mode of the truss seat against vertical force is fracture of the fillet welds at the stand-off-to-spandrel connection. Strength of the fillet welds at this connection is summarized in Table K–9.

Table K–9. Exterior seat capacity against vertical force.

Temp. (°C)	Connection Capacity against Vertical Force (kip)							
	#1013	#1111	#1212	#1311	#1313	#1411	#1511	#1611
20	94	94	111	94	94	140	193	207
50	94	94	111	94	94	140	193	207
100	94	94	111	94	94	140	193	207
200	93	93	110	93	93	139	192	206
300	91	91	108	91	91	136	187	201
400	84	84	100	84	84	126	172	184
500	69	69	81	69	69	102	136	146
600	45	58	53	60	45	78	84	90
700	29	26	34	27	29	35	38	41

Capacity of Exterior Seat against Horizontal Tensile Force: The connection capacity of truss seats that follow failure sequence (A), as shown in Fig. K–27, equals the failure load for mode (3) defined previously. The connection capacity of truss seats that follow failure sequence (B) equals the failure load for mode (2). The connection capacity of truss seats that follow failure sequence (C) equals the failure load for mode (4) plus the developed resistance from the gusset plate. The results of the exterior seat capacity calculations are summarized in Table K–10. Note that the strength of the truss seat #1013 increases by about 38 percent at a temperature of about 100 °C. For temperatures less than 100 °C, the capacity is controlled by the gusset seat fillet weld strength, and for temperatures in excess of 100 °C, the bolt reaches the end of its travel in the elongated bolt hole and increases the capacity of the connection.

Table K–10. Exterior seat capacity against horizontal tensile force.

Temp. (°C)	Connection Capacity against Tensile Force (kip)							
	#1013	#1111	#1212	#1311	#1313	#1411	#1511	#1611
20	100	104	182	134	182	134	134	134
50	100	104	182	134	182	134	134	134
100	138	104	181	134	181	134	134	134
200	135	103	180	133	180	133	133	133
300	130	101	174	130	174	130	130	130
400	115	93	156	120	156	120	120	120
500	84	75	117	96	117	96	96	96
600	42	49	67	62	67	62	62	62
700	20	25	32	31	32	31	31	31

Capacity of Exterior Seat against Horizontal Compressive Force: Under compressive force, the gusset plate will buckle before the bolts shear off. Compression strength of the gusset plate governs the truss seat capacity. The compressive strength of the gusset plate is summarized in Table K–11.

Table K–11. Compression strength of gusset plate.

Temp. (C)	Compression Strength of Gusset Plate (kip)							
	#1013	#1111	#1212	#1311	#1313	#1411	#1511	#1611
20	77	69	99	90	99	90	90	90
50	76	68	98	89	98	89	89	89
100	74	66	96	87	96	87	87	87
200	71	63	91	83	91	83	83	83
300	67	60	87	79	87	79	79	79
400	62	55	80	72	80	72	72	72
500	48	42	61	55	61	55	55	55
600	20	17	25	22	25	22	22	22
700	6	5	8	7	8	7	7	7

Capacity against Combined Vertical and Horizontal Force: Interaction relationships for combined vertical and horizontal forces are under development.

K.7.4 Modeling Connection Failure by Break Elements

In this section, simplified finite element models of the exterior and interior seat, knuckle, stud on strap anchor, and stud on spandrel are described. These connection models were developed for incorporation in the floor truss analysis to capture the connection failure modes and determine the sequence of the failure modes that may lead to the failure of the floor truss.

The developed simplified model of these connections simulates the loss of connection resistance after failure either by exceeding the connection force capacity or by exceeding the allowable deformation (truss walking off the seat). The connection capacity can also be temperature-dependent. The finite element modeling assumptions are as follows:

Break element, a unidirectional linear spring element with the capability of turning on and off during an analysis, is used for modeling connection failure. The element is a part of the structure that connects two "active" nodes in the "on" mode and disconnects them in the "off" mode, depending on the relative displacement of two "control" nodes. The break element is defined as follows:

$$B_m[iI,j,dof_{ij});(k,l,dof_{kl});(K,\Delta_0)] \tag{11}$$

where m is the break element number, i and j are the active nodes, dof_{ij} is the degree of freedom for the active nodes, k and l are the control nodes, dof_{kl} is the degree of freedom for the control nodes, K is the elastic stiffness of the break element, and Δ_0 is the differential displacement limit of the control nodes.

A beam element with temperature-dependent thermal expansion material properties is used to make the connection capacity temperature-dependent. This is done by using the deformation of the beam element from thermal expansion to control the status (on/off) of the break element. Figure K–30 illustrates the basic mathematical model of the connection. The connection capacity is made temperature-dependent by defining the thermal expansion of the beam element to be temperature dependent.

Basic mathematical model:

– Let node l and i have same displacement.

– In this example, control node k and l relative displacement has the form:

$$U_k - U_l = \frac{P}{K} + \alpha L \Delta T$$

– Control element status is by definition

$$U_k - U_l \leq \Delta_0, \text{ status : on}$$
$$U_k - U_l > \Delta_0, \text{ status : off}$$

– Define break element to turn off when capacity, P_u, has been reached

$$\Delta_0 = \frac{P_u}{K} + \alpha L \Delta T$$

– Element capacity at room temperature is given as

$$P_{u.rm} = K\Delta_0$$

– Hence for a given P_u and ΔT relationship, the required thermal expansion to turn element off can be found by

$$\alpha = \frac{P_{u.rm} - P_u}{KL\Delta T}$$

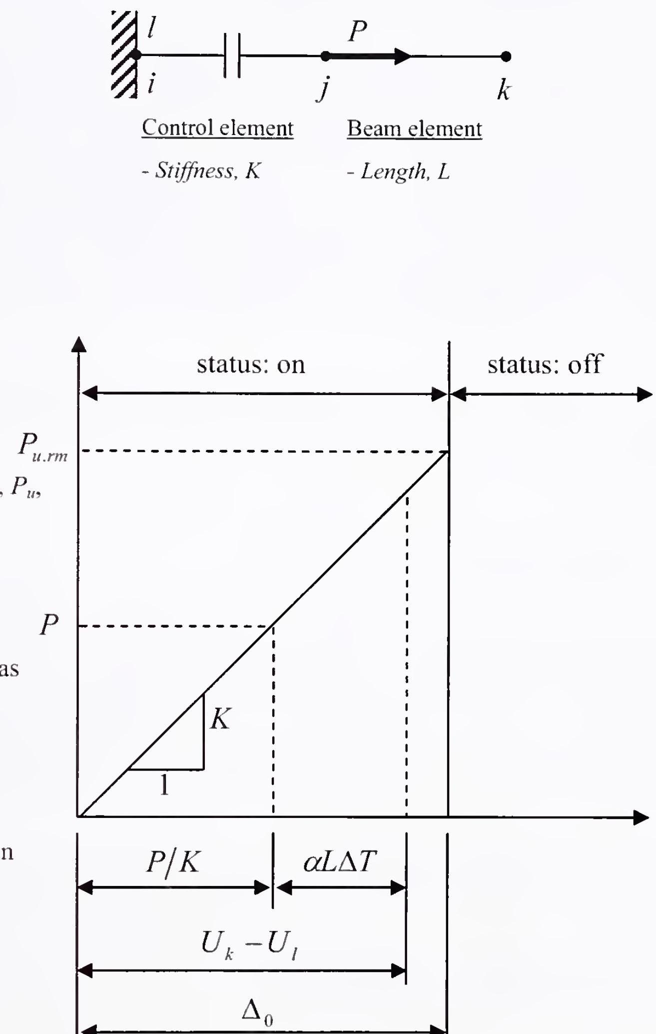

Figure K–30. Basic mathematical model of connection failure.

Multiple connection failure modes require use of different break elements that are connected together in a logical manner. For example, to model independent failure modes, that is, one failure mode that does not cause other failures, break elements are connected in parallel. If one break element turns off, the other break elements remain. For dependent failure modes, break elements are connected in series. If one break element turns off, then all elements turn off.

Simplified Model of the Interior and Exterior Seat

The failure modes of the interior seat include (1) the truss walking off the support, (2) exceeding the vertical temperature-dependent shear capacity of the truss seat, and (3) exceeding bolt temperature-dependent shear capacity when bolt bears against slotted hole. These failure modes are captured by using four break elements and two beam elements as shown in Fig. K–31. Results of the simplified seat model capturing failure from the truss walking off support and failure from exceeding seat vertical shear capacity are shown in Fig. K–32 and Fig. K–33, respectively, which depict the relationship between the horizontal and vertical seat forces and the horizontal truss travel distance.

When truss reaction force on the seat is large in horizontal tension and small in vertical shear, the failure mode is bolt shearing off followed by truss walking off the support as shown in Fig. K–32. Bolt shear is controlling the seat horizontal resistance capacity. Bolt shear by itself however does not cause the truss to lose its vertical support, but it is the prerequisite of truss walking off the seat. The travel distance for a truss to walk off an interior seat is 4 in. When truss reaction force on the seat is large in vertical shear and small in horizontal tension, the failure mode is exceeding the seat vertical shear capacity as shown in Fig. K–33. This failure mode will cause the truss to lose both its vertical and horizontal support from the seat.

The simplified model of the exterior seat is the same as the simplified model of the interior seat, except for an additional beam element and a break element to model failure of the gusset plate shown in Fig. K–34.

Simplified Model of the Knuckle

Knuckle failure modes that must be captured by the simplified model are the horizontal shear and vertical tensile failure, which are both temperature-dependent. Finite element modeling assumptions for the knuckle are: (1) the knuckle has resistance in all translational DOF, (2) the knuckle does not have a vertical compression capacity limit, (3) capacities in the horizontal shear and vertical tension are dependent, and (4) vertical compression resistance is independent of the capacities in the other directions. Knuckle failure is captured by using 15 control elements and 5 beam elements as shown in Fig. K–35.

Simplified Model of the Stud on Strap Anchor and Stud on Spandrel

Simplified models of stud on strap anchor and stud on spandrel were developed using the same technique as described for the knuckle model.

K.7.5 Truss Model

Objectives

The objectives of the truss model study are to:

- Capture the potential failure modes and failure sequence of the truss under combined gravity load and thermal load;
- Develop an understanding of the relative importance of different structural features and failure modes; and
- Develop a simplified model that replicates the expected failure and the limit loads of the truss to be used for analysis of the full floor subsystem model.

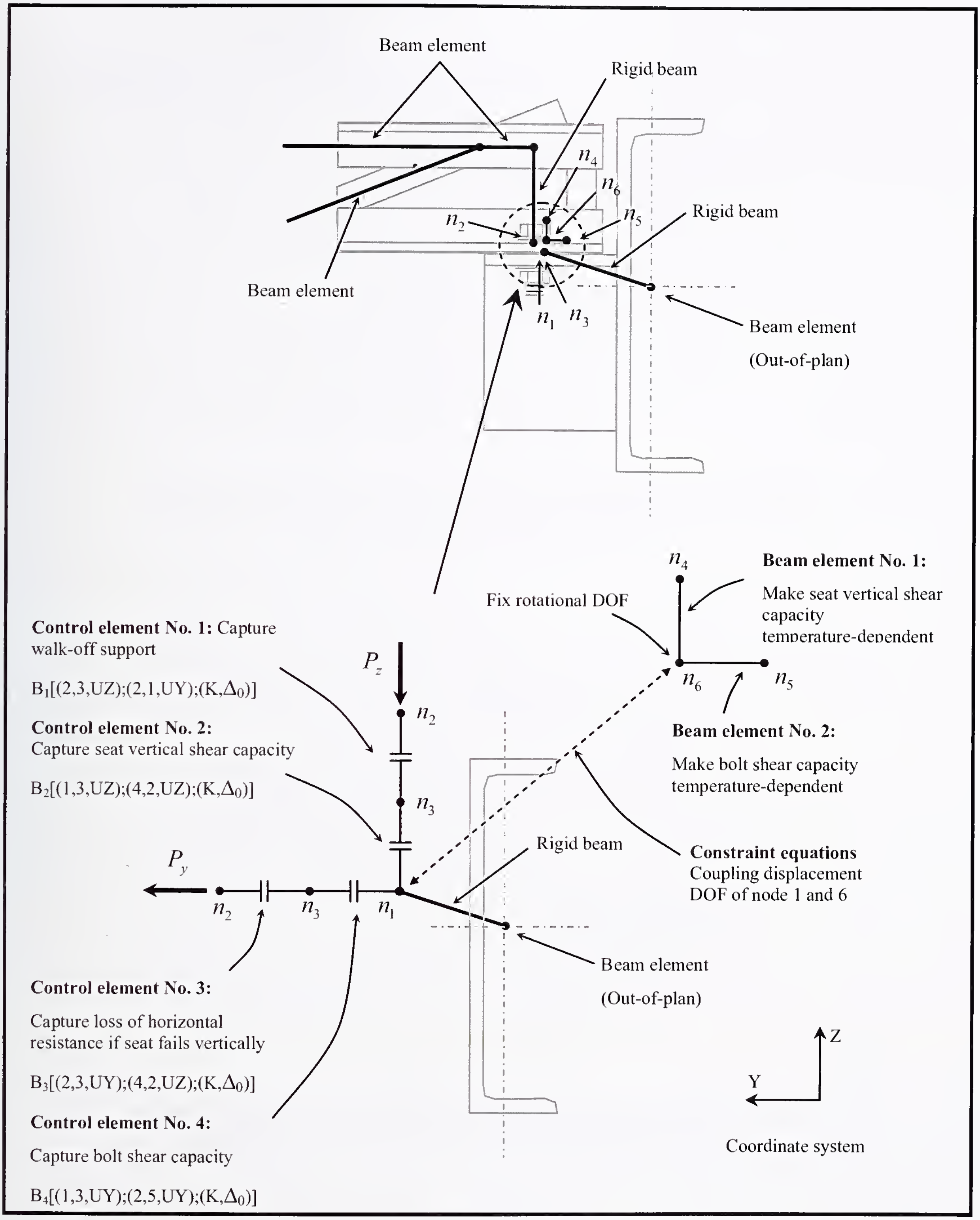

Figure K–31. Simplified model of interior seat.

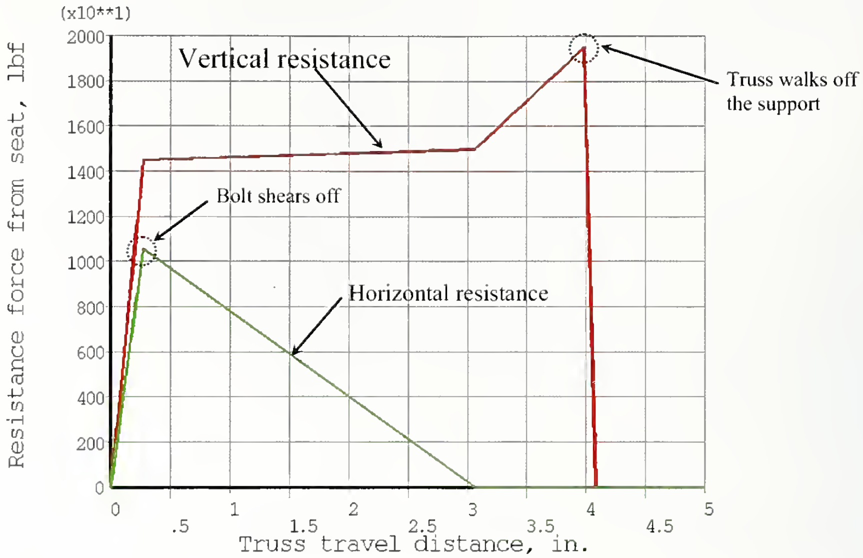

Figure K–32. Results of simplified seat model capturing failure from truss walking off interior seat.

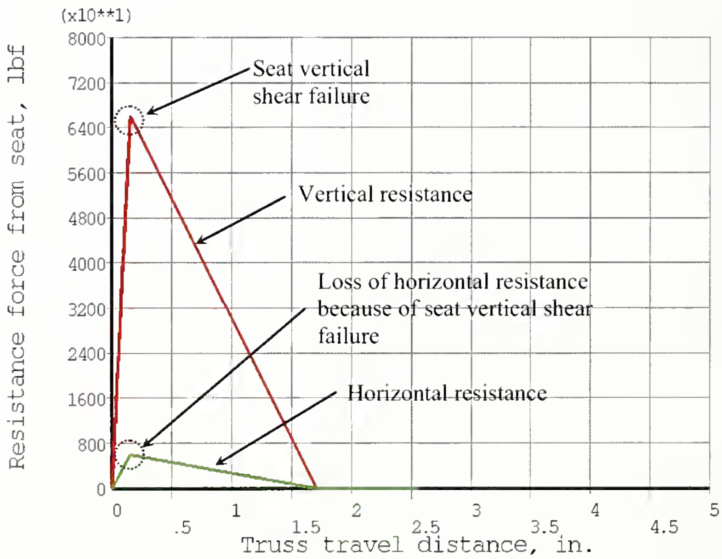

Figure K–33. Results of simplified seat model capturing failure from exceeding the interior seat vertical shear capacity.

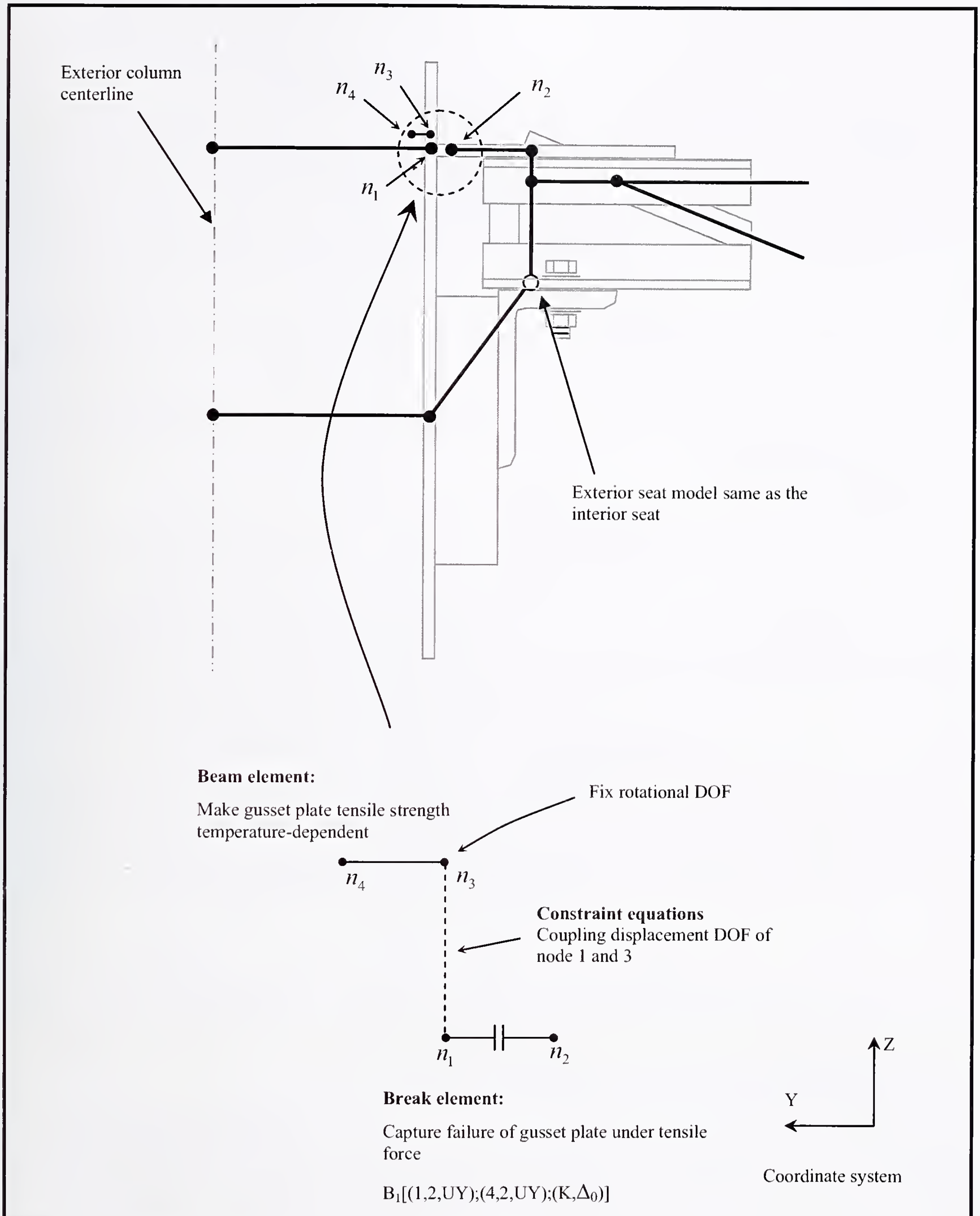

Figure K–34. Simplified model of exterior seat.

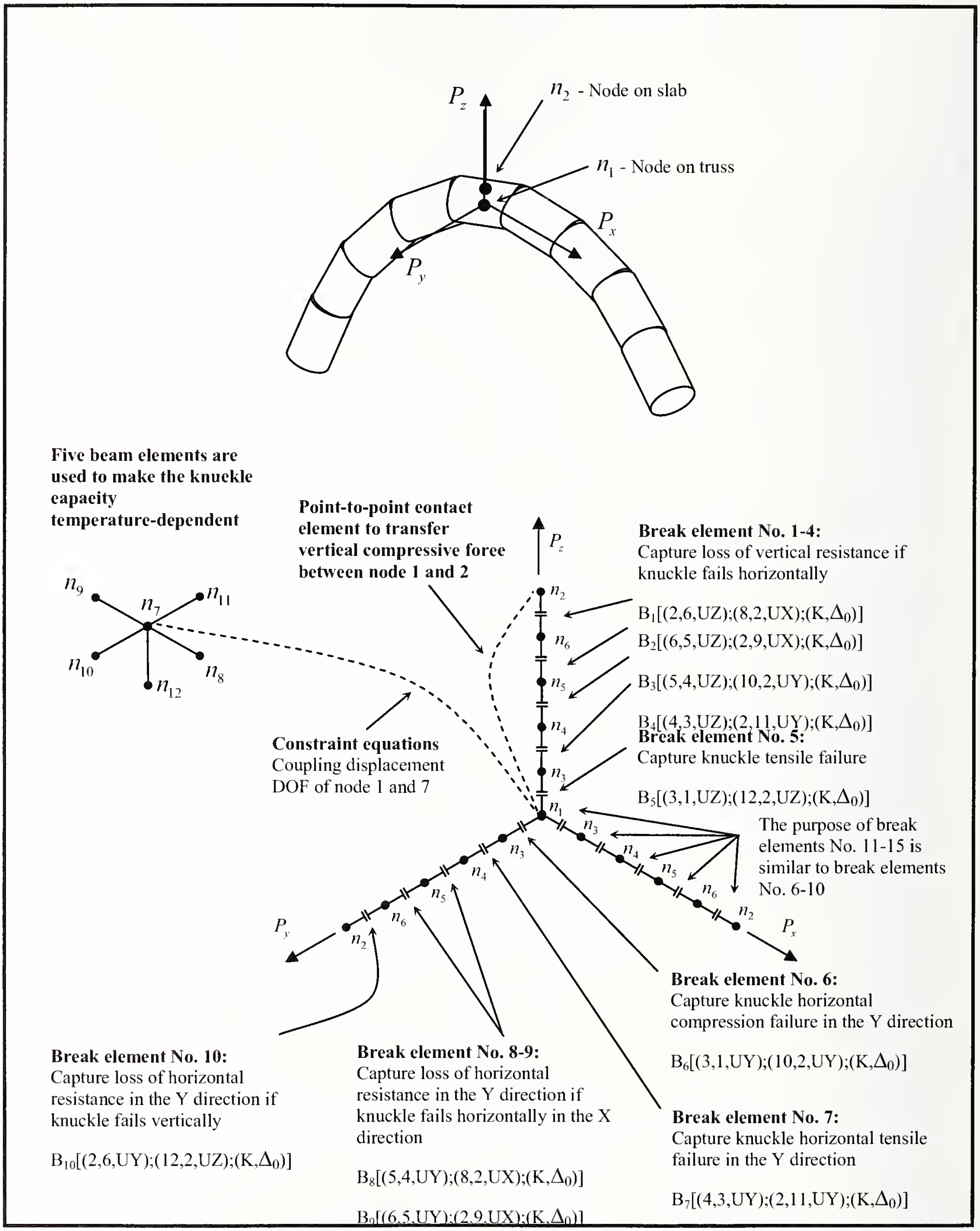

Figure K–35. Simplified model of knuckle.

Failure Modes

The model can capture the following failure modes:

Softening and Sagging of Truss—The top and bottom chords and diagonals of the truss are exposed to the hot gas layer below the floor slab. As described in Section K.5, the steel in the truss exhibits stiffness degradation, yield strength reduction, plastic softening, and creep at high temperatures. A truss with softened chords sags. The heat may also reduce the stiffness and strength of the concrete slab, especially its bottom layer where temperature is the highest, and around the knuckle where concrete temperature rises by conduction through the steel.

In addition to direct thermal effects, sagging and weakening of the truss can be caused by the following failure modes:

- Buckling or failure of web diagonal members, which reduces the truss action and causes the truss to act as a catenary;
- Buckling or failure of the top and bottom chord members;
- Knuckle failure and loss of composite action of the concrete slab and the steel truss; or
- Weld failure between the diagonal and the chord.

Loss of Support of Truss—The truss can fail by loss of support due to seat failure. Loss of support at either the exterior or interior seat can be caused by the extreme sagging and catenary action of the truss due to plastic deformation and buckling of truss members.

As discussed under Boundary Conditions later in this section, the bottom chord of the truss is restrained in the lateral direction at the bridging truss locations. Although the out-of-plane deformation of the bottom chord due to thermal expansion of bridging trusses will result in a reduction in the vertical load capacity of a primary truss, the truss model studied here cannot capture this phenomenon. The interaction between the bridging trusses and the primary trusses is intended to be captured in the full floor model.

Model Description

Figure K–36 shows the truss model. A typical long-span truss designated C32T1 (SHCR 1973:WTC Drawing Book 7, Sheet AB1–2) is modeled to study its response to failure when subjected to dead and live loads and thermal loads. The model includes the following:

- One truss of the pair of trusses at column line 143 of floor 96 in WTC 1;
- Two exterior columns (columns 143 and 144) with half the area and bending properties, and a length of 24 ft (12 ft above and below the floor level);
- The portion of the spandrel between the two exterior columns;

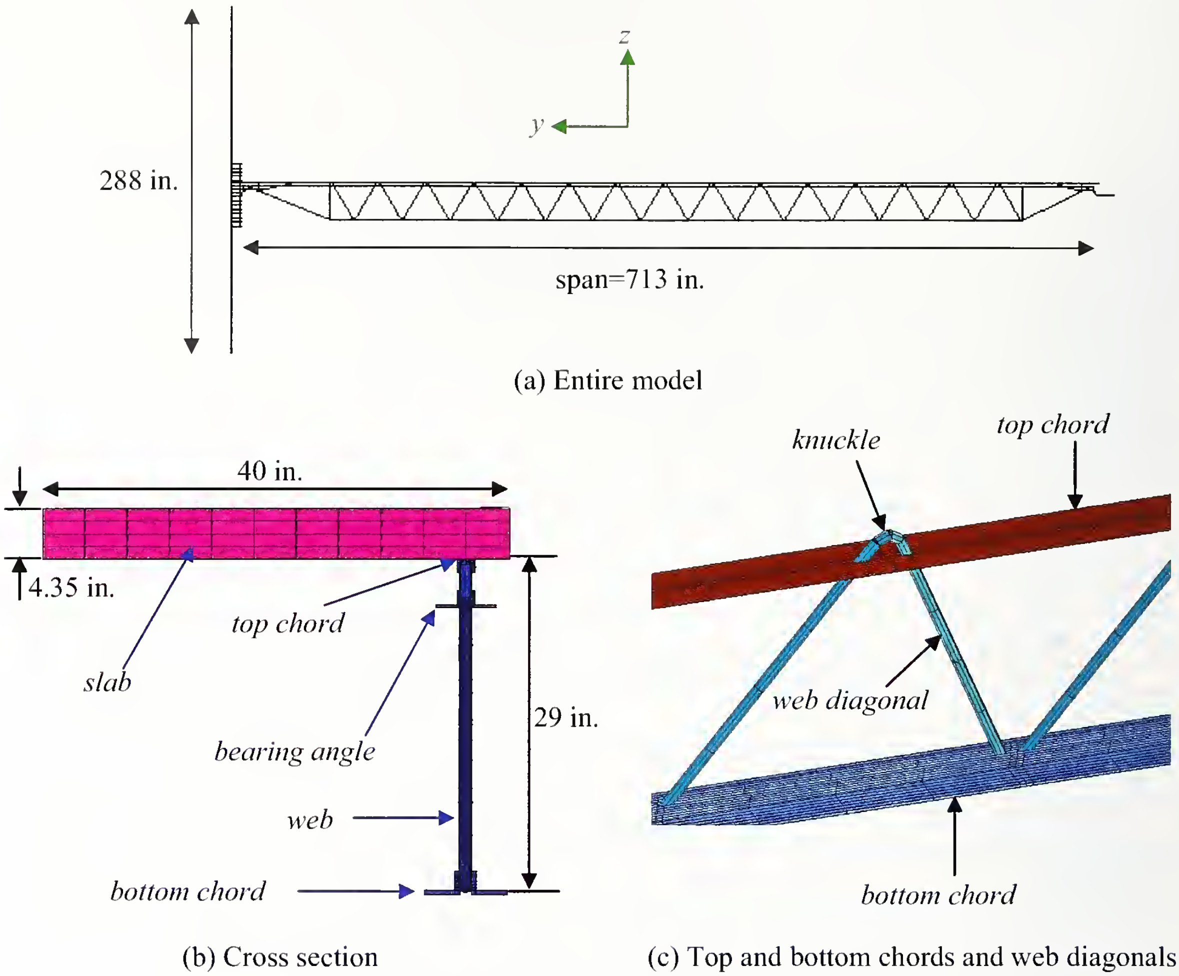

Figure K–36. Truss model.

- The portion of the slab (40 in. wide) between the two exterior columns;
- One strap anchor that is attached to the truss top chord, concrete slab and the adjacent exterior column (column 144); and
- Exterior and interior seats, and the gusset plate at the exterior end.

A typical slab section consists of 4 in. thick lightweight concrete on 22 gauge metal deck with flutes 6.8 in. on centers. Two layers of welded wire fabric were provided in the slab. The reinforcement ratios are 0.21 and 0.735 in the directions along and transverse to the truss, respectively. A flute is 2 in. wide at the top, 1.25 in. wide at the bottom, and 1.47 in. high. An equivalent thickness of 4.35 in. is used as the slab thickness in the truss model. By using the equivalent thickness, the bending stiffness in the direction transverse to the truss is about 15 percent higher than the actual stiffness. However, since the bending in the transverse direction in this truss model is insignificant, the slab is modeled as an isotropic plate. The metal deck and the welded wire fabric are not included in the truss model.

The top and bottom chords and the diagonals of the truss are modeled by 3–D quadratic finite strain beam (BEAM189) elements with temperature-dependent elastic, plastic, and creep material properties. The top chord consists of double angles of 1 1/2 × 2 × 0.25 (long legs horizontal), while the bottom chord consists of double angles of 3 × 2 × 0.37 (long legs horizontal). Web members are round bars of either 1.09 in. or 1.14 in. diameter. A typical diagonal member has a 1.09 in. diameter. Top and bottom chords are divided into four elements between panel points, and a diagonal is also divided into four elements between top and bottom chords. The concrete slab is modeled with 4-node finite strain shell (SHELL181) elements. The nodes of the concrete slab are located at the neutral plane of the concrete slab with an offset relative to the nodes of the top chords. The cast iron model (Hjelm model) can be used with the SHELL181 elements that allow different "yield" in tension and compression. A low "yield stress in tension" is used to simulate cracking.

At knuckle locations, the top chord elements and the elements representing the concrete slab are connected by control elements (COMBIN37) with capacities determined from the detailed knuckle analysis. By including point-to-point contact (CONTA178) elements, compression can always be transferred even after knuckles fail. Studs on the strap between the top chord and column 144 are also modeled by COMBIN37 elements that connect the strap to the slab and have temperature-dependent capacities. The slab and the strap are tied by the COMBIN37 elements horizontally while their vertical displacements are coupled. The exterior and core seats are modeled by COMBIN37 elements that have temperature-dependent capacities determined from the seat analysis. A stud on the spandrel is also modeled by a COMBIN37 element, which ties the spandrel with the slab and has temperature-dependent capacities. Because only one 5/8 in. stud was provided over 80 in. between the slab and the spandrel, a half stud capacity is considered for the stud in the model. In addition, the first stud on the strap is located near this stud on the spandrel. Therefore, COMBIN37 elements between the slab and the spandrel have a capacity of a combination of these studs, including a group effect. Damping unit connecting the truss bottom chord to the spandrel plate is assumed to have little effect on the behavior of the floor truss under sustained loading; therefore, it was not included in the model.

Three–D elastic beam (BEAM44) elements model the exterior columns. SHELL63 elastic shell elements model the spandrel.

Boundary Conditions

Boundary conditions on the truss model are shown in Fig. K–37.

The entire top chord of the truss is supported in the x direction. The bottom chord is supported in the x direction at four bridging truss locations. Two edges of the concrete slab are restrained against rotations about the y and z axes, but can move in the x direction.

The interior truss seat is fixed in all directions. The exterior seat is fixed to the spandrel. The truss is pinned at both exterior and interior truss seats.

The exterior end of the slab is tied to the spandrel by only COMBIN37 elements representing studs. The interior end of the slab is fixed in the z direction and in rotation about the z direction. In the y direction at the interior end of slab, break elements that have temperature-dependent tensile capacities are implemented as show in Fig. K–38. Therefore, the interior slab end is fixed in the y direction until the tensile force exceeds the capacity that is calculated based on the amount of steel reinforcement (#3@10″ top and #4@12″ bottom).

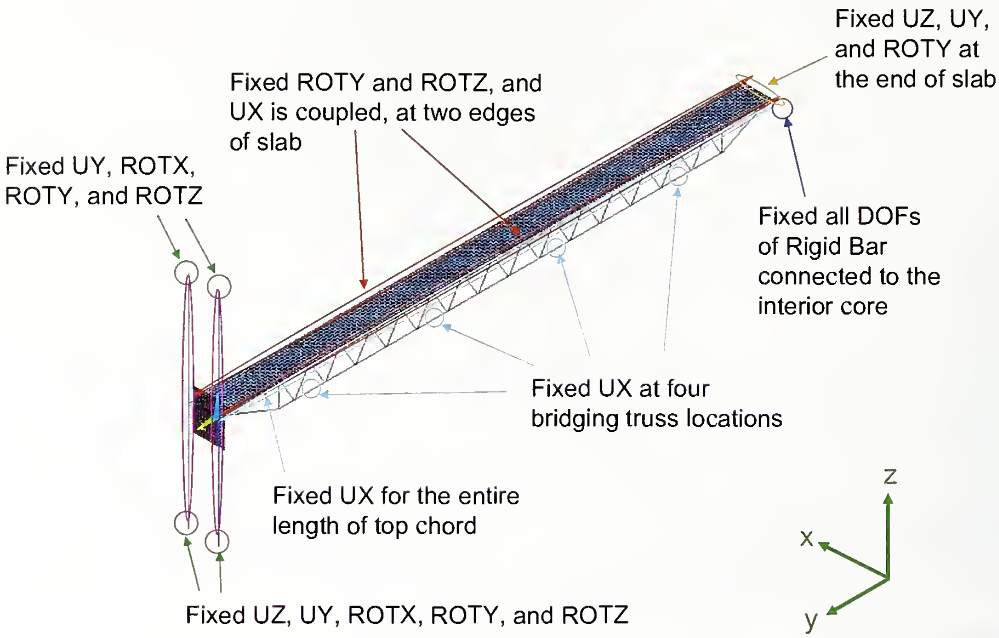

Figure K–37. Boundary conditions.

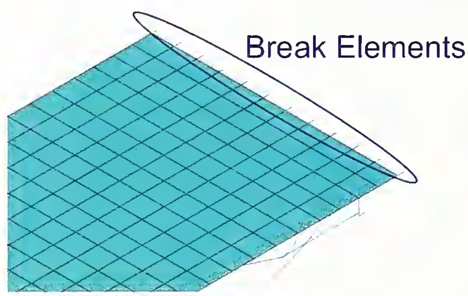

Figure K–38. Break elements at the interior end of slab.

In the analysis with increasing gravity load, a model different from the current model is used, where boundary conditions of the slab are slightly different from the current model described above. In this model, the exterior end of the slab is tied to the spandrel, and the core end of the slab is fixed in the y and z directions and in rotations about the x and z directions. Also, COMBIN37 elements for seats are not included in this model.

Loading

The loading on the truss model consists of gravity dead and live loads and temperature time-histories for all steel members, including the truss seats. The gravity loads include weight of the structure, 8 psf superimposed dead load (including nonstructural dead loads due to architectural items and fixed service equipment), and 13.75 psf of live load equal to 25 percent of design live load of 55 psf. The thermal load is a linear temperature gradient through the slab from 300 °C at the top surface of the concrete slab to

700 °C at the bottom surface of the slab. The temperature is ramped from 20 °C to 700 °C in steel members; from 20 °C to 700 °C at the bottom surface of the slab and from 20 °C to 300 °C at the top surface of the slab at 1,800 s; thereafter, the temperatures do not change for another 1,800 s. Temperature is not applied to the columns.

In order to determine the effect of debris load on the truss behavior, a parametric study will be performed.

Material Properties

Table K–12 shows material assignments for different structural components in the truss model.

Table K–12. Material assignments in truss model.

Structural Component	Specified Yield Strength	Material ID
Top chord	50 ksi	21
Bottom chord	50 ksi	21
1.09 in. diameter web	36 ksi	20
1.14 in. diameter web	50 ksi	21
Strap	36 ksi	1
Column 143	65 ksi	15
Column 144	65 ksi	15
Spandrel	42 ksi	11
Lightweight concrete slab	3,000 psi (f'c)	83

Columns 143 and 144 and the spandrel, use only elastic properties. In the current model, the concrete slab also remains elastic.

Resistance Welds

Table K–13 shows the resistance weld strength between a chord (double angles) and a diagonal based on the test data found at Laclede Steel. Weld strength shown in Table K–13 is the sum of the capacities of two resistance welds. Figure K–39 compares resistance weld strength between top or bottom chord and a diagonal with yield strength of a diagonal at elevated temperatures. As can be seen in Fig. K–39 (a), a typical diagonal (1.09 in. diameter) will yield before the resistance weld fails. For 1.14 in. diameter diagonal, the resistance weld strength cannot yield the bar at temperatures below 550 °C, as can be seen in Fig. K–39 (b). However, shop drawings show additional arc welds between the chord and 1.14 in. diameter bar at most locations.

Table K–13. Resistance weld strength.

Chord	Diagonal Size (in.)	Average Strength (kip)
Top chord	1.09	36.9
Top chord	1.14	37.7
Bottom chord	1.09	41.0
Bottom chord	1.14	40.5

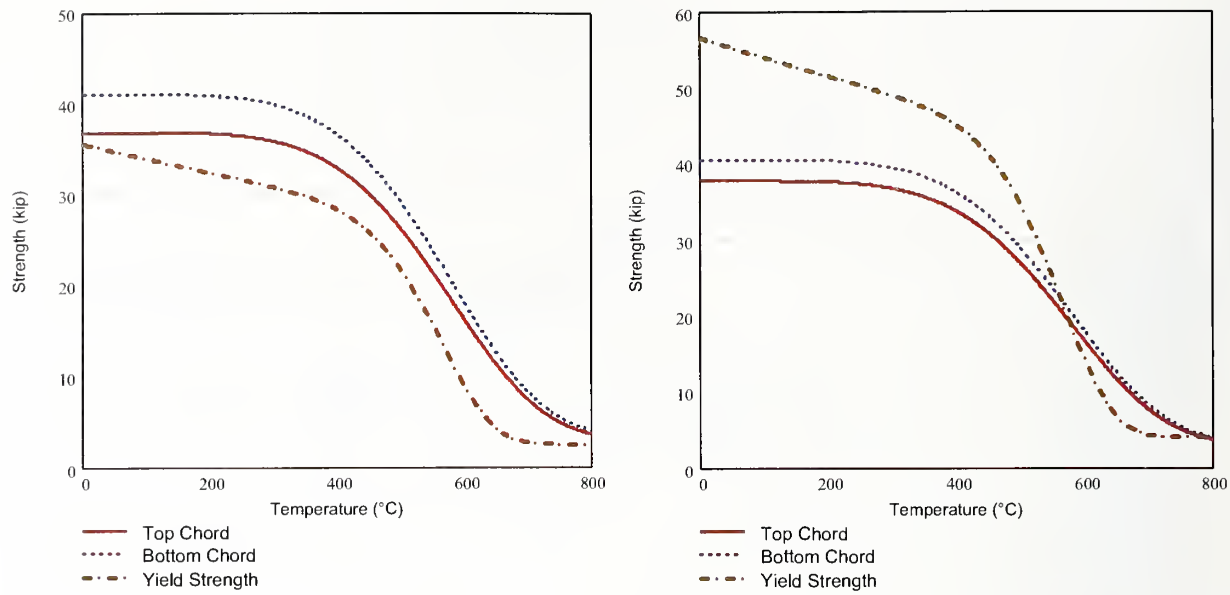

(a) 1.09 in. diameter bar (b) 1.14 in. diameter bar

Figure K–39. Comparison of resistance weld strength and yield strength of web member at elevated temperatures.

Current Status

The truss model can capture the following:

- Temperature-dependent elastic material properties for both steel and concrete;
- Temperature-dependent steel plasticity;
- Buckling of truss members;
- Failure of knuckle—loss of composite action;
- Failure of studs on the strap;
- Failure of stud between the spandrel and the concrete slab; and
- Failure of the exterior and interior truss seats.

The following features are being added to the truss model:

- Crushing and cracking of concrete;
- Creep strain in steel at elevated temperatures; and
- Failure of welds (Calculations show section yielding can occur prior to weld failure in nearly all cases.).

Model Verification

The maximum vertical displacement is checked against the single truss model extracted from the ANSYS full floor model that was converted from the SAP full floor model. The difference in the vertical displacement is only 3.5 percent.

FEA Results

Gravity Loading—The maximum calculated vertical deflection is 1.1 in. downward. The maximum calculated horizontal column deflection is 0.022 in. inward. The maximum forces in top chord, bottom chord, and diagonal are 13,357 lb, 39,514 lb, and 7,647 lb, respectively.

Gravity Plus Thermal Loading—The analysis is carried out dynamically with 5 percent Rayleigh damping. To shorten the run time, the total time period is set to 1.0 s for the temperature ramp. The analysis proceeded to a temperature of T=663 °C. Figure K–40 shows horizontal and vertical displacement results. A positive horizontal displacement indicates that the exterior columns are pushed out, and a negative vertical displacement indicates that the truss is deflected downward. At 340 °C, the horizontal displacement at the exterior column starts to decrease. At 560 °C, the exterior columns are pulled in, and the truss becomes catenary from that point on.

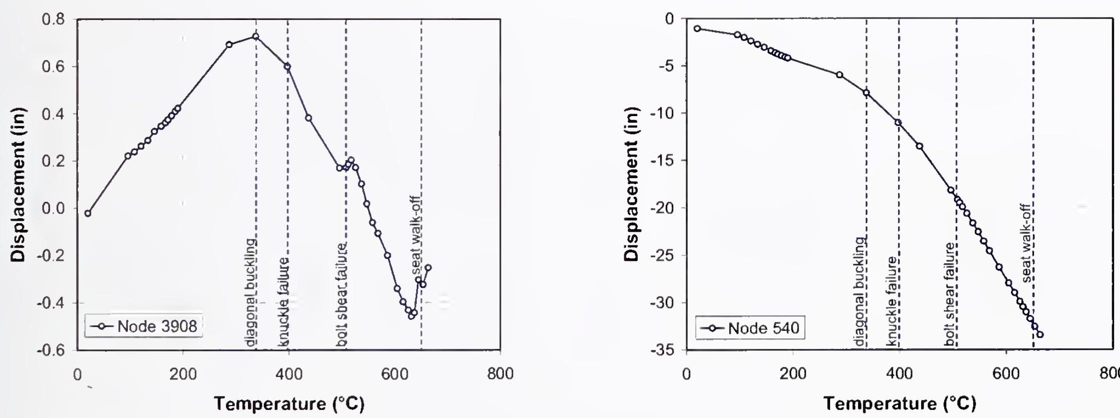

(a) Horizontal displacement at column 143

(b) Vertical displacement at midspan

Figure K–40. Displacement versus temperature.

Figure K–41 shows axial forces in the truss members. In the figure, Py is the axial force at yield and equals the product of the net area of the member and the yield strength which varies with temperature. Pc is the compressive strength per AISC formula (AISC 2003) for the top chord with fixed ends in Fig. K–41 (a) and for 1.09 in. diameter diagonal bar with pinned ends in Fig. K–41 (c).

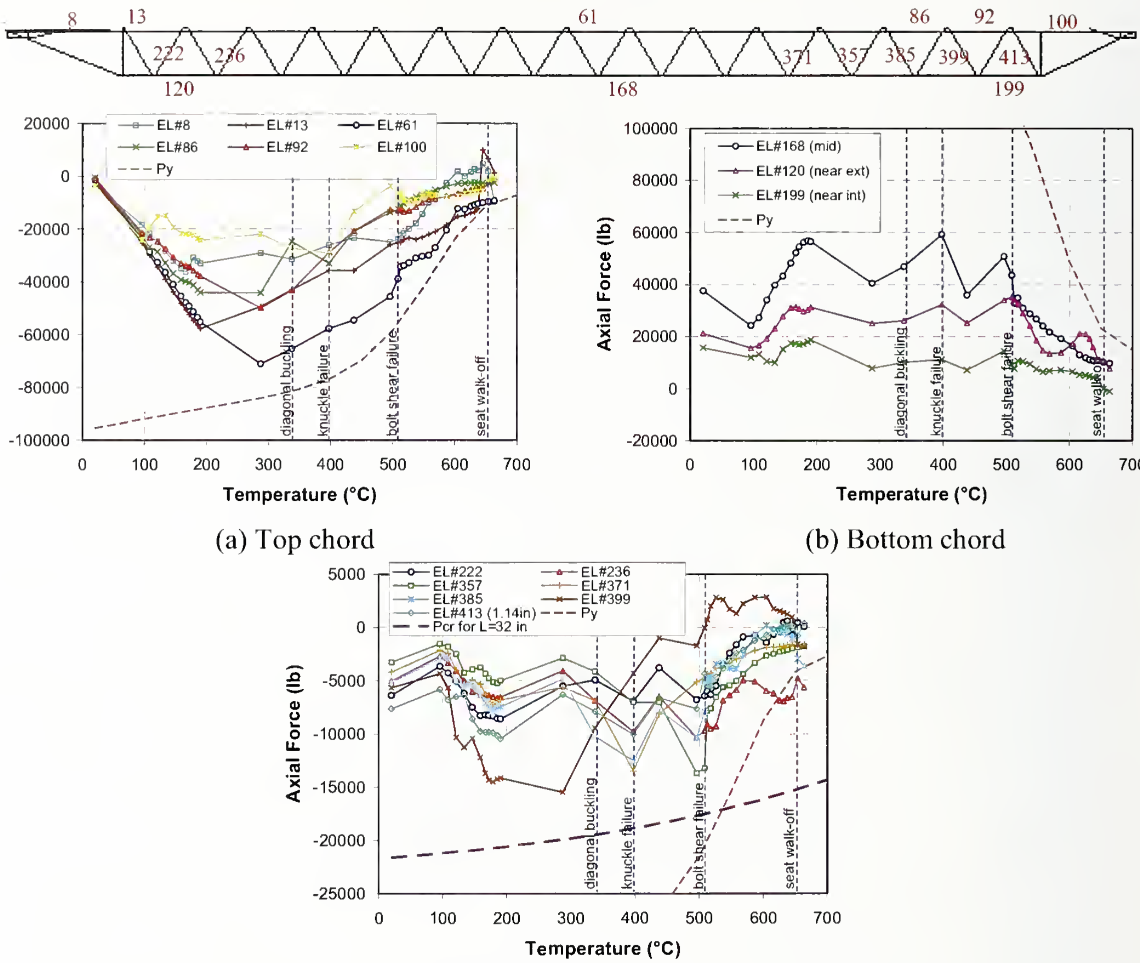

(c) Compression diagonal

Figure K–41. Axial force in truss members versus temperature.

Figure K–42 (a) shows the top chords yielding beyond 300 °C. This is due to a significant difference of coefficients of thermal expansion (CTE) between concrete and steel. At 500 °C, the CTE of steel is twice that of lightweight concrete. Bottom chords are still in the elastic range at the end of analysis. Some diagonals are bent significantly in the plane of the truss by high axial force and end moments (see Fig. K–42 for the deformed shape at the interior end). This diagonal buckling starts at approximately 340 °C.

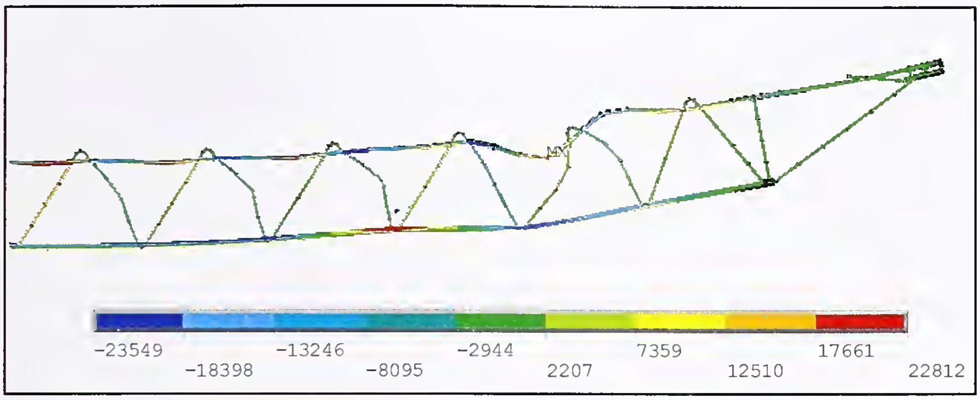

Figure K–42. Axial stress contour in the truss members at 663 °C (displacement magnification factor = 1.0).

Figure K–43 shows knuckle forces in the y direction (longitudinal truss direction) and the z direction (vertical direction). The capacity of a knuckle in the y direction is assumed to be 30,000 lb, and in the z direction 15,000 lb in tension. Knuckles 14 and 15 fail due to horizontal shear around 400 °C. Knuckle 1 also fails due to the horizontal shear around 650 °C.

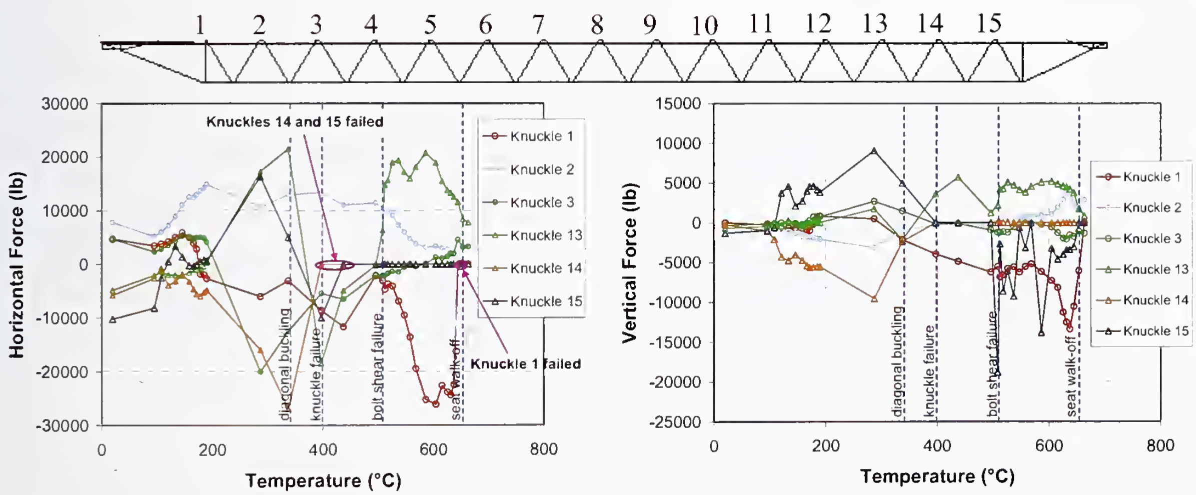

(a) Horizontal Force

(b) Vertical Force

Figure K–43. Force in the knuckles versus temperature.

Figure K–44 (a) and (b) show horizontal and vertical reaction forces at seats, respectively. At 510 °C, the interior seat bolt shears off. At 650 °C, the truss walks off the interior seat. At 660 °C, the gusset plate at the exterior end fails in tension.

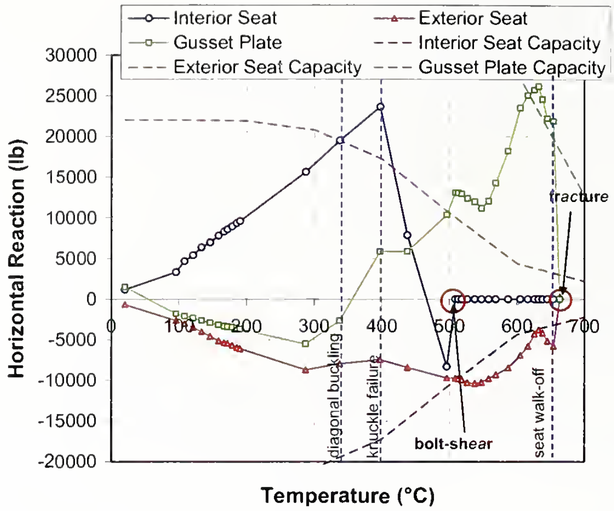

(a) Horizontal reaction force

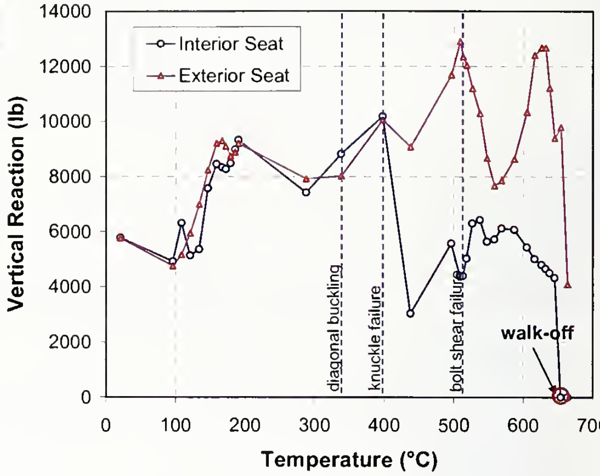

(b) Vertical reaction force

Figure K–44. Reaction forces at seats.

Additional Debris Load

The capacity of the truss model against additional debris load is determined by increasing the gravity loading at room temperature. The analysis is performed with the previous model, where boundary conditions of the slab are as described in the section "Bounding Conditions." Let us define load factor as the ratio of the gravity load plus debris weight to the gravity load, where gravity load includes self weight, superimposed dead load, and 25 percent of the reduced live load. The analysis was terminated at a load factor of 3.4. Figure K–45 (a) shows midspan vertical displacement versus load factor. At 2.4 times the gravity loading, 11 knuckles from the core end fail in the truss direction. At 2.8 times the gravity loading, the fourth knuckle from the exterior end fails. Figure K–45 (b) shows the sum of horizontal reaction forces measured at the exterior columns. Note that seat capacities are not modeled in this analysis.

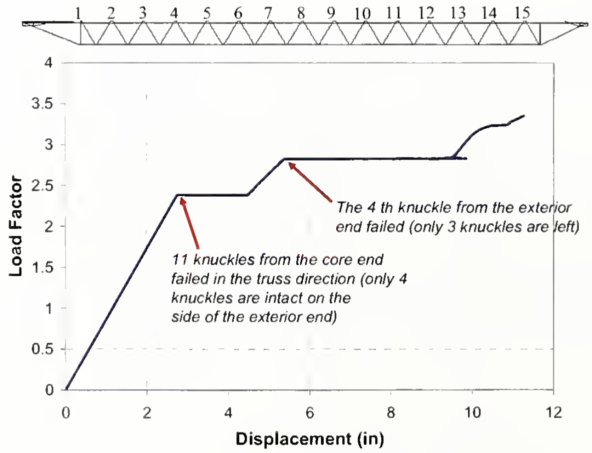

(a) Load factor versus midspan vertical displacement

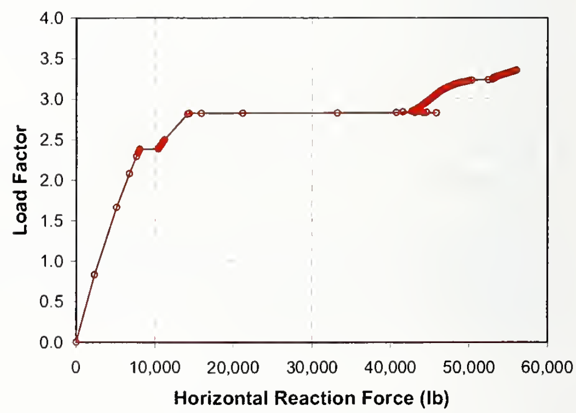

(b) Load factor versus horizontal reaction force

Figure K–45. Finite element analysis results from increasing gravity.

Summary and Discussion

The truss behavior under the gravity plus thermal loading, where the temperature is ramped up to 663 °C can be summarized as follows:

- Top chords yield above 300 °C due to the difference in CTEs of steel and lightweight concrete.
- Compression diagonals start to buckle in the plane of the truss due to a high axial force and end moments at 340 °C.
- At 400 °C, knuckles start to fail.
- The interior seat bolt shears off at 510 °C.
- The truss walks off the interior seat at 650 °C, followed by fracture of the gusset plate at the exterior end at 663 °C.

The results for the additional debris weight show that the knuckles start failing when the load factor is 2.4. Most knuckles fail before load factor reaches 3.0. After the knuckle failure, the truss loses composite action between the truss and the concrete slab, and the vertical displacement increases significantly. As a result, horizontal reaction force increases.

Models of the truss including knuckles with temperature-dependent capacities, diagonal weld failure, and concrete cracking and crushing are under study.

Simplified Model

To be used in the full floor subsystem model, the truss model will be simplified based on the results from the truss model analysis. Characteristics of the simplified truss model are listed in the following:

- The geometry of the truss will be preserved.
- Pin-ended Link elements will be used for truss members.
- User-defined elements will be used to model failure modes of knuckles, seats, and diagonal members. They will be implemented at the ends of link elements.
- Slab softening or cracking will be incorporated into the model.

K.8 EXTERIOR WALL SUBSYSTEM

The exterior wall subsystem represents the impact zone and includes nine prefabricated wall panels, three panels high by three panels wide.

The exterior wall subsystem model includes nine columns, extending vertically from the column splice located below floor 91 to the column splice above floor 99, and nine spandrels, extending horizontally from the spandrel splice located at mid-span between columns 149 and 150 to the spandrel splice at mid-span between columns 158 and 159, of the WTC 1 exterior wall.

Figure K–46 shows the subsystem pictorially. Tables K–14 through K–16 give the properties of the column component plates, the spandrels, and the column and spandrel splices. Figure K–47 shows pictorially the spandrel plate thickness, nominal yield strengths, and spandrel splice types. Figure K–48 shows the column plates notation used.

The odd numbered columns support floor trusses. Pairs of strap anchors extend diagonally from the top chord of truss pairs to the even numbered columns. The trusses and the straps partially brace the columns both in-plane and out-of-plane of the exterior wall.

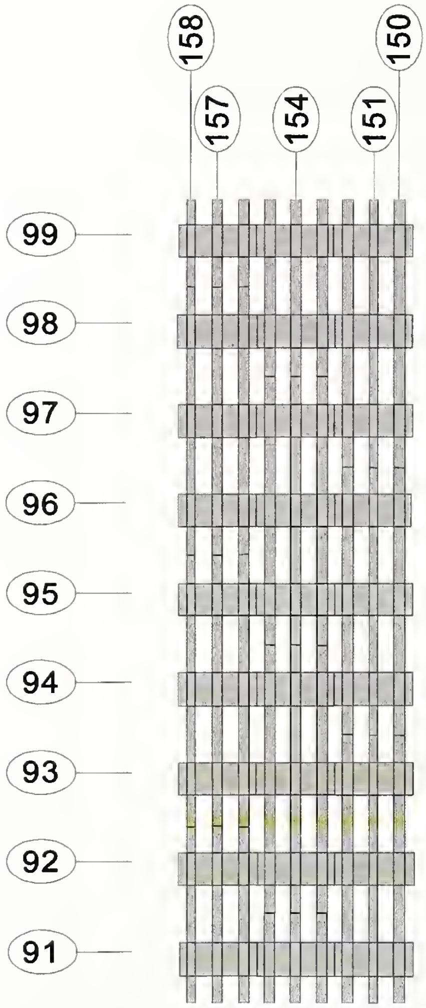

Figure K–46. Exterior wall subsystem structure.

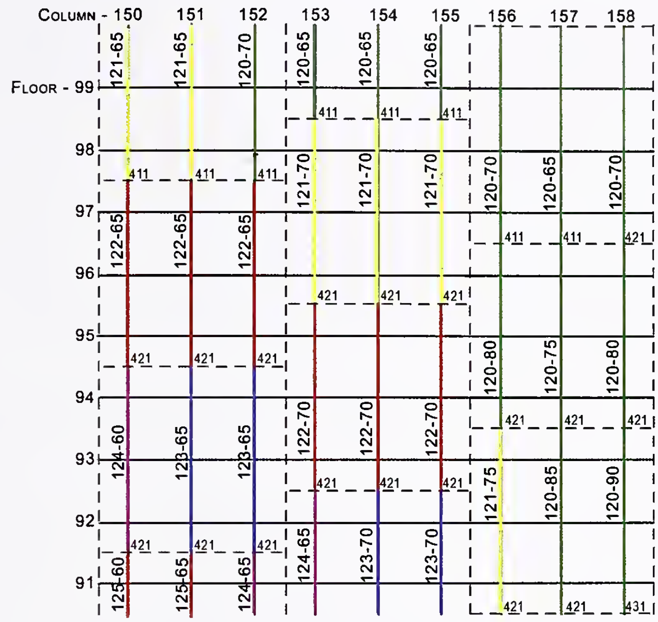

XXX-XX - Indicates type and nominal yield strength of column
xxx - Indicates type of column splice

a) Columns and Column Splices

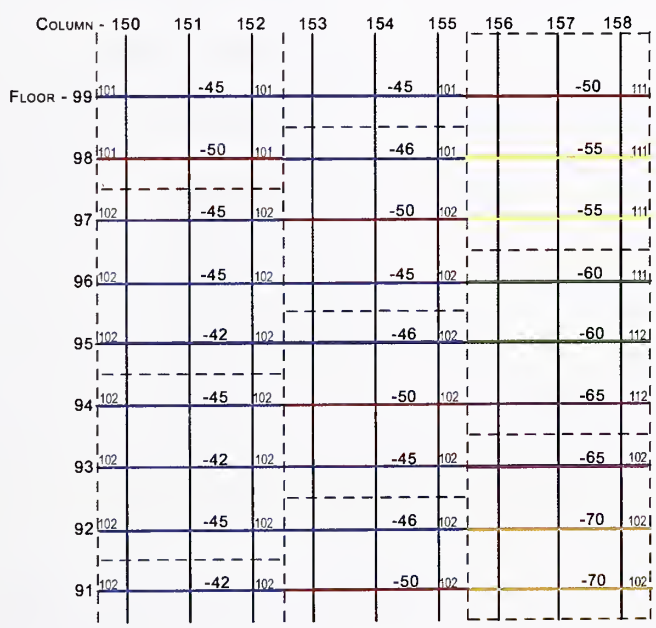

XXX-XX - Indicates nominal yield strength of spandrel
xxx - Indicates type of spandrel splice
Spandrel Thickness 3/8 in.

b) Spandrels and Spandrel Splices

Figure K–47. Column and floor number materials and splice types.

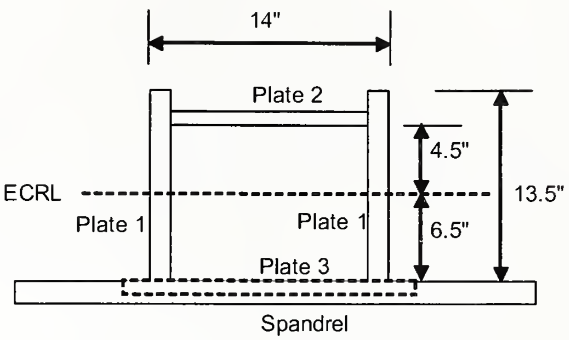

Figure K–48. Spandrels and spandrel splices.

Table K–14. Column sectional properties.

Column Type	Plate 1 l × t	Plate 2 l × t	Plate 3 l × t	Col. Type ID
120	13.5 × 0.25	13.5 × 0.25	15.75 × 0.25	0
121	13.5 × 0.3125	13.375 × 0.25	15.75 × 0.25	1
122	13.5 × 0.375	13.25 × 0.25	15.75 × 0.25	2
123	13.5 × 0.4375	13.125 × 0.25	15.75 × 0.25	3
124	13.5 × 0.5	13 × 0.25	15.75 × 0.25	4
125	13.5 × 0.5625	12.875 × 0.25	15.75 × 0.25	5

Note: All spandrels in wall model are 52 in. deep × 3/8 in. thick.

Table K–15. Spandrel splice details.

Spandrel Splice Type	Number of Bolts/Row	Total Number of Rows	Bolt Spacing	Gage	Overall Splice Plate Dimensions	Bolt to Centerline of Splice	Gap B/W Spandrels	Spandrel Splice ID
101	6	2	5@9		49 × 6.75 ×.25	1.875	0.75	101
102	8	2	3,6,3@ 9,6,3		49 × 6.75 ×.25	1.875	0.75	102
111	6	4	5@9	3	49 × 12.75 ×.25	1.875	0.75	111
112	8	4	3,6,3@ 9,6,3	3	49 × 12.75 ×.25	1.875	0.75	112

a. All spandrel splices use 7/8 in. A325 bolts; spandrel plate yield strength is 36 ksi.
b. Holes in spandrel are 1/4 in. larger than bolts; holes in plates are bolt + 1/16 in. or option to match spandrel holes.

Table K–16. Column splice details.

Column Splice Type	Butt Plate Thickness	Number of Bolts	Bolt Diameter	Gage	Bolt Spacing	Column Splice ID
411	1.375	4	0.875	3.5	6	411
421	1.625	4	0.875	3.5	6	421
431	1.875	4	1	3.5	6	431

a. Butt plates have specified yield strength of 50 ksi.
b. Bolts are A325.

K.8.1 Description of Exterior Wall Subsystem Model

Figure K–49 shows the model in elevation. BEAM189 elements model the columns. SHELL181 plate elements model the spandrels. Figure K–50 shows the number of elements used to model columns and spandrels. MPC184 rigid elements connect the center of gravity of a column to the mid-plane of a spandrel at each shell element. Figure K–51 shows this use of the MPC184. MPC184 rigid elements also model the spandrel connections. A simplified model, consisting of two BEAM189 elements for each of the four bolts, four pairs of CONTA178 contact elements at the faying (contact) surfaces, and MPC184 rigid elements connecting the tops of the bolts to the CONTA178 contact elements, model the column splice. COMBIN37 elements model the fracture of the column splice bolts.

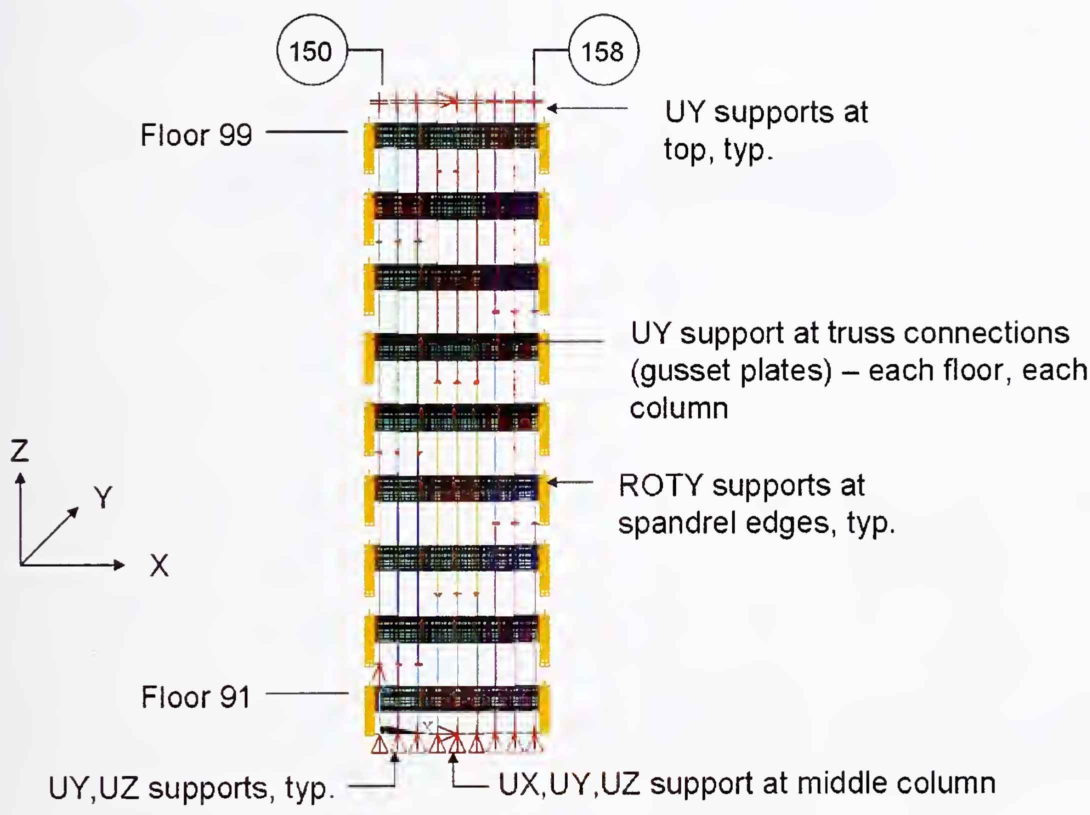

Figure K–49. Exterior wall subsystem model, viewed from inside of WTC 1.

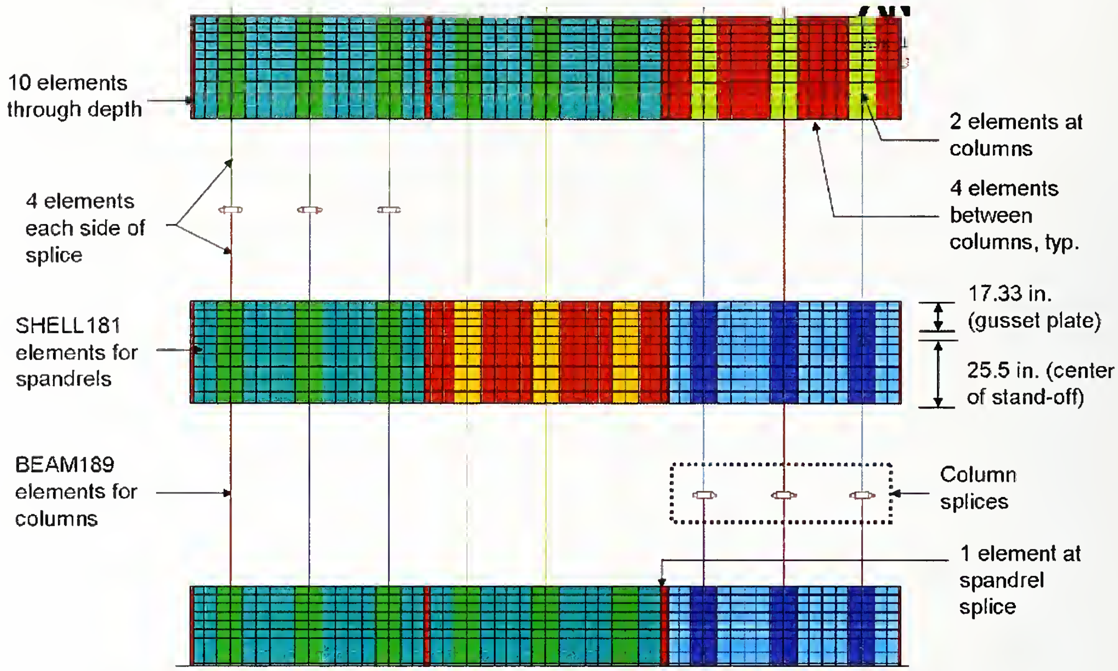

Figure K–50. Portion of exterior wall subsystem model showing number of elements used.

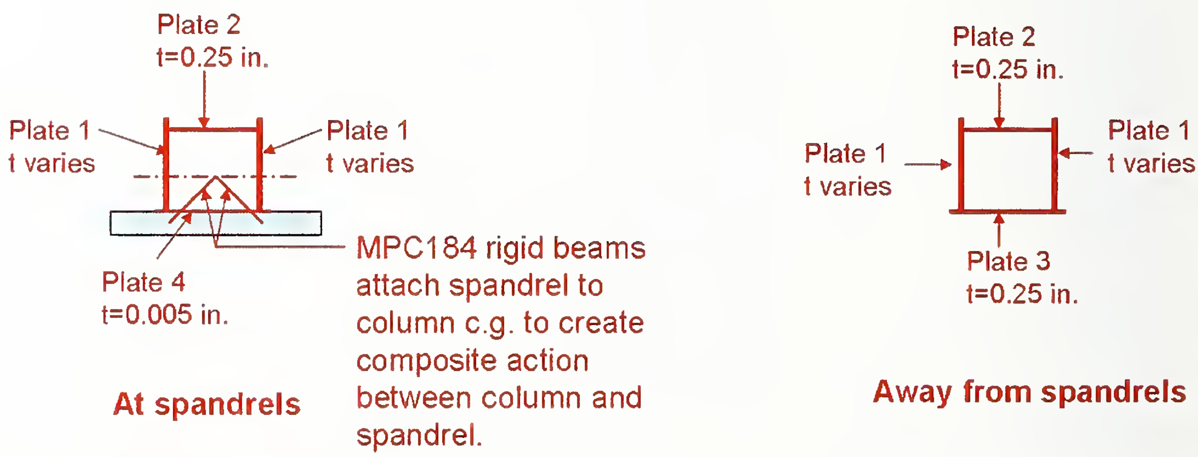

Figure K–51. Schematic representation of columns used in the exterior wall subsystem model.

The capabilities of the BEAM189 and SHELL181 elements include large deflections, plastic deformation, and creep at elevated temperatures. Materials are assigned as described in Section K.5.

The loads on the model include the following:

- Self weight;
- Dead load of floor trusses;

- 25 percent of floor live load;
- Column splice bolt preload; and
- Temperatures of fire scenarios.

A concentrated vertical load and an out-of-the-wall-plane moment due to the dead and live load of the structure above floor 99 load the top of each column. A concentrated vertical load and an out-of-the-wall-plane couple due to the dead and live load of the floor truss load each odd numbered column at the truss seats. Mean temperature at the center of gravity of the column and a linear gradient in each of two directions through the section of the column strain the BEAM189 elements at each node. Temperatures at the nodes strain the SHELL181 elements. Loads and/or deflections at the truss seats model the outward motion or the caternary action of the floor truss due to fire scenarios. The 7/8 in. diameter column splice bolts are preloaded with 36.05 kip (AISC 1964).

Simple supports out of the plane of the wall restrain the tops and the bottoms of all columns in the model. In addition, supports horizontally in the plane of the wall restrain the top and the bottom of central column 154. Simple supports in the vertical direction restrain the bottoms of all columns in the model. Symmetry conditions are imposed on the spandrels at the extremities of the model, except that the spandrels are free to expand in the plane of the wall. In the plane and out of the plane of the wall restraints brace the column at floor truss seats and diagonal straps.

The model captures the following failure modes:

- Column collapse due to large lateral deformations;
- Column buckling due to loss of bracing at floor truss seats and diagonal straps;
- Failure of column splice bolts; and
- Failure of spandrel splice bolts.

The model does not capture the local buckling of the column plates and the formation of plastic hinges due to the interaction of local plate buckling and high stresses in the column from axial load and bending moments. Section K.8.4 below includes the justification for excluding this structural behavior from the wall subsystem model.

K.8.2 Validation of the Exterior Wall Subsystem Model

The behavior of models of the following components of the exterior wall subsystem validate the exterior wall subsystem model:

- Model of a one-story-high exterior column.
- Model of a nine-story-high exterior column.

- Detailed and simplified models of the column splice.
- SAP2000 and ANSYS models of a prefabricated wall panel.

K.8.3 Model of One-Story High Exterior Column

Figure K–52 shows the model of a one-story-high exterior column. The model includes a one-story-high portion of column 151 extending from floor 95 to floor 96 and portions of spandrels at floor 95 and floor 96. The model also represents column 151 from floor 96 to floor 97 since the dimensions, plate thicknesses and material properties are identical to those of column 151 from floor 95 to floor 96. SHELL181 plate elements model the plates of the column and the spandrels. CERIG rigid elements connect the center of gravity of the column to its component plates and the spandrel at both the top and bottom of the model. The column is simply supported in three directions at the bottom and simply supported in the horizontal direction at the top. Increments of axial displacement applied at the top load the model.

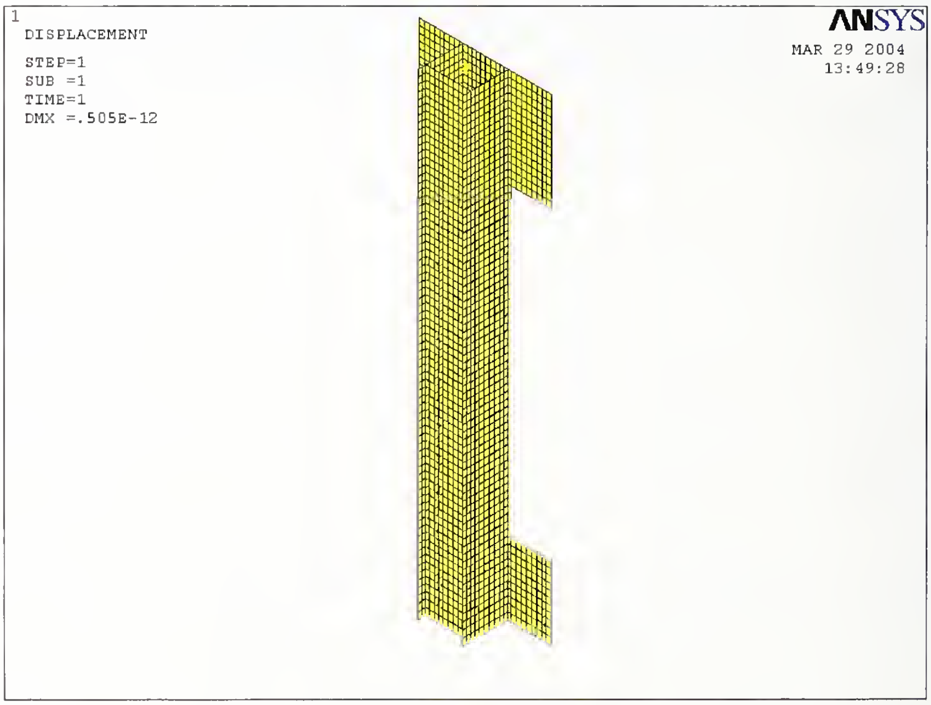

Figure K–52. One-story exterior column model.

Figure K–53 shows the variation of axial load with enforced axial displacement and resulting lateral deflection at room temperature and 700 °C. This figure also shows the hand calculated column load levels at room temperature and 700 °C for:

- Local buckling of Plate 2 and Plate 3;
- Uniform yielding of the column; and
- Axial load due to dead and live load at floor 96 in the exterior wall subsystem model.

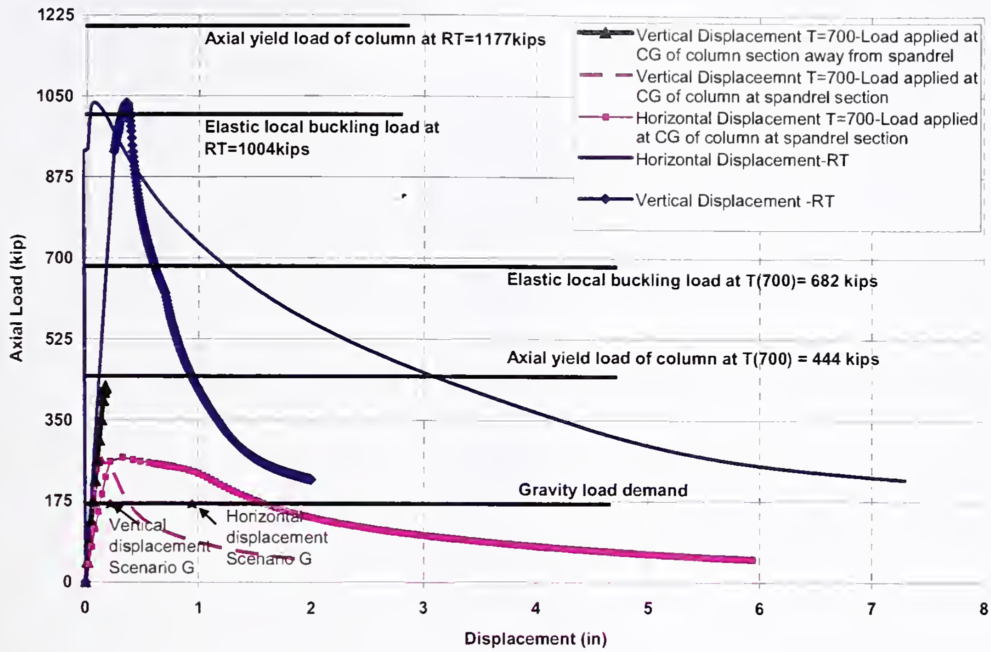

Figure K–53. Load-deflection of column at room temperature and 700 °C.

Figure K–54 shows the local bucking deformation of Plate 2 and Plate 3 at the maximum load level. Figure K–55 shows a plastic hinge at mid-height of the column for an axial displacement of 2 in. Figure K–56 shows the presence of local buckles in Plate 2 and Plate 3 at the maximum load.

Figure K–53 shows that at room temperature Plate 2 and Plate 3 buckle locally at a load that is less than the maximum column load, but that at 700 °C the column yields before it buckles locally. This figure also shows that the expected column demand load of 175 kip is substantially lower than the local buckling load at room temperature and the column yield load at 700 °C. For these results, the axial displacement was applied along the center of gravity of the column cross section away from the spandrel. If axial displacement is applied at center of gravity of the column cross section at the spandrel, there will be additional bending moment in the column section away from the spandrel. The presence of moments reduces the axial load capacity of the column. The resulting load-deflection diagram is also shown in Fig. K–53.

K.8.4 Model of Nine-Story High Exterior Model

Figure K–57 shows the nine-story-high exterior column model. The model includes column 151 extending from near mid-height between floor 91 and floor 92 to mid-height between floor 100 and floor 101, spandrels at floors 92 through 100, and column splices located at the mid-height between floors 94 and 95 and floors 97 and 98. SHELL181 plate elements model the plates of the column, the spandrels, the butt plates at the column splice, and the stiffeners. BEAM189 elements model the column splice bolts. CONTA174 and TARGE170 elements model the faying surfaces of the column splice. MPC184 rigid elements connect the tops of the bolts to the butt plates. At the bottom the column is restrained from displacement and rotation in all three directions. At the top the column is restrained from translating in the horizontal directions and from twisting.

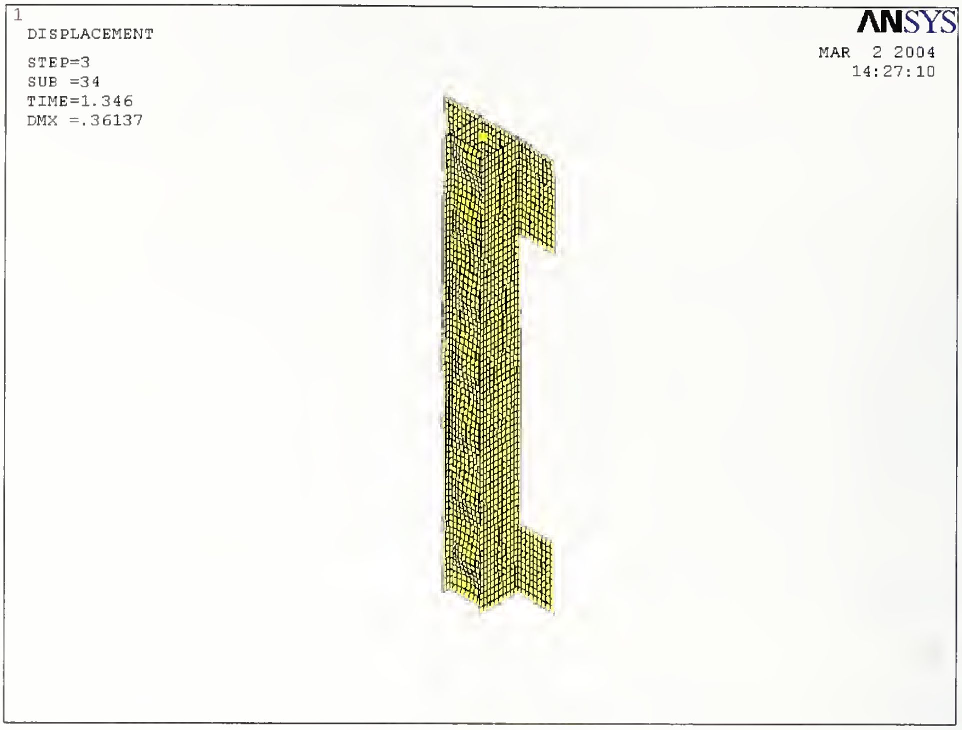

Figure K–54. Local buckling of column at room temperature.

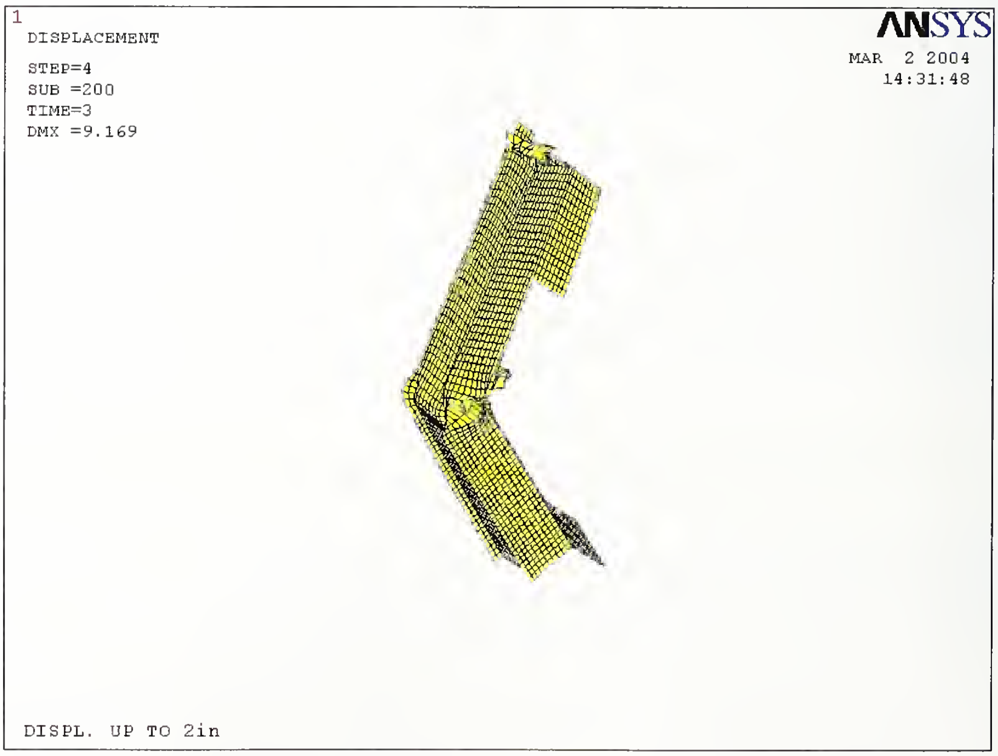

Figure K–55. Plastic hinge in column at room temperature.

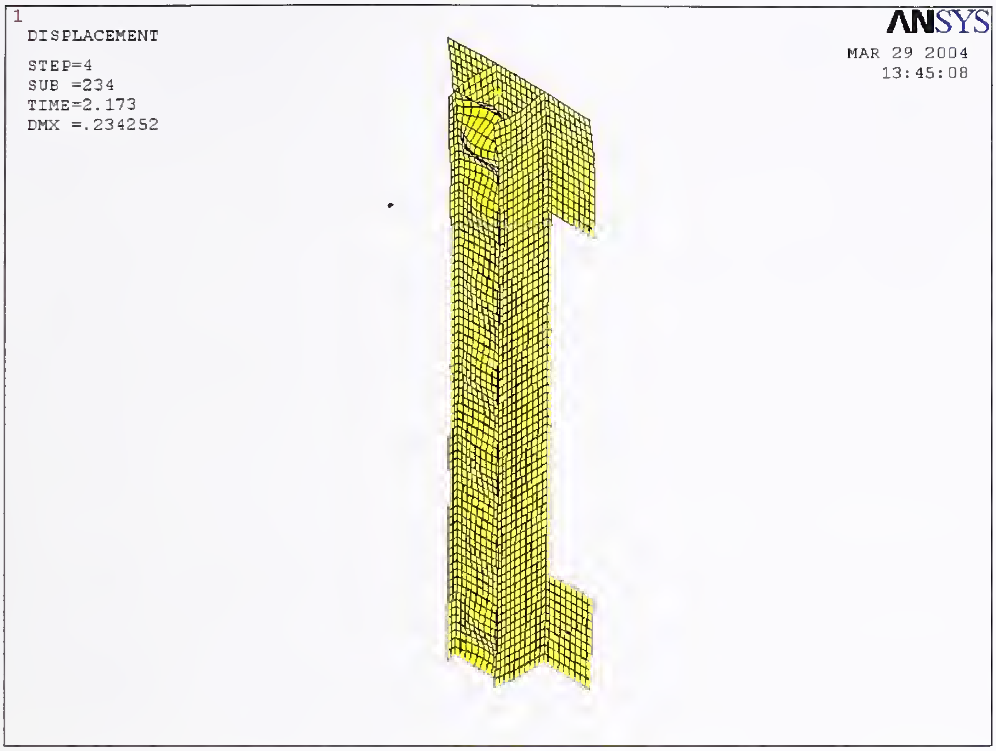

Figure K–56. Deformed shape of column at maximum axial load at 700 °C.

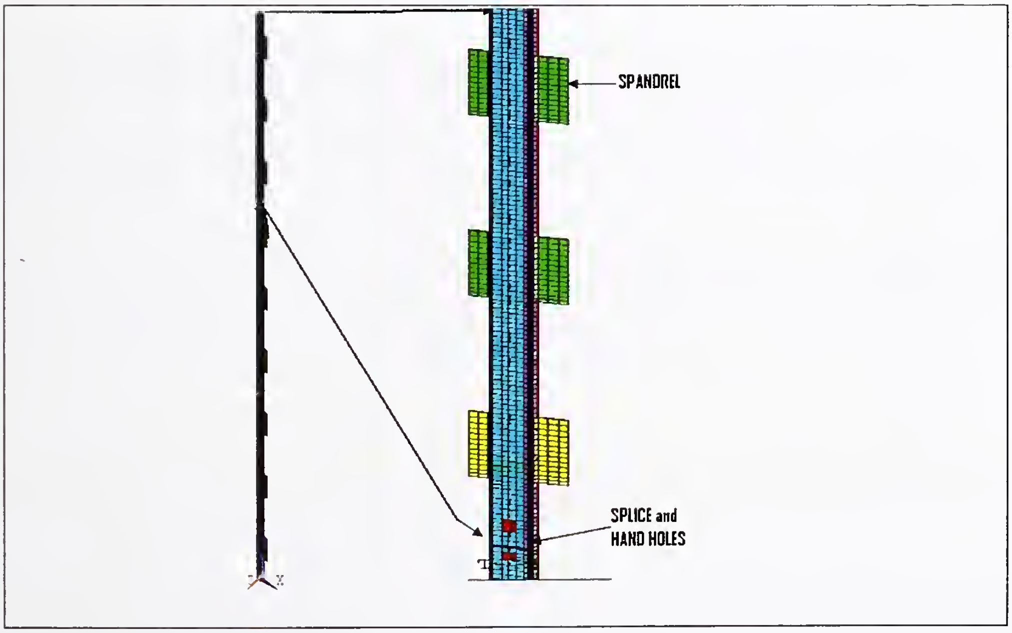

Figure K–57. Nine-story column model.

The capabilities of the BEAM189 and SHELL181 elements include large deflections and plastic deformation. For these elements, gives the material property identification numbers, which in turn are described in Chapter 4 above.

The loads on the model include the following:

- Self weight;
- Dead load of floor trusses;
- 25 percent of floor live load;
- Column splice bolt preload; and
- Temperature of Fire Scenario G.

In Fire Scenario G, the fire starts on floors 95, 96, and 97 and spreads to floors 93 through 98. Gas temperature reaches 1,100 °C. Convection cools the outside face of the column. Radiation heats the other three faces. The inside face of the column is not fireproofed. Temperatures are provided at 200 s intervals up to 5,000 s. Figure K–58 shows the variation of the maximum temperature anywhere in the column with time and the yield stress at the point of maximum temperature. The temperature reaches a maximum of 706 °C at 5,000 s.

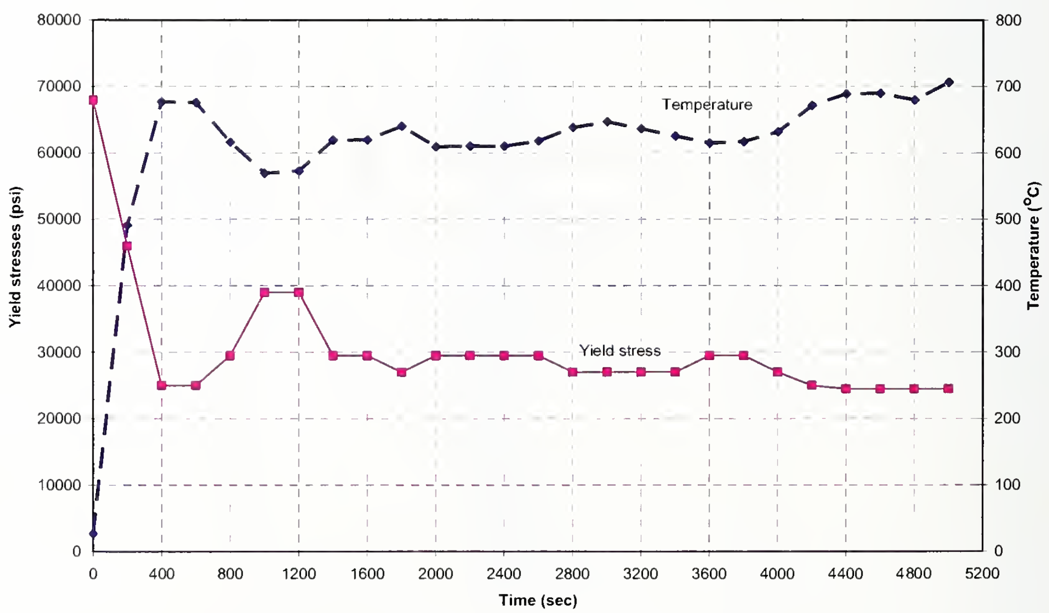

Figure K–58. Variation of maximum temperature and corresponding yield stress with time, fire scenario G.

To account for the dead and live load of the structure above floor 100 and of the floors that connect to the column, concentrated vertical loads and bending moments about a horizontal axis in the plane of the wall are applied to the top of the column and at all truss seats. Furthermore, the 7/8 in. diameter column splice bolts are preloaded to 36.05 kip (AISC 1964).

Figure K–59 shows the variation of maximum tensile and maximum compressive stresses with time and the corresponding yield stress. Figure K–60 shows the deformed shape of the column at 400 s when the compression stress in the column is a maximum. Figure K–60 also shows the deformed shape of the column at 3,200 s when the tensile stress in the column is a maximum. Figure K–60 also shows the deformed shape of the column at 5,000 s when the temperature in the column is a maximum.

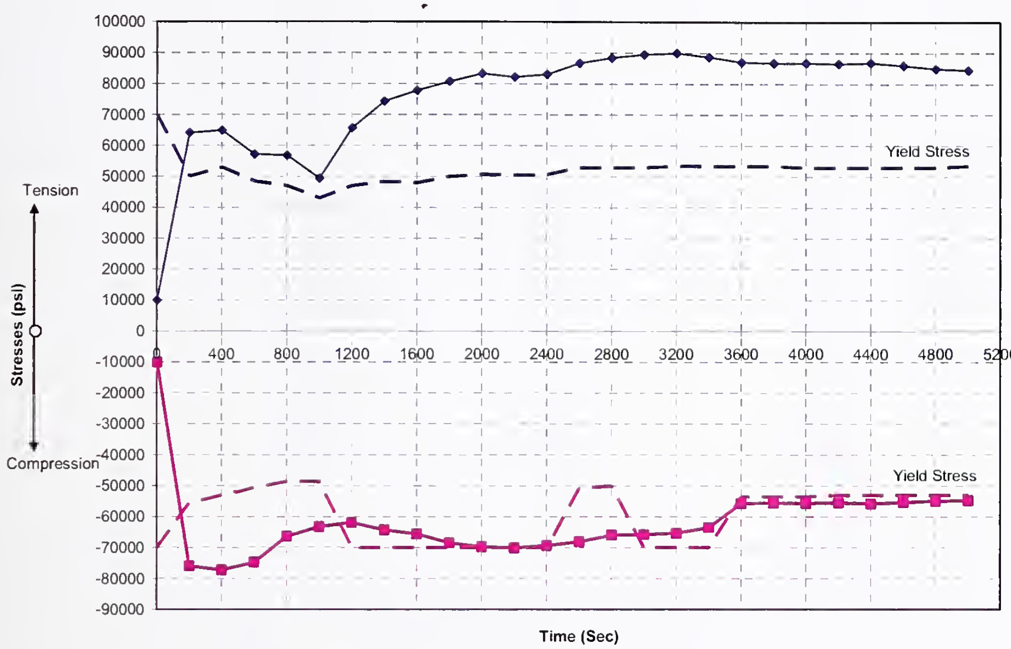

Figure K–59. Maximum compressive and tensile axial stress and corresponding yield stress with time, fire scenario G.

Figure K–59 shows that the tensile and compressive stresses exceed the yield stress for most times during the duration of the fire.

Figure K–60 shows that for Fire Scenario G, an extreme scenario that assumes no fireproofing on the inside face of the column, plastic hinges do not form in the column. This justifies the exclusion of local buckling of the column plates from the wall subsystem model.

K.8.5 Models of the Column Splice

The plate model of the column splice, shown in Fig. K–61 includes a 92 in. tall section of the nine-story column model centered on the column splice located below floor 98.

Figure K–62 shows a simplified model of the column splice. The simplified model consists of two BEAM 189 elements for each of the four bolts, four pairs of CONTA178 contact elements at the faying surfaces, and MPC184 rigid elements connecting the ends of the bolts to the CONTA178 contact elements. A BEAM189 element extends from each side of the splice to match the length of the plate model. Figure K–63 shows the details that model the faying surfaces of the splice.

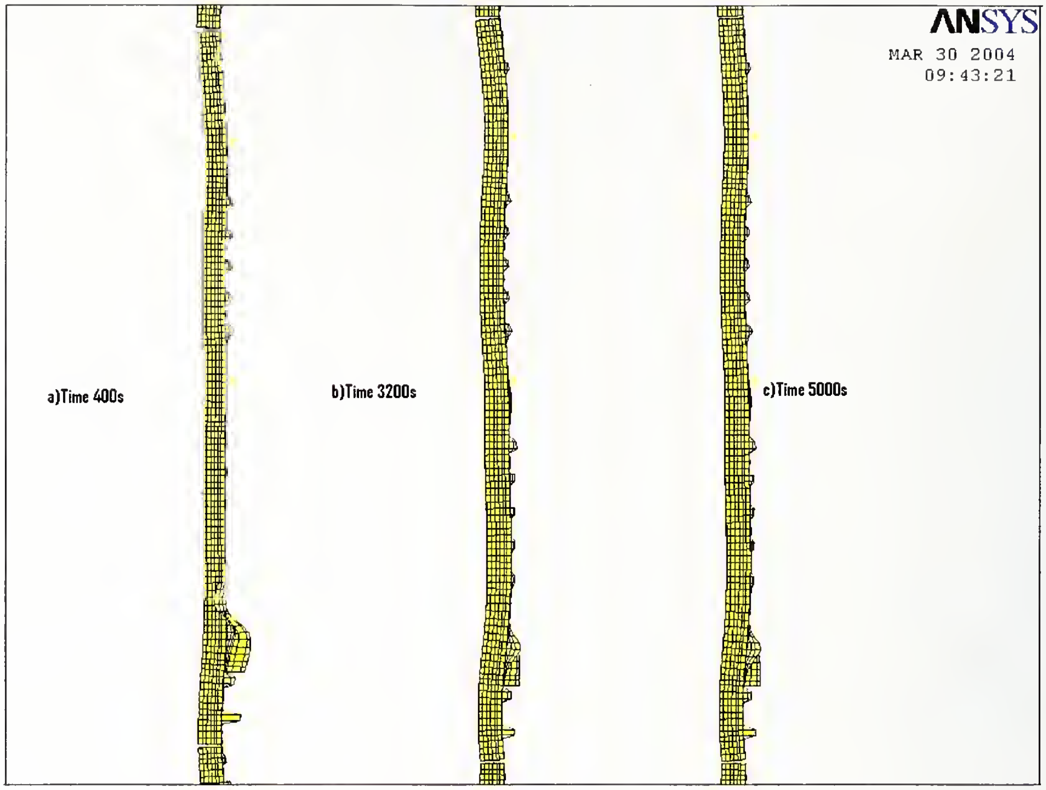

Figure K–60. Deformed shape of column at 400 s, 3,200 s, and 5,000 s (floors 95–97).

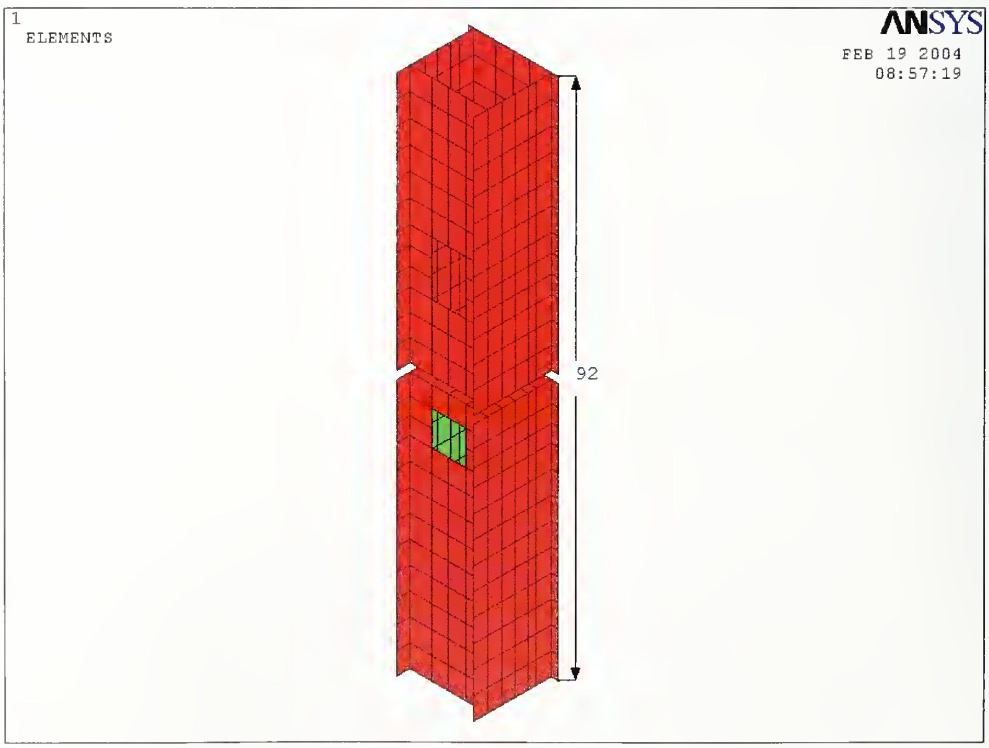

Figure K–61. Plate model of column splice, floors 97-98.

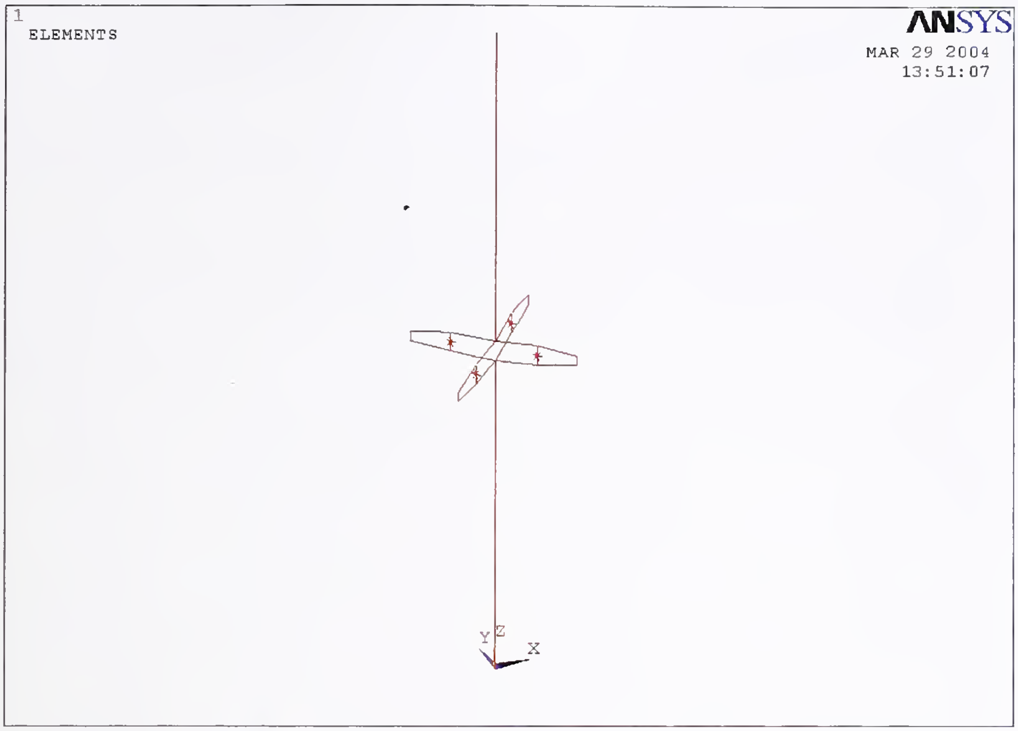

Figure K–62. Simplified model of column splice.

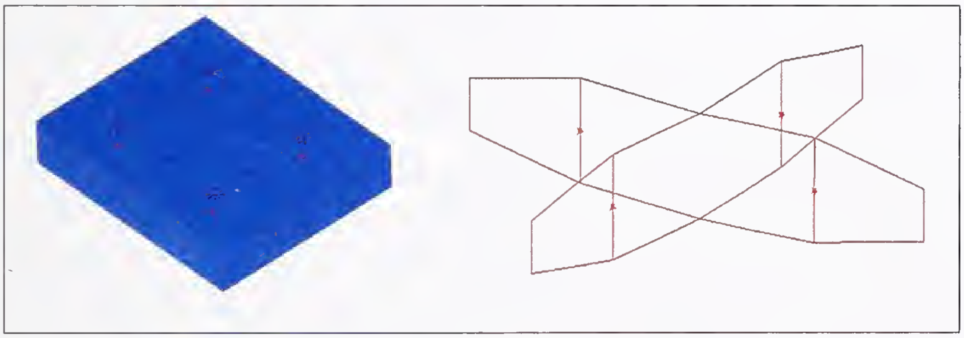

Figure K–63. Column splice details, plate model and simplified model.

Both models are subjected to the following loads:

- Axial tension;
- Shear transverse to the plane of the wall;
- Moment out of plane of the wall;
- Moment in plane of the wall; and
- Torsion.

Figure K–64 shows the variation of axial displacement with axial force load. Figure K–65 shows the variation of transverse displacement with transverse shear fore. These figures show excellent agreement of the simplified model with the plate model.

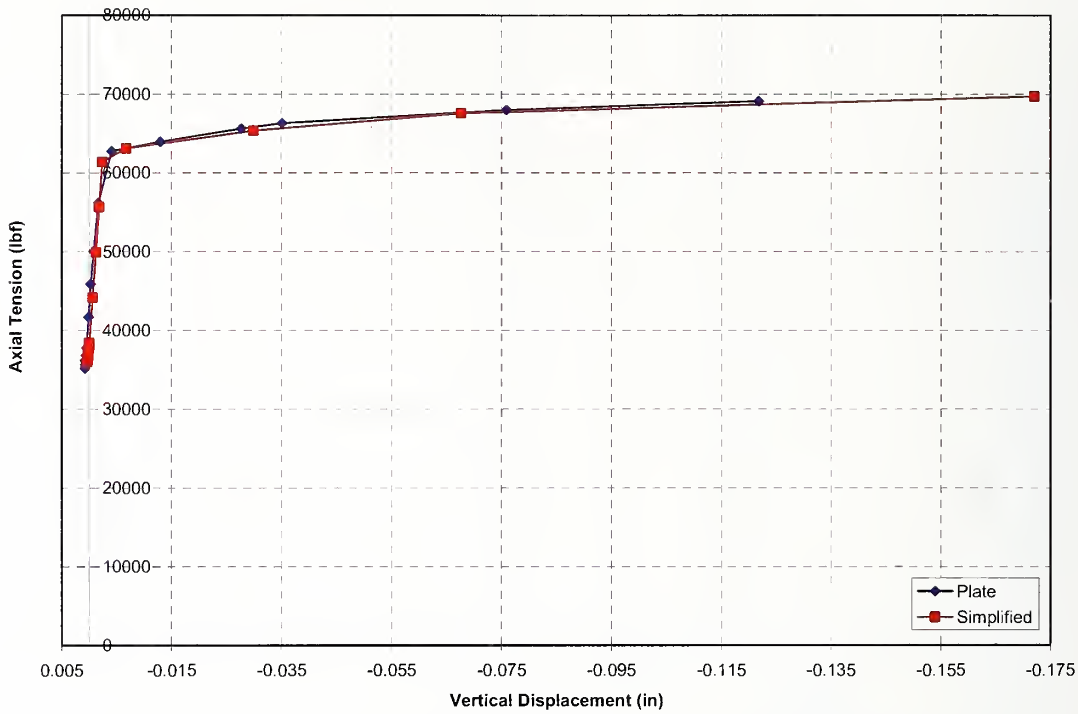

Figure K–64. Variation of axial displacement with axial load.

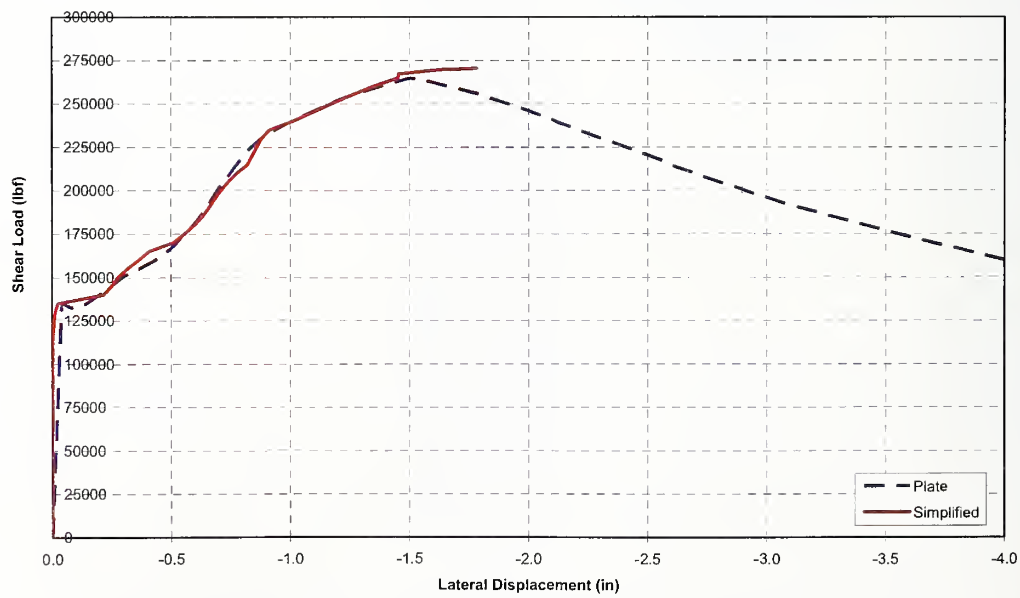

Figure K–65. Variation of lateral displacement with shear load.

Figure K–66 shows the rotation variation with out-of-plane of the wall moment. Figure K–67 shows the rotation variation with in-plane-of-the-wall moment. Figure K–68 shows the twist variation with torque. Figures K–66, K–67, and Fig. K–68 show large differences between the results of the simplified and plate models of the column splice. These differences are due to the fixed locations of pivot points in the simplified model, provided by pairs of CONTA178 point-to-point contact elements, about which the faying surfaces rotate. The CONTA174 and TARGE170 surface contact elements for the faying surfaces in the plate model permit the location of the pivot point to adjust to the demand of the applied moment. Adjusting the location of the point-to-point contact elements can minimize these differences, but they cannot be eliminated. In the exterior wall subsystem model, the locations of the single point contact elements in the column splices will be adjusted and the sensitivity of the response of the model results to these locations computed.

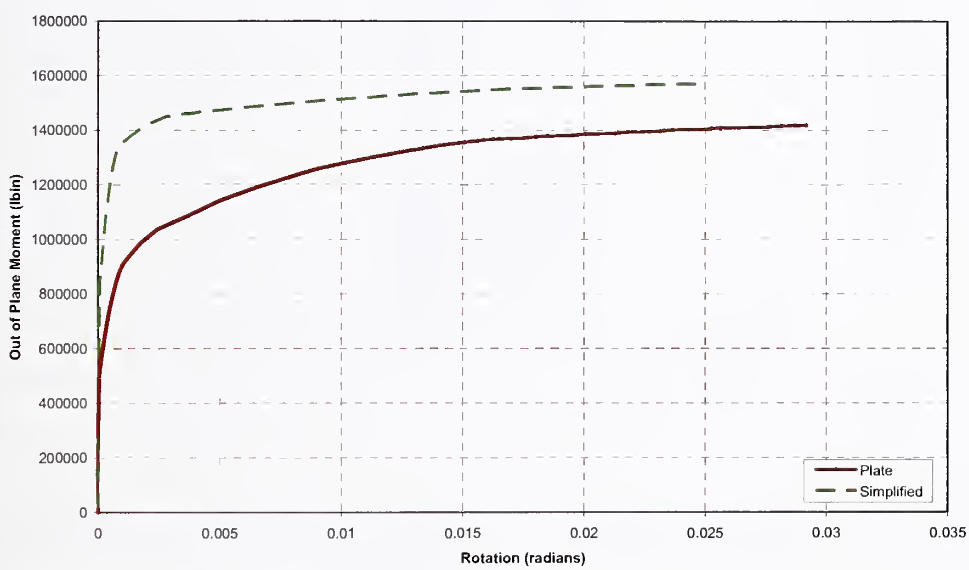

Figure K–66. Variation of rotation with moment, out of wall plane.

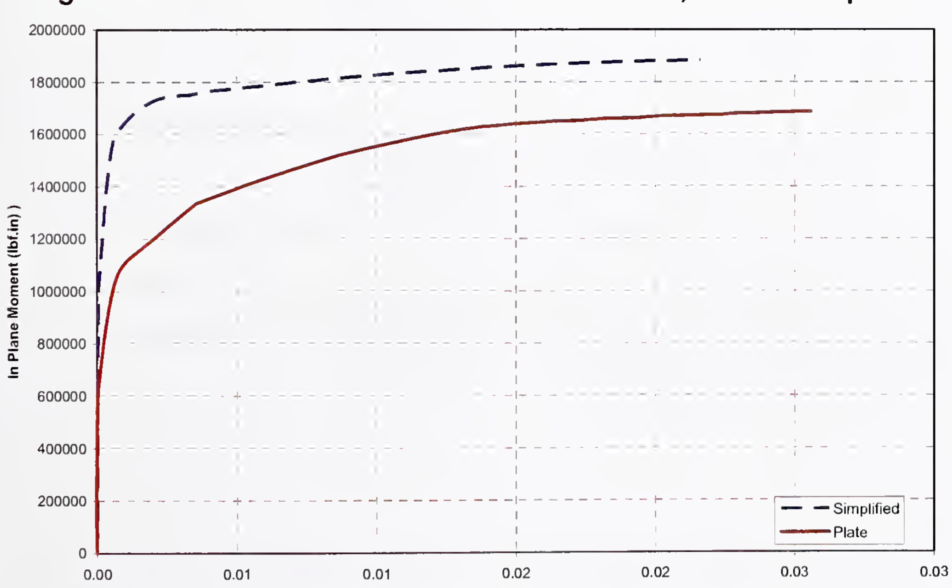

Figure K–67. Variation of rotation with moment, in plane of wall.

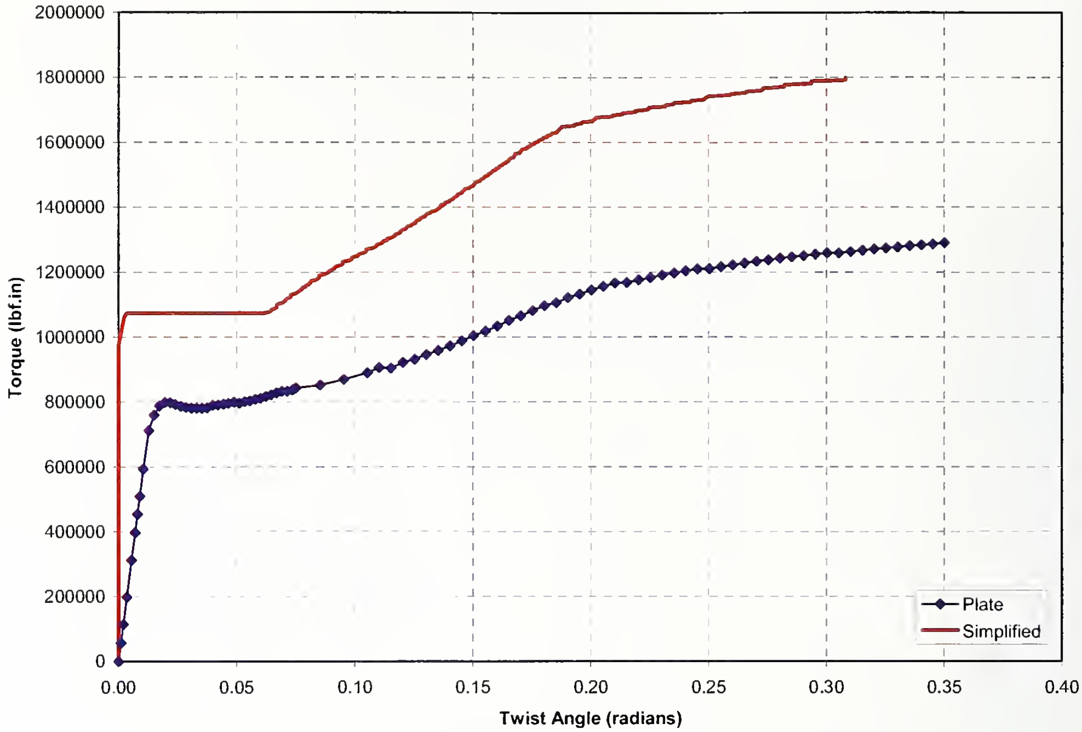

Figure K–68. Variation of twist angle with torque.

K.8.6 Prefabricated Panel Model

Description of Model

Figure K–69 shows the SAP2000 model of a typical prefabricated panel at floors 79 to 82. The model is modified as follows:

- Eliminated self-weight from loading conditions.
- Provided stiff members at the tops of the columns and replaced the four concentrated loads with a single concentrated load.
- Added out-of-plane of the wall supports (UY) at top of columns for out-of-plane loading.

Figure K–70 shows the ANSYS model for matching the behavior of the SAP2000 exterior wall subsystem model. In the ANSYS version of the panel model BEAM189 elements model the columns and MPC184 rigid elements attach the spandrels to the columns.

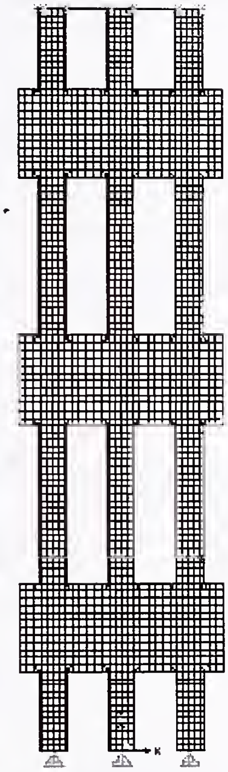

Figure K–69. SAP2000 model of prefabricated panel.

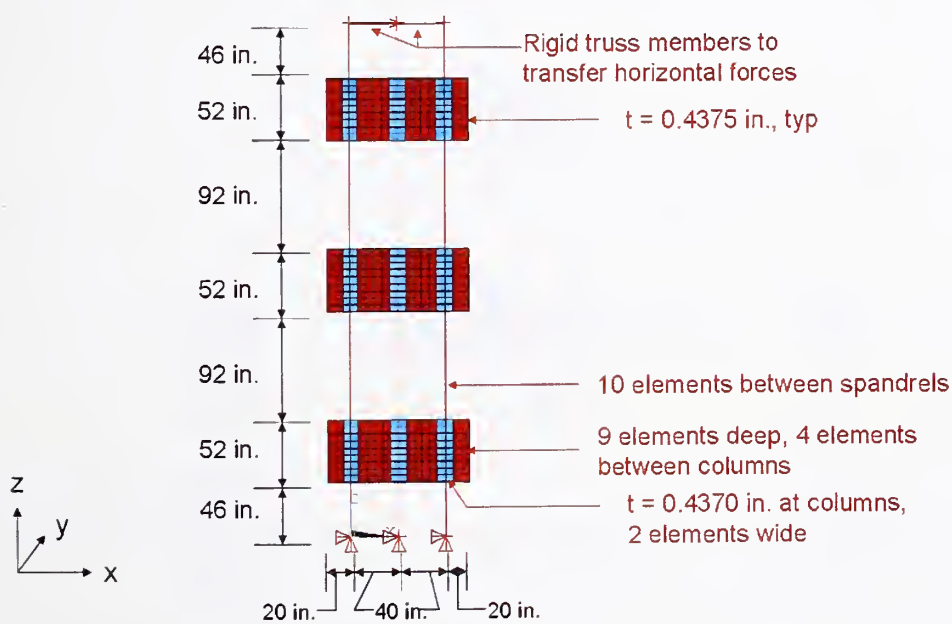

Figure K–70. ANSYS model of prefabricated panel showing geometry and number of elements used.

Both models are subjected to the following loadings at room temperature:

- A concentrated vertical load (FZ) at the top of one of the outside columns.
- A concentrated horizontal load in the plane of the wall (FX) at the top of one of the outside columns. The stiff members described above distribute this shear load evenly to the tops of all three columns.
- A concentrated transverse load (FY) on the middle column at floor 81.

The above loadings do not include self-weight. Figure K–71 shows the various loadings applied to the ANSYS model.

Simple supports in the plane and out of the plane of the wall (UX,UY) restrain the tops of the columns. Simple supports in all three directions restrain the bottoms of the columns. The spandrels at the extremities of the model are free. See Figure K–71.

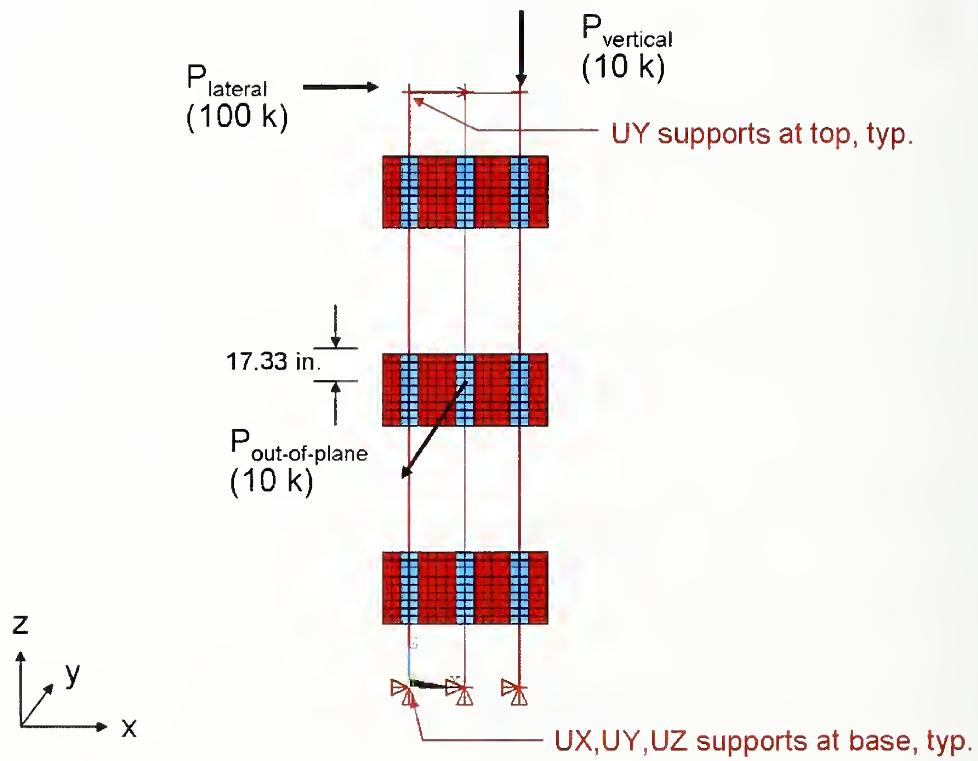

Figure K–71. ANSYS model of prefabricated panel showing loading and boundary conditions.

Validation Results

Figures K–72 through K–74 show deflected shapes and indicate the displacement at the points of applied load for the SAP and ANSYS models. Table K–17 summarizes the differences in reactions and displacements between the SAP and ANSYS models.

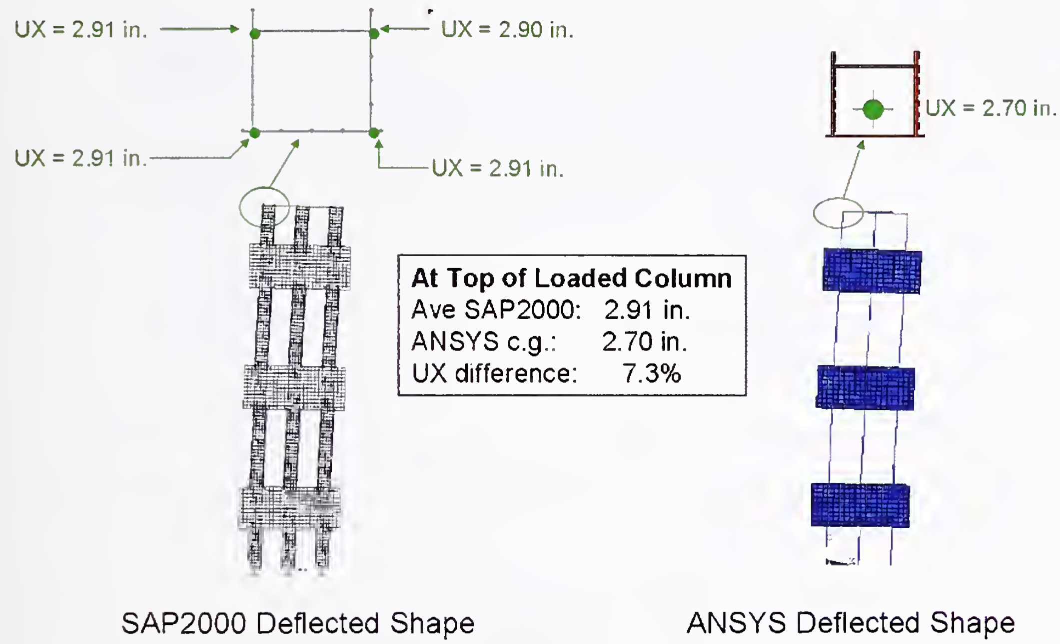

Figure K–72. Deflection of prefabricated panels under 100 kip lateral load.

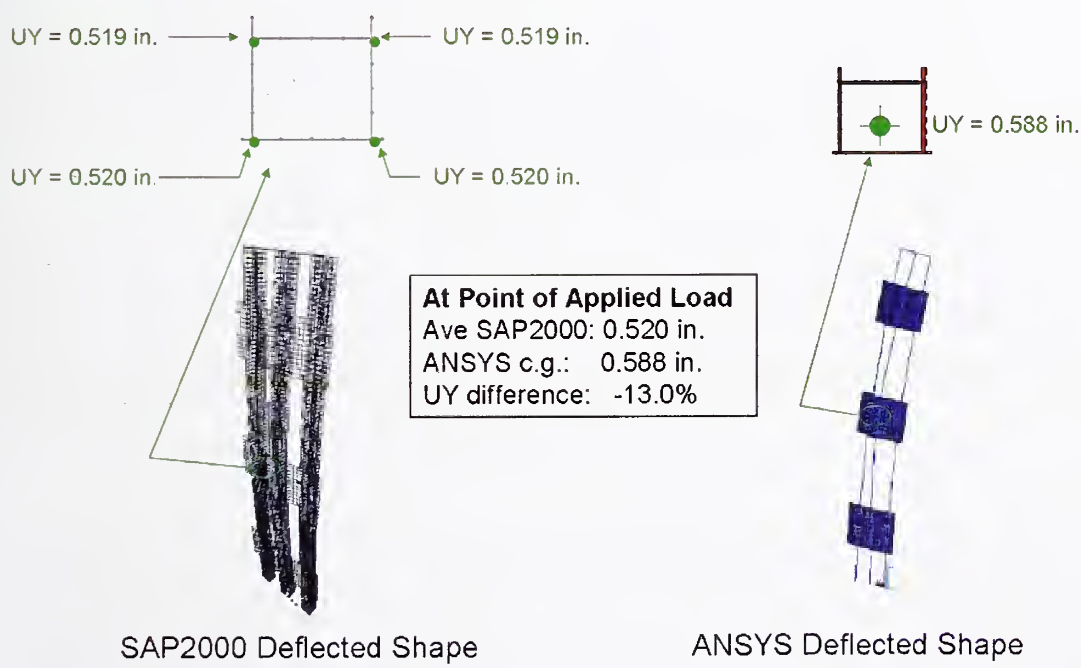

Figure K–73. Deflection of prefabricated panels under 100 kip transverse load.

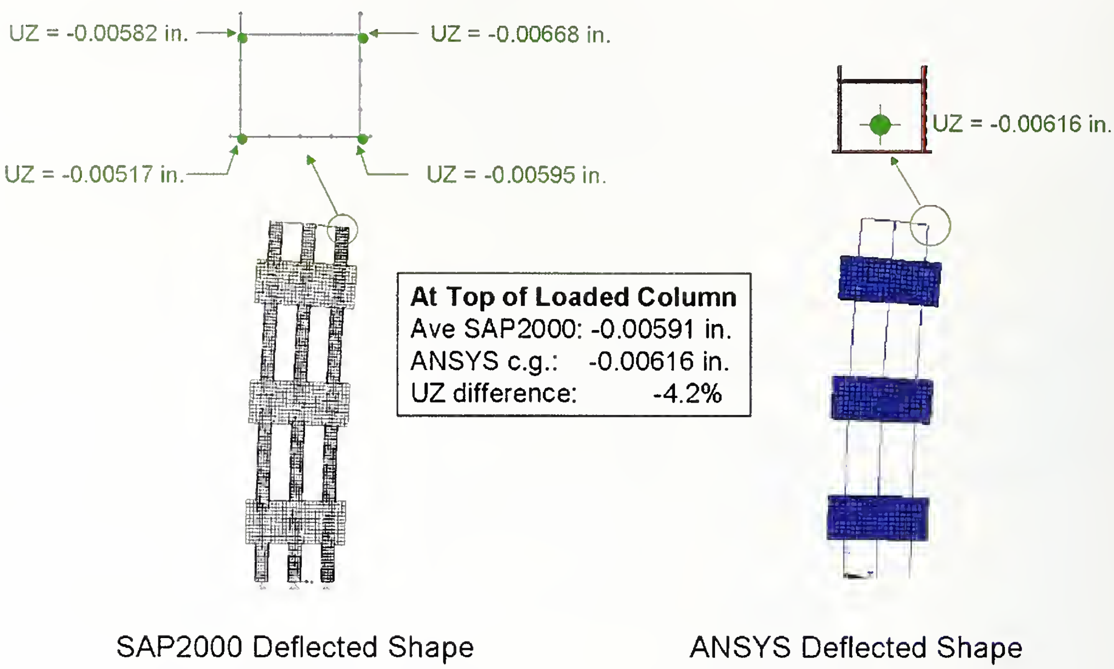

Figure K–74. Deflection of prefabricated panels under 10 kip vertical load.

Table K–17. Validation results.

Loading Condition	SAP2000/ANSYS Displacements[a] Difference Range	
Lateral FX	RX: -2 % to +1 %	UX: 7 %
Transverse FY	RY: -6 % to +7 %	UY: -13 %
Vertical FZ	RZ: -1 % to +2 %	UZ: -4 %

a. Displacements considered at tops of columns for FX and FZ, and at points of load application for FY.

K.8.7 Ongoing Work on the Exterior Wall Subsystem Model

The ongoing work includes the following:

- Stability of a two-story-high exterior column unbraced at the middle floor.
- Stability of a three-story-high exterior column braced at the top and bottom floor levels only.
- Stability of nine-story-high exterior column (floor 92 to 100) unbraced at floors 96 and 97 and subjected to fire scenarios.
- Response of exterior wall model to fire scenarios

K.9 FLOOR TRUSS DYNAMIC RESPONSE DUE TO IMPACT OF DROPPING FLOOR

K.9.1 Impact of Dropping Floor

The failure of dropping floor may occur due to thermal response and/or additional debris weight on the truss, and/or as a result of the aircraft impact. A floor truss or a group of floor trusses could lose support at both the exterior and interior supporting ends and drop onto the floor below. This failure mode, which is shown in Fig. K–75, will be referred to as "full truss drop." Alternatively, a floor truss or a group of floor trusses could lose support on one side and drop down to impact the floor below. This failure mode, which is also shown in Fig. K–75, will be referred to as "partial truss drop."

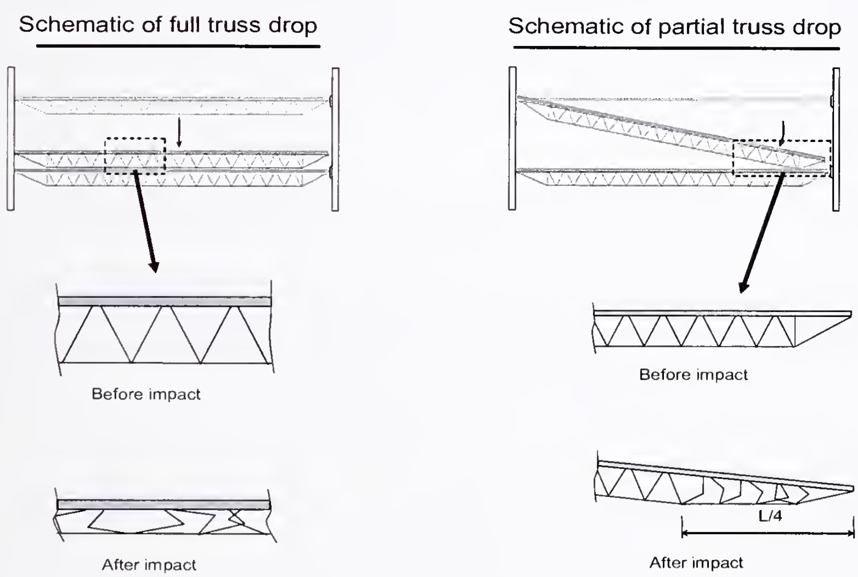

Figure K–75. Schematic of full truss or partial truss drop and diagonal crushing at impact.

K.9.2 Purpose and Scope

The purpose of this study is to determine the dynamic response of the target truss from the impact of full and partial truss drop, to determine whether the target truss seats can resist such an impact load and to determine whether the target truss will lose its composite action, become a catenary, and thus fail to restrain the exterior column to which it is connected against instability.

K.9.3 Method of Analysis

The simulation of a floor drop is idealized with a truss drop. This has the inherent assumption that all seats for the floor fail simultaneously to cause a full or partial drop. The dynamic response of the target truss from the impact of a dropping truss is calculated using conservation of energy principle. The potential energy of the truss just before drop, which is a function of drop height, converts to the kinetic energy of the truss just before impact. As the dropping truss starts to impact the target truss, the diagonal members of the dropping truss are assumed to deform plastically to absorb some of the kinetic energy.

The energy absorption due to crushing of the furniture and partitions are neglected in this study. The energy absorption due to diagonal member crushing reduces the kinetic energy available at impact to deform the target truss. All the diagonal members are assumed to deform plastically for the full truss drop case, while only one quarter of the diagonal member are assumed to deform plastically for partial truss drop, representing one quarter of the length of the truss that may come in contact at impact with floor below. The kinetic energy loss at the time of impact of the dropping truss and the target truss is calculated based on conservation of momentum. The two trusses are assumed to travel together after the impact, at one-half of the velocity of the dropping floor before impact.

The dynamic load due to the impact of the dropping truss onto the target truss will result in the target truss to deform plastically beyond the static load due to the weight of the two trusses. The maximum dynamic deformation of the trusses is calculated by conservation of energy principle assuming that the resistance of the truss is a bilinear function of displacement. This assumption is based on fitting the FEA calculated acceleration-deflection relationship of target truss as shown in Fig. K–76.

K.9.4 Results

The ratios of demand-to-seat capacity for the gravity loads of the dropped and impacted trusses moving together for temperatures of 20 °C, 400 °C, 600 °C, and 700 °C; and the gravity plus dynamic impact loads for temperatures of 20 °C and 400 °C, are calculated. The demand-to-capacity ratio of less than one shows that the truss seat has sufficient capacity to resist the load, and the demand-to-capacity ratio of larger than one, implies that the seat could fail. The range of the demand-to-capacity ratios are due to the different assumptions for the amount of energy loss due to crushing of the diagonal members of the dropped truss.

The demand-to-capacity ratio of the long-span truss for gravity loads is shown in Table K–18 and for gravity plus impact load is shown in Table K–19. The result for gravity load alone shows that both the exterior and interior truss seats have sufficient capacity to support the weight of two floors for all temperatures considered. The result for gravity plus impact load shows that at temperatures below 400 °C neither the exterior nor interior truss seat is expected to fail. Peak deflection response due to gravity and the dynamic impact of the dropping truss is given in Table K–20. The results show that at room temperature, and more so at 400 °C, the impacted truss will deflect to an extent that it loses composite action, and become a catenary. At 400 °C the truss walks off the interior seat. Obviously, a catenary truss is not able to restrain the exterior column against transverse movement and cannot restrain it from instability. Although a truss response to increasing acceleration at 700 °C has not yet been developed, the strength reduction of the truss seats clearly indicates that the failure of truss seats will occur. The results for long-span truss, for partial truss drop, and for the short-span truss are in progress.

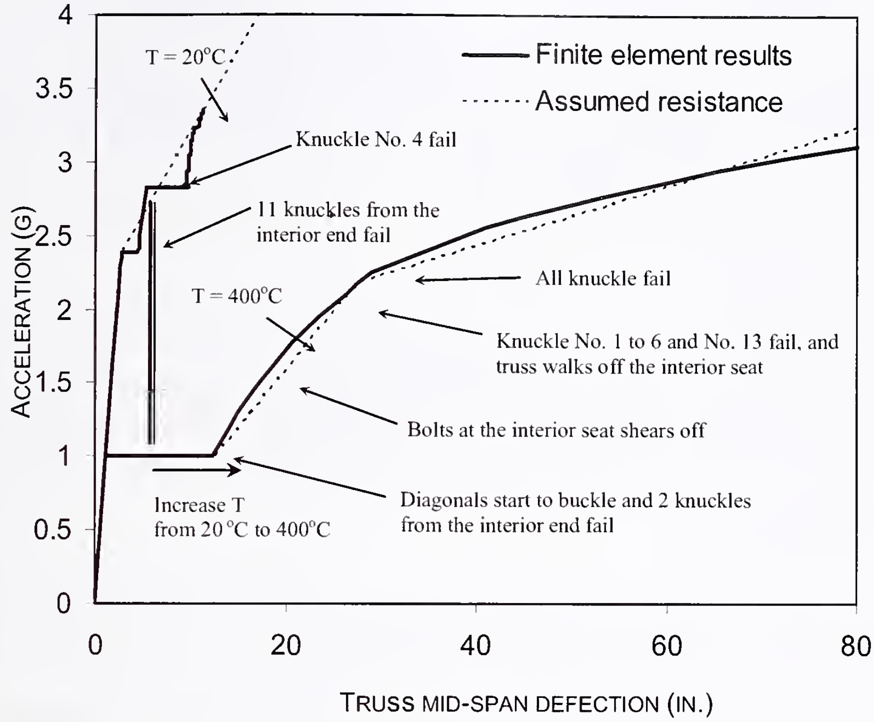

Figure K–76. Target truss resistance against increasing acceleration.

Table K–18. Demand-to-Capacity ratio of long-span truss for static gravity load.

Temp. (°C)	Demand (kip)	Capacity (kip)		Demand/Capacity	
		Int. Seat	Ext. Seat	Int. Seat	Ext. Seat
20	26.4	187.3	140.0	0.14	0.19
400	26.4	166.9	125.7	0.16	0.21
600	26.4	81.6	77.8	0.32	0.34
700	26.4	37.2	35.5	0.71	0.74

Table K–19. Demand-to-Capacity ratio of long-span truss for dynamic impact load from full truss drop.

Temp. (°C)	Demand (kip)	Capacity (kip)		Demand / Capacity	
		Int. Seat	Ext. Seat	Int. Seat	Ext. Seat
20	38.6 - 65.3	187.3	140.0	0.21 - 0.35	0.28 - 0.47
400	39.1 - 45.2	166.9	125.7	0.23 - 0.27	0.31 - 0.36

Table K–20. Peak deflection response due to static gravity and dynamic impact.

Temp. (°C)	Static Deflection (in.)	Dynamic Deflection (in.)		
20	2.3	7.6	-	25.4
400	24.2	66.4	-	89.6

K.9.5 Conclusions

At room temperature, the impact of a dropping truss will not cause failure of truss seats, but will cause the impacted truss to deform into a catenary. At 400 °C, the impacted truss will walk off the interior seat. In either case, the impacted floor will not restrain the exterior column against transverse movement and instability. The impact of a dropping truss at 700 °C will cause failure of truss seats.

K.10 REFERENCES

ACI (American Concrete Institute) Committee 209. 1992. "Prediction of Creep, Shrinkage, and Temperature Effects in Concrete Structures", ACI 209R–92.

AISC (American Institute for Steel Construction). 2001. Manual of Steel Construction: Load and Resistance Factor Design, 3rd ed.

AISC (American Institute for Steel Construction). 2003. Manual of Steel Construction, Load and Resistance Factor Design.

ANSYS, Inc. 2004. Theory Reference, ANSYS, Inc.

ASTM (ASTM International). 2001. "Standard Test Methods for Fire Tests of Building Construction and Materials," ASTM Standard Test Method E119.

Bartlett, F.M. and MacGregor, J.G. 1996. "Statistical Analysis of the Compressive Strength of Concrete in Structures," ACI Materials Journal, March–April, pp. 158–168.

Fields, B.A. and Fields, R.J. January 1991. The Prediction of Elevated Temperature Deformation of Structural Steel Under Anisothermal Conditions, NIST.

Fields, R. March 22, 2004. Recommended Multiaxial Fracture Criterion, NIST.

LERA (Leslie E. Robertson Associates). 2001. The World Trade Center Design Criteria. Worthington, Skilling, Helle, and Jackson, original document dated 8/20/65.

LERA (Leslie E. Robertson Associates). August 2003. Development of Structural Databases and Baseline Models for the World Trade Center (WTC) Towers–Progress Report #4: Structural Analysis Computer Models.

Phan, Long T. December 1996. Fire Performance of High-Strength Concrete: A Report of the State-of-the-Art, NIST.

Phan, Long T. December 2003. Properties of Concrete at Elevated Temperature, NIST.

Seanz, L.P. 1964. "Discussion of Equation of the Stress-Strain Curve of Concrete by Desayi and Krishman," Journal of the American Concrete Institute, Col. 61, No. 9, pp. 1229–1235.

SHCR (Skilling, Helle, Christiansen, Robertson). 1973a. World Trade Center Drawing Book 8, Concrete Reinforcing, Chapters 1-4.

SHCR (Skilling, Helle, Christiansen, Robertson). 1973b. World Trade Center Drawing Book 7, Floor Panels and Truss Details, Chapters 1-5.

Stevick, G.R. March 1994. "Failure of Welds at Elevated Temperatures," Welded Research Council Bulletin 390, Welding Research Council, pp. 1–39.

This page intentionally left blank.

TABLE OF CONTENTS

LIST OF FIGURES

LIST OF TABLES

Appendix L
INTERIM REPORT ON WTC 7

L.1 BUILDING DESCRIPTION

L.1.1 Purpose

Project 6 addresses the first primary objective of the technical investigation led by the National Institute of Standards and Technology (NIST) of the 47-story World Trade Center (WTC) disaster: to determine why and how WTC 7 collapsed. Specifically, the objective of this Project is to determine the response of structural components and systems to the impact damage and fire environment in WTC 7, and to identify probable structural collapse mechanisms.

L.1.2 Scope of Work

The structural response of WTC 7 to damage from debris and fires is being evaluated to identify possible collapse sequences and critical components that are consistent with the videographic and photographic records, interview accounts by individuals that were in or around WTC 7, and other available data. This work is being conducted in two tasks:

- Task 1, Structural response analysis to identify critical components
- Task 2, Structural analysis of possible collapse initiation hypotheses

The analytical work is being conducted with the assistance of Gilsanz Murray Steficek LLP.

The scope of work under Task 1 includes (a) develop a nonlinear global structural model of WTC 7 and evaluate its performance under design gravity loads, (b) identify credible failure sequences for the structural model with service loads and initial structural damage by analyzing the effect of component failures (that may have occurred directly or indirectly from fires) on the structural system stability, (c) identify dominant failure modes for critical components and subsystems determined in (b) for service loads and elevated structural temperatures, (d) conduct parametric studies of critical subsystems to identify influential parameters, and (e) develop approaches to simplify structural analyses for global modeling and analyses.

Selected technical results and finding for progress on Task 1 (a), (b), and (c) are presented in the following sections: a description of the WTC 7 structural design, observations of damage, fires, and the structural collapse, and the working collapse hypothesis developed to date.

L.1.3 Introduction

WTC 7 was a 47 story commercial office building, completed in 1987. Its location relative to the WTC Plaza is shown in Fig. L–1. It contained approximately 2 million ft^2 of floor area. The overall dimensions of WTC 7 were approximately 330 ft long, 140 ft wide, and 610 ft tall. The typical floor was similar in size to a football or soccer field (see Fig. L–2). The gross floor area was about 75 percent of that contained in the Empire State Building. The building was constructed over a pre-existing electrical substation owned by Con Edison. The original plans for the Con Ed Substation included supporting a high-rise building, and the foundation was sized for the planned structure. However, the final design for WTC 7 had a larger footprint than originally planned. Section L.1.4 describes the WTC 7 foundation.

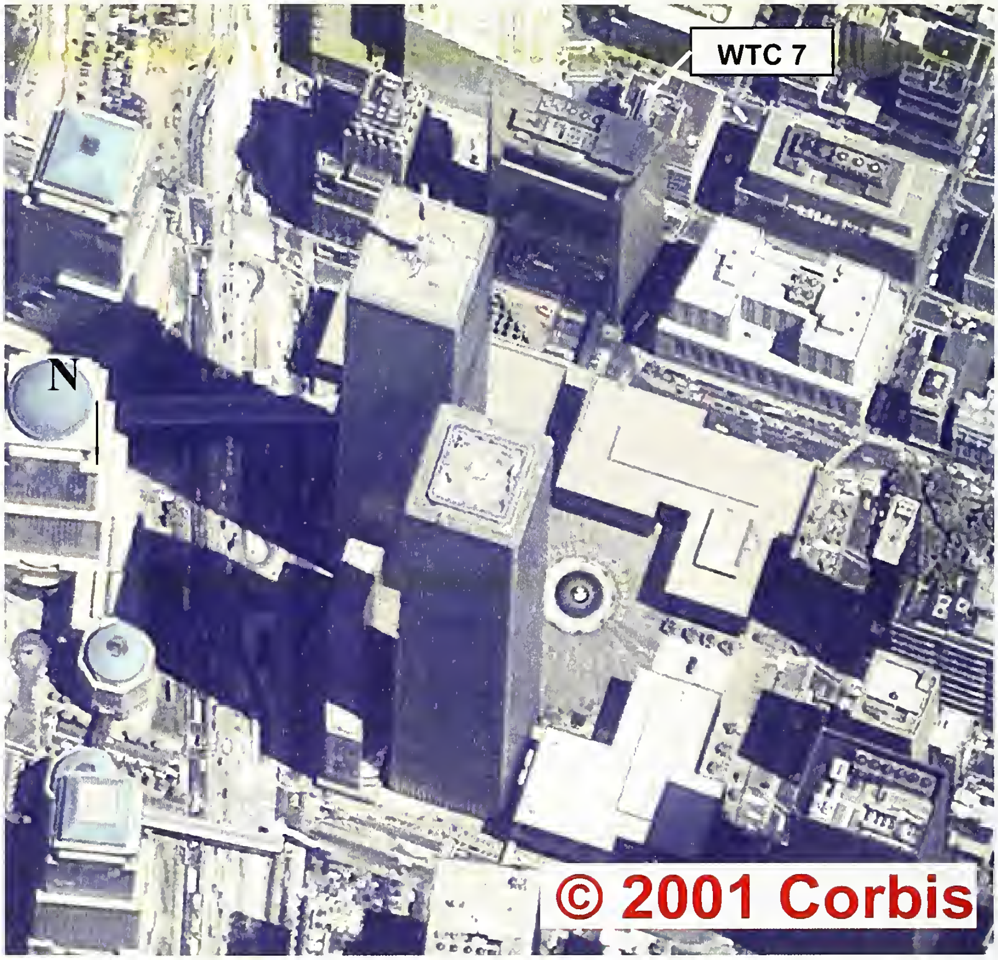

Figure L–1. WTC complex.

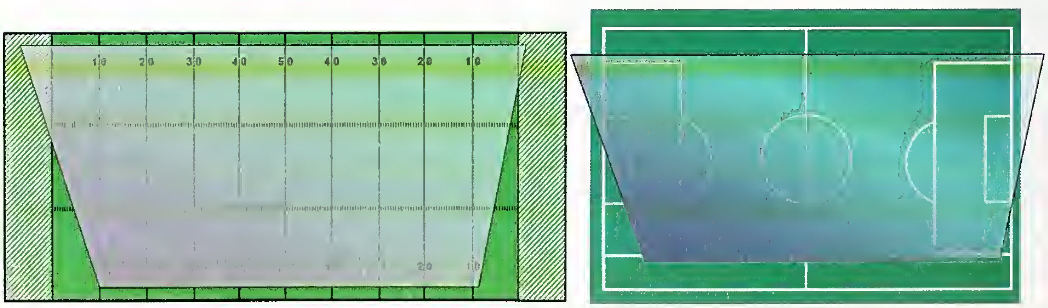

A. Comparison to Football Field B. Comparison to Soccer Field

Figure L–2. Size comparison of WTC 7.

WTC 7 was located immediately to the north of the main WTC Complex, approximately 350 ft from the north side of WTC 1. It occupied the block bounded by Vesey Street on the south, Barclay Street on the north, Washington Street on the west, and West Broadway on the east. It was connected to the WTC complex with a 120 ft wide elevated plaza at the Floor 3, and a 22 ft wide pedestrian bridge, also at Floor 3.

Above Floor 7, the building had typical steel framing for high-rise construction. The floor systems had composite construction with steel beams supporting concrete slabs on metal deck, with a floor thickness of 5.5 in. The core and perimeter columns supported the floor system and carried their loads to the foundation. The perimeter moment frame also resisted wind forces. Columns above Floor 7 did not align with the foundation columns, so braced frames, transfer trusses, and transfer girders were used to transfer loads between these column systems, primarily between Floors 5 and 7. Floors 5 and 7 were heavily reinforced concrete slabs on metal decks, with thicknesses of 14 in. and 8 in., respectively. The following sections describe the components and subsystems of WTC 7.

L.1.4 Foundations

WTC 7 and the electrical substation were supported on caisson foundations. When the substation was constructed in 1967, provision was made for a future office tower by including capacity to carry both the substation and the weight of a future building. Caissons were also installed in the property adjacent to the substation, for the proposed future building. When WTC 7 was constructed approximately 20 years later, it was significantly larger than the originally proposed building, and required additional caissons to be installed, as shown in Fig. L–3.

The typical caisson consisted of several components: a 30-in., 36-in., or 42-in. diameter steel casing, a heavy rolled or built-up steel core shape, vertical reinforcing bars, spiral rebar, and concrete fill. At the base of the caisson core, a pattern of shear studs was placed to help transfer the load from the steel caisson core into the encompassing concrete, from which it passed into the rock. The caissons extended through the soil, and were socketed (seated) in the bedrock, approximately 60 ft below the surface. There were vertical caissons as well as battered (or sloped) caissons to carry the lateral load. Above the caissons were heavy grillages composed of built up steel girders. Grillages transferred loads between the building columns and the caissons.

The distance between the caisson grillages and the first floor varied between 8 ft and 30 ft. This region was braced by reinforced concrete walls with thicknesses varying from 1 ft to 2.5 ft. Many of the WTC 7 steel columns were embedded in these walls, and supporting steel braces were made composite by the addition of shear studs along the height of embedment.

Areas between the concrete walls were backfilled with compacted gravel fill and then covered with a concrete slab on grade or framed slab to form closed cells and bring the structure up to the required elevation. In some cases, the area was left unfilled and used to house fuel tanks.

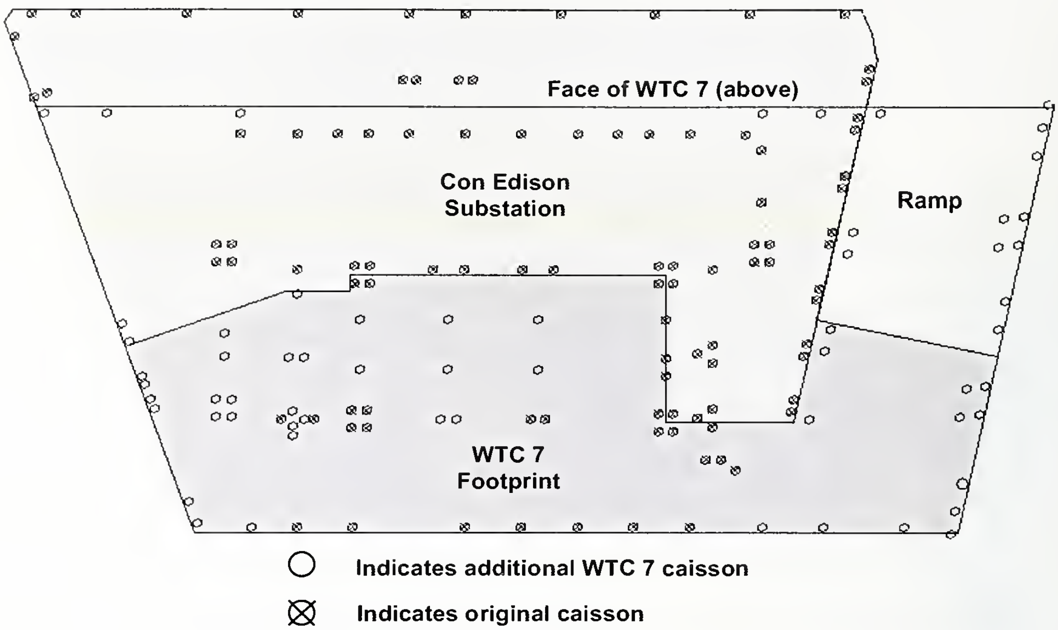

Source: McAllister 2002.

Figure L–3. WTC 7 to foundations.

L.1.5 Con Edison Substation

The Con Ed Substation was constructed in 1967 and consisted of a steel framed structure with cast-in-place concrete floors and walls. It was placed on the northerly portion of the site and extended approximately 40 ft north of the north facade of WTC 7, as shown in Fig. L–4. Its southerly boundary was irregular, but extended approximately one-third to two-thirds of the width of WTC 7. The Con Ed Substation was three stories in height.

The substation's lateral system consisted of a moment frame along the northern row of interior columns. Along the south edge of the substation there was a braced frame. This braced frame was coincident with the north side of the WTC 7 core, at columns 64, 67, 70, and 73. Lateral loads from WTC 7 were passed directly from the core above to the Con Ed braced frame below. There were also two moment frames within the substation oriented in the north-south direction, one on each end of the WTC 7 core.

The WTC 7 columns, which were within the perimeter of the substation, were supported by substation columns. During the construction of WTC 7, heavy plates were welded to the tops of the existing substation columns which then received the new building columns.

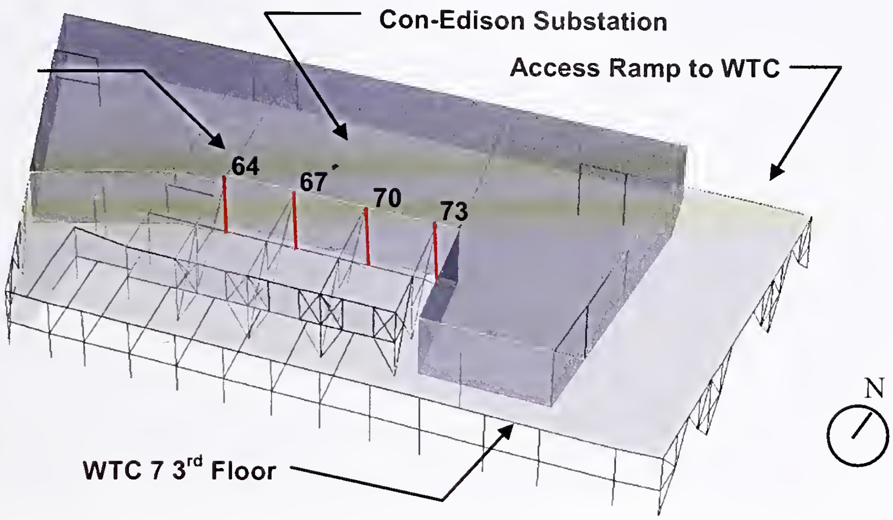

Figure L–4. Con Ed substation location relative to the WTC 7 building.

L.1.6 Floor Systems

Typical Floor Systems Above Floor 7

The typical floor framing system, shown in Fig. L–5, was composed of rolled steel wide-flange beams with composite metal decking and concrete slabs. Floors 8 through 45 had essentially the same framing plan, but the core layout varied over the height of the building.

Floors 8 through 45 had floor slabs that were composed of 3 in., 20 gage metal deck with 2.5 in., 3,500 psi normal weight concrete, for a total thickness of 5.5 in. There was one layer of 6x6 W1.4xW1.4 welded wire mesh within the concrete. The drawings show a second layer of mesh placed over girders at the slab edges. The fastening requirements for the metal deck are not shown on the drawings, but standard practice provides puddle welds 12 in. on-center at the beams and side lap welds, screws, or button-punching at 36 in. on-center between adjacent panels of deck. The drawings contain a note calling for 1.5 in., 20 gage deck with 4 in. concrete topping (5.5 in. total) in the elevator lobbies, where there was a 3 in. floor finish specified by the architect.

Typical floor framing for Floors 8 through 20 and Floors 24 through 45 consisted of 50 ksi wide-flange beams and girders. Between the core columns was a grid of beams and girders. Core girders ranged in size from W16x31 to W36x135, depending on the span and load. (W16x31 describes a steel wide-flange beam, sometimes referred to as ‘I’ beams; the nomenclature indicates the cross-section is nominally 16 in. deep and weighs 31 lb per lineal foot.) Beams spanned directly between the core and the exterior of the building, at approximately 9 ft on-center spacing. On the north and east sides, the typical beam was a W24x55 with 28 shear studs, spanning 53 ft. On the south side, the typical beam was a W16x26 with 24 shear studs spanning 36 ft. Between the exterior columns were moment connected girders that formed part of the lateral system of the building. On Floors 10, 19, and 20, a portion of the floor framing was

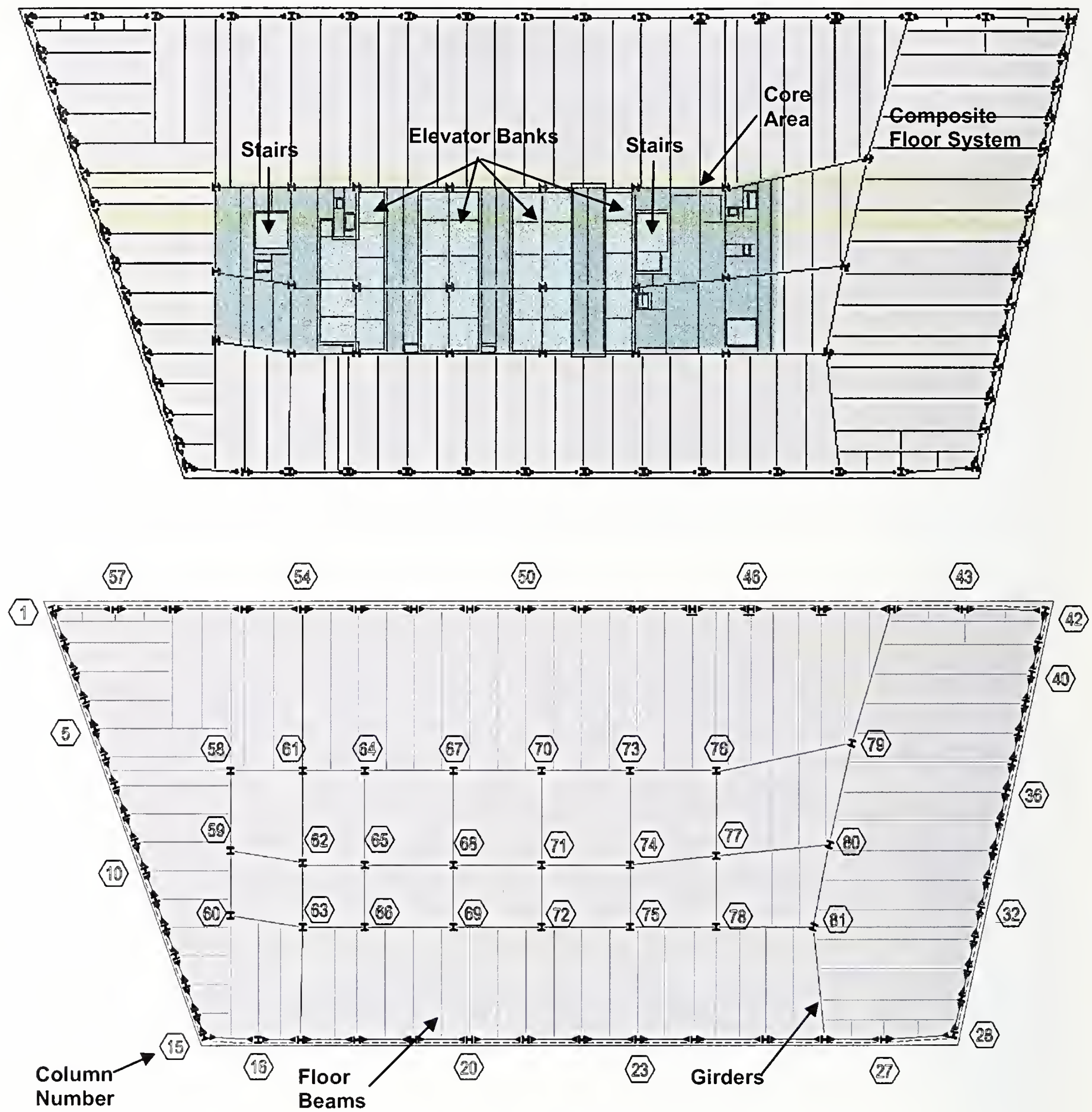

Figure L–5. Floors 8 to 45 plan.

reinforced with plates attached to the bottom flange. Certain connections at these floors were also reinforced.

Floors 21 to 23 had slightly heavier steel framing than the typical floors. Core girders were generally one size class larger than the typical floor; the beams between the core and the south facade were W16x31 instead of W16x26. There were additional studs on the W24x55 beams on the north and west sides.

Most of the beams and girders were made composite with the slabs through the use of shear studs. Typically, the shear studs were 0.75 in. in diameter by 5 in. long, spaced 1 ft to 2 ft on center. Studs were not indicated on the design drawings for many of the core girders. The design drawings specified design forces for connections and suggested a typical detail, but did not show specific connection designs; this is standard practice on the U.S. east coast. The erection drawings indicate that design shear forces for the typical beam and girder connections were to be taken from the American Institute of Steel Construction (AISC) beam design tables for beams without shear studs, using 1.5 times those forces for beams with shear studs.

According to a paper by Salvarinas (1986), who was the project manager for Frankel Steel, which fabricated the steel for WTC 7, the typical floor beam to girder and girder to core column connection was a single shear plate, although end plate and double angle connections were also used. The typical beam to exterior column connection was a seated connection. The typical bolt size for the simple shear connections is cited as 0.875 in. in diameter ASTM A325, where A325 is a standard specification for a structural bolt specified by ASTM International. The bolt size used for heavier brace and moment connections was 1 in. in diameter ASTM A490. Information on the specific connection details used is unavailable at this time.

Other Floors

The remaining floors, Floors 1 to 7 and Floors 46 to 47, were atypical and are described below and in Figs. L–6 through L–15.

Floor 1 was built adjacent to the substation and included the truck ramp for the WTC complex. The first floor is shown in Fig. L–6. The floor was framed with steel beams that were encased in a formed concrete slab. The floor slab was 14 in. thick, with typical #5 reinforcement bars (5/8 in. rebar) at a 10 in. to 12 in. spacing and #6 rebar at 9 in. spacing for the bottom reinforcement; #5 rebar at 12 in. spacing was used for temperature reinforcement. The southeast portion of the floor above the WTC truck ramp had a 6 in. formed concrete slab with #4 rebar at 12 in. spacing for top and bottom reinforcement; #4 rebar at 18 in. spacing was used for temperature reinforcement.

The floor slab for Floors 2, 3, 4, and 6 had a 3 in., 20 gage metal deck with 3 in. 3,500 psi normal weight concrete, for a total thickness of 6 in. Floors 2 and 3 were also partial floors adjacent to the substation. In addition, they had a floor opening on the south side to form the atrium above the ground level lobby (see Figs. L–7 and L–8). Floor 4 was above the substation and had a large opening over most of the south side of the building, to form a double-height space above the 3rd floor lobby (see Fig. L–9). Floor 6 had two openings on the floor to form a double-height mechanical space, one at the east side and the other one at the southeast corner (see Fig. L–12). Truss #2 and column 80 were located in this double-height mechanical space.

The 5th floor slab was 11 in. of 3,500 psi normal weight concrete on top of a 3 in., 18 gage composite metal deck for a total slab thickness of 14 in. The slab was heavily reinforced, with #7 rebar at 12 in. spacing for top reinforcement in both directions and #9 rebar at 12 in. spacing for bottom reinforcement that acted as additional diaphragm chord reinforcement in many areas. This floor also had 36 ksi steel WT sections (W, or wide-flange, sections cut in half to look like a 'T' section) embedded in the 11 in. concrete slab above the deck. The WT sections were designed to act as a horizontal truss within the plane of the floor between the perimeter and core columns (see Figs. L–10 and L–11).

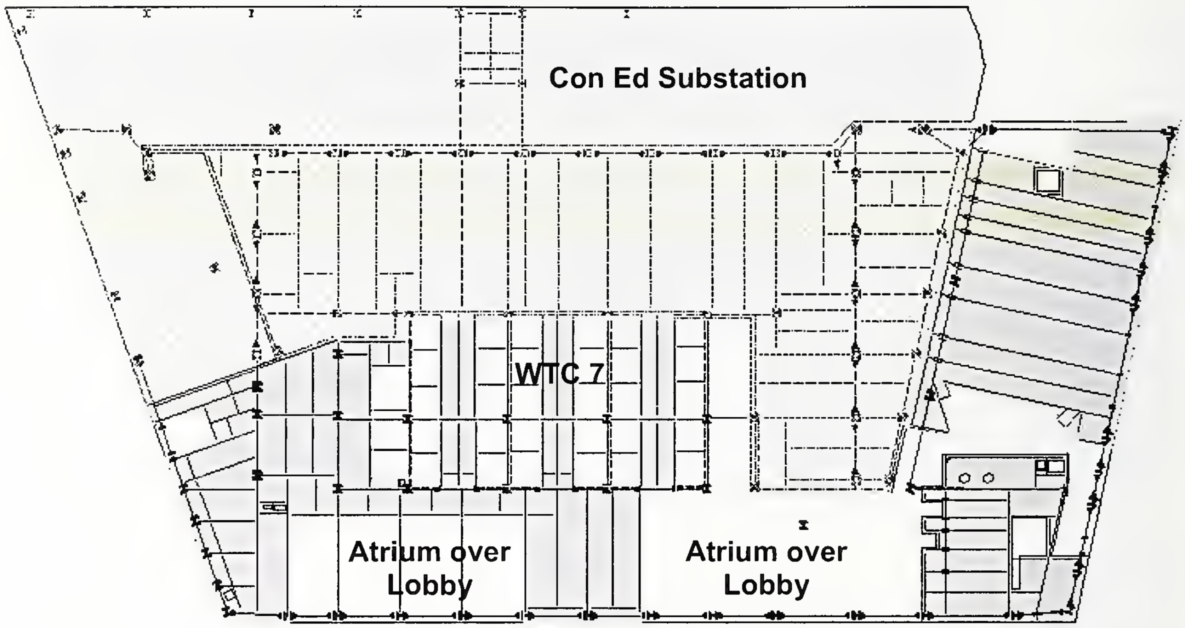

Figure L–6. Floor 1 plan.

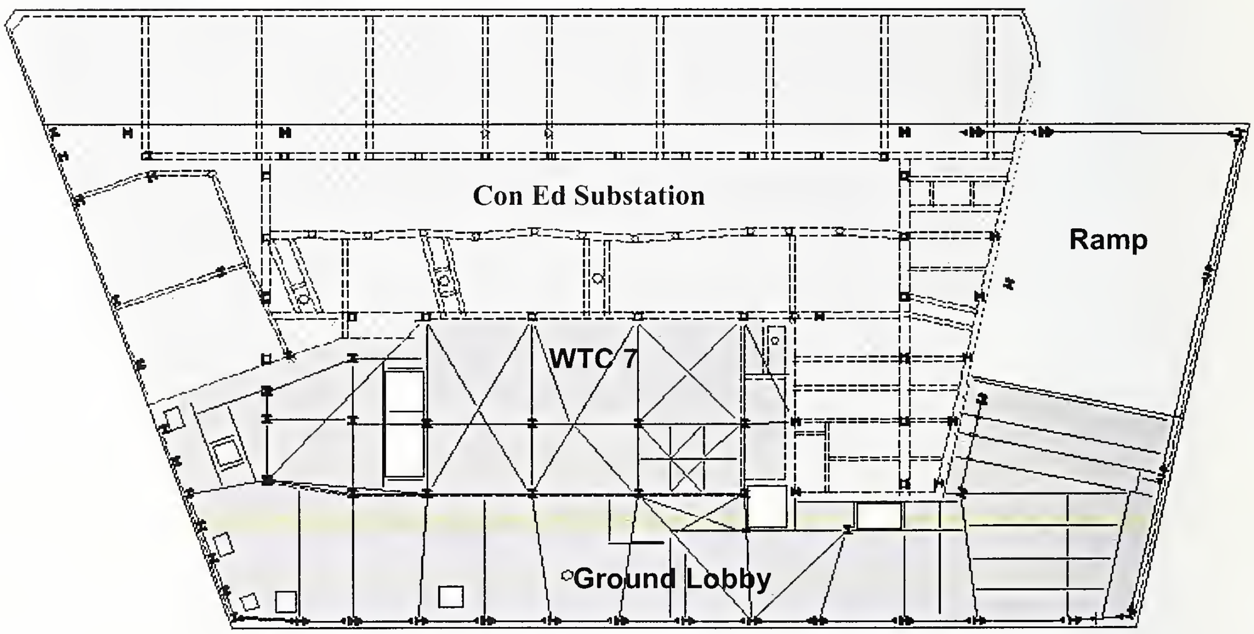

Figure L–7. Floor 2 plan.

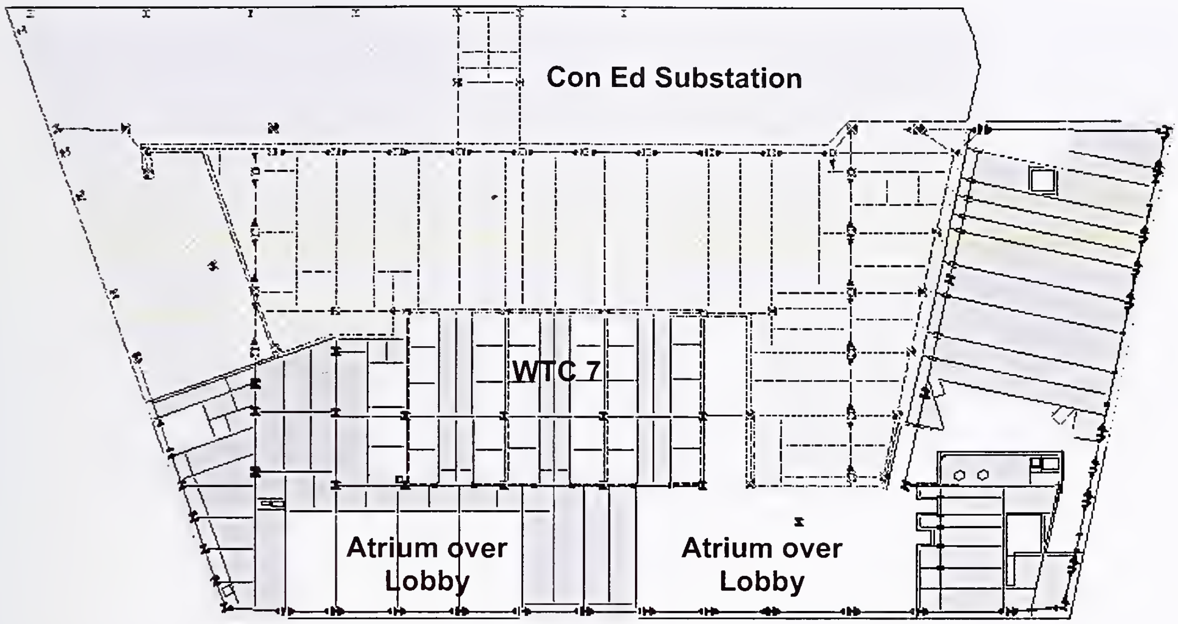

Figure L–8. Floor 3 plan.

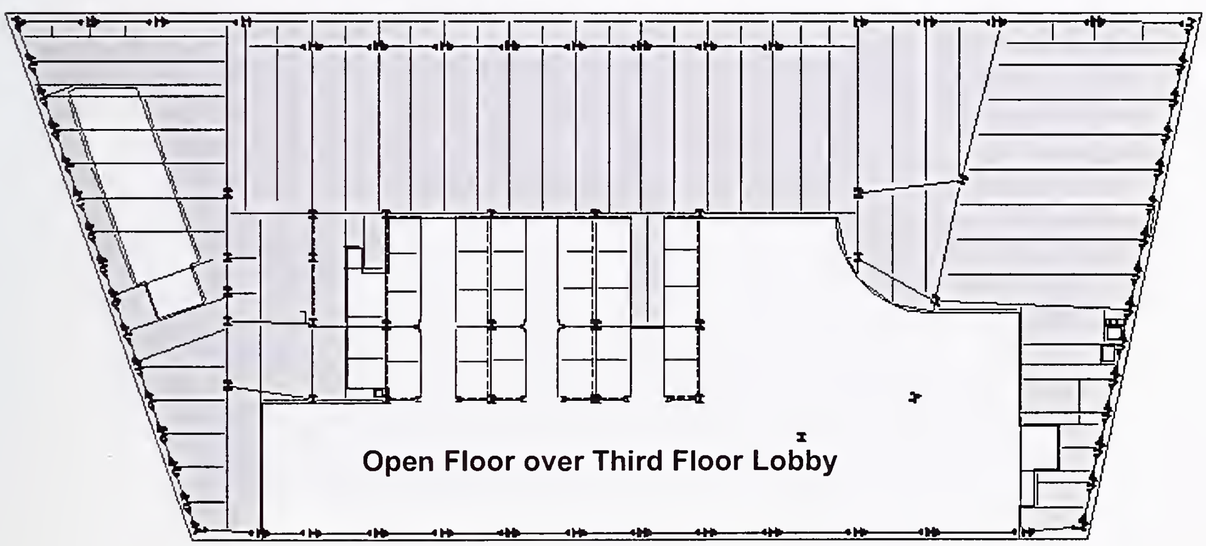

Figure L–9. Floor 4 plan.

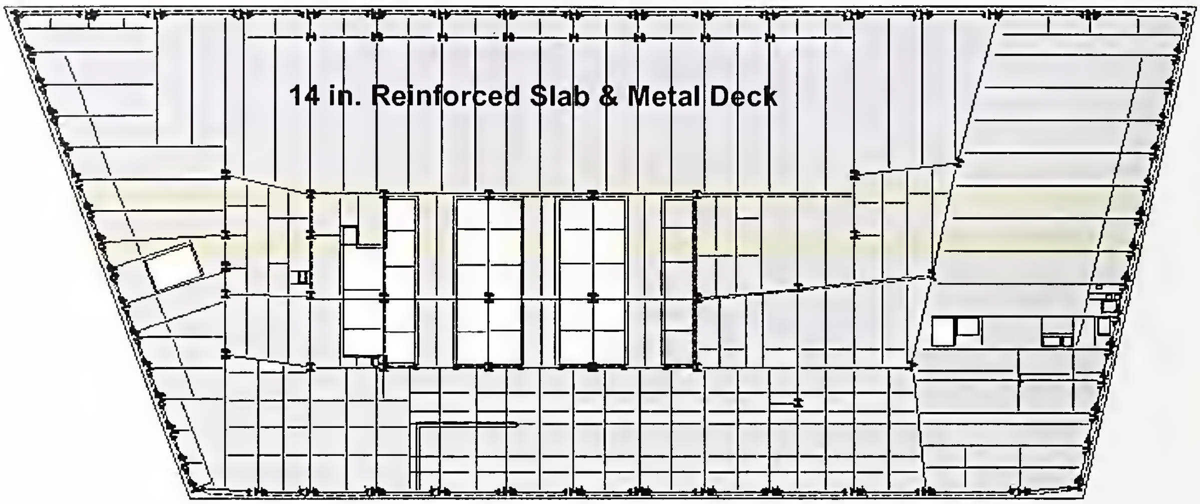

Figure L–10. Floor 5 plan.

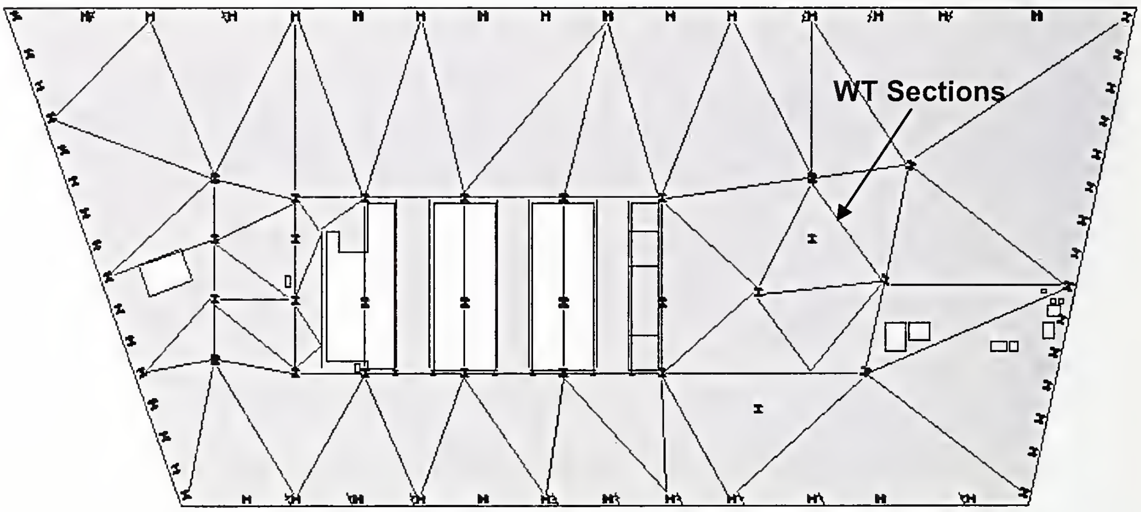

Figure L–11. Floor 5 diaphragm plan.

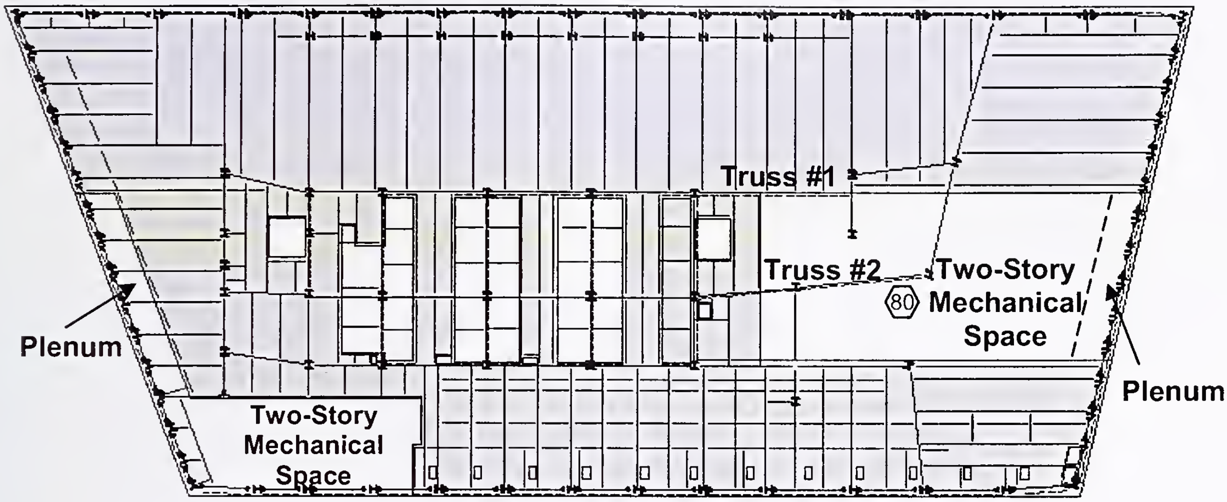

Figure L–12. Floor 6 plan.

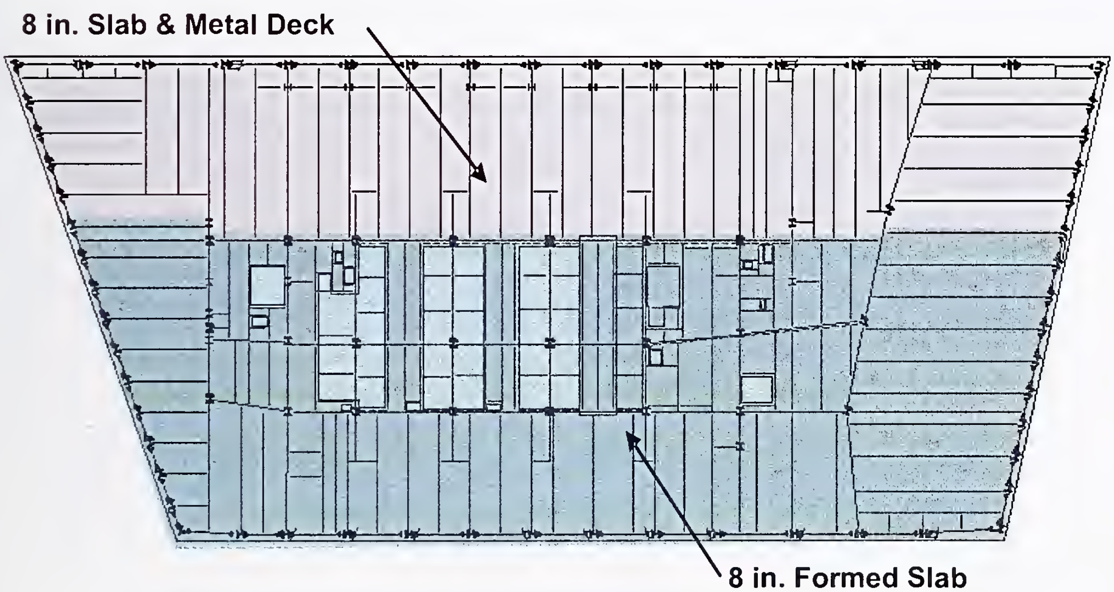

Figure L–13. Floor 7 plan.

The 7th Floor slab consisted of 5 in. of 3,500 psi normal weight concrete on top of 3 in., 18 gage composite metal deck, for a total thickness of 8 in. The slab was reinforced with #5 rebars at 6 in. on-center in both directions. Regions of the slab on the south side of the building had 8 in. of formed concrete without any metal deck. In these regions two layers of steel reinforcing were provided (see Fig. L–13).

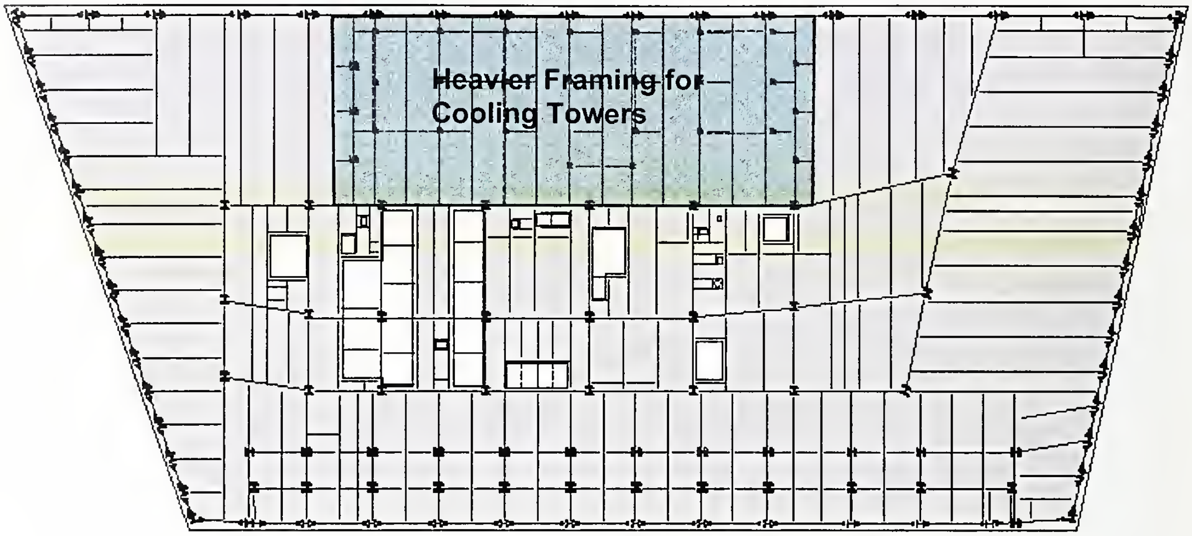

Figure L–14. Floor 46 plan.

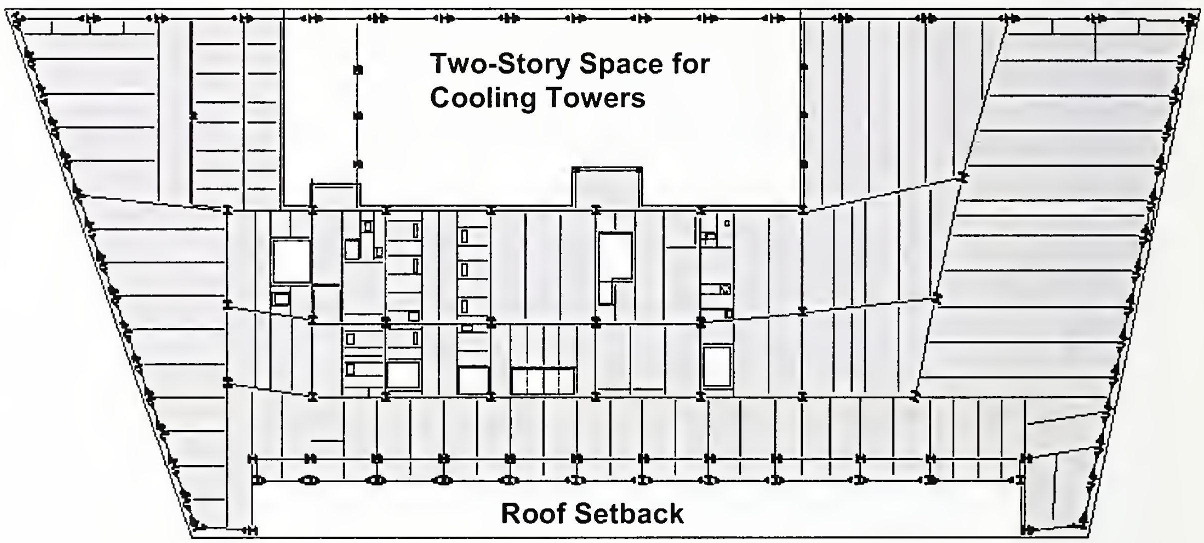

Figure L–15. Floor 47 plan.

Floors 41 and 43 had the east half removed to provide double height spaces. Columns in these areas and areas of Floors 40 and 42 had been reinforced to provide adequate capacity for the additional height and change in use by tenants. By 2001, Floors 41 and 43 had been reconstructed to provide full floor space. Specifics of this reconstruction are not available at this time.

The 46th Floor had heavier framing to support the cooling towers and dunnage on the north side, (alternating W36x150 with W36x260 under the posts) and the setback roof on the south side (alternating W21x44 with W36x150 under the posts). There was a 6 in. reinforced concrete slab in a portion of the core and under the cooling towers (see Fig. L–14).

Floor 47 had a double height space extending from the 46th Floor to the underside of the roof for the cooling towers on the north side. There was also a setback roof on the south side at Floor 46 (see Fig. L–15).

Roof and Penthouses

The roof had a concrete slab on metal deck, the top of which sloped 3 in., from an 8.5 in. thickness to a 5.5 in. thickness, to provide drainage. The wire mesh in this slab was 6x6 W2.4xW2.4, which was 70 percent heavier mesh than at the typical floor. There were slab openings for the cooling towers on the north and the setback roof on the south. The area above the cooling towers was framed in steel, with areas of grating spanning between the beams. A series of diagonal WT 6x9 members under the grating provided diaphragm action in this area. The east side of the floor was reinforced to carry the east penthouse and its contents. Specifics of this reinforcement are not available at this time.

The west penthouse roof was framed in steel with the floor slab increased to a 6 in. thickness. The framing and roof reinforcement for the east penthouse and the mechanical equipment screenwall are not available at this time. Layout of these areas has been determined from photographs, as shown in Fig. L–16.

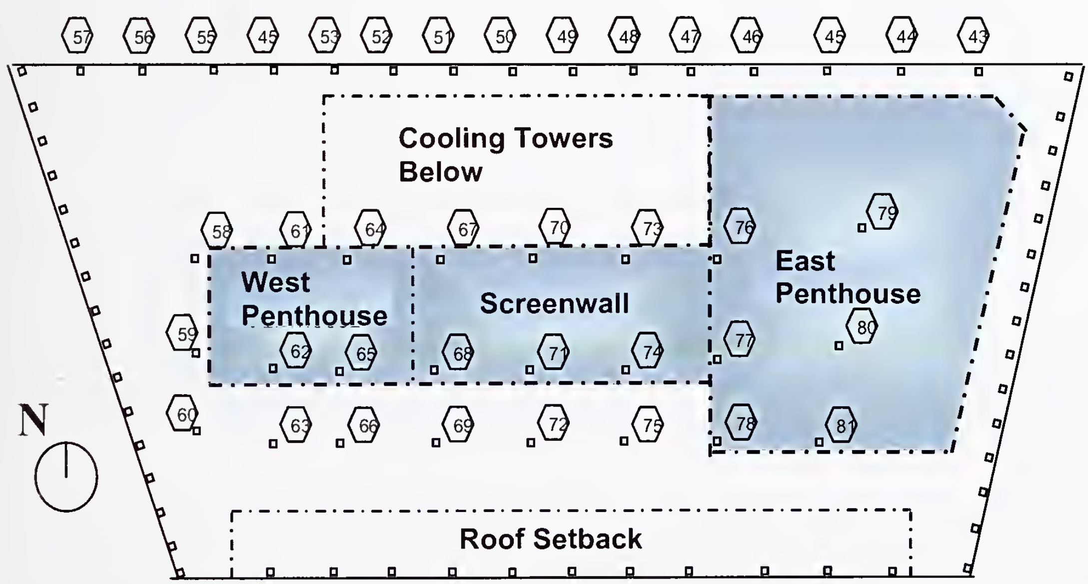

Figure L–16. Roof layout.

L.1.7 Columns

Core columns were primarily rolled wide-flange shapes of grade 36 or 50 steel. As the loads increased towards the base of the building, many of these column sizes were increased through the use of built-up shapes. These built-up columns had a W14x730 core with cover plates welded to the flanges (to form a box) or web plates welded between the flanges as shown in Fig. L–17. The reinforcing plate welds were specified to be continuous 0.5 in. fillet welds at the cover plates and 0.313 in. minimum at the web plates. Plate thickness ranged from 1.5 in to 8 in. Reinforcing plates were specified as follows:

Plate thickness t (in.):

2 < t < 4	ASTM A588 Grade 50
4 < t < 6	ASTM A572 Grade 42
t > 6	ASTM A588 Grade 42

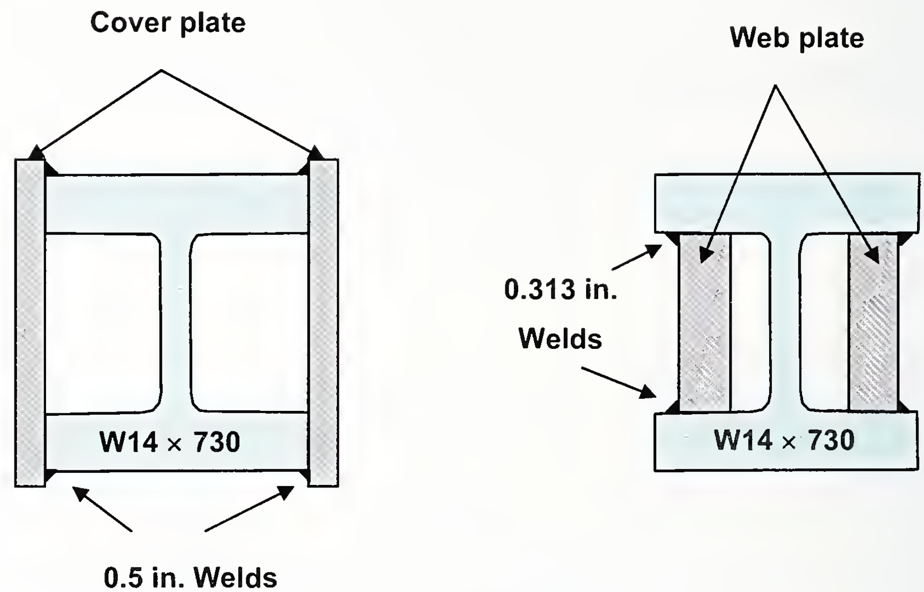

Figure L–17. Typical built-up column details.

Typical core column splices were shown on available erection drawings. The adjoining surfaces of columns were specified to be milled. The splice plates were welded or bolted to the outsides of the column web and flanges. Built-up columns were also milled at their bearing ends but the splice plates were fillet welded to the cover plates.

Perimeter columns were nominally 14 in. wide-flange shapes (W14) of ASTM A 36 steel. Perimeter column splices were similar to the core column splices.

L.1.8 Column Transfer Trusses and Girders

The layout of the substructure and Con Edison columns did not align with the column layout in the upper portion of WTC 7. Therefore a series of column transfers were constructed. These transfers occurred primarily between Floors 5 and 7. See Fig. L–18 for a schematic rendering of the transfers.

Columns 47 through 54, at the north facade, were transferred at Floor 7 by cantilever girders to bring them in line with the substation columns, offset 6 ft to 9 ft to the south. The back-span of these cantilevers was supported by the north side core columns. The eastern most cantilever girder was connected to truss #1, and the western most cantilever girder was connected to truss #3 (see Fig. L–18).

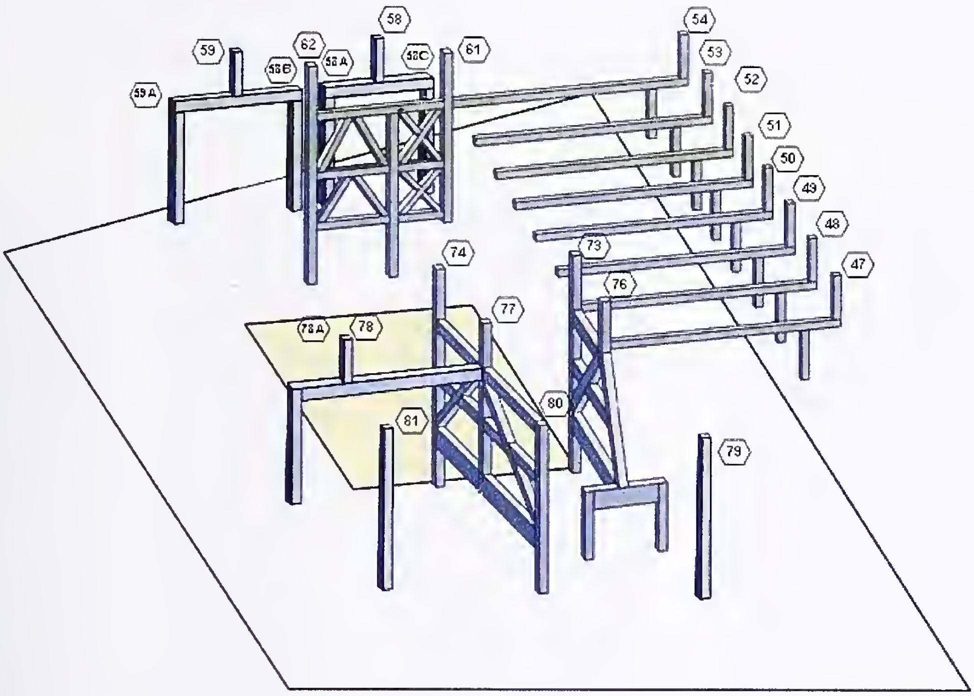

Figure L–18. 3D schematic view of transfer trusses and girders between Floors 5 and 7.

Column 76 was supported at Floor 7 by truss #1. The west side of truss #1 is supported by column 73, while the east side is supported by a transfer girder running north-south which is, in turn, supported by columns E3 and E4 at Floor 5.

Columns 58, 59, and 78 were transferred by simply supported girders at Floor 7. Column 78 was supported at Floor 7 by a transfer girder that was supported at its north end by truss #2. Column 77 was also supported by truss #2. Truss #2 was supported by column 74 at its west end and by column 80 at its east end.

Column 61 was supported by truss #3. Truss #3 runs north-south and was supported by columns 62 and 61A. Truss #3 has a 10 ft cantilever span between column 61 and column 61A and an 18 ft back span to column 62.

L.1.9 Lateral System

Above Floor 7, WTC 7 had a perimeter moment frame. Exterior columns were typically rolled W14 shapes of ASTM A36 grade steel. Column trees were fabricated for the east and west facades with field splices occurring every other story in the columns and at the spandrel beam midspan between columns, where the tree stubs were spliced with a bolted connection. On the north and south facades, the moment frames were constructed with spandrel connections at the face of the columns. Some column splices were shown on the erection drawings to be partial penetration groove welds between the column flanges.

At Floors 5 to 7 and Floors 22 to 24, there was a perimeter belt truss, shown in Fig. L–19. Below Floor 7, a combination of moment and braced frames around the perimeter and a series of braced frames in the core, is shown in Fig. L–20. The strong diaphragms of Floors 5 and 7 transferred load from the perimeter to the core. Above the loading dock at the south facade, two of the columns were hung from the belt truss at Floors 5 through 7. Above the Con Edison vault at the north facade, eight columns were also hanging from the belt truss between Floors 5 and 7.

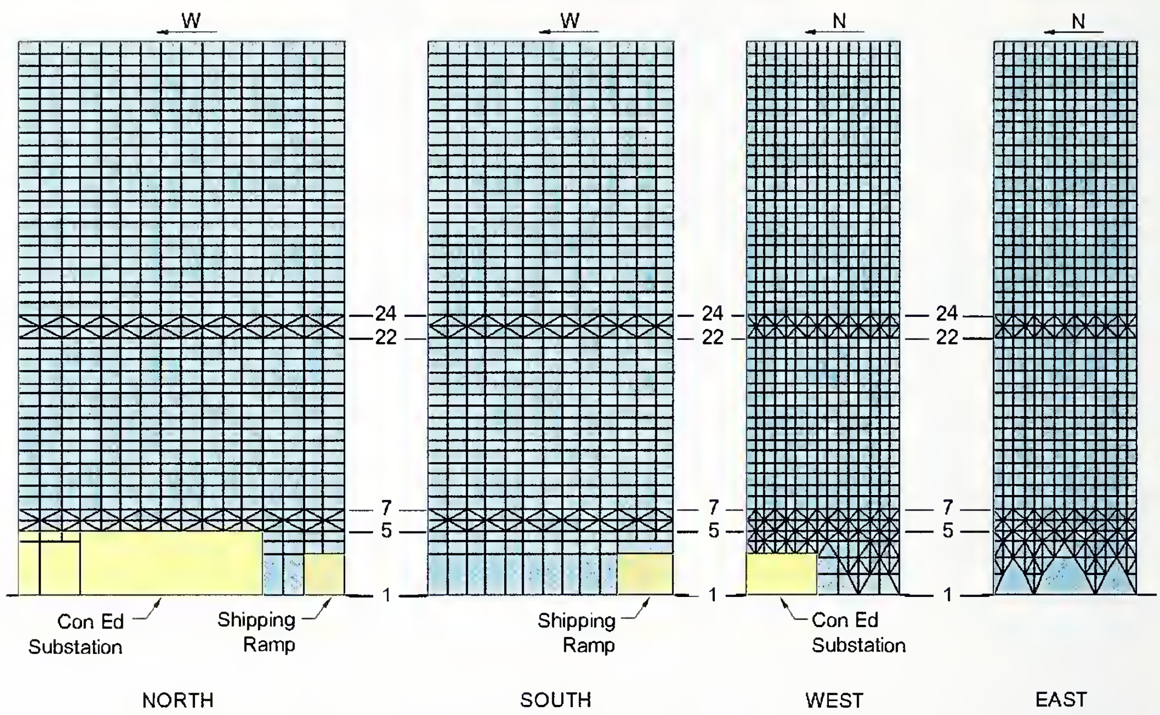

Figure L–19. Perimeter lateral system elevations.

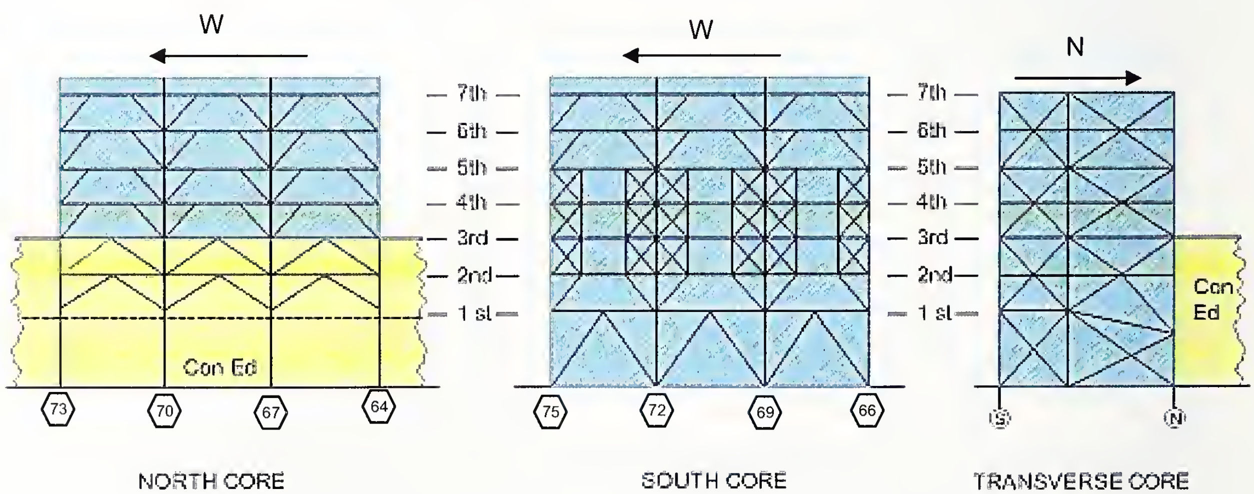

Figure L–20. Core lateral system.

L.2 OBSERVATIONS OF STRUCTURAL COLLAPSE

This section presents observed data and events from available drawings, photographic and videographic records, interviews, and other data sources for WTC 7 to identify damage and fire locations. Damage to WTC 7 from debris impact from WTC 1 and WTC 2 is summarized in Section L.2.2, followed by known fire growth and progression in Section L.2.3. The observed exterior sequence of collapse events from photographic and videographic records are described in Sections L.2.4 and L.2.5, where collapse observations are considered from the plan and elevation views of the structure, respectively. These observations have been used for developing possible collapse initiation locations and progression mechanisms, which are presented in Section L.3.

L.2.1 Damage from WTC 1 and WTC 2 Collapses

To place the events leading to the global collapse of WTC 7 into context, it is helpful to summarize the events of September 11, 2001:

8:46 a.m.	WTC 1 was struck by an aircraft
9:03 a.m.	WTC 2 was struck by an aircraft
9:59 a.m.	WTC 2 collapsed
10:28 a.m.	WTC 1 collapsed
5:21 p.m.	WTC 7 collapsed

After WTC 1 collapsed, the south face of WTC 7 was obscured by smoke, making direct observation of damage from photographs or videos difficult or impossible. The source of the smoke is uncertain, as large fires were burning in WTC 5 and WTC 6, as well as those noted below in WTC 7. The light but prevalent winds from the northwest caused the smoke to rise on the leeward, or south, side of the building. The following information about damage seen in WTC 7 was obtained from interviews of people in or near the building:

After WTC 2 collapsed:

- Some south face glass panes were broken at lower lobby floors
- Dust covered the lobby areas at Floors 1 and 3
- Power was on in the building and phones were working
- No fires were observed

Reported close to time of WTC 1 collapse:

- East stair experienced an air pressure burst, filled with dust/smoke, lost lights
- West stair filled with dust/smoke, lost lights, swayed at Floors 29 through 30, and a crack was felt (in the dark) on the stairwell wall between Floors 27 through 28 and Floors 29 through 30
- Floors 7 and 8 had no power, air was breathable but not clear

- Phone lights on Floor 7 were on but could not call out

After WTC 1 collapsed:

- Heavy debris (exterior panels from WTC 1) was seen on Vesey Street and the WTC 7 promenade structure at the third floor level

- Southwest corner damage extended over Floors 8 to 18

- Damage was observed on the south face that starts at the roof level and severed the spandrels between exterior columns near the southwest corner for at least 5 to 10 floors. However, the extent and details of this damage have not yet been discerned, as smoke is present.

- Damage to the south face was described by a number of individuals. While the accounts are mostly consistent, there are some conflicting descriptions:

  – middle one-fourth to one-third width of the south face was gouged out from Floor 10 to the ground

  – large debris hole near center of the south face around Floor 14

  – debris damage across one-fourth width of the south face, starting several floors above the atrium (extended from the ground to 5th floor), noted that the atrium glass was still intact

  – from inside the building at the 8th or 9th Floor elevator lobby, where two elevator cars were ejected from their shafts and landed in the hallway north of the elevator shaft, the visible portion of the south wall was gone with more light visible from the west side possibly indicating damage extending to the west

At 12:10 to 12:15 p.m.:

- Firefighters found individuals on Floors 7 and 8 and led them out of the building

- No fires, heavy dust or smoke were reported as they left Floor 8

- Cubicle fire was seen along west wall on Floor 7 just before leaving

- No heavy debris was observed in the lobby area as the building was exited, primarily white dust coating and black wires hanging from ceiling areas were observed

Photographs support some of these reports and show additional damage at the upper portions of the building. Figure L–21 is an aerial view of WTC 7 after the collapse of WTC 1. There is no visible debris on the roof; some minor damage is seen on the south side at the parapet wall. Figures L–22a and L–22b show the reported damage between Floors 8 to 18 at the southwest corner. Much of the damage above Floor 18 appears to be nonstructural. The black areas on the facade indicate areas of burned out fires. Note the heavy smoke obstructing any observations along the south face. Study of this photograph indicates that at least two exterior columns were severed. Figures L–23a and L–23b show the debris on Vesey Street in front of WTC 7 after the collapse of WTC 1. The pedestrian bridge (L–23a) and the promenade (L–23b) appear to be standing, although damaged. Exterior panels from WTC 1 can be seen on Vesey Street and on the promenade. The approximate extent of possible damage due to debris from WTC 1 is shown in Fig. L–23c.

Figure L–21. Photograph of roof after WTC 1 collapse.

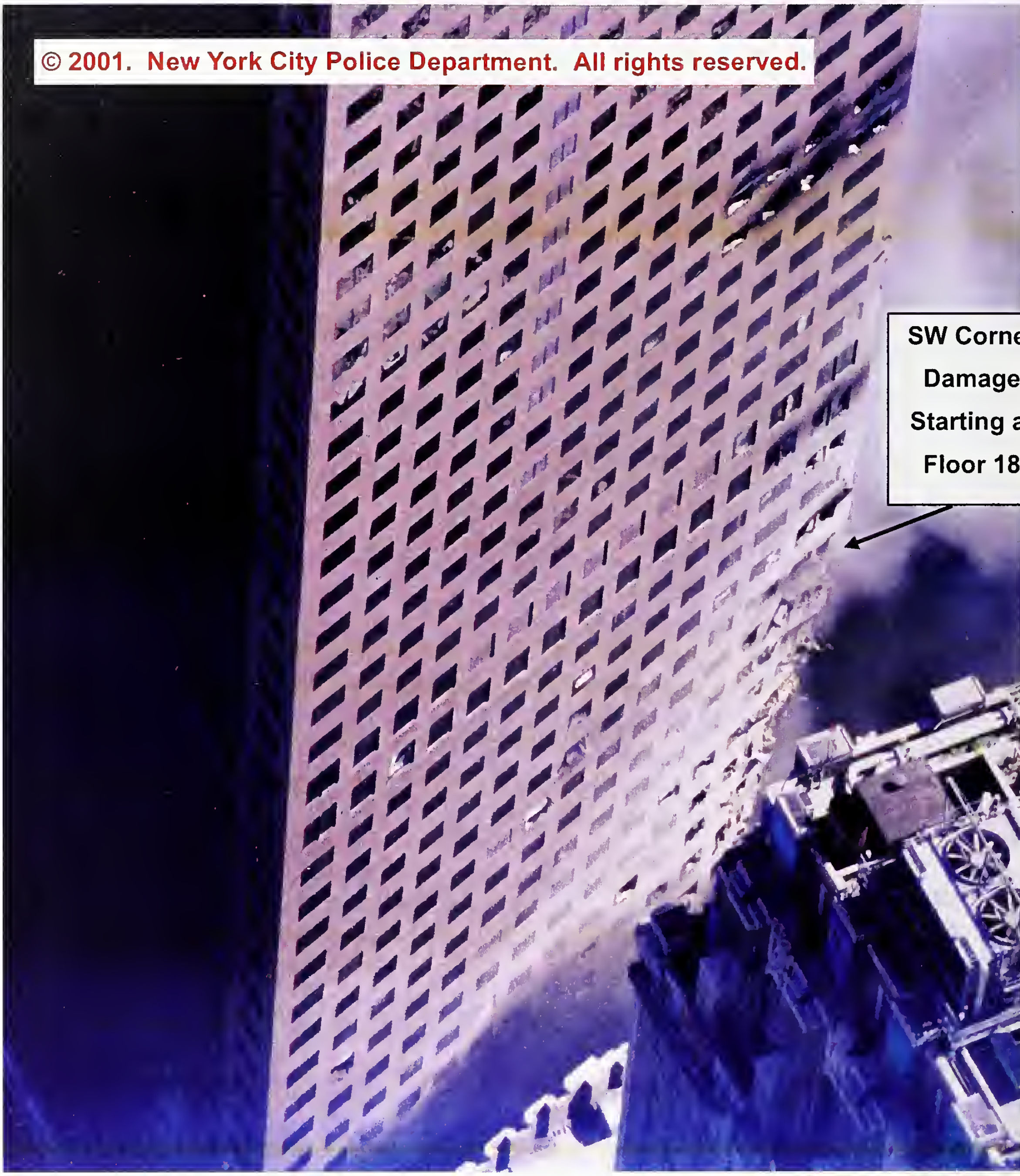

Figure L–22a. Debris damage around Floor 18 of the southwest corner.

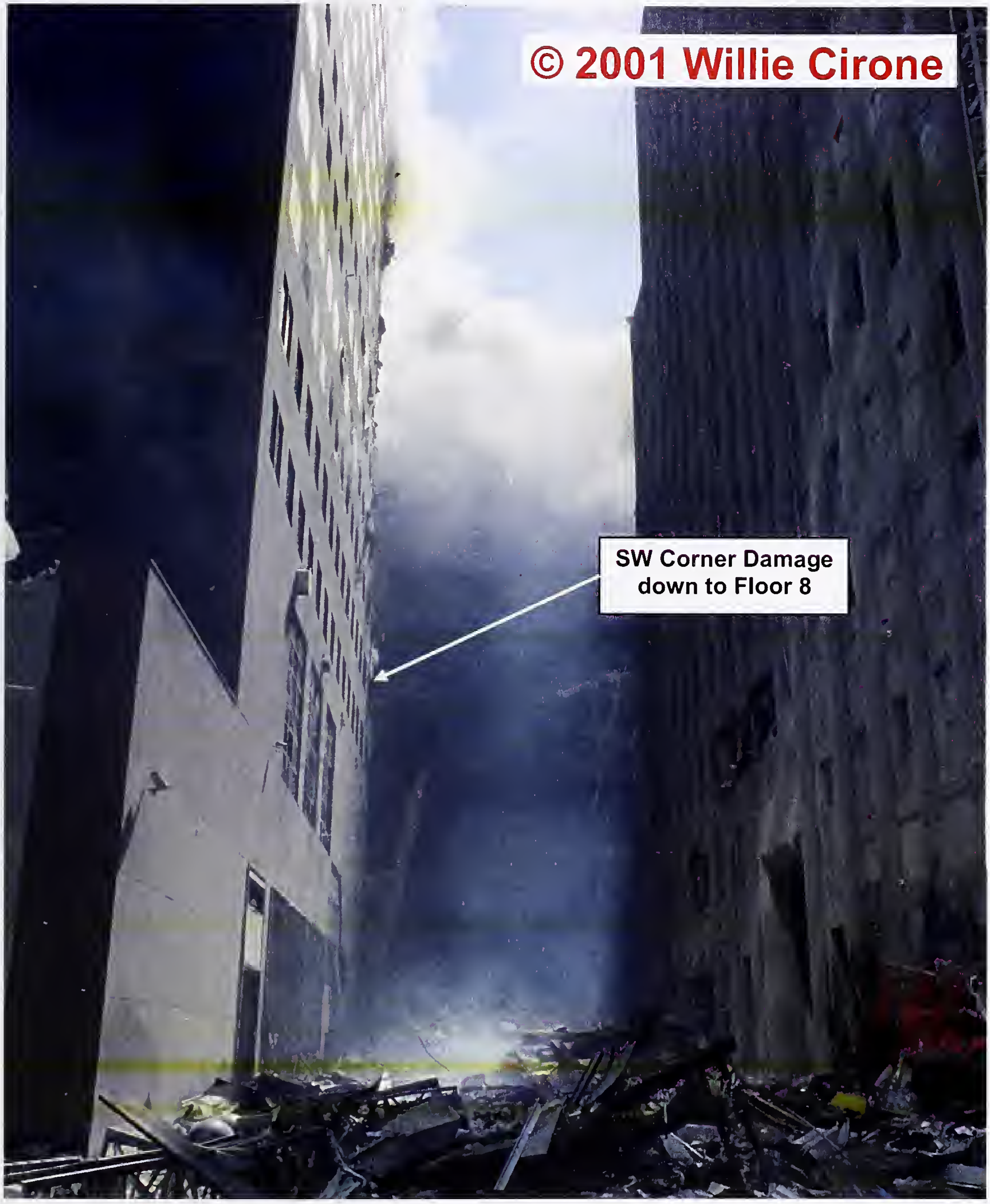

Figure L–22b. Debris damage around Floor 8 of the southwest corner.

Figure L–23a. Pedestrian bridge and debris on Vesey Street after WTC 1 collapsed.

L.2.2 Observed Fire Locations

Photographs and videos were used to determine fire locations and movement within WTC 7. Most of the available information is for the north and east faces of WTC 7. Information about fires in other areas of the building was obtained from interviews, and is summarized as follows:

From 11:30 a.m. to 2:30 p.m.:

- No diesel smells reported from the exterior, stairwells, or lobby areas
- No signs of fire or smoke were reported below the 6th Floor from the exterior, stairwells or lobby areas
- In the east stairwell, smoke was observed around Floors 19 or 20, and a signs of a fully involved fire on the south side of Floor 23 were heard/seen/smelled from Floor 22.
- Interviews place a fire on Floor 7 at the west wall, toward the south side, at approximately 12:15 p.m.

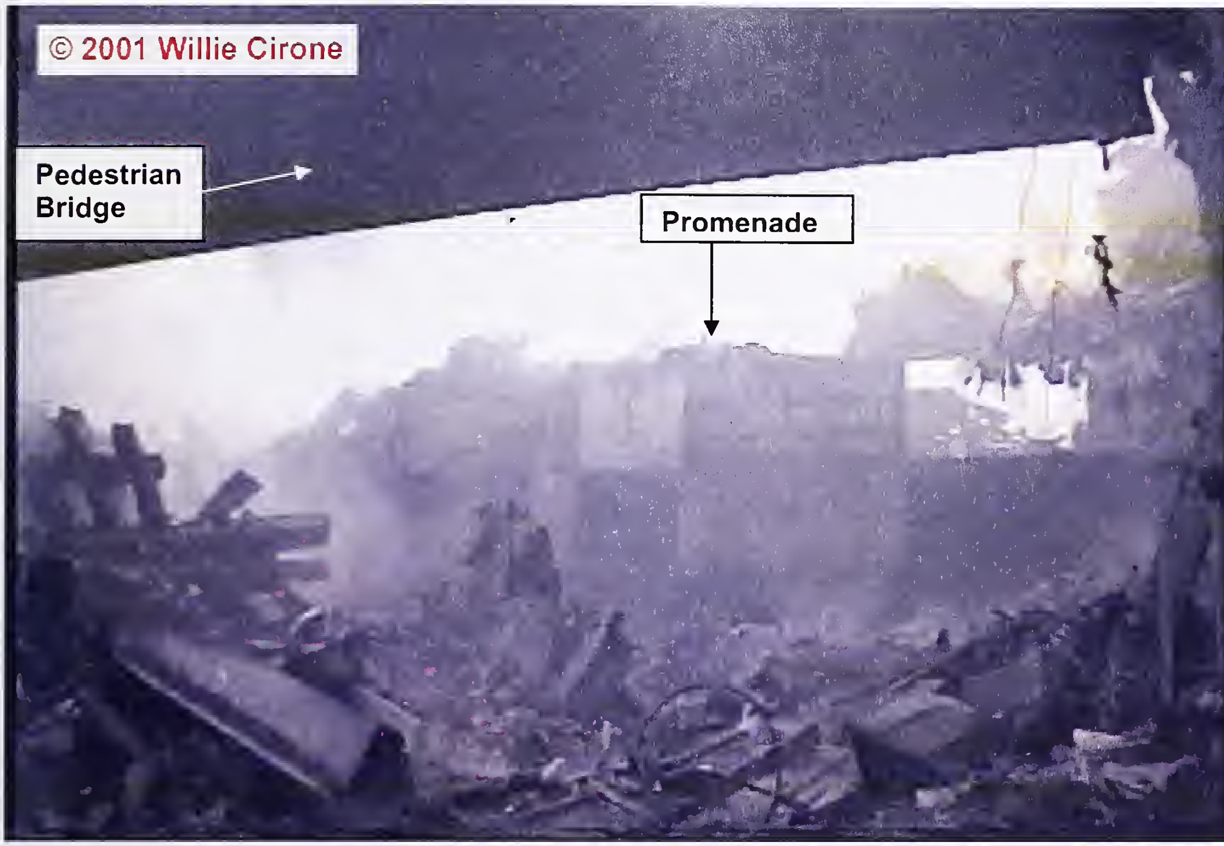

Figure L–23b. WTC 7 Promenade and debris on Vesey Street after WTC 1 collapsed.

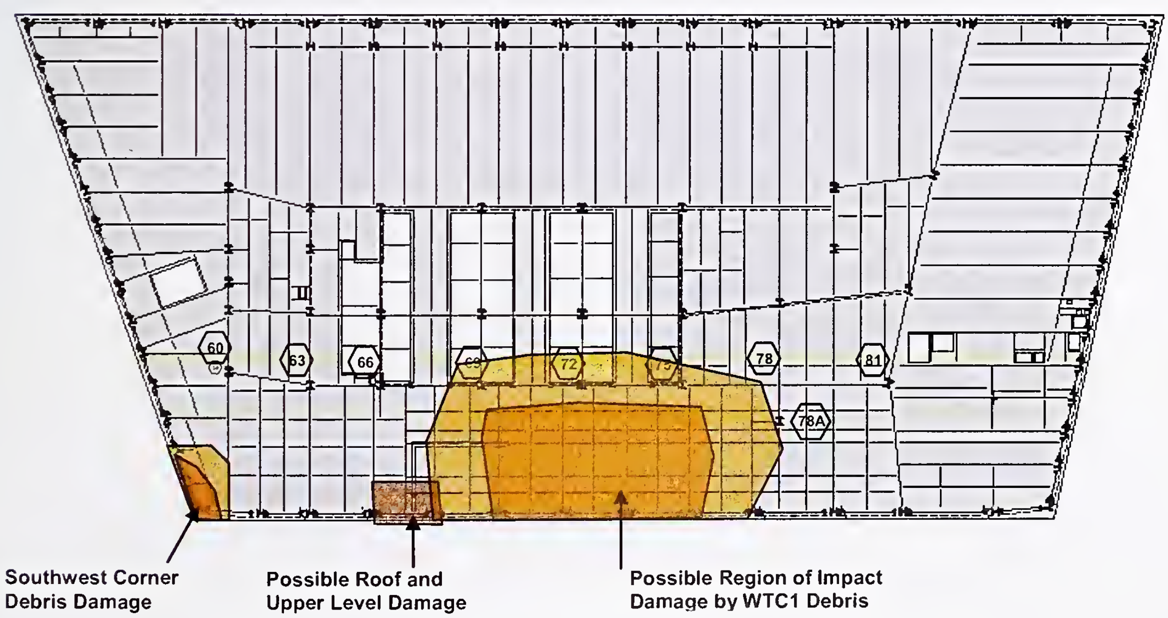

Figure L–23c. Possible extent of debris damage in plan.

- From West and Vesey Streets near the Verizon Building, fires were observed in floors estimated to be numbered in the 20s and 30s.

Looking from the southwest corner at the south face:

- Fire was seen in the southwest corner near Floor 10 or 11
- Fire was seen on Floors 6, 7, 8, 21, and 30
- Heavy black smoke came out of a large, multi-story gash in the south face

Looking from the southeast corner of the south face:

- Fire seen on Floor 14 (reported floor number) on south face; the face above the fire was covered with smoke
- Fire on Floor 14 moved towards the east face

Looking at the east face:

- Fire on Floor 14 (reported floor) moved along east face toward the north side

Photographs and videos were used with these interview accounts to document fire progression in the building. The fires seen in photographs and videos are summarized:

Before 2:00 p.m.

- Figures L–22a shows fires that had burned out by early afternoon on Floors 19, 21, 22, 29, and 30 along the west face near the southwest corner.

2:00 to 2:30 p.m.

- Figure L–24a shows fires on east face Floors 11 and 12 at the southeast corner. Several photos during this time show fires progressing north.

3:00 to 5:00 p.m.

- Around 3 p.m., fires were observed on Floors 7 and 12 along the north face. The fire on Floor 12 appeared to bypass the northeast corner and was first observed at a point approximately one third of the width from the northeast corner, and then spread both east and west across the north face.
- Some time later, fires were observed on Floors 8 and 13, with the fire on Floor 8 moving from west to east and the fire on Floor 13 moving from east to west. Figure L–24b shows fires on Floors 7 and 12.
- At this time, the fire on Floor 7 appeared to have stopped progressing near the middle of the north face.

Figure L–24a. Fires on Floors 11 and 12 on the east face.

Figure L–24b. Fires on Floors 7 and 12 on the north face.

- The fire on Floor 8 continued to move east on the north face, eventually reaching the northeast corner and moving to the east face.
- Around 4:45 p.m., a photograph showed fires Floors 7, 8, 9, and 11 near the middle of the north face; Floor 12 was burned out by this time.

L.2.3 WTC 7 Collapse Observations

The collapse of WTC 7 was recorded on several videos from locations northeast and northwest of the building. Study of these videos led to the development of the timeline in Table L–1, which lists the visible external sequence of events. Figures L–25 to L–28 are images from a CBS News Archives video that show key points observed during the collapse.

The deformed shape of the east penthouse roof shows that the middle fell before the sides (see Fig. L–25), as the whole penthouse drops into the main building (see Fig. L–26). This may imply that support initially remained on the east and west edges of the east penthouse. Therefore, the perimeter columns on the east side of the building which have not already been considered least likely, may be considered less likely locations for collapse initiation.

Table L–1. Timeline of WTC 7 collapse as observed from the northwest.

Time Interval (s)	Total Time (s)	Observation from CBS Video
0.0	0.0	- First movement of east penthouse roofline downwards
0.9	0.9	- East penthouse kink between columns 44 and 45 (Fig. L–25) - First 2 windows at Floor 40 fail between columns 44–45 (windows 9 and 11 from east end)
0.3	1.2	- 4 more windows fail at Floor 40 - East penthouse submerged from view (now inside building)
0.5	1.7	- 3 windows break at Floor 41, Floor 43, Floor 44
0.5	2.2	- East penthouse completely submerged (Fig. L–26)
1.8	4.0	- Windows break along column 46 at Floors 37 and 40
3.0	7.0	- West penthouse and screenwall begin to move downward into building - Movement of entire north face of WTC7 (visible above Floor 21)
0.2	7.2	- West end of roof starts to move
0.5	7.7	- East end of roof starts to move - Kink formed in north facade along column 46-47
0.4	8.2	- West penthouse and screenwall submerged - Windows fail between Floors 33–39 around column 55 - Global collapse initiates (Fig. L–27 and L–28)

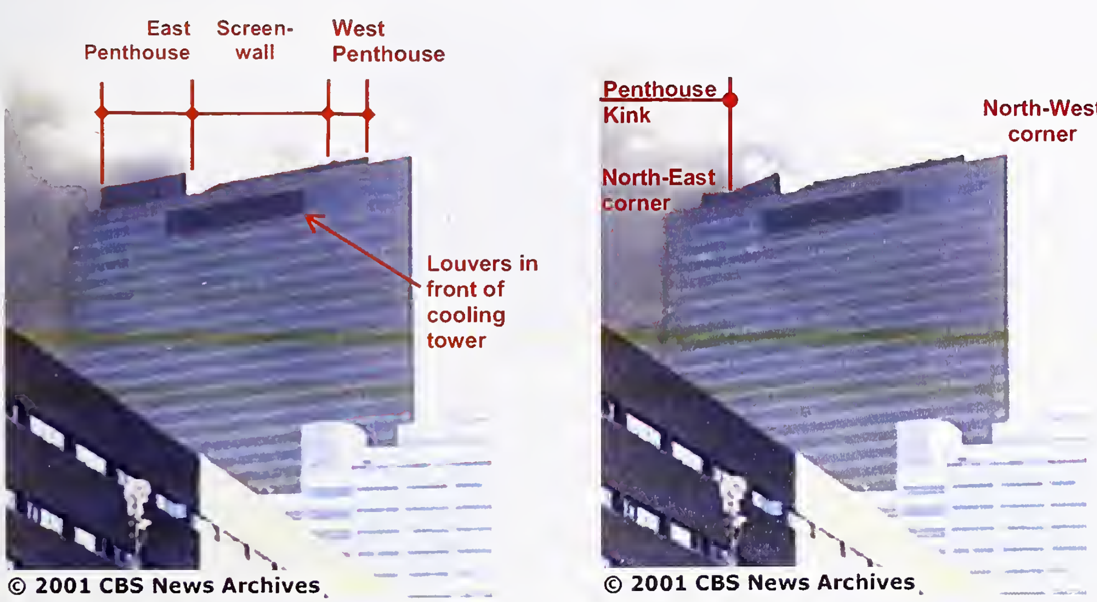

Figure L–25. East penthouse kink.

Figure L–26. East penthouse sinks (2.2 s).

Figure L–27. Center screenwall and west penthouse sink (7.9 s).

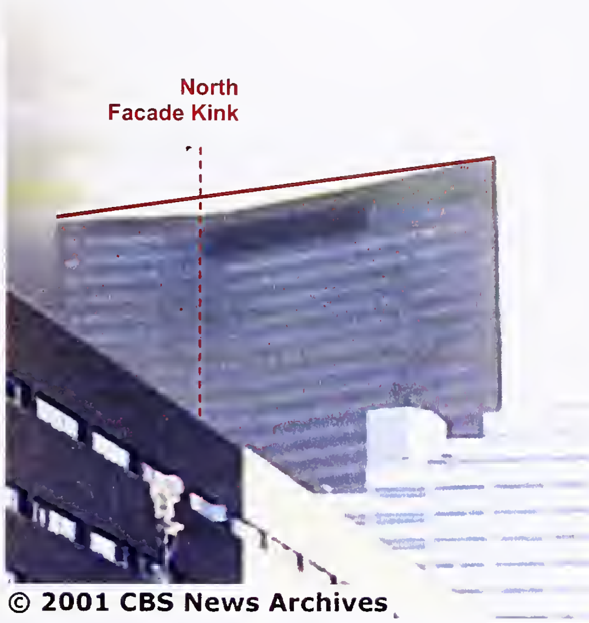

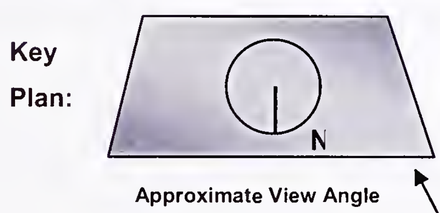

Figure L–28. Global collapse.

Possible Locations of Collapse Initiation

Columns 76, 77, 78, 79, 80, and 81 appear to have direct influence on the collapse initiation of the east penthouse. A failure of any of these columns, truss #1 or #2, or the east transfer girder, or some combination of these components, with possible contribution of adjacent framing and floor systems, could be considered possible locations of the initiating events that led to the observed collapse of the east penthouse.

L.2.4 Interpretation of Collapse Initiation Observations in Elevation

In addition to determining some possible locations of the collapse initiation locations within the plan of the structure, it is also helpful to use the available collapse documentation to identify possible locations in the building elevation for the initial failure.

Least Likely Locations of Collapse Initiation–Penthouse Failure Mechanism

Because the first visible failure is in the east penthouse, one possible collapse initiation mechanism involves a local failure of the penthouse framing, which then progressed down the structure with floors sequentially impacting upon those below. There are two reasons that this scenario may be considered unlikely.

First, there was no visible abnormal loading locally applied to cause a local failure at the East Penthouse. The photograph in Fig. L–21 shows the east penthouse sustained no damage due to the collapse of the WTC towers. The videographic records do not show any visible fire in or near the penthouse prior to collapse.

Second, Fig. L–25 shows a snapshot as the east penthouse starts to collapse. When the roof of the penthouse starts to fall, a line of windows (roughly in line with columns 79 to 81) has broken over the entire height of the visible region. In free fall, it would take 3 to 4 seconds for an object to fall from the roof elevation to the height of the bottom visible broken window, around Floor 33. Since the bottom window is broken nearly simultaneously when the kink is seen at the east penthouse, the initial failure may be assumed to have propagated upward from the lowest window breakage rather than propagated downward from the top of the building. Therefore, initial failure within the penthouse may be considered unlikely.

Less Likely Locations of Collapse Initiation–High Elevation Column Failure Mechanism

Another possible collapse initiation mechanism may be the failure of a column in the upper elevations of the building. The collapse could have progressed vertically upward by pulling down the floors above the failed column as debris landed on and sequentially crushed the floors below.

The timing required for this mechanism, in accordance with gravitational acceleration, requires that any column locations significantly above the 13th floor (the lowest visible floor in photographic and videographic records) may be considered unlikely failure initiation locations. The lack of observed fires in the floors above Floor 13 also reduces the likelihood of failure initiating in this region of the building.

Possible Locations of Collapse Initiation Mechanism

Based on review of the photographic and videographic records, a failure of any column within the plan area shown in Fig. L–29, and below Floor 13, likely contributed to the collapse initiation. This includes columns 76, 77, 78, 79, 80, and 81, truss #1, truss #2, column 78A, the east transfer girder and adjacent framing and floor systems within this region (see Fig. L–30).

L.2.5 Interpretation of Collapse Progression Observations

Interior columns 79, 80, and 81, were located directly below the east penthouse on the roof and supported large tributary areas. It appears that some sequence of component failures in the region identified in Figs. L–29 and L–30 led to the failure of one or more of these columns, as discussed above. The failure progressed vertically upward within the failed bay to the roof level, based upon observations of window breakage relative to failure of rooftop structures, and was first visible from the exterior when the east penthouse lost support (see Fig. L–26).

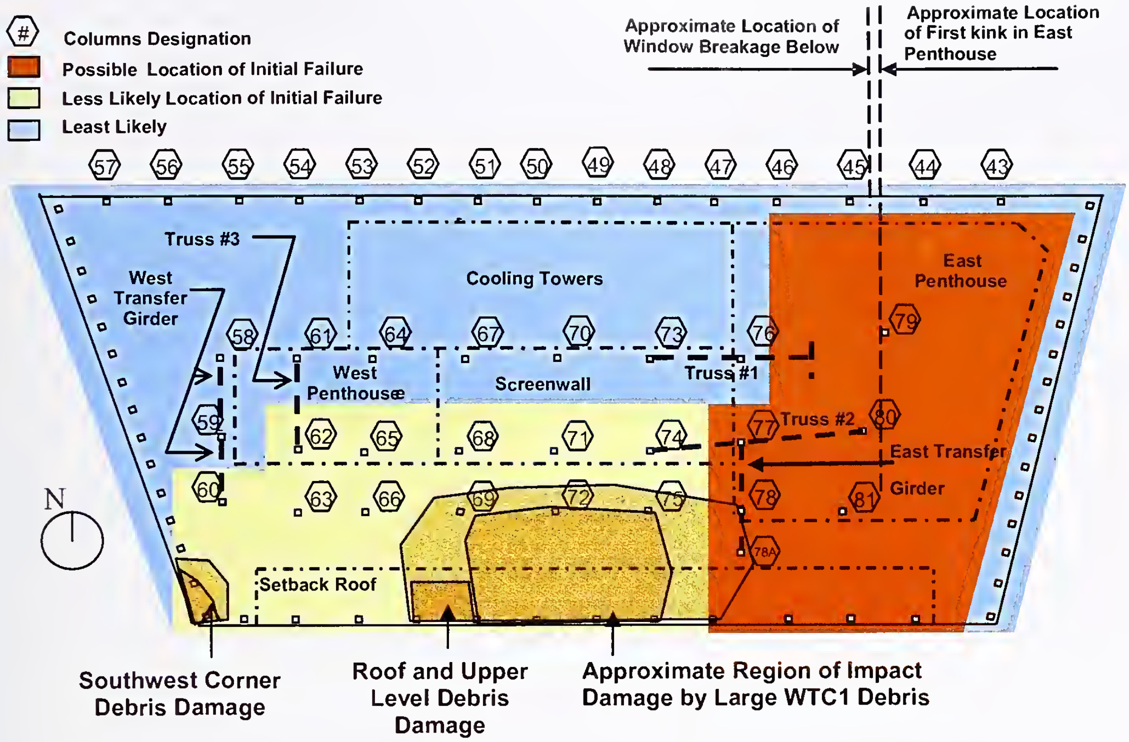

Figure L–29. Plan view of regions for collapse initiation.

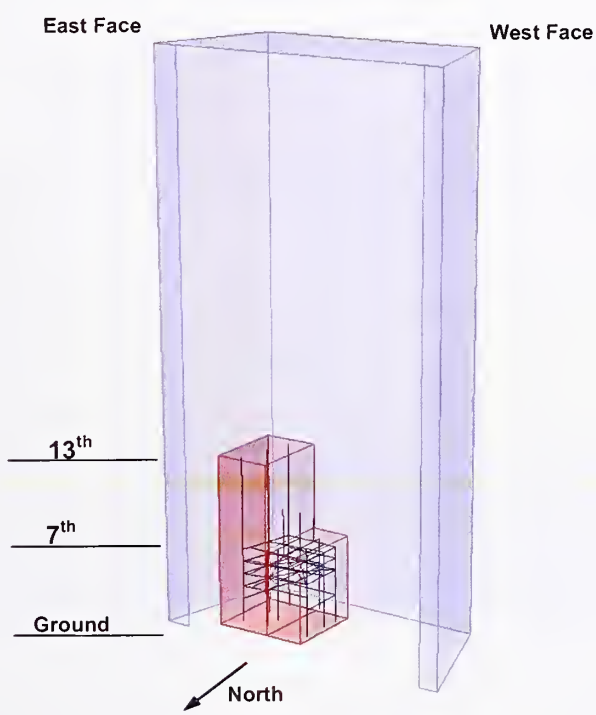

Figure L–30. Likely region of initiating component failures based on videographic and photographic records of fire and collapse.

The 5 s to 6 s delay between the failure of the east penthouse and the failure of the screenwall and west penthouse (shown in Fig. L–27) approximates the time it would take for the debris pile from the vertical failure progression on the east side of the building to reach Floors 5 to 7 and damage the transfer trusses and girders in this area.

A kink developed in the north facade approximately where column 76 projects to the north face. The kink may have formed in the plane of the north facade or it may represent a displacement in the structure along this line towards the south. The area of this kink correlates to the easternmost cantilever transfer at Floor 7. All of the Floor 7 cantilever transfer girders had back spans supported along the line of the north core columns, of which the easternmost one was supported by truss # 1. This north facade kink also coincides with the girders at the eastern edge of the cooling tower area at Floor 46.

When the screenwall and the west penthouse sank into the building, a line of windows broke from Floor 44 down to the bottom of the visible range, which is approximately at Floor 33 on the west side of the structure (see Fig. L–27). This area aligns with column 61, which is supported by the cantilevered end of transfer truss #3 between Floors 5 and 7, as shown in Fig. L–31. This suggests that the observed window breakage may be related to the failure of column 61 or truss #3.

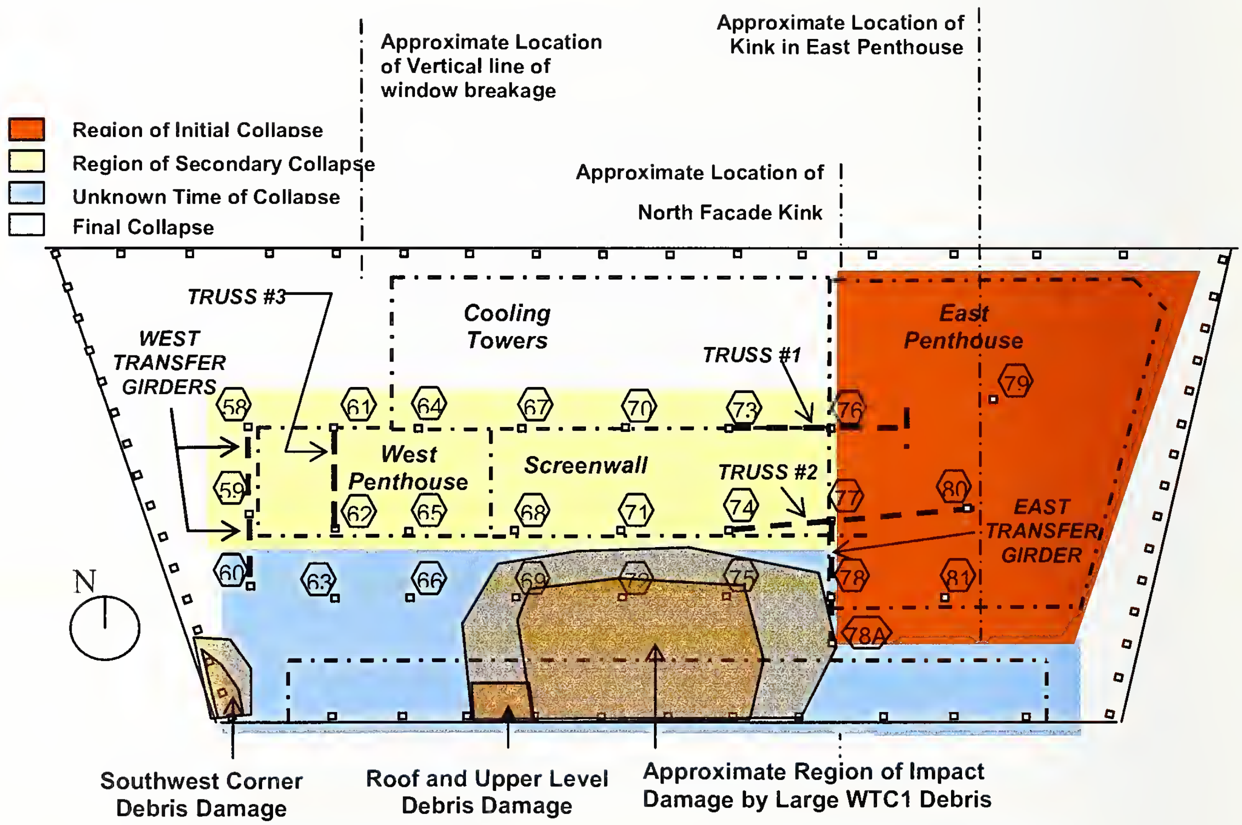

Figure L–31. Plan View of Collapse Progression.

The simultaneous failure of screenwall and west penthouse structures, window breakage on the west side of the north facade, and initiation of global collapse (see Fig. L–28) indicates that the building loads could no longer be supported. Horizontal progression of the collapse appears to have occurred after the vertical collapse on the east side of the building. The greater strength of Floors 5 and 7 relative to the other floors and the transfer trusses between these floors suggests that this region of the building played a key role in destabilizing the remaining core columns, and the global collapse occurred with few external signs prior to the system failure.

All of the photographic and videographic records show the north facade collapsing from below the visible area; the facade appears to sink into the ground without any sign of the other floors in the visible portion of the building collapsing. This may indicate that the collapse of the facade starts below the area visible in the photographic and videographic records.

L.2.6 Debris Field

The debris of WTC 7 was mostly contained within the original footprint of the building. From aerial photos, the debris visible on top of the pile is mostly façade structure. This failure sequence suggests that the interior of the building collapsed before the exterior. See Fig. L–32.

L.2.7 Summary

The possible region of collapse initiation and progression has been refined and can be limited based upon available data as follows:

- Based upon the observed fire locations, it appears that the initiating collapse event may have occurred on Floors 5 through 13.
- Due to the pattern of window breakage, it appears that the initiating collapse event may have occurred below Floor 13 and then progressed vertically upward to the east penthouse.
- Since the middle of the east penthouse roofline appears to fall first, it is possible that the initiating collapse event occurred at columns or transfer components with direct influence on the footprint of the east penthouse.
- The north facade kink and the window breakage on the west side of the north facade as the screenwall and west penthouse began to fall into the building core suggest that a horizontal collapse mechanism occurred between Floors 5 and 7, as there are vertical discontinuities in line with each of these elements between Floors 5 and 7.
- The relatively small debris field, with the exterior moment frame visible on top of the building debris, an internal collapse mechanism is likely.

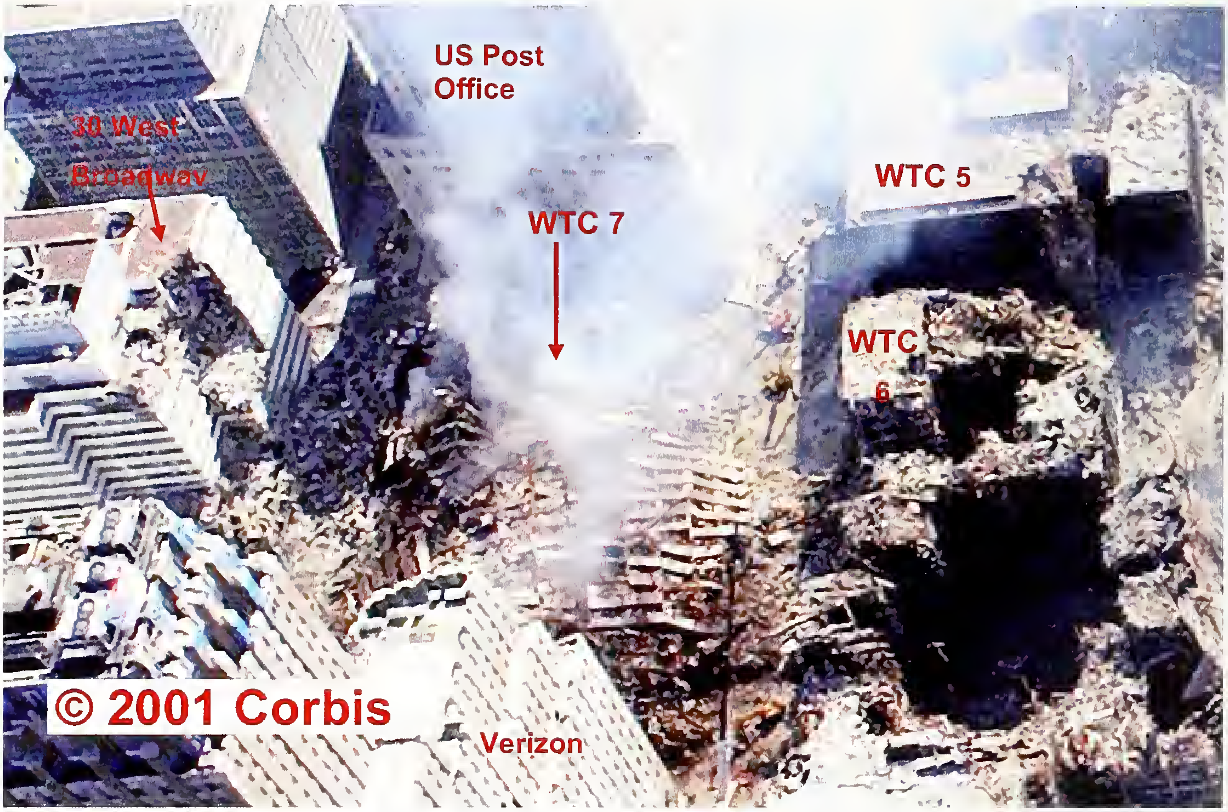

Figure L–32. Aerial view of WTC 7 after collapse.

The working collapse hypothesis can be summarized in Figs. L–33 and L–34, which illustrate the components of the observed collapse event: collapse initiation and vertical progression, horizontal progression, and global collapse.

L.3 COLLAPSE HYPOTHESIS

L.3.1 Introduction

WTC 7 suffered a global collapse. The initiating cause or causes of this collapse, and its sequence of events, are still being investigated though fire appears to have played a key role and there may have been some physical damage on the south side of the building.

To develop a working hypothesis for the collapse sequence, it is useful to subdivide the problem into several phases. Many factors and structural components may have contributed to the start of the collapse, but there must have been an initiating event. After the collapse initiated, it progressed to other parts of the building, leading to their failure as well. From the observations of the collapse (see Section L.2), it appears that first there was a vertical failure progression, from some point in the lower eastern portion of the building up to the east penthouse. After a time lag of approximately five seconds, the screenwall and west penthouse were observed to begin sinking into the core area. This suggests that there was a horizontal progression of the collapse towards the west. Since the screenwall and west penthouse fell almost simultaneously, it is reasonable to assume that the horizontal progression captured all the columns that support these building parts.

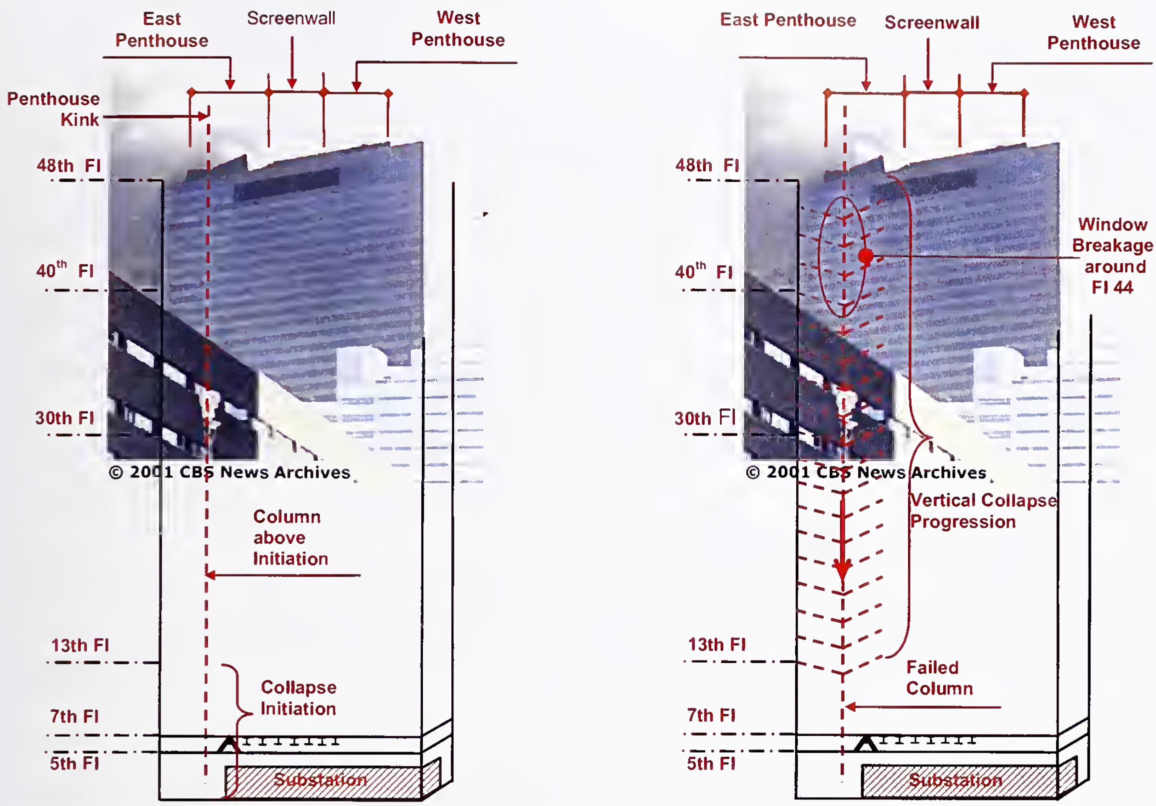

Figure L–33. Collapse initiation and vertical progression on the east side of WTC 7.

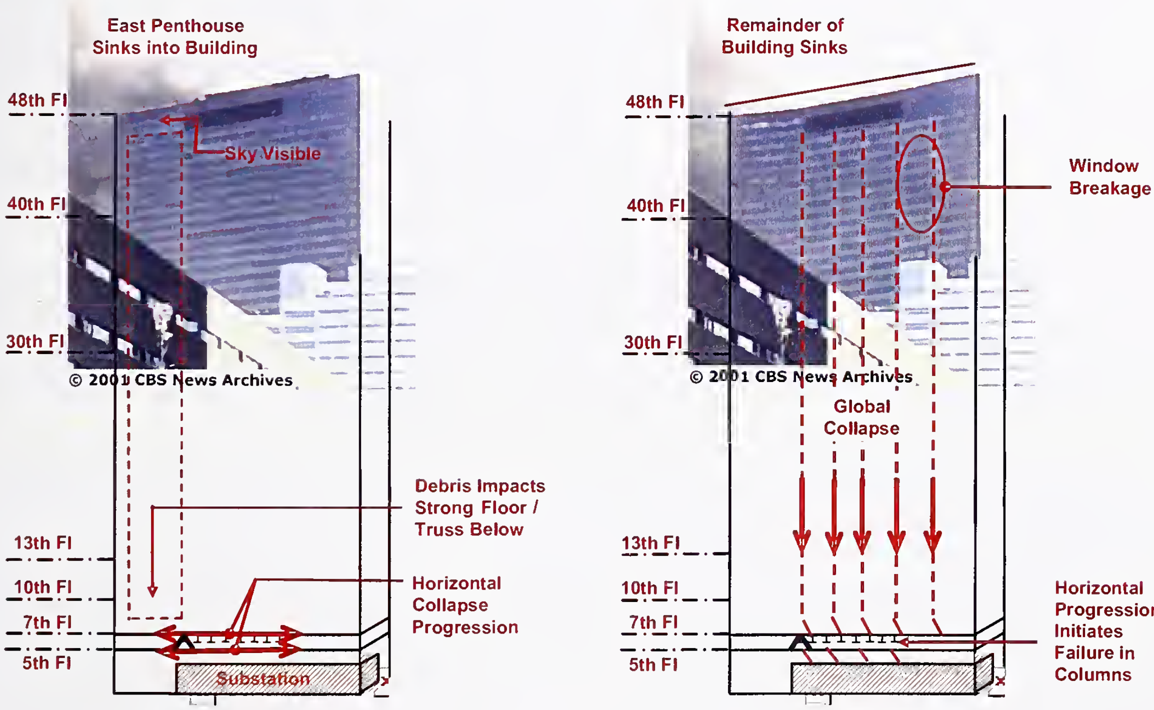

Figure L–34. Horizontal progression to the west side of WTC 7.

Within each phase of the collapse shown in Fig. L–35, the initiating event, vertical progression, horizontal progression, and global collapse, exist many possible scenarios. Scenarios have been developed from available observations of the collapse and are explored with event trees. Preliminary analyses, combined with the observations of collapse, can be used to prune the list of postulated scenarios to a relatively small number of possible collapse hypotheses. These possible hypotheses will then be analyzed in successive levels of detail to try to determine one or more probable sequence of events leading to the building collapse.

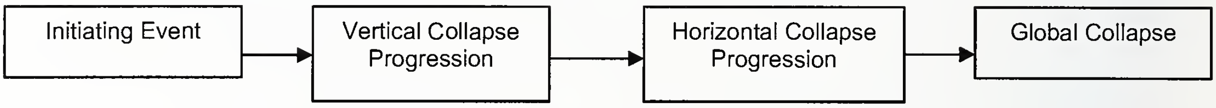

Figure L–35. Phases of WTC 7 building collapse.

L.3.2 Collapse Initiation Scenarios

For the collapse to have started, there must have been a component or group of components that failed first, referred to here as the initiating event, as shown in Fig. L–36. The initiating event may have included structural components severed or damaged by falling debris (I1.1) and/or structural components affected by fires (I1.2).

I1.1 Initiating Components Fail Due to Debris Damage From WTC 1 of WTC 2: The initiating components may have included perimeter or interior columns that were severed or damaged by falling debris from WTC 1 or WTC 2.

- **I2.1 Debris Damage to South Facade Columns:** Perimeter columns on the south face and the southwest corner were reported or observed in photographic and videographic records to have been severed or damaged after WTC 1 collapsed. If the initiating event was due to damage to the perimeter moment frame, then it would have started along the south or southwest facade. Photographic and videographic records show that columns on the north and east facades were undamaged by debris impact.

  – **I3.1 Perimeter Moment Frame Arrests Failure Progression:** Analysis of the global structure indicates that the structure redistributed loads around the severed and damaged areas. A progression of column failure to adjacent columns would have been arrested by the vierendeel action of the perimeter moment frame, which could span across a sizeable opening due to the strength and stiffness of the frame.

  – **I2.2 Debris Damage to Interior Columns:** Interior columns may have been severed or damaged by impacting debris.

  – **I3.2 Interior Columns Fail Immediately:** If interior columns had been severed or severely deformed, they may have failed immediately.

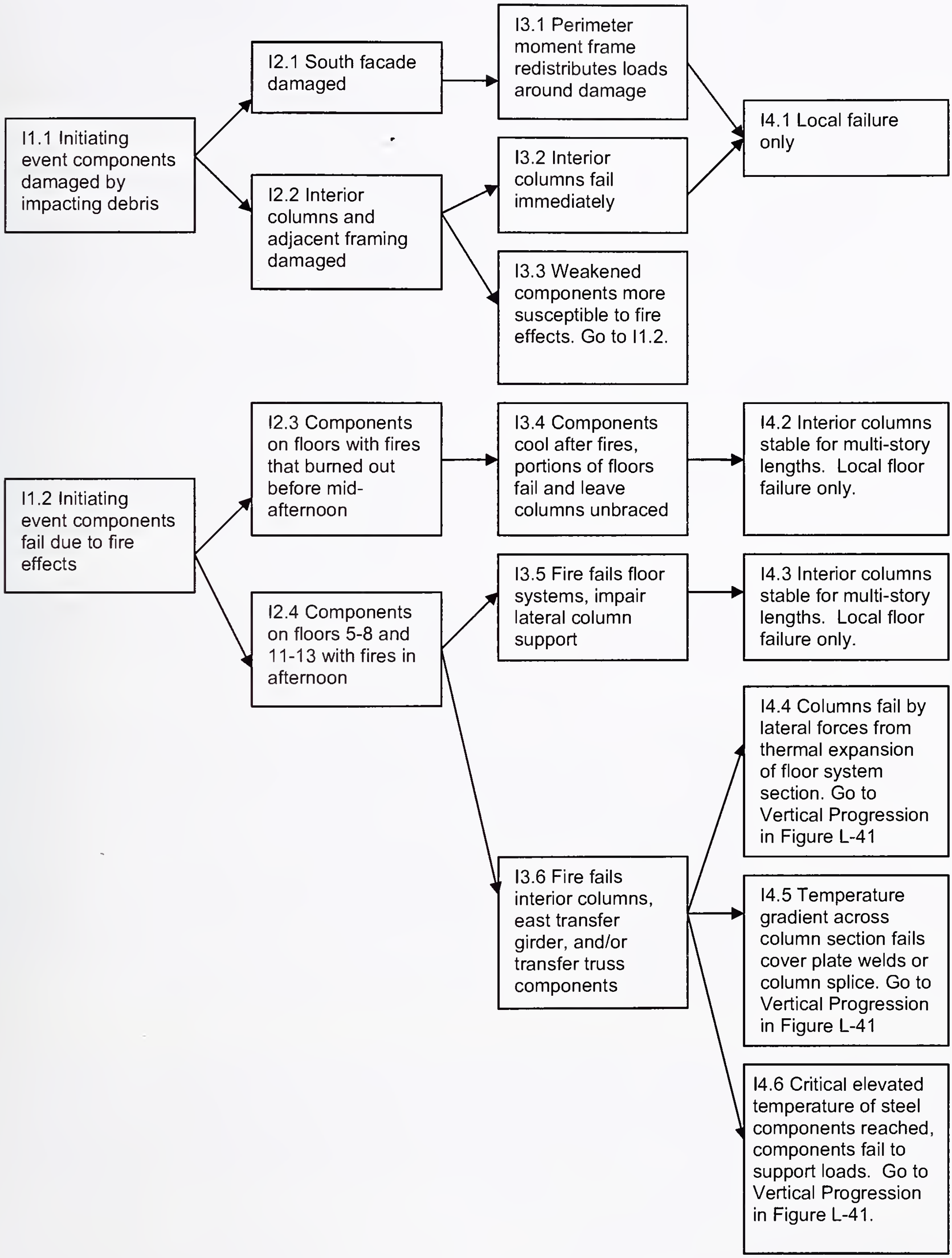

Figure L–36. Collapse initiation scenarios.

- **I4.1 Localized Failure at Interior Columns:** If the interior columns failed just after impact, this likely resulted in a local failure only, since the building continued to stand for almost 7 hours after WTC 1 collapsed. This failure could have progressed vertically upward to the roof level within the bays immediately adjacent to the failed columns, yet from the northern vantage point of the photographic and videographic observations, would not have been visible.

– **I3.3 Interior Columns Remain Standing But Damaged:** If interior columns were weakened by damage from debris, but retained sufficient capacity to carry their loads, then additional loading and/or fire effects would have been required to cause their failure. Debris impact may have damaged the structural steel fireproofing without significantly deforming the structural component.

I1.2 Initiating Components Fail Due to Fire Effects: Fires had been burning in WTC 7 for many hours, as observed in the photographic and videographic records (see section L.2). The initiating event may have been caused by fire effects on structural components.

- **I2.3 Components on Floors With Burned Out Fires:** If the initiating components failed from fire effects, then locations where fires had burned out by mid afternoon could possibly been affected by the cooling which occurs after a fire. No fire was observed or reported in the afternoon on Floors 1–5, 10, or above Floor 13.

  – **I3.4 Floor Systems Fail:** The cooling that may have occurred as the fires burned out in an area may have generated thermal contraction forces, which may have induced tensile forces at floor-to-column connections.

    - **I4.2 Unbraced Columns:** If floor systems failed, one or more columns may have lost lateral bracing. At a floor where fires were noted, interior columns were comprised of W14x730 cores and reinforcing plates, and could support several stories unbraced without failure. As an example, the column capacity curve of column 79 between Floors 5 to 9 is shown in Fig. L–37. Column load-carrying capacities shown in this figure are based on the AISC column capacity formulas (AISC 2001). The column is not very sensitive to the number of stories of unbraced column length, K. This column, which had a service load stress of approximately 21 ksi, would be approaching its load carrying capacity for an unsupported length of four stories if it was also subject to a uniform temperature of 500 °C.

- **I2.4 Components on Floors With Fire:** If the initiating components failed because of fire effects, then locations with uncontrolled fires would be more likely for the initiating event. From available data of fire locations in WTC 7, likely locations would include Floors 5, 6, 7, 8, 9, 11, 12, and 13. No fires were observed on Floor 5, but the lack of windows and the presence of fuel systems on the south, west, and north floor areas indicate that fire should be considered as a possibility on this floor.

  – **I3.5 Floor System Failure:** The fires could have caused the failure of portions of one or more floor system and its framing connections.

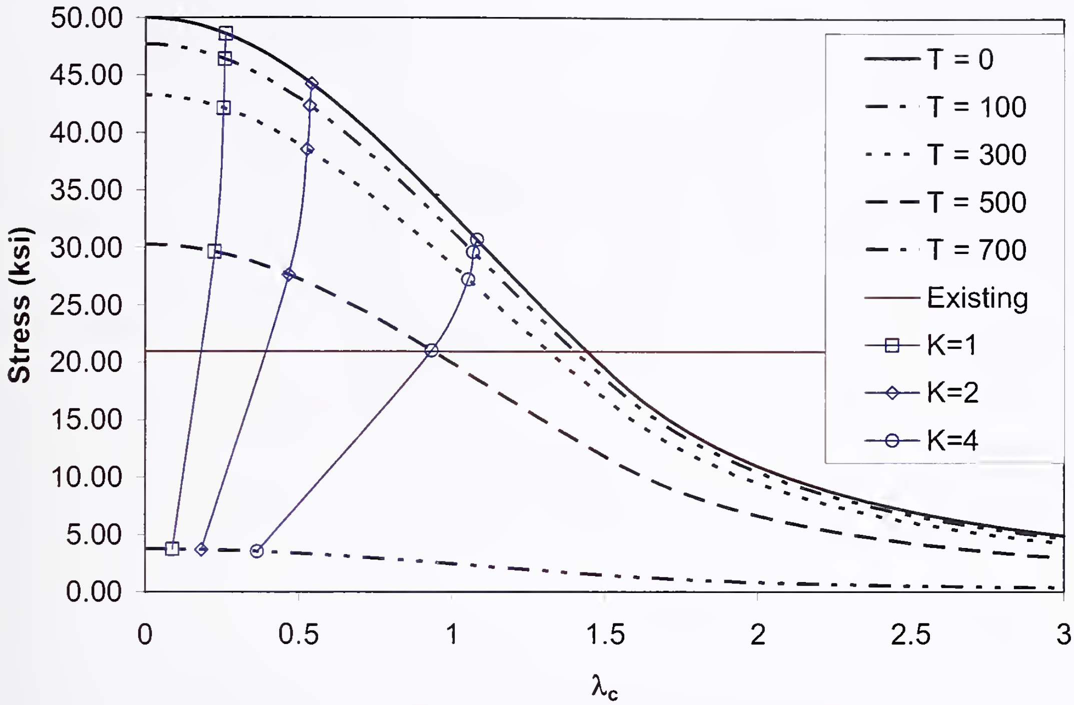

Figure L–37. Column 79 capacity versus temperature and unbraced length K.

- **I4.3 Unbraced Columns:** If floor systems failed, one or more columns may have lost lateral bracing. See I4.2 for discussion.

– **I3.6 Columns, Transfer Girders or Transfer Trusses Fail:** The fires could have failed interior columns, transfer girders, transfer trusses, or their framing connections.

- **I4.4 Lateral Displacements:** Fire effects may have caused column instability failure by lateral displacements from asymmetric thermal expansion of the floor system. Such thermally-induced displacements must overcome the restraining effect of the remaining floor system against further lateral deflection of the column.

- **I4.5 Temperature Gradients:** Fire effects may have caused the failure of columns and other components through the forces induced by temperature gradients through their cross section. Bending and shear forces may be induced that are sufficient to yield either the column splice or reinforcing plate welds. Analysis of a one-story segment of interior column 79 indicates that the cover plate weld would begin to yield at a mean temperature of 490 °C with a 200 °C gradient across the section, as shown in Fig. L–38. Other mean temperature and gradient combinations may also cause this type of failure.

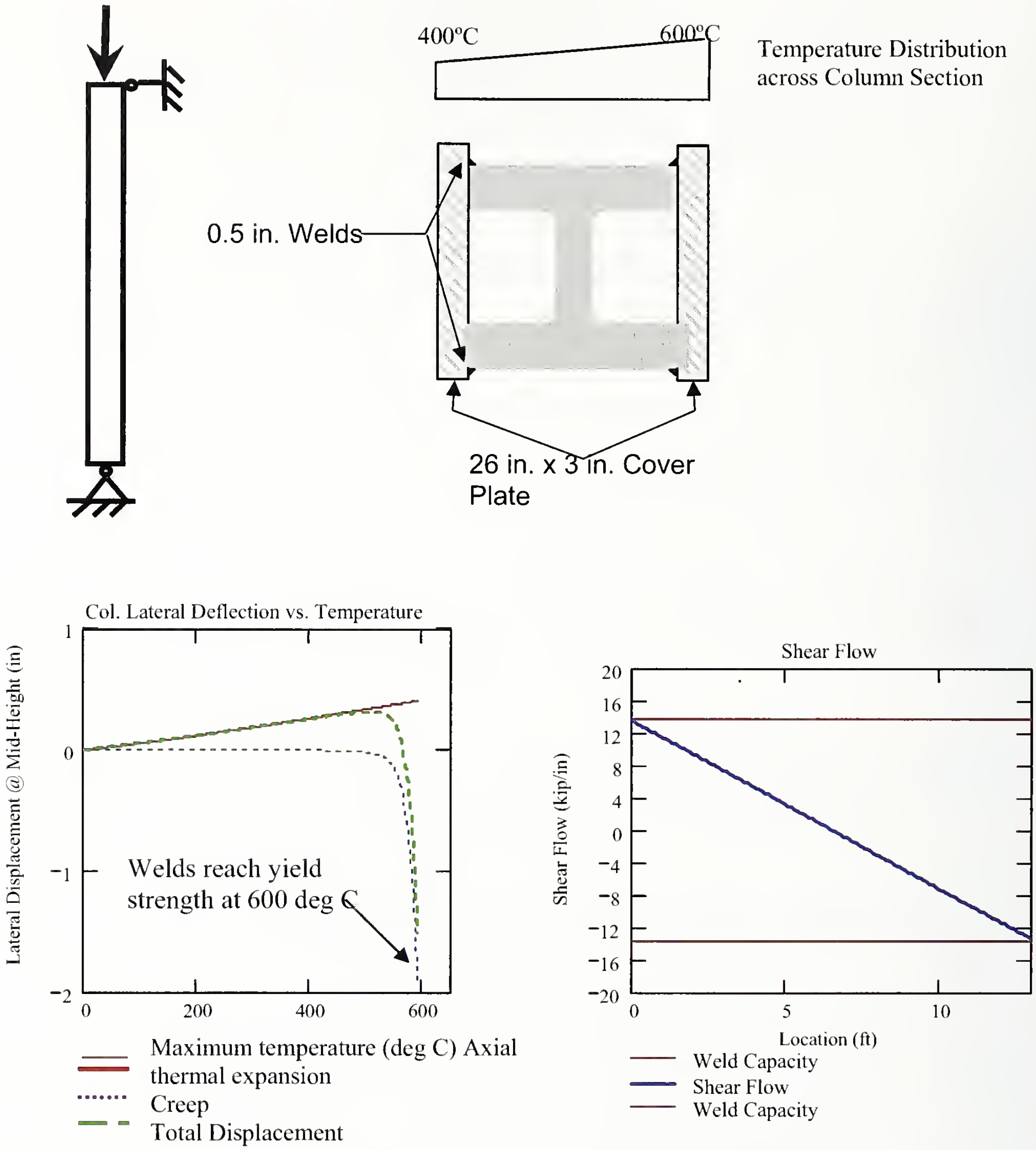

Figure L–38. Effects of temperature gradient on interior column 79.

- **14.6 Uniform High Temperatures:** If initiating event components were sufficiently exposed to fire effects to be uniformly heated to elevated temperatures, the steel strength would be reduced below that required to support the load. Figure L–39 shows that for interior columns subject to service loads (shown as approximately 20 ksi of compressive stress), uniform steel temperatures of approximately 570 °C would result in column failure.

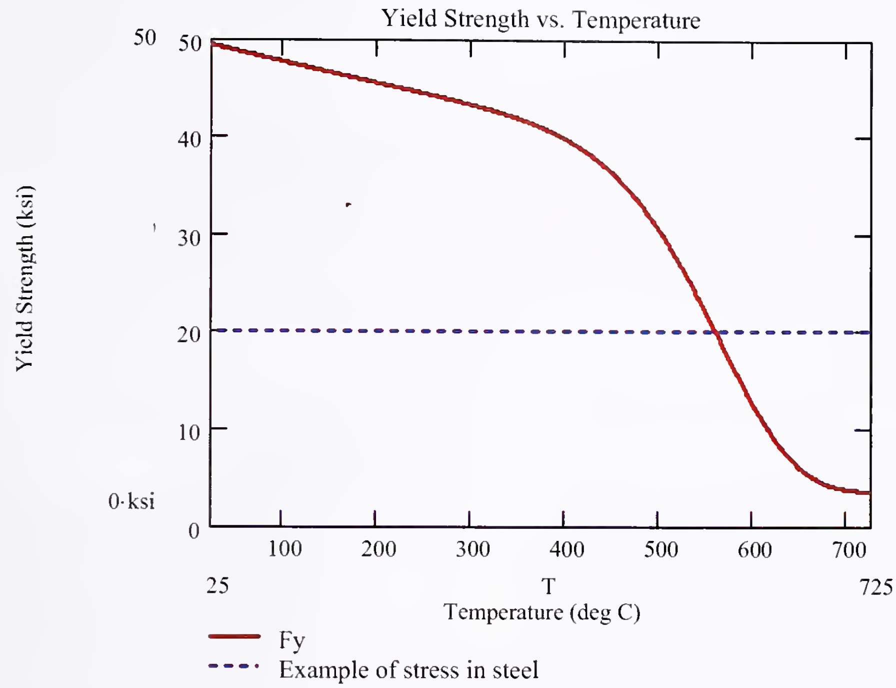

Figure L–39. Steel strength versus temperature.

L.3.3 Vertical Progression Scenarios

After the initiating component or components failed, there must have been a progression of the failure from the initiating event to other locations. To reflect the observed failure of the east penthouse, the failure likely progressed vertically upwards. Figure L–40 shows possible vertical progression scenarios. The initiating component could have failed by any of the failure sequences listed under the collapse initiation scenarios in Fig. L–36. This component could have been one of the columns under the east penthouse. It could also have been one of transfer trusses #1 or #2 under the east penthouse.

A collapse mechanism model was created to capture possible collapse initiation at the roof and the east penthouse. The model seeks to simulate only the kinematics of the collapse mechanism when columns are removed. Several columns were tested for removal. The resulting geometry change was then compared to the observed collapse of WTC 7.

V1.1 Perimeter Columns Fail: Had the initiating component been any perimeter column, most likely it would have been at floor levels with debris impact damage (possible range extends from the ground level up to floors 15 to 20) or the floors possibly experiencing fire (Floors 5, 6, 7, 8, 9, 11, 12, or 13).

- **V2.1 Collapse Does Not Progress:** If a group of perimeter columns failed, the perimeter framing above this area would have redistributed its loads, due to the redundancy of the moment frame.

V1.2 Core Columns Not Directly under East Penthouse Fail: Had the initiating component been a core column that was not under the east penthouse, most likely it would have been at floor levels with debris impact damage (possible range extends from the ground level up to Floors 15 to 20) or the floors

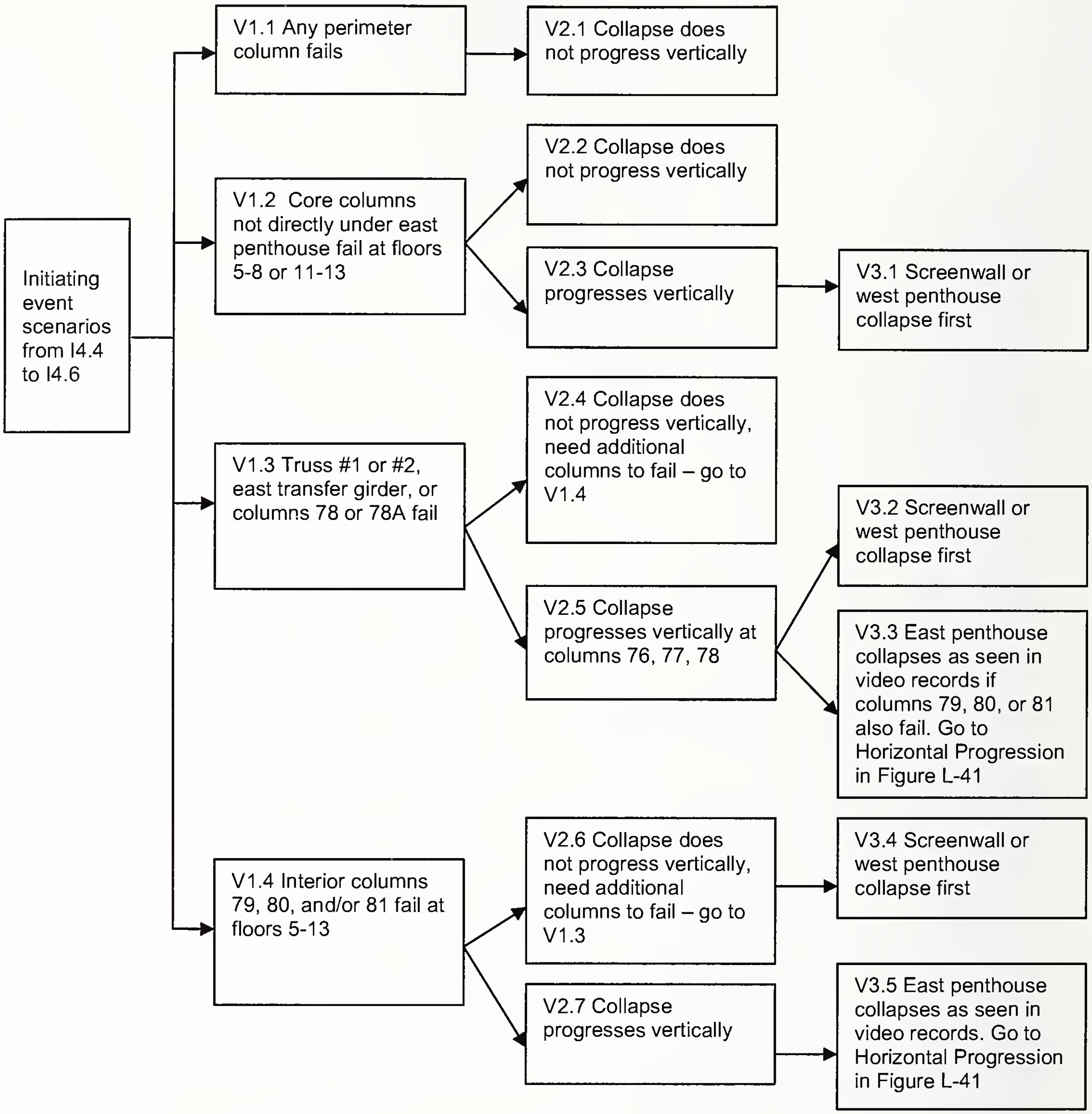

Figure L–40. Vertical collapse progression scenarios.

possibly experiencing fire (Floors 5, 6, 7, 8, 9, 11, 12, or 13). However, a core column may have failed following the failure of adjacent columns or framing members.

- **V2.2 Collapse Does not Progress:** If core columns failed, the loads above the failed columns may have been redistributed to adjacent columns through the core floor system. If the loads could not be redistributed, then additional failures in one or more components would have been necessary to progress the collapse.

- **V2.3 Collapse Progresses:** From this initial failure, the portion of the column above the failure could have fallen, progressing the failure vertically upwards.

- **V3.1 Something Else Besides East Penthouse Observed to Collapse First:** Had the failure of core columns progressed upwards, then the first exterior sign of the internal failure likely would have been seen in the screenwall or west penthouse, which are located above the core columns. A collapse mechanism analysis performed for the removal of columns 61, 64, 67, 70, and 73 produced geometry changes that differed from the observed collapse. For the scenario where each of these columns fails and the failure progresses upwards to the roof line as the adjacent floors cannot redistribute the loads, the screenwall or the west penthouse collapses, and no kink develops in the east penthouse (see Figs. L–41, L–42, and L–43).

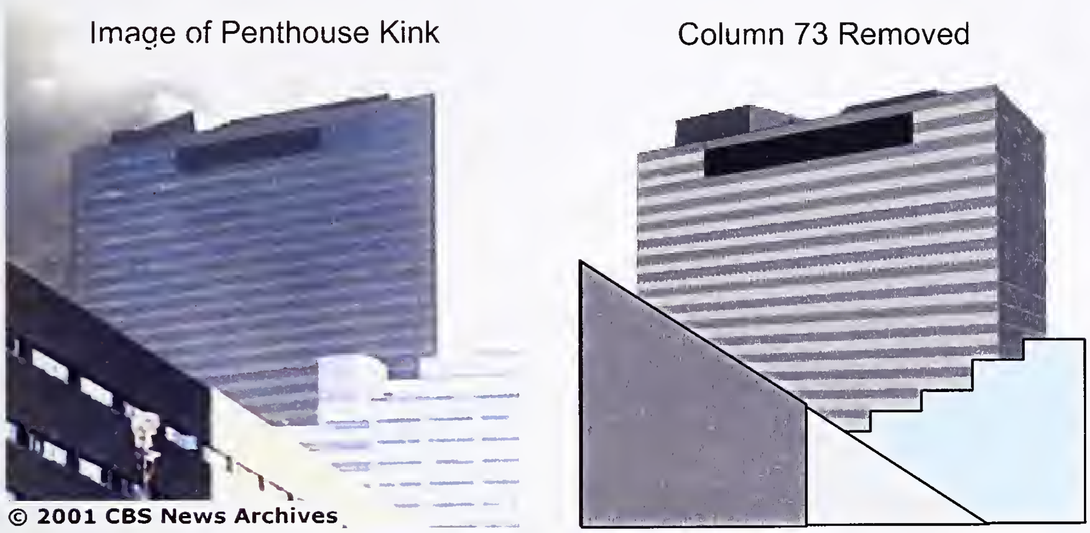

Figure L–41. Geometry changes for removal of column 73.

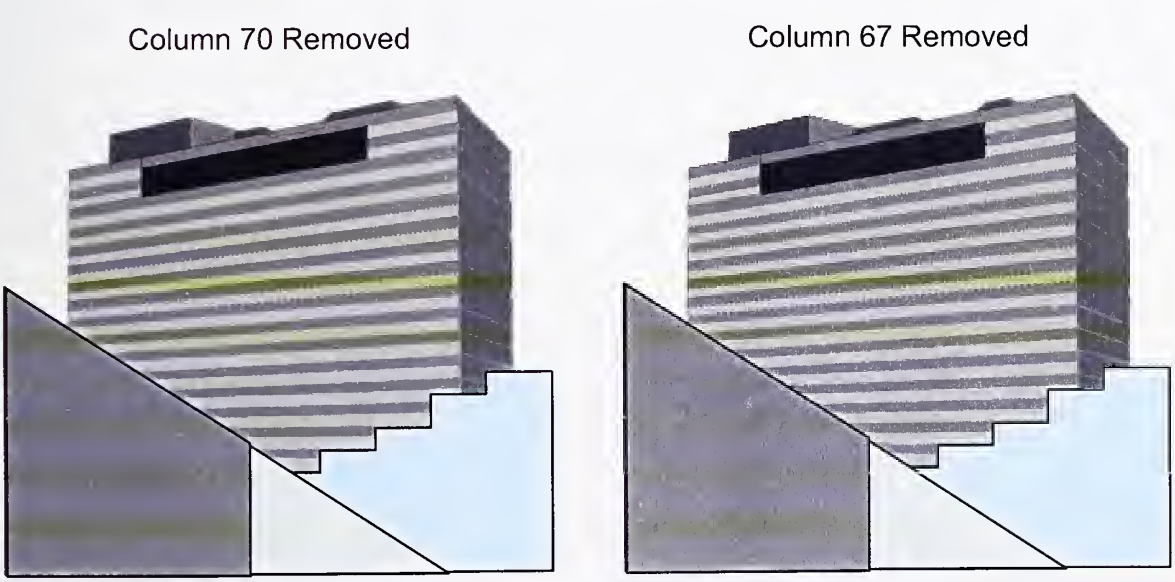

Figure L–42. Geometry changes for removal of columns 70 and 67.

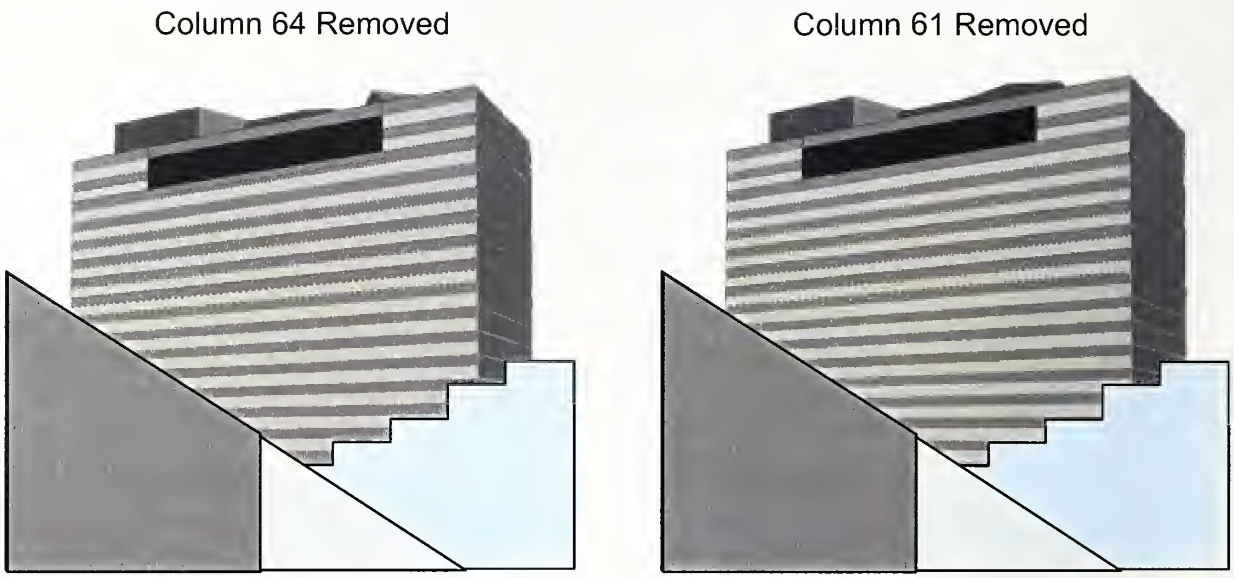

Figure L–43. Geometry changes for removal of columns 64 and 61.

V1.3 Truss #1 or Truss #2 East Transfer Girder, or Columns 78 or 78A Fail: Had the initiating component been truss #1 or truss #2, most likely there would have been debris impact damage or possibly fires at Floors 5 or 6. However, truss #2 failure could have followed the failure of the east transfer girder or columns 78 or 78A.

- **V2.4 Collapse Does Not Progress:** If truss #1 or #2 failed, the floor framing, including the Floor 7 diaphragm, may have redistributed the loads to adjacent columns. Had this occurred, additional failures in one or more components would have been necessary to progress the collapse. For instance, the columns 76, 77, 78, 79, 80, or 81 may also have failed, and the combined effect of both component failures could have been sufficient to overcome the supporting strength of the floor systems.

- **V2.5 Collapse Progresses:** If truss #1 failed, column 76 would lose its support at Floor 7, and the failure could have progressed vertically upwards if the floors could not redistribute column 76 loads. If truss #2 failed, columns 77 and 78 would lose their support at Floor 7, and the failure could have progressed vertically upwards if the floors could not redistribute the loads from columns 77 and 78.

    - **V3.2 East Penthouse Collapses Differently Than Observed:** If truss #1 or truss #2 failed and the failure progressed vertically upward to the roof level, the exterior deformations observed in the roof structures would be different from what was actually observed. Column 76 supported the west side of the east penthouse and the east end of the screenwall. A collapse mechanism analysis performed for the removal of column 76 produced a geometry change that shows the west side of the east penthouse and the east end of the screenwall deflecting downward (see Fig. L–44).

Column 76 Removed

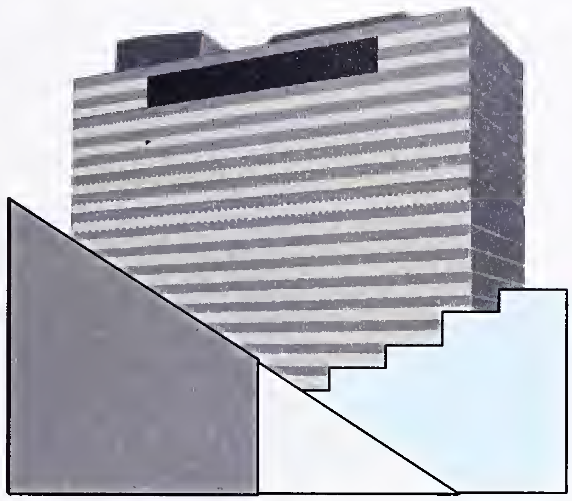

Figure L–44. Geometry changes for removal of column 76.

- **V3.3 East Penthouse Collapses as Observed:** Had the failure of columns 76 or 77 and 78 been followed by the failure of columns 79, 80, or 81, such that the failure of column 79, 80, or 81 progressed upwards, while the vertical progression of failure above columns 76, 77, and 78 was arrested, then the first exterior sign of the internal failures could have been observed at the center of the east penthouse roof.

V1.4 Interior Columns 79, 80 or 81: Had the initiating component been column 79, 80 or 81, most likely the failure would have occurred at the floors possibly experiencing fire (Floors 5, 6, 7, 8, 9, 11, 12, or 13).

- **V2.6 Collapse Does Not Progress:** If only one of columns 79, 80, or 81 failed, the floor systems above the failure area may have redistributed the column loads to adjacent columns. Had this occurred, additional failures in one or more components would have been necessary to progress the collapse vertically upwards. For instance, both columns 79 and 80 may have failed, and the loads of both columns could have been sufficient to overcome the supporting strength of the floor systems.

- **V2.7 Collapse Progresses:** If only one of columns 79, 80, or 81 failed, the floor systems above the failure area may have not been able to redistribute the column loads to adjacent columns. The floor system above Floor 7 had beams and girders, concrete slabs on metal deck, wire mesh in tenant floor areas, and rebar in the core area slabs. These floor systems do not appear to have sufficient bending or catenary action to redistribute loads for failure of column 79, 80, or 81. A calculation of the catenary action that might be developed by the beams and girders framing into column 79, assuming the floors try to redistribute the loads above the area of column 79 failure, found that the girder connections reach their capacity at approximately 10 percent of the estimated service loads and the connections probably fail at approximately 25 percent of the service loads. If the floor-to-column connections had not failed, the beams would have started to yield axially at approximately 40 percent of the service load present.

- **V3.4 East Penthouse Collapses Differently than Observed:** The collapse could have progressed upwards, but the failure caused in the east penthouse could be different than what was actually observed.
- **V3.5 East Penthouse Collapses as Observed:** Had the failure of the column progressed upwards, then it could have been reflected in the observed collapse of the east penthouse, which sits directly above columns 79, 80, and 81. Also, the kink observed in the roof of the east penthouse was in line with these columns. A collapse mechanism analysis performed for the removal of column 79 produced a deformed shape with a kink in the roof of the east penthouse (see Fig. L–45). This is a possible collapse scenario.

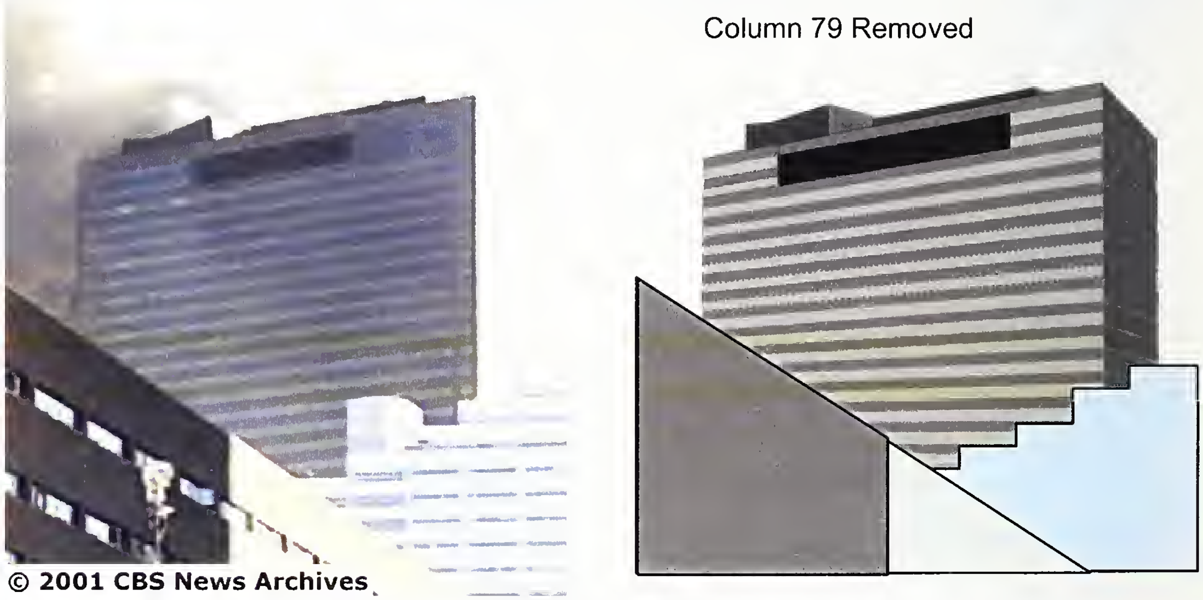

Figure L–45. Geometry change for removal of column 79.

L.3.4 Horizontal Progression Scenarios

After the east penthouse was observed to sink into the building core, approximately five seconds lapsed before the screenwall and west penthouse were observed to also sink into the building core. The screenwall and west penthouse movements occurred almost simultaneously with the global collapse of the structure. From these external observations, it appears that after the vertical progression failure on the east side of the building, the failure progressed horizontally across the core. The horizontal progression of the collapse could have started due to any of the likely vertical progression scenarios, which are shown in Fig. L–46.

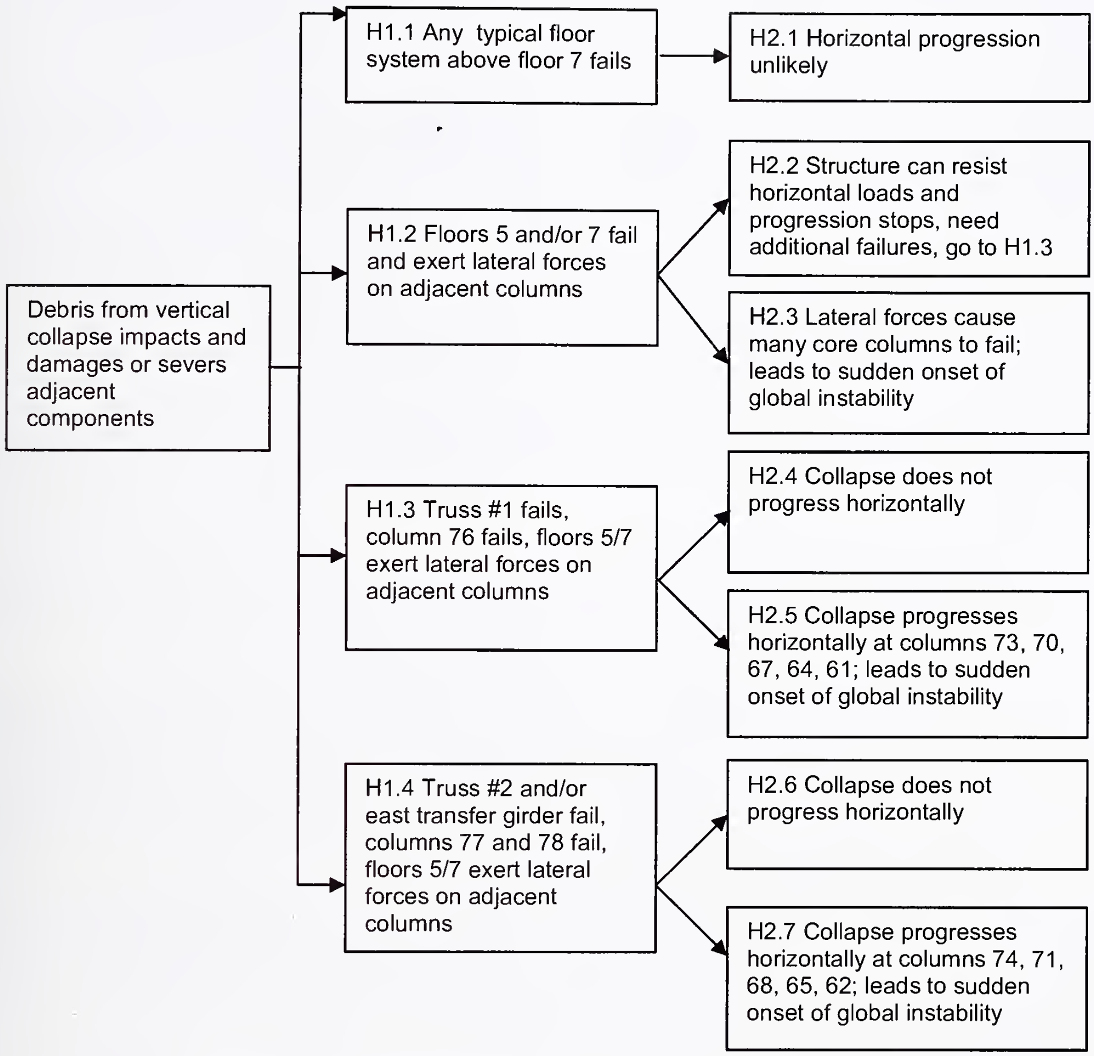

Figure L–46. Horizontal collapse progression scenarios.

The likely region in which the horizontal progression occurred is in the lower portion of the building, around Floors 5 and 7. Floor 5 had a 14 in. reinforced concrete slab on metal deck. The slab was heavily reinforced, and contained steel WT sections embedded in the slab. The WT sections were arranged in a diagonal pattern, like a horizontal truss, within the plane of the floor between the perimeter and core columns. Floor 7 had an 8 in. reinforced concrete slab on metal deck with rebar in each direction. The beams between interior columns at Floors 5 and 7 were much larger than at other floors, and the beam-to-column connections were able to transfer more of the beam axial and bending load capacity. These strong lateral ties between the interior columns may have been able to impose lateral displacements on adjacent columns. Transfer trusses and girders between Floors 5 and 7 transferred loads from the columns above Floor 7 to the foundation columns below Floor 5.

Assuming that a vertical collapse of one or more bays occurred over the height of the building, a large pile of debris would have fallen on Floor 7 and below. Such a large amount of debris is likely to have severed the Floor 7 slab and damaged or severed any transfer truss or girders in the vicinity. For a vertical collapse on the east side of the building, transfer trusses #1 and #2 and the east transfer girder may have been damaged, particularly the east diagonals of the trusses. The scenarios below describe possible responses of Floors 5 and 7 following a vertical collapse of one or more bays.

H1.1 Floor Systems above Floor 7: Typical tenant floors above Floor 7 were constructed with concrete slabs metal deck with wire mesh reinforcement. The steel framing connections were designed for shear loads only, though they could likely resist some degree of tensile catenary forces.

- **H2.1 Collapse Does Not Progress:** For any interior column failure above Floor 7, the tenant and core floor systems are not able to develop sufficient axial tensile loads for imposing lateral deflections on adjacent columns. It is likely that the floor system within a bay will fail before a column failure is propagated horizontally to adjacent columns.

H1.2 Floors 5 and 7: Floors 5 and 7 were thicker and more heavily reinforced than the typical floor systems, and may have been subjected to a large debris load from a vertical collapse within one or more bays.

- **H2.2 Collapse Does Not Progress:** Floors 5 and 7 may fail at connections to adjacent columns before developing any tensile forces large enough to cause other column failures through lateral displacements, halting the horizontal progression.

- **H2.3 Collapse Progresses:** Floors 5 and 7 may impose large tensile forces at the adjacent columns to cause lateral displacements that fail the columns. The failure mechanism could occur at the column splice, located just above Floor 5 and Floor 7, rather than through the column section. The simultaneous occurrence of column instability in many core columns would cause a sudden and large change in the structural system capacity.

H1.3 Truss #1: If one of the diagonals of truss # 1 (see Fig. L–47) was damaged or severed by collapse debris from the vertical progression, there would be a horizontal force developed in the Floor 7 slab as column 76 became unstable. The floor beam between column 76 and column 73 would try to restrain column 76 movement through tensile forces to column 73.

- **H2.4 Collapse Does Not Progress:** The horizontal tensile force would tend to pull the line of columns 73, 70, 67, 64, and 61 towards the east. The continuity of the Floor 7 slab and the presence of braced frames around the north core column line makes the simultaneous lateral displacement of the core columns less likely, as such displacements within a rigid slab may similarly displace other columns, including perimeter columns.

- **H2.5 Collapse Progresses:** The failure of column 76 may create its own vertical collapse, due to the inability of the floor systems above to redistribute the loads and fail at the column splices near Floors 5 and 7 as shown in Fig. L–48. If column 76 cannot be restrained and there is a vertical collapse of the surrounding bay, it would cause a debris pile at the lower floors which may then destabilize adjacent columns.

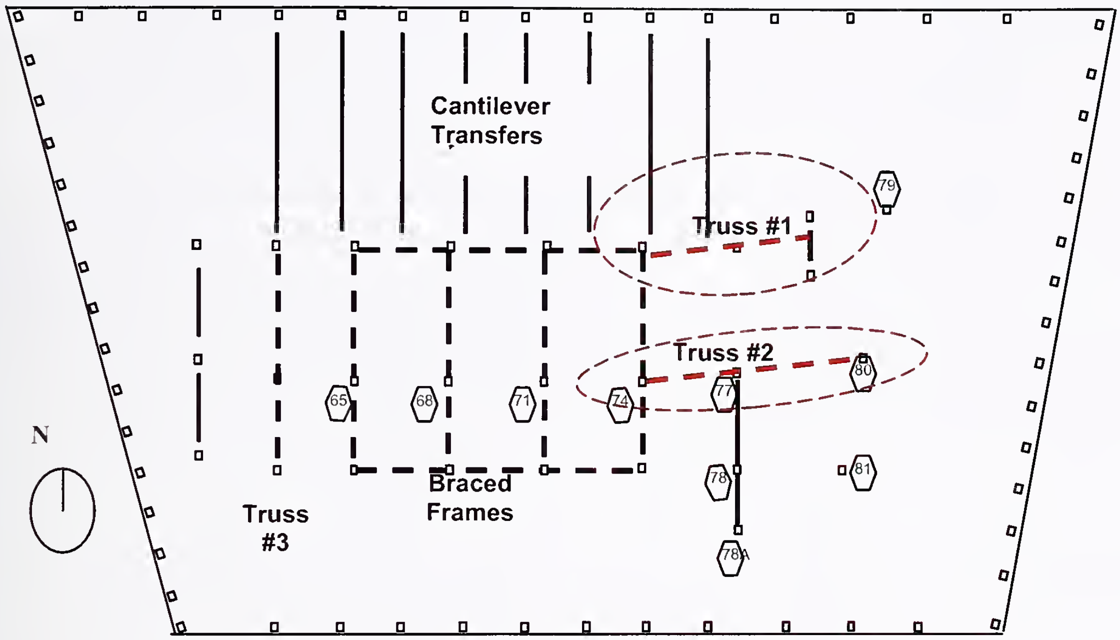

Figure L–47. Transfer components between Floors 5 and 7.

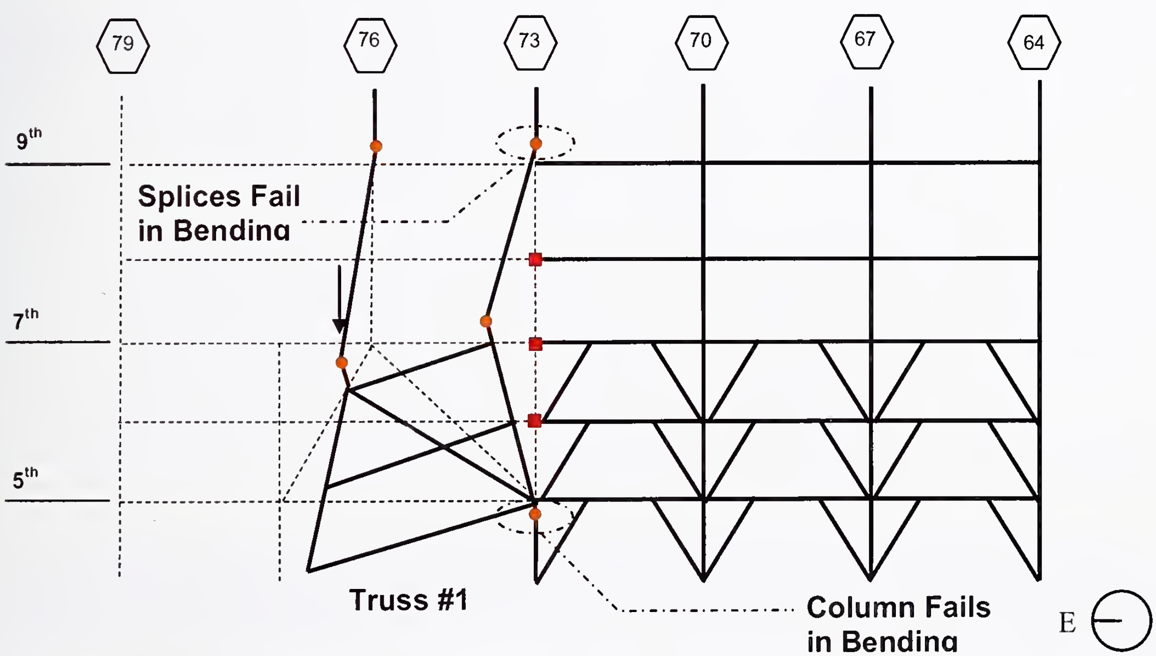

Figure L–48. Horizontal progression mechanism for truss #1 failure.

H1.4 Truss #2 and/or East Transfer Girder: If one of the diagonals of truss # 2 and/or the east transfer girder was damaged or severed by collapse debris from the vertical progression, there would be a horizontal force developed in the Floor 7 slab as columns 77 and 78 became unstable.

- **H2.6 Collapse Does Not Progress:** The Floor 7 slab may fail at adjacent columns prior to imposing lateral displacements sufficient to fail the columns or their splices.

- **H2.7 Collapse Progresses:** The horizontal tensile force would tend to pull the line of columns 74, 71, 68, 65, and 62 towards the east. The general absence of the Floor 7 slab and braced frames around the center core column line, due to the presence of elevators shafts, creates a more likely scenario for the simultaneous lateral displacement of the center core columns without similarly displacing other core columns. The possible result is a failure of all the columns at their splices, as shown in Fig. L–49.

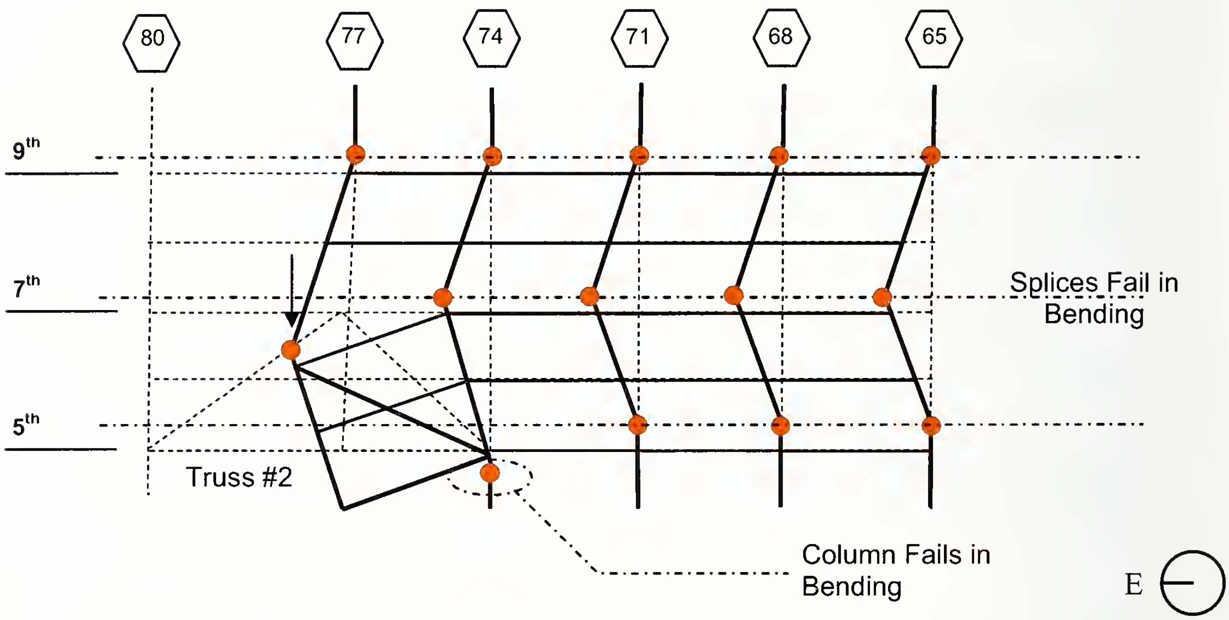

Figure L–49. Horizontal progression mechanism for truss #2 failure.

L.3.5 Summary of Working Collapse Hypothesis

The working collapse hypothesis has been developed around four phases of the collapse that were observed in photographic and videographic records: the initiating event, a vertical progression at the east side of the building, and a horizontal progression from the east to west side of the building, leading to global collapse.

From an analysis of the observed collapse sequence, the following general sequence of events appears possible:

1. Debris damaged the south face of the perimeter moment frame and some interior core framing on the south side. The debris impact severed approximately a quarter to a third of

the south face perimeter columns. The damaged floors are less certain, but reports indicate they occurred between the ground and up to Floors 15 or 20. The extent of damage, both structural and to fireproofing, of core framing is not known, but damage to elevator cars and shafts was reported to have occurred around columns 69 to 78 at Floors 8 or 9.

2. Fires were observed after the collapse of WTC 1. Fires were observed after 2 pm on Floors 7, 8, 9, 11, 12, and 13. Fires were not observed on Floor 5, but this may be due to the lack of windows. The presence of a fuel distribution system and the possibility of damage at the south face from WTC 1 debris impact, indicates that fires may have been present on Floor 5.

3. The initiating event may have included a number of structural components, though the relative role of impact damage and fire need further investigation. Possible components that may have led to the failure of columns 79, 80, and/or 81 include interior columns 69, 72, 75, 78, and 78A, the east transfer girder (which supports column 78A and frames into transfer truss #2), and adjacent framing and floor systems.

4. A vertical collapse appears to have occurred after interior columns 79, 80, and/or 81 failed. This failure mechanism would progress vertically upward within the failed bay to the roof level, as analysis indicates that the floors would not be able to redistribute their loads.

5. The debris from a 40-story vertical collapse on the east side of the building would fall down onto the strong diaphragms at Floors 5 and 7 and possibly onto transfer trusses #1 and #2, and/or the east transfer girder. Damage and loading on these floors and transfer components would generate lateral forces which would cause the failure of the remaining core columns. The horizontal progression requires further analysis and investigation, but observations indicate that the remaining core columns appeared to fail almost simultaneously, approximately 5 second after the east penthouse failed.

6. The core columns failed and redistributed loads until the building loads could no longer be supported. Once the core columns failed, the cantilever girders which supported the north facade also failed. The remaining perimeter columns at the east, south, and west facades were either left unsupported or were pulled down with the interior collapse. The global collapse occurred with few external signs prior to the system failure.

The working hypothesis, for the collapse of the 47-story WTC 7, if it holds up upon further analysis, would suggest that it was a classic progressive collapse that included:

- An initial local failure due to fire and/or debris induced structural damage of a critical column, which supported a large span floor area of about 2,000 ft^2, at the lower floors (below Floor 14) of the building,

- Vertical progression of the initial local failure up to the east penthouse bringing down the interior structure under the east penthouse, and

- Horizontal progression of the failure across the lower floors (in the region of Floors 5 and 7 that were much thicker and more heavily reinforced than the rest of the floors), triggered by damage due to the vertical failure, resulting in disproportionate collapse of the entire structure.

The working hypothesis will be revised and updated as results of ongoing, more comprehensive analyses become available.

L.3.6 Technical Approach for Analysis of the Working Collapse Hypothesis

There are many possible collapse scenarios that have been postulated in the preceding section. Many of the scenarios will not produce the observed sequence of global collapse events and can be classified as unlikely. Likely collapse scenarios will be identified through analyses that test the postulated phases of collapse against observations. It is equally important to test scenarios that are not predicted to match the observed data. The testing of the postulated collapse scenarios will be conducted through hand calculations, simplified nonlinear thermal-structural analysis, and full nonlinear thermal analysis.

L.4 REFERENCES

American Institute of Steel Construction Inc., Manual of Steel Construction, Load and Resistance Factor Design, Third Edition, 2001. Chapter 16-E.

McAllister, T., ed. 2002. World Trade Center Building Performance Study: Data Collection, Preliminary Observations, and Recommendations. FEMA 403. Federal Emergency Management Agency. Washington, DC, May.

Salvarinas, John J. 1986. Seven World Trade Center, New York, Fabrication and Construction Aspects, *Proceedings of the 1986 Canadian Structural Engineering Conference*, Vancouver, Canadian Steel Construction Council, Ontario. February 24-25.

TABLE OF CONTENTS

List of Figures

Appendix M
Interim Report on 2-D Analysis of the WTC Towers Under Gravity Load and Fire

M.1 SUMMARY

A two-dimensional (2-D) finite element model is developed to provide insight and evaluate some aspects of a possible collapse sequence for the World Trade Center (WTC) towers. For a prescribed temperature distribution that corresponds to a two-story, quarter-span fire, and for a three-story fire derived from fire dynamics simulation, diagonals of the heated trusses buckle inelastically, causing considerable sag in the fire floors. This behavior puts a high-tension demand on the truss connections to the perimeter column, which remains at moderate temperatures in this model and does not experience buckling. Because neither the prescribed nor the derived temperature distributions are necessarily representative of the actual fire, and the material properties are approximate, further work is needed to evaluate the collapse sequence and develop findings regarding the actual event.

M.2 INTRODUCTION AND REVIEW

Within days of the collapse of the WTC towers on September 11, 2001, publications postulating the mechanism of the collapse began to circulate. A substantial effort was launched by the Federal Emergency Management Agency (FEMA) and the American Society of Civil Engineers (ASCE), culminating in a preliminary building performance study (McAllister 2002). Quintiere et al. calculated the elastic buckling strength of a single diagonal of a floor truss, assuming pinned end conditions, and suggested that the buckling of such thin members exposed to fire might have initiated the collapse (Quintiere et al. 2002). More recently, Usmani et al. performed a series of 2-D, nonlinear finite element analyses of a 12-story vertical frame that comprises a perimeter column and, at each floor, a truss and floor slab supported by the column and the tower core (Usmani et al. 2003). The temperature distribution in the steel and concrete members was characterized by an assumed time-dependent profile. Usmani et al. concluded that column instability caused by the loss of bracing normally provided by floors led to overall structural collapse (Usmani et al. 2003).

The objective of this report is to present a simplified analysis approach to evaluate some aspects of the collapse sequence of the WTC towers. The analysis is based on a 2-D model that is simple and can be easily used to evaluate a wide variety of conditions. The structural system was modeled independently of connection details. At this stage, connections are the object of a separate analysis that can draw on the results presented here concerning demand upon connections at various stages of fire development.

M.3 STRUCTURAL MODEL

The vertical plane considered in the model includes perimeter column 109 on the North face of WTC 1, and five longitudinal floor trusses and slabs (floors 94 to 98). The center of the airplane impact was at floor 96, and column 109 was the intact column closest to the edge of the initial damage zone (McAllister 2002). The column extends 22 m (72 ft) to a height of six floors, and both its upper and lower ends are pinned, with the upper end free to translate vertically. The upper chords of the floor trusses are simply supported at the internal end, and connected to the perimeter column by hinges. In the actual structure, a double floor truss carries a tributary floor slab 2 m (80 in.) wide and is supported by two perimeter columns, whereas in the present model a single truss supported by a single perimeter column carries a 1 m (40 in.) wide slab. The floor spans 18.3 m (60 ft) from the perimeter column to the core. The model is similar to that of Usmani et al. (2003), except it has fewer floors.

The principal reason for including only five floors in the analysis is to have the simplest model that will still capture salient features of the collapse of the towers. The fire applied to the model only heats two floors, and the remaining floors remain cool and provide lateral restraint to the perimeter column under study. Since the ends of the perimeter column in this simple model are hinged, the model ignores the rotational restraint supplied by the continuous column if additional floors are considered. Thus the short model is less stiff than a taller model (such as the 12-floor model developed by Usmani [2003] and would buckle sooner (or at a lower mechanical or thermal load), if global buckling should occur at all. As far as translational restraint is concerned, only a very small amount of lateral bracing can have a tremendous effect on the buckling strength (Winter 1958), and the cool floors one or two stories away from the fire can be replaced by a support that does not allow horizontal translation. One additional reason for including only five floors is to provide a guide for and allow comparisons with the results of a three-dimensional study, where several full floors are included. The size of the three-dimension model is a concern.

The trusses, slabs and the column that supports them are simulated by three-node beam finite elements, capable of modeling a wide variety of cross sections, with a mesh density and number of integration points specified by the user. One particularly attractive feature of these elements is the capability of supporting linear temperature gradients across their section and along their length.

M.4 MATERIAL PROPERTIES

The various steels range in nominal yield strength from 250 MPa (36 ksi) in the floor trusses to 450 MPa (65 ksi) in the column (McAllister 2002). They are all modeled by bilinear stress-strain curves, with a tangent modulus about 0.5 percent of the elastic modulus. Figures M–1 and M–2 show the steel properties for the temperature range used in the analysis. Usmani et al. (2003) used similar steel properties.

The lightweight concrete slab is also modeled as a bilinear, ductile material (Fig. M–3), with compressive strength of 20 MPa or 3,000 psi (McAllister 2002). The top chord of the floor truss is assumed to act in a perfectly composite way with the slab and allow the tensile strength at the bottom of the slab to be equal in magnitude to the compressive strength at the top. This choice of a simple, bilinear material overestimates the tensile capacity of the slab. As well, the simplification inherent in transforming the steel top chord into an equivalent concrete section disregards the differential thermal expansion between steel and concrete. A more accurate concrete model (currently being developed) may show slab failure or a smaller horizontal tension at the connection between floor and column than the present results.

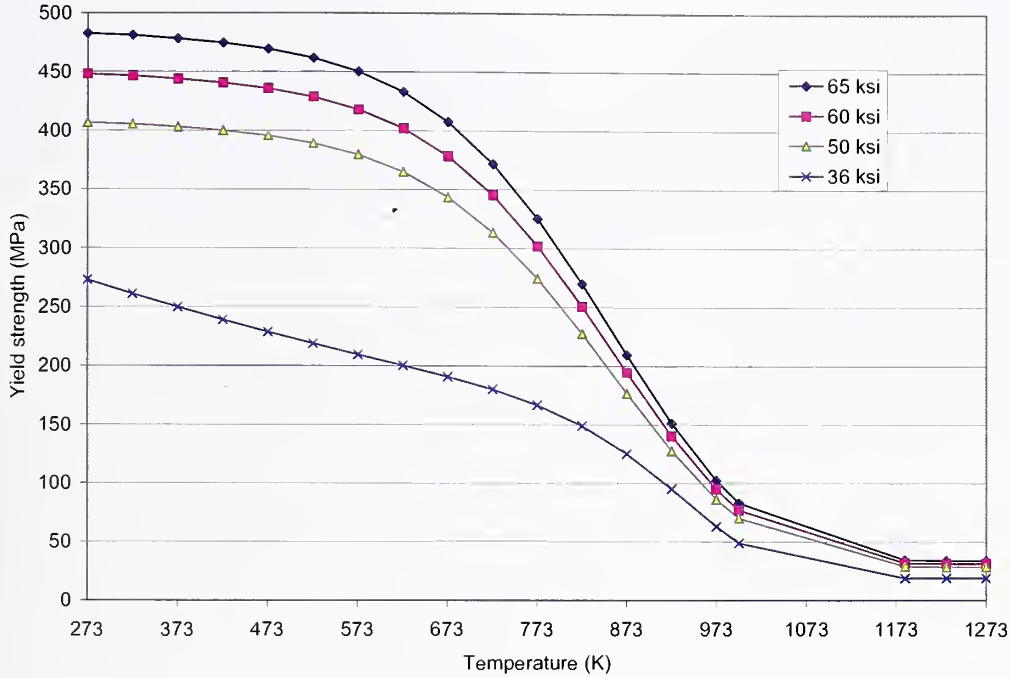

Figure M–1. Yield strength of steels used in model.

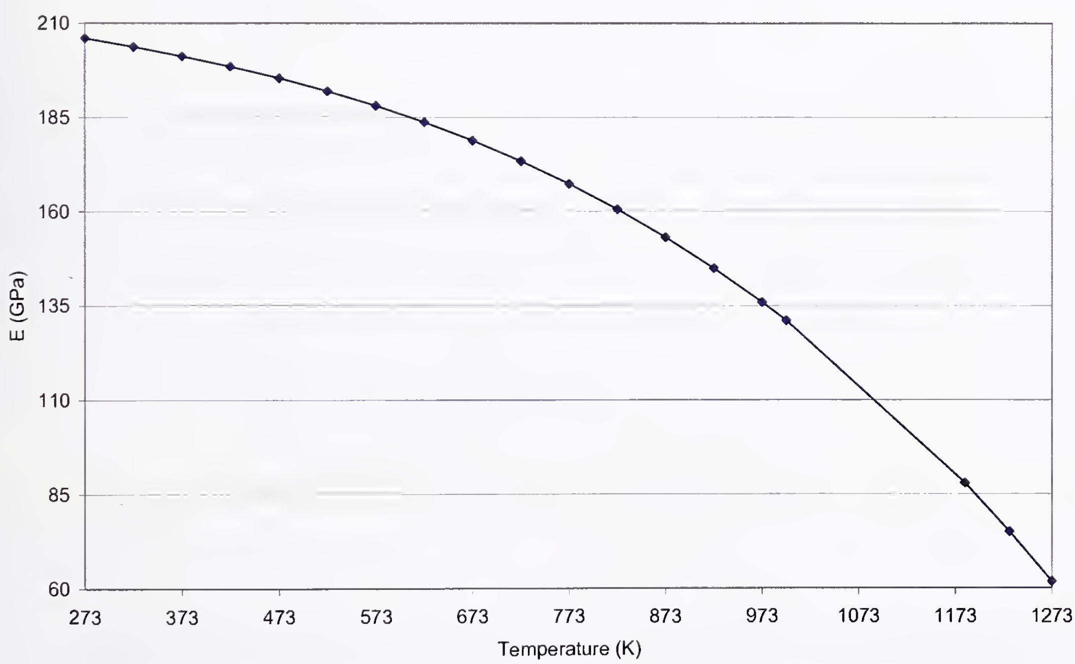

Figure M–2. Modulus of elasticity of steels used in model.

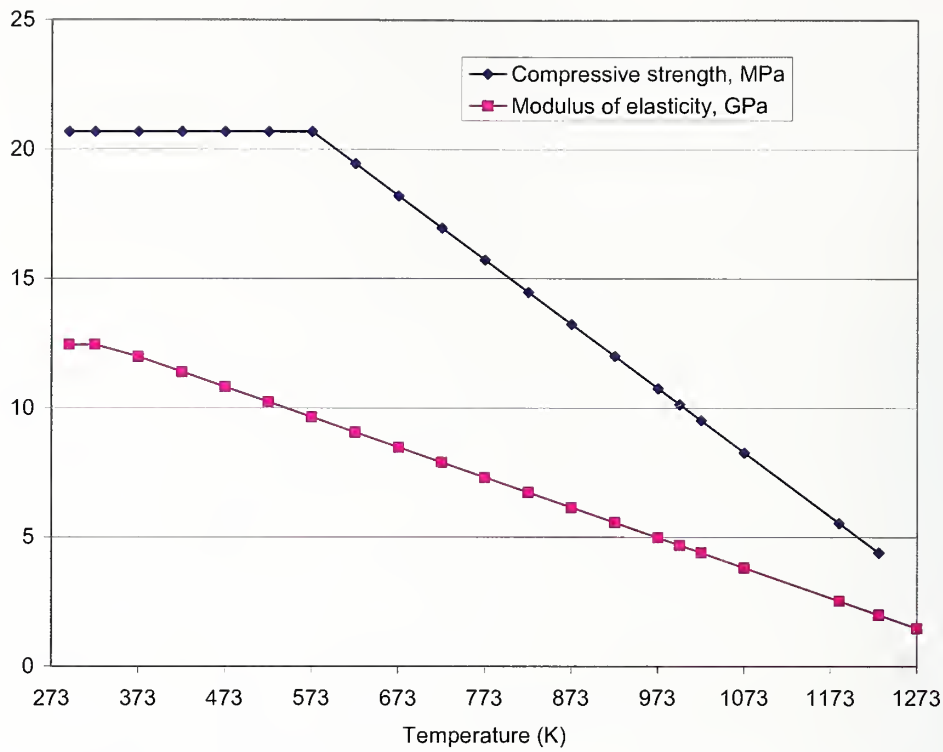

Figure M–3. Mechanical properties of concrete slab as modeled.

M.5 LOADING

The floor slabs are acted upon by a dead load of 3.3 kPa (70 psf) and a live load of 720 Pa (15 psf). The column load, determined by a linear, static finite element analysis of the global, damaged structure, includes the weight of the floors above and a surcharge due to load transfer from the columns damaged or missing after the airplane impact (Appendix D, Section D.2.4 of this report). The top of the column is loaded by a 1,100 kN (250 kip) axial compressive force and a 2,000 N·m (18 kip·in.) clockwise moment (compared to 540 kN or 120 kip, and 1,800 N·m or 16 kip·in. counter clockwise moment before damage). In addition, the column self-weight is applied along its length. For comparison, Usmani et al. (2003) used loading consistent with the FEMA report (McAllister 2002) and applied 40 percent of the gravity loads of the tributary floor strips above the model to the top of the perimeter column.

The behavior of the structure and its eventual collapse are greatly influenced by thermal loads. This report first performs an analysis based on a conventional fire, which provides a useful first approximation to the behavior of the building in fire. For comparison with the work of Usmani et al. (2003), a single temperature distribution T represented by an exponential function of time t, with a reference temperature $T_0 = 300$ K, is used. The time rate of change of the temperature, represented by coefficient $a = 0.005$, depends, among other factors, on the location and intensity of the fire, and the quality of the insulation.

$$T(t) = T_0 + (T_{\max} - T_0)(1 - e^{-at}) \tag{1}$$

A two-floor fire, with maximum temperature T_{max} = 1,273 K, heats the structure on floors 95 and 96, over the quarter-span closest to the perimeter column. Over that span, the slab of floor 95 is uniformly heated, whereas the slabs of floors 94 and 96 have linear temperature gradients across their thickness, with the bottom of slab 94 and the top of slab 96 remaining at 300 K at all times. In the three-quarters of the span not directly under fire, the temperature decreases linearly from the maximum at quarter-span to room temperature at the core. Between floors 94 and 96, the column temperature is also described by Eq. (1), with T_{max} = 400 K, whereas the rest of the column remains at 300 K at all times.

The finite element model was used further by applying to it a second temperature distribution (Fig. M–4) that corresponds to a more realistic, physics-based fire, generated by NIST's Fire Dynamics Simulator in a manner consistent with initial conditions appropriate for the WTC towers following the aircraft impacts. The gas temperatures associated with the fire were used to calculate structural member temperatures and temperature gradients, assuming an insulation thickness of 19 mm (3/4 in.) for truss members and 36 mm (1.4 in.) for the perimeter column. The fire considered in this application is more widely spread than the conventional fire, and covers four floors, with the entire floor span heated. Floor 94 (lowest) remains unheated, and the column is only moderately heated. Linear temperature gradients are modeled across the column section and the slab thickness of heated floors. The peak temperature of 1,230 K is obtained at the end of 25 temperature load steps, each 200 s apart.

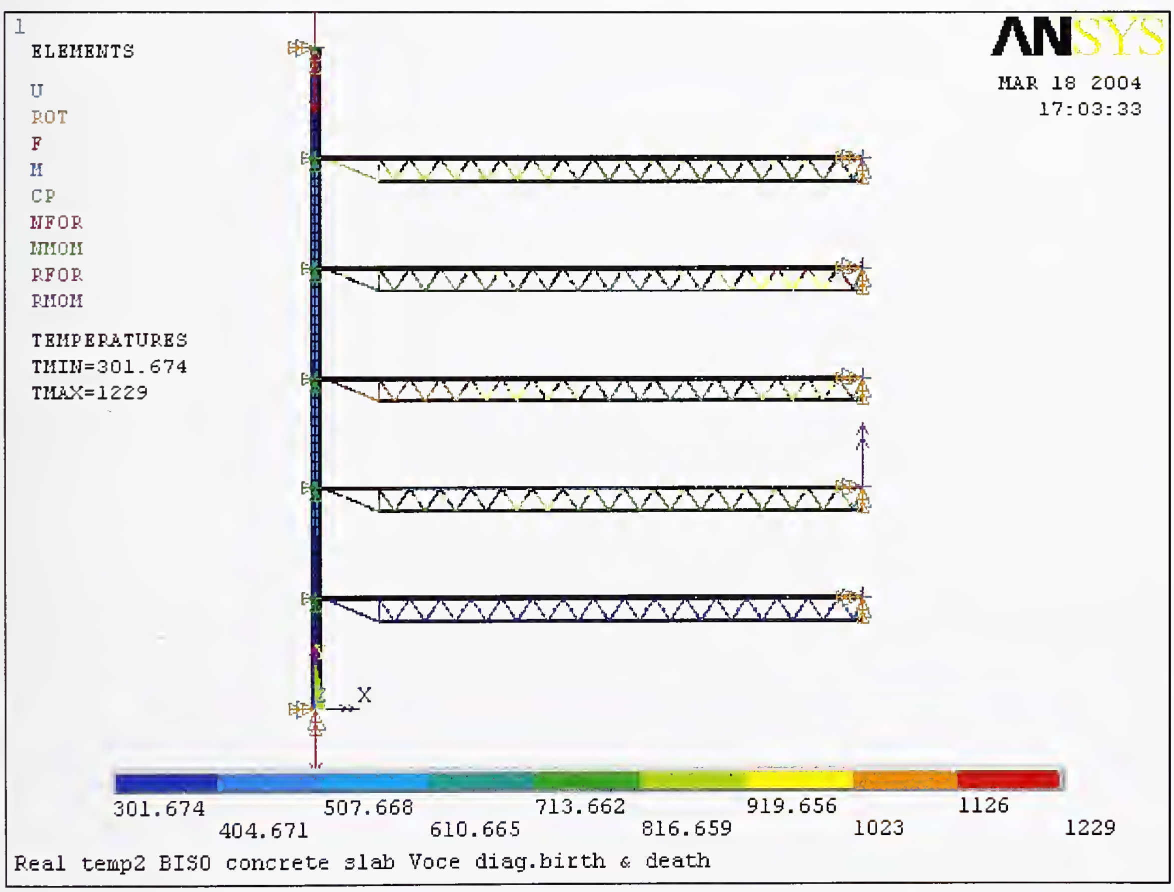

Figure M–4 Temperature distribution (K) of "real fire" scenario 2-04.

M.6 RESULTS

Nonlinear, static, large deformation analysis accounting for the magnification of flexural deflections due to axial load (P-delta effect) was performed. Member stiffness matrices are updated during the analysis to account for the P-delta effect, and when a member stiffness gets close to zero, excessive lateral deflection occurs and the member is considered to have buckled. The first analysis proceeded in eight load steps, the first corresponding to gravity loads at the start of the fire (normal room temperature). Subsequent steps occurred at 200 s intervals, with the maximum temperature attained, to within 1 K, at 1,400 s. As required in the computation, the load steps are further divided into substeps (up to several hundreds). Results for the conventional fire are shown in Figs. M–5, M–6, and M–7.

At room temperature, even under the severe load redistribution due to the damage caused by the airplane impact, the structure still behaves linearly. The maximum floor sag is 35 mm (1.4 in.), causing the horizontal span to decrease and the column to pull in slightly. Approaching 200 s and a temperature of 915 K (the temperatures referred to in these results are the hottest temperatures in the structure at any given time), the heated truss begins to show distress, especially in the compressed diagonal and vertical web members, which buckle inelastically. This means these heated steel members do not buckle elastically, but rather reach yielding in compression. Buckling is then governed by the tangent modulus of steel, which is about 0.5 percent of the elastic modulus, and the members immediately buckle after yielding, in the inelastic range. At 200 s, the maximum floor sag increases to 335 mm (13.2 in.), and the column is pushed out (peak of 38 mm or 1.5 in.) by the thermal expansion of floor 95. At that time, the connection of floor 95 to the perimeter column experiences its maximum compression of 125 kN (28 kip). Because slab 96 has a thermal gradient with its top surface at room temperature, its lateral expansion is much smaller than for slab 95, and its sag is larger. The connection between slab 96 and the column is always in tension (Fig. M–6). As expected, slab 94, heated at the top and cool at the bottom, bows upward. As the temperature continues to rise, more of truss 95 web members buckle inelastically, and the increasing sag begins to pull the column in. The horizontal deflection of the column becomes positive (inward), and the connection force between column and floor 95 turns to tension. This inward movement of the column relieves the tension in the connection between the column and floor 96. Further temperature rise causes further weakening in truss 96, which eventually becomes active in pulling the column in. At the peak temperature of 1,273 K, the maximum lateral deflection in the column (183 mm or 3.3 in.) occurs at floor 96, inward, and the connection between the column and floor 96 experiences a tension of 185 kN (42 kip).

Under the second fire scenario, the structure exhibits similar behavior. Figures M–8, M–9, and M–10 show the resulting deflections. Inelastic buckling of the diagonals causes considerable vertical deflection of the heated floors beyond a maximum temperature of 900 K. At 1,220 K, the sag of floors 96 and 97 overcomes the outward push on the perimeter column due to thermal expansion of floors, and pulls the column inward. This transition causes the column to temporarily straighten up, causing the overall floor deflection to be less. Figures M–11 and M–12 show severe horizontal tension greater than 120 kN (27 kip) at the connection of floors with the internal column (floor 95) and external column (floor 96).

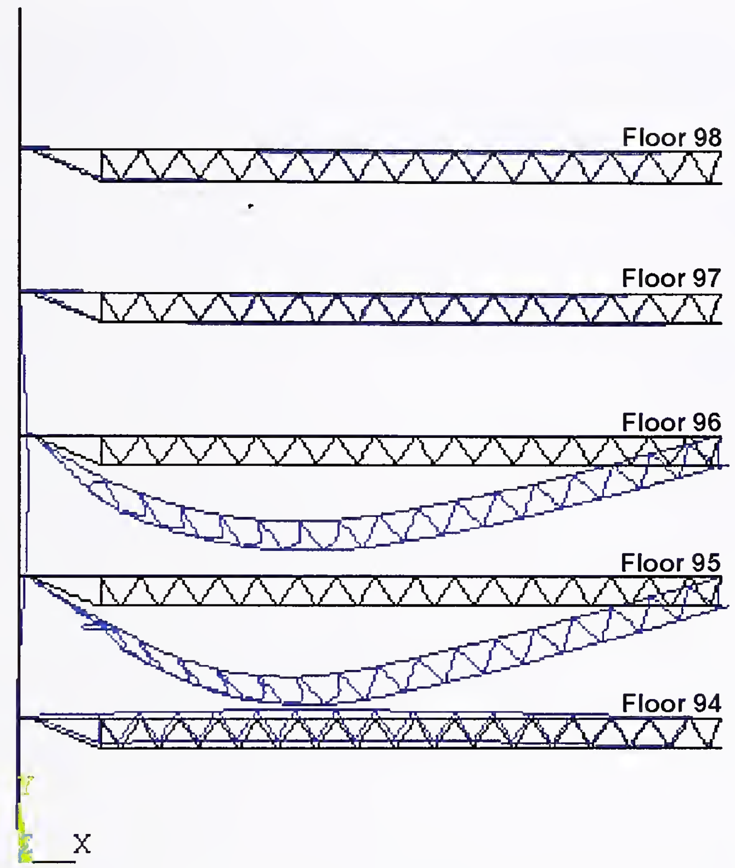

Figure M–5. Deformed shape at 1,273 K (not to scale).

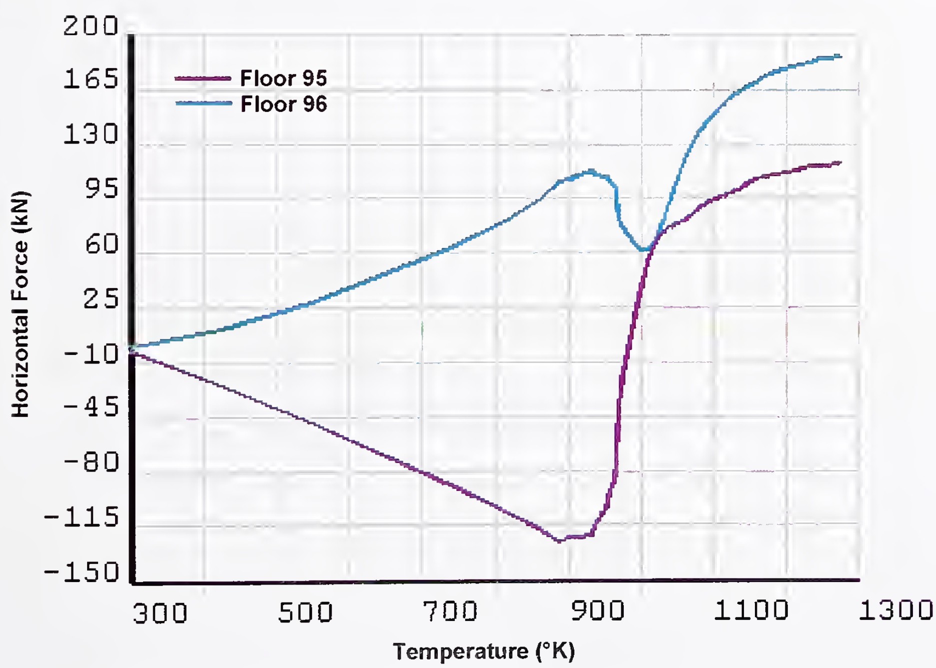

Figure M–6. Horizontal force (kN) between column and floors versus temperature (K).

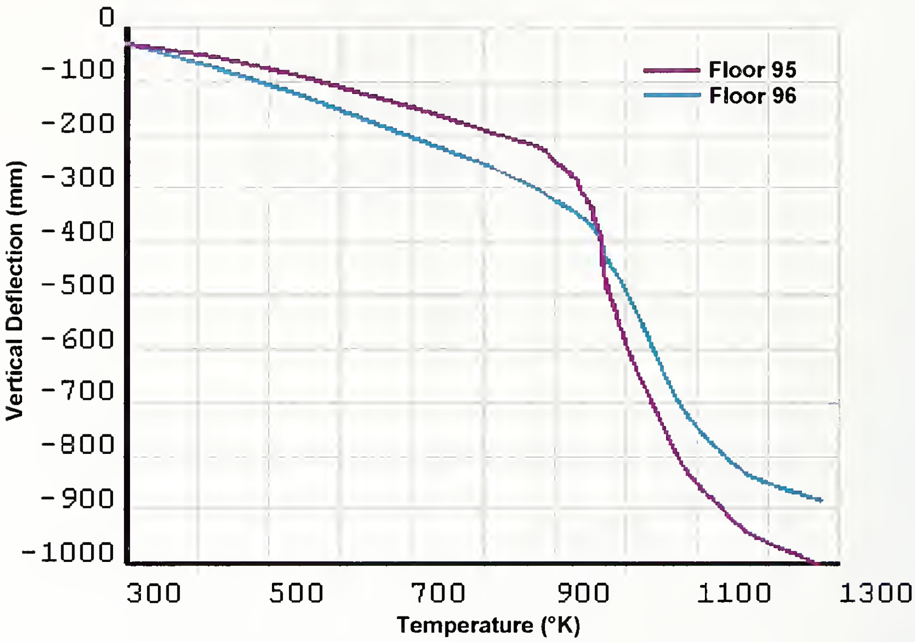

Figure M–7. Vertical deflections (mm) of floors versus temperature (K).

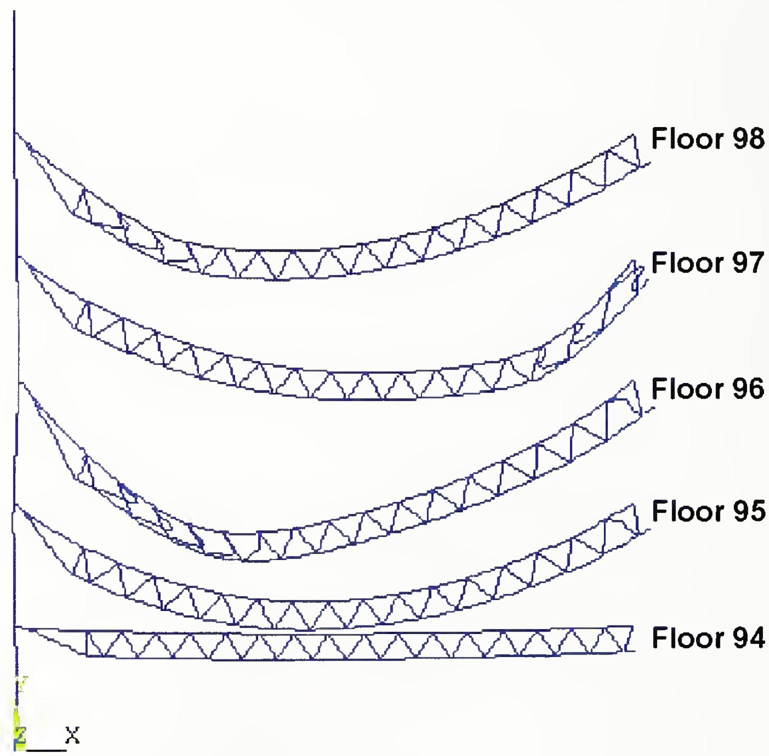

Figure M–8. Overall deflected shape for fire scenario 2-04 (not to scale).

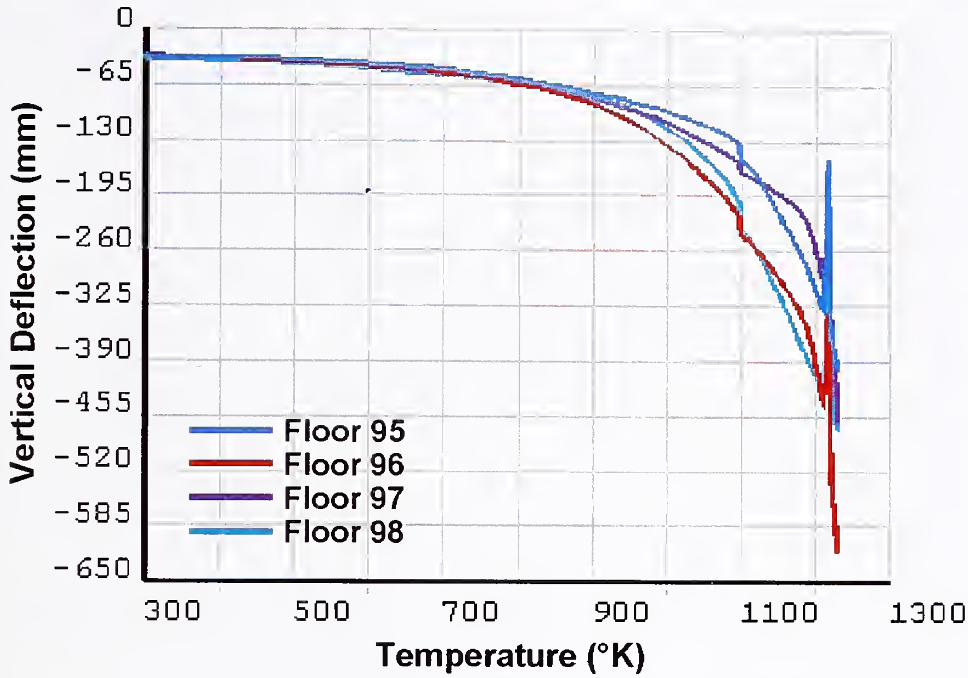

Figure M–9a. Maximum deflection of floors 95–98 for fire scenario 2-04.

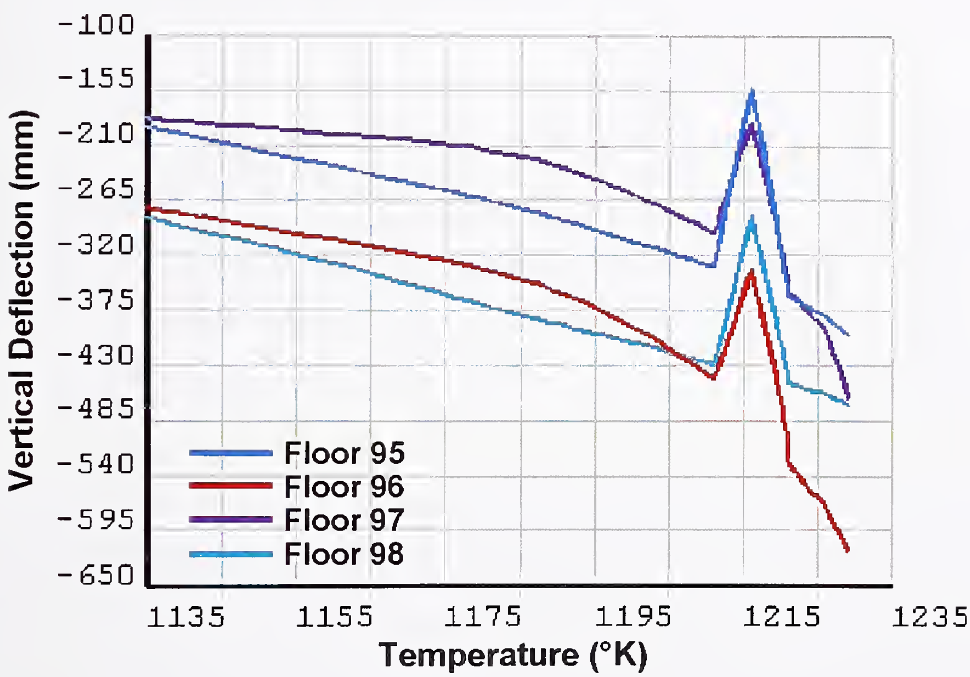

Figure M–9b. Maximum deflection of floors 95–98 for fire scenario 2-04: details of Fig. M–9a at high temperatures.

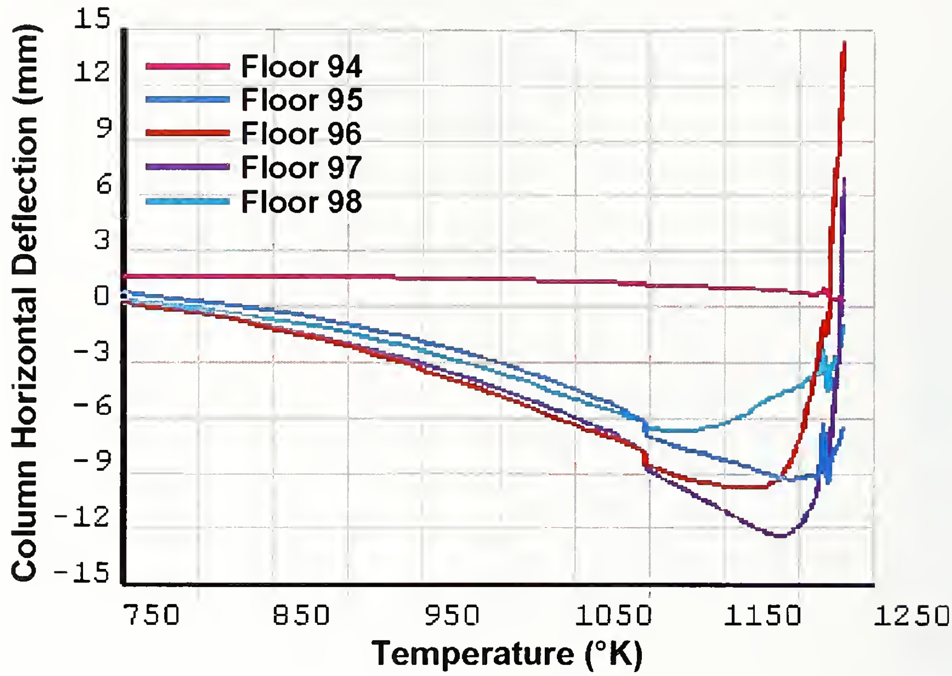

Figure M–10. Perimeter column lateral deflection for fire scenario 2-04.

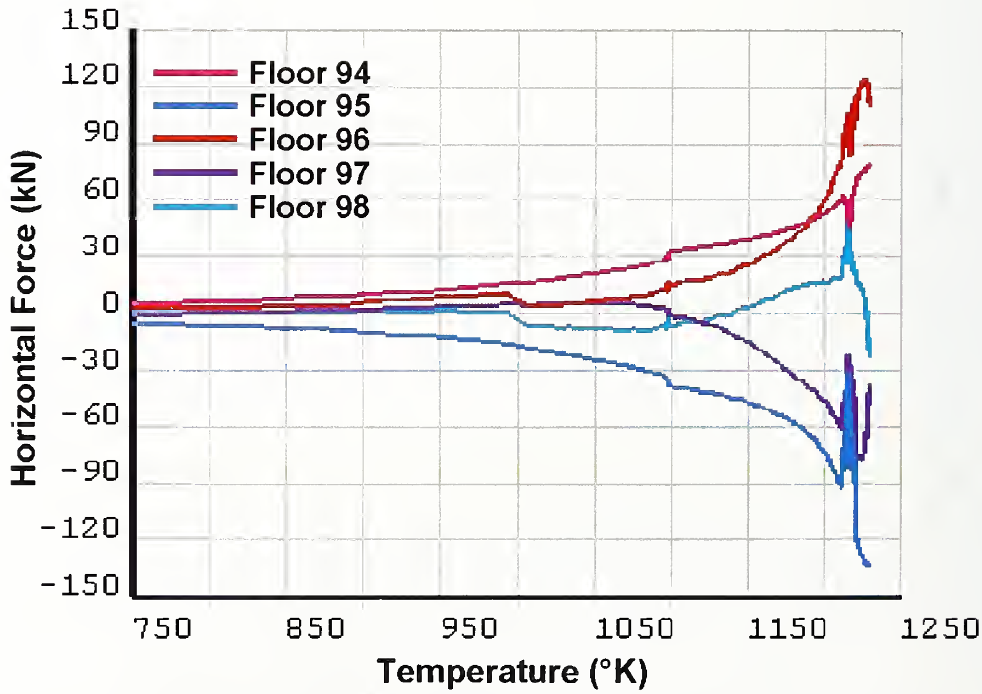

Figure M–11. Horizontal force at connection between floor and internal column for fire scenario 2-04.

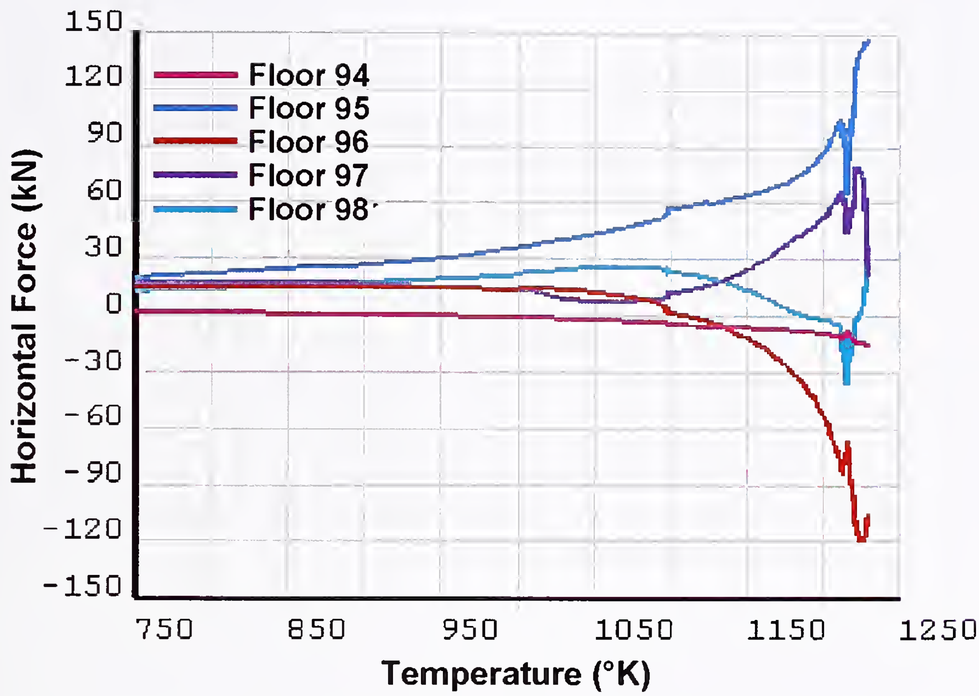

Figure M–12. Horizontal force at connection between floor and external column for fire scenario 2-04.

NIST analysis of connections is ongoing and will indicate whether this or other connections can supply the calculated demand, and if not, at what temperatures connection failures will occur. In this regard, the loss of composite behavior of the concrete slab with the steel truss may occur at a temperature and strain level yet to be determined.

For comparison with Quintiere et al. (2002), the present results show that the truss diagonals buckle *inelastically*, and there is considerable reserve strength after the first diagonal buckles. At the highest temperatures analyzed, seven diagonal and the vertical web members had buckled in each of the floors heated by the conventional fire. This conclusion assumes that the various structural connections maintain their integrity throughout the fire.

M.7 CONCLUSIONS

A model has been developed to provide insight and evaluate some aspects of a possible collapse sequence of the WTC towers. Its results are subject to the following qualifications: (1) the approximate nature of the material properties used, especially the concrete slab; (2) connection failures are not considered, although information is provided on demand experienced by the connections; and (3) the model is two-dimensional. In one of the two cases covered by this report, the temperature distribution of the members is selected from among those assumed by Usmani et al. (2003). In the second case, the temperature distribution is physically based, and was obtained by using the NIST Fire Dynamics Simulator with reasonable initial conditions associated with a damaged tower. In both cases, the diagonals buckle inelastically, causing considerable sag in the fire floors. This behavior puts a high-tension demand on the column, which remains at moderate temperatures in this model (same temperature as in Usmani et al. [2003]), and does not experience buckling. This is the major difference between these results and Usmani et al., even though the heated trusses in the present model are exposed to a much higher temperature and the column to a more severe load that reflects load redistribution in the damaged structure. One possible explanation for the difference is that failure modes may be sensitive to material properties.

M.8 NOTE

For confirmation, a 12-floor model (from floors 91 to 102) was developed and loaded with the same floor load and conventional temperature distribution described by Eq. 1 (Usmani et al. 2003) and mentioned above. Compared to case 1 reported earlier, the hinged column end conditions, the heated floors (95 and 96) and the bending moment applied on top of the perimeter column are the same, but the axial compression is reduced (950 kN or 210 kip) because of the fewer floors above the model. Results of the 12-floor model, shown in Figs. M–13, M–14, and M–15, are very similar to those of the 5-floor model, thus confirming the discussion in Section M.3.

M.9 REFERENCES

McAllister, T., ed. 2002. *World Trade Center Building Performance Study: Data Collection, Preliminary Observations, and Recommendations*. FEMA 403. Federal Emergency Management Agency. Washington, DC, May.

Quintiere, J. G., M. DiMarzo, and R. Becker. 2002. A suggested cause of the fire-induced collapse of the World Trade Towers, *Fire Safety Journal*, vol. 37, no. 7. October, pp. 707-716.

Usmani, A. S., Y. C. Chung, and J. L. Torero. 2003. How did the WTC towers collapse: a new theory, *Fire Safety Journal*, vol. 38, no. 6. October, pp. 501-533.

Winter, G. 1958. Lateral bracing of columns and beams, *ASCE Journal of Structural Division*, Proc. 1561. March. Also in ASCE Transactions 3044.

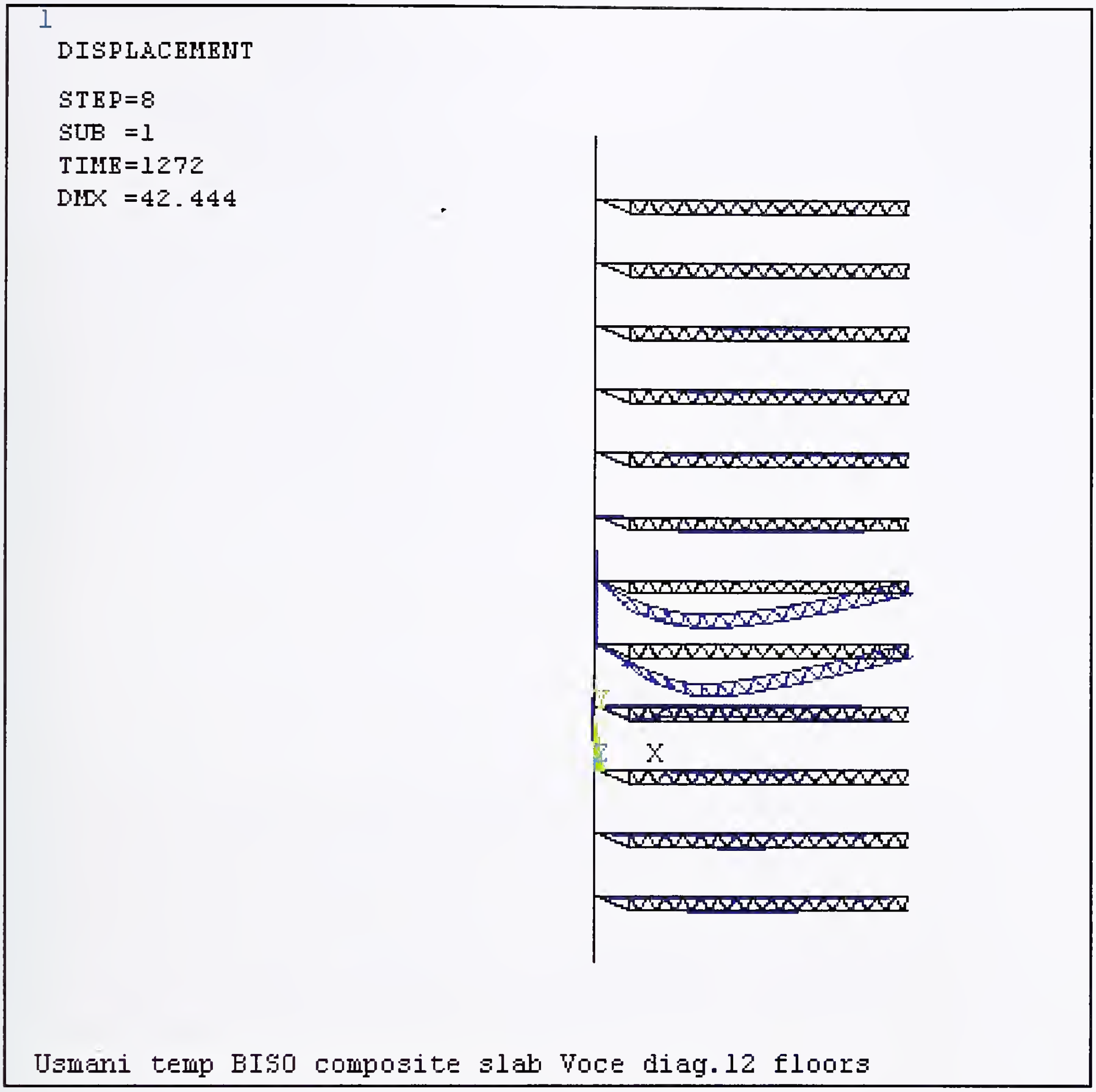

Figure M–13. Overall deflection (not to scale) of 12-floor model (floors 91–102) subjected to gravity loads and with floors 95 and 96 under conventional fire: at the maximum temperature of 1,272 K, the maximum deflection is 1.08 m.

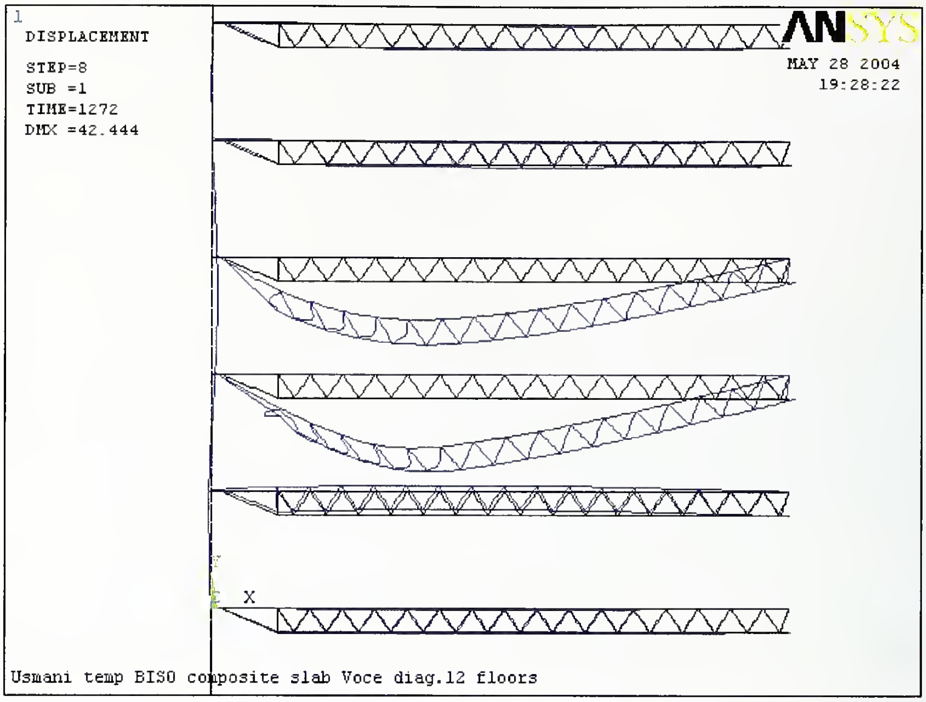

Figure M–14. Details of floors 93–98 for the 12-floor model shown in Fig. M–13 (compare with Fig. M–5).

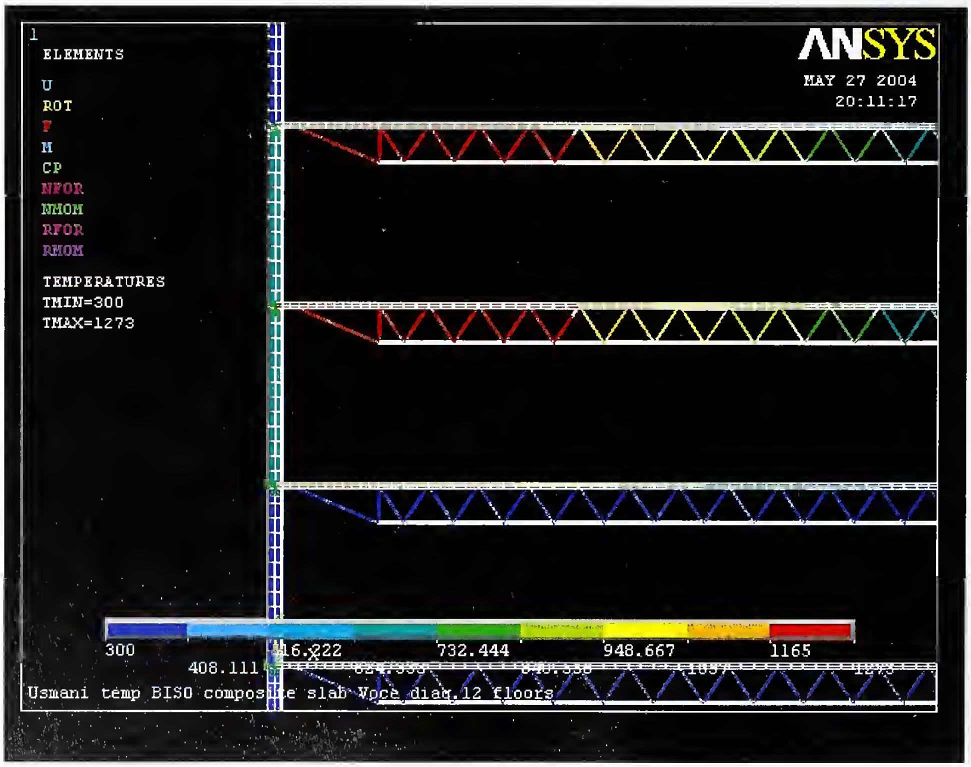

Figure M–15. Details of temperature distribution of floors 92–95 for 12-floor model: note temperature gradients across slab thickness of floors 93 and 95, and cool column.